Cy. 4

ORNL-4560
UC-25 – Metals, Ceramics, and Materials

FUELS AND MATERIALS DEVELOPMENT PROGRAM

QUARTERLY PROGRESS REPORT

FOR PERIOD ENDING MARCH 31, 1970

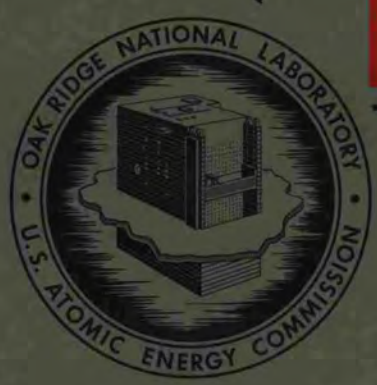

OAK RIDGE NATIONAL LABORATORY
operated by
UNION CARBIDE CORPORATION
for the
U.S. ATOMIC ENERGY COMMISSION

Printed in the United States of America. Available from Clearinghouse for Federal
Scientific and Technical Information, National Bureau of Standards,
U.S. Department of Commerce, Springfield, Virginia 22151
Price: Printed Copy $3.00; Microfiche $0.65

ORNL-4560

Contract No. W-7405-eng-26

METALS AND CERAMICS DIVISION

FUELS AND MATERIALS DEVELOPMENT PROGRAM QUARTERLY PROGRESS REPORT FOR PERIOD ENDING MARCH 31, 1970

Compiled by

P. Patriarca

Edited by

D. J. Rucker

AUGUST 1970

OAK RIDGE NATIONAL LABORATORY
Oak Ridge, Tennessee
operated by
UNION CARBIDE CORPORATION
for the
U.S. ATOMIC ENERGY COMMISSION

FOREWORD

This quarterly progress report describes research and development on nuclear fuels and materials performed at the Oak Ridge National Laboratory for the U.S. Atomic Energy Commission. This work is either sponsored by or of particular interest to the Fuels and Materials Branch of the Division of Reactor Development and Technology.

Progress on these programs is reported for the three major divisions of the work — Fast Reactor Technology, Space Power Technology, and General Reactor Technology — under the appropriate AEC activity titles listed below.

AEC Activity Title	AEC Activity Number
PART I. FAST REACTOR TECHNOLOGY	
FUELS	
DEVELOPMENT OF LMFBR OXIDE FUELS	04 40 02 01 1
DEVELOPMENT OF HIGH-PERFORMANCE LMFBR FUELS	04 40 02 01 1
EFFECT OF POWER CYCLING ON LMFBR FUEL-CLADDING BEHAVIOR	04 40 02 01 1
LMFBR FUEL ELEMENT DESIGN AND MODEL DEVELOPMENT	04 40 02 01 1
CLADDING AND OTHER STRUCTURAL MATERIALS	
MECHANICAL PROPERTIES OF ALLOYS IN REACTOR ENVIRONMENTS	04 40 02 03 1
DEVELOPMENT OF LMFBR CLADDING AND STRUCTURAL MATERIALS	04 40 02 01 1
FABRICATION DEVELOPMENT FOR LMFBR STAINLESS STEEL TUBING	04 01 61 01 5
WELDING DEVELOPMENT FOR LMFBR VESSELS AND COMPONENTS	04 40 02 04 1
SHIELDED METAL-ARC WELDING FOR LMFBR COMPONENTS	04 01 61 01 5
NONDESTRUCTIVE TESTING TECHNIQUES FOR LMFBR	04 40 02 04 1
SODIUM CORROSION STUDIES	04 40 02 02 1
DEVELOPMENT OF FAST-REACTOR NEUTRON-ABSORBER MATERIALS	04 40 02 02 1

*Research sponsored by Division of Space Nuclear Systems.

CONTENTS

CLADDING AND OTHER STRUCTURAL MATERIALS

PART II. SPACE POWER TECHNOLOGY

FUELS

CLADDING AND OTHER STRUCTURAL MATERIALS

PART III. GENERAL REACTOR TECHNOLOGY

FUELS

CLADDING AND OTHER STRUCTURAL MATERIALS

SUMMARY

PART I. FAST REACTOR TECHNOLOGY

FUELS

1. DEVELOPMENT OF FAST REACTOR OXIDE FUELS

About 1.5 kg of microspheres containing $(U,Pu)O_2$ were prepared for loading into fuel pins for the Experimental Breeder Reactor-II (EBR-II). Analysis during this quarter by autoradiography, electron microprobe, and γ-ray spectroscopy indicated that the concentrations of Pu in the microspheres were variable in certain of the sublots provided. We attributed this variation in Pu concentration to failure to thoroughly mix the separately prepared UO_2 and PuO_2 sols. Because of this variation, we had to prepare an additional 0.9 kg of microspheres for the EBR-II experiments. Analyses of this additional material showed them to be homogeneous with respect to concentrations of Pu and U. We developed final, detailed procedures for loading the EBR-II unencapsulated pins by the Sphere-Pac process and for obtaining the required pellet densities of 83, 88, and 93% of theoretical density. Several hundred pellets of controlled density for the EBR-II 37-pin subassembly were prepared. Other activities concerned with the fabrication of the 37-pin subassembly included qualification of raw materials, welding development, fabrication and inspection of components and equipment, and preparation of procedures. Analysis of the activities listed by the critical-path schedule shows that the project is approximately 42% complete. The design of the ORNL fuel pin for the 37-pin subassembly was approved by the EBR-II project.

A sol-gel Sphere-Pac capsule containing $(U,Pu)O_2$ has sustained a calculated burnup of 9.2 fissions per initial actinide metal atom (FIMA) in the Engineering Test Reactor (ETR), and irradiation of the capsule is continuing at a peak heat rate of 15 kw/ft with a target burnup of 10% FIMA. The third instrumented capsule being irradiated in the Oak Ridge Research Reactor (ORR), which contains one Sphere-Pac Fuel pin and one

sol-gel pellet fuel pin of the same composition and smear density, has been operated to a temperature of 1935°C at the center of the fuel. The preliminary results from this capsule show that the Sphere-Pac fuel has lower central temperatures than the pellets at a given heat rate, indicating that the Sphere-Pac pins have a higher effective coefficient of heat transfer between the fuel and cladding. The difference is not large and may be insignificant with respect to experimental accuracy. However, it is further evidence that the Sphere-Pac fuel, on the basis of thermal performance, performs almost identically like pelletized fuels. Two instrumented capsules to be irradiated in the ETR were completed and shipped to the ETR late in the quarter. The purpose of these capsules is primarily chemical interaction between fuel and cladding for Sphere-Pac and pellet fuels under peak LMFBR thermal conditions.

Postirradiation examination of six fuel pins tested in the Transient Reactor Test Facility (TREAT) and containing sol-gel-derived $(U,Pu)O_2$ pellets and Sphere-Pac microspheres continued. Dimensional data indicate no significant changes in pin diameter except for an ovality of 0.001 to 0.005 in. in one pin and a localized ovality of 0.0015 at the bottom of another pin. Another significant result was that stereomicroscopy showed that the Sphere-Pac fuel restructured, even with the extremely short exposure experienced by the fuel in TREAT. No obvious changes occurred in the structure of the pellets used in the tests.

We are continuing the irradiation in the encapsulated Sphere-Pac $(U,Pu)O_2$ fuel pin in subassembly X050 in the EBR-II. At the end of this reporting period, the calculated peak burnup was 5.6% FIMA.

2. DEVELOPMENT OF HIGH-PERFORMANCE LMFBR FUELS

We examined the sinterability of (U,Pu)N powders derived from an alloy and compared it with the behavior of powders derived from mechanical mixtures of UN and PuN. With proper pretreatment, the mechanically mixed materials can be sintered to reasonably dense structures that have microstructures and precision lattice parameters identical to those obtained from powder synthesized from a U-Pu alloy of the same U-Pu molar composition. We observed difficulties in synthesizing

nitride powders from the alloy in that they tended to contain small concentrations of free metal after synthesis was apparently complete. We are studying the effects of annealing on the lattice parameter of PuN and the phases derived when powders are synthesized from U-Pu alloy. We produced 185 pellets of (U,Pu)N from an alloy and 45 sintered UN specimens for use in the irradiation program.

3. EFFECT OF POWER CYCLING ON LMFBR FUEL-CLADDING BEHAVIOR

Because of the sparsity of pertinent data under liquid-metal-cooled fast breeder reactor (LMFBR) conditions, the first two irradiation experiments in this program were designed for near-term application to the Fast Flux Test Reactor (FTR). These will investigate (1) whether schemes of fuel management that involve significant power increases will be limited by mechanical interactions of fuel and cladding during power cycling and (2) whether power cycling is, indeed, of concern when the fuel element is designed to maximize these interactions.

4. LMFBR FUEL ELEMENT DESIGN AND MODEL DEVELOPMENT

The models used for fuel swelling and release of fission gas in the FMØDEL code were normalized and compared with experimental data for $(U,Pu)O_2$ fuel pins.

Light microscopy, conventional replica electron microscopy, and scanning electron microscopy were used to characterize the microstructure and the size distribution and location of bubbles of fission gas in a low-burnup Sphere-Pac $(U,Pu)O_2$ fuel pin.

Parametric calculations were performed with the FMØDEL code to investigate the effects of recent correlations for cladding swelling on the cladding stress-strain distribution and diametral expansion of a typical liquid-metal-cooled fast breeder reactor (LMFBR) fuel pin.

A review of the physical properties of type 316 stainless steel was completed. A subsequent section on mechanical properties is in progress, and the part on tensile properties is nearly completed.

Tensile yield data on type 316 stainless steel tubing were summarized. Creep equations for the British cold-worked modified type 316 stainless steel were suggested for use in modeling studies. Creep curves were produced for annealed type 316 stainless steel to investigate whether significant recovery occurs following stress reductions. No such effect was observed; however, additional experiments are planned with LMFBR-grade tubing.

CLADDING AND OTHER STRUCTURAL MATERIALS

5. MECHANICAL PROPERTIES OF ALLOYS IN REACTOR ENVIRONMENTS AND DEVELOPMENT OF LMFBR CLADDING AND STRUCTURAL MATERIALS

We examined samples of type 304 stainless steel that had been irradiated to a fluence of 4×10^{22} neutrons/cm^2 (> 0.1 Mev) at 370 to 800°C. The density change reached a maximum at an irradiation temperature of 450 to 500°C. Dislocation structures were produced at irradiation temperatures up to 630°C, but none were produced above 770°C. With increasing irradiation temperature to about 570 to 630°C, the concentration of voids decreased and their size increased. Samples irradiated at 770 to 840°C contained cavities that we believe are He bubbles.

Comparative studies of the void densities and sizes in pure metals and in alloys reveal several important differences in behavior. The results seem to support a model for alloys in which compositional changes surrounding voids reduce the local diffusion rates and limit the growth of the voids. Voids in pure metals seem to grow without bound.

The importance of irradiation temperature on the property changes that occur in stainless steels has been demonstrated repeatedly. Since the maximum void size is a unique function of the irradiation temperature, we suggest that microstructure may be a useful method for determining the irradiation temperature.

6. FABRICATION DEVELOPMENT FOR LMFBR STAINLESS STEEL TUBING

We continued studies to show the relationship among processing variables, mechanical properties at elevated temperature, and physical defects of tubing.

Varying the temperature of heat treatment between 750 and 775°C did not greatly influence the final grain size of type 316 stainless steel.

We found no significant differences in the stress-rupture properties at 650°C when we compared type 316 stainless steel with ultrafine grain size after 20% cold work and in the stress-relieved condition. In both conditions, the tubing had unusually high ductility for material not in the recrystallized condition.

7. WELDING DEVELOPMENT FOR LMFBR VESSELS AND COMPONENTS

Continuing our study of the submerged-arc process, we prepared multipass weldments in 1-in.-thick plate to investigate the effect of heat input on mechanical properties at elevated temperatures. We also prepared welds using each of the four fluxes available commercially for the submerged-arc welding process in order to study the effect of flux composition on properties. Approximately 200 in. of weld in 1-in.-thick plate were produced for fracture-mechanics studies at the Naval Research Laboratory and for associated studies at ORNL.

Tests of the mechanical properties of the experimental weldments are continuing. Initial tests show the submerged-arc specimens to be substantially weaker but to have higher ductility than the shielded metal-arc specimens. Several heat treatments are also being studied, including a solution anneal and an anneal plus aging to agglomerate carbides. Both treatments appear to improve ductility without decreasing rupture strength. Scanning electron microscope fractography shows a strong correlation between the solidification substructure and ferrite distribution and the fracture path and appearance.

8. SHIELDED METAL-ARC WELDING FOR LMFBR COMPONENTS

The "prototypic" Fast Flux Test Facility (FFTF) submerged-arc weldments in 2-in.-thick plate were completed. Tests of mechanical properties and fracture studies on 14 shielded metal-arc weldments are continuing. Although optical metallographic examination revealed no significant differences in microstructure, the properties of strength and ductility vary markedly.

Aging before testing reduced ductility, confirming that the loss of ductility as a function of rupture time is an aging phenomenon. Third-stage creep was most strongly affected; as rupture life increased, a greater portion of the fracture surface showed fracture between phases. Formation of sigma phase is believed to be responsible for the lack of ductility.

Additions of several minor elements resulted in strengthening: B, P, C, and Si in order of decreasing potency.

9. NONDESTRUCTIVE TESTING TECHNIQUES FOR LMFBR

New circuit modules were constructed that are common to both the phase-sensitive instrument and the new instrument that measures both the size and depth of defects. Stainless steel welds containing intentional flaws are being examined with the schlieren system.

Construction was begun on many of the components for the prototypical instrument for measuring changes in magnetic permeability in stainless steel tubing.

10. SODIUM CORROSION STUDIES

The partitioning of O between V alloys and Na was investigated at 600°C. The addition of Cr to V lowers the concentration of O entering into solid solution during equilibration with Na. The effect of O contamination on the creep rate of unalloyed V was determined at 600°C. The creep rate was higher in an atmosphere containing a small partial pressure of O_2 (5×10^{-7} torr) than in ultrahigh vacuum. However, the addition of O to V before creep testing had a negligible effect on creep in the ultrahigh vacuum. A bimetallic thermal-convection loop composed of V and type 304 stainless steel was examined following operation with Na for 3000 hr at a maximum temperature of 700°C. Insert specimens of V increased in C, N, and O; the specimens of stainless steel were decarburized. The interstitial changes in the V specimens lowered elongation and increased yield strength at room temperature. The oxidation of type 316 and 304L stainless steel was studied at 760°C in a 99% N_2–1% O_2

mixture containing 100 ppm H_2O. Both alloys exhibited excellent resistance to scaling, and the oxidation resistance of type 316 stainless steel to oxidation was markedly better in this gas mixture than in moist air. The effect of Na leakage on the oxidation of type 304L stainless steel was studied in the N_2 + 1% O_2 mixture at 760°C. At relatively fast leakage rates, the escaping Na had only a small effect on the wall of the tubing and reacted mainly with surrounding thermal insulation. With smaller leaks, a film of Na_2O_2 was formed on the stainless steel surface and materially increased the oxidation rate.

11. DEVELOPMENT OF FAST-REACTOR NEUTRON-ABSORBER MATERIALS

We examined structural changes in boron carbide during annealing. Adding B to a boron carbide powder to raise the ratio of B:C from 3.6 to 5.0 before annealing eliminated void formation during the heat treatment at 1500 and 2000°C. Adding C to lower the ratio of B:C from 3.6 to 3 increased the volume of voids. The size of the voids was larger at 2000°C than at 1500°C.

We refined a technique for producing Debye-Scherrer x-ray patterns of irradiated boron carbide. Free graphite present in the unirradiated samples was not detectable on the x-ray patterns of the irradiated sample.

Boron carbide powders with a ratio of B:C of 3.6 were irradiated at 350°C in the Oak Ridge Research Reactor (ORR) to measured burnups of 6.6 to 9.4% ^{10}B atoms. Helium release for all samples was between 5.0 and 5.8%.

PART II. SPACE POWER TECHNOLOGY

FUELS

12. DEVELOPMENT OF URANIUM MONONITRIDE FUELS

The middle fuel pin of capsule UN-3 failed after 5800 hr of operation at a cladding-surface temperature of 1370°C. Several short cracks

were visible in the cladding over the fueled region of the pin. Visual examination and dye penetrant tests established that the claddings of the top and bottom fueled pins remained sound during the irradiation test. Metallographic examination of the failed (middle) pin showed that the fractures in the T-111 cladding (W lined) were primarily intergranular. These fractures are preceded by spherical voids, the nature of which is not yet known. Intergranular separations that originated at the inner surface and extended through half the wall thickness were also present in the unfailed region of the cladding. The electron microprobe analysis showed no evidence of U in either the T-111 cladding or the W lining. The top and bottom fuel pins were examined by neutron radiography; the length of the fuel column of each pin had increased by 2.3% during irradiation. The pellet interfaces were clearly shown for the top pin, but the fuel column of the bottom pin appeared to be a continuous body.

CLADDING AND OTHER STRUCTURAL MATERIALS

13. CLADDING MATERIALS FOR SPACE ISOTOPIC HEAT SOURCES

We determined the tensile properties of two experimental V-Co-Ni alloys at high temperatures and, as expected, found the ordered alloy superior to the disordered alloy and much less sensitive to temperature. We prepared Pt and Ir alloys for evaluation, and the oxidation of one, Pt–21 at. % Cr–4 at. % W, was determined at 1000°C in air.

We fabricated capsule shapes from Nb–1% Zr, Mo, and Mo–0.5% Ti by back extrusion at 1200°C and are evaluating the use of Mo coatings and higher temperatures in an attempt to back extrude Ta–10% W and T-111 capsules.

14. PHYSICAL AND MECHANICAL METALLURGY OF REFRACTORY ALLOYS

An apparatus for measuring the creep properties of T-111 in low-pressure N_2 is nearing completion. The hardness of Ta–65% Hf increases in diamond pyramid hardness by about 250 as a result of aging for 7 min

at 850°C. An electron-beam-melted ingot of this alloy can be cold forged without difficulty. A Ta–40% Zr alloy was prepared for x-ray studies to verify whether a miscibility gap exists in the system.

Rupture times for welds of T-111 are equal to those for the base metal at low stresses but are shorter at high stresses. The creep properties of C-129Y were measured at 980, 1095, and 1205°C. Studies on the remelt temperatures of filler metals for brazing continue. The thermal conductivity, electrical resistivity, and thermopower of Ta–5% W were measured between 80 and 400°K.

15. TUNGSTEN METALLURGY

High-purity W sheet was produced by chemical vapor deposition for welding studies. We also deposited tubing and sheet of W-low Re alloys. Sheet containing 2% Re or less contained significantly fewer nodules than the W–5% Re material. In preliminary experiments, we attempted to deposit W with a dispersion of TiO_2 by means of the reaction of a mixture of H_2, WF_6, $TiCl_4$, and H_2O gases.

Continued studies showed that at 1650 and 2000°C the creep strength of W in 10^{-5} torr O_2 is only 1/3 to 1/5 of what it is in a vacuum of 10^{-7} torr. Initial results from creep-rupture tests of high-purity chemically vapor deposited W at 1400, 1650, and 2200°C show significantly higher reduction in area at 2200°C for this material than was found in previous studies. Additional long-time creep data for arc-melted W, W–5% Re, W–26% Re, and W–25% Re–30% Mo showed lower values for the time to produce 1% creep than was previously predicted from the Larson-Miller parameters.

In our welding studies we determined the welding variables, preheat temperature, and stress-relief treatment needed to weld chemically vapor deposited W and arc-melted W–25% Re sheet successfully by the gas W-arc process.

16. FAST-NEUTRON IRRADIATION EFFECTS ON ELECTRICAL INSULATORS

An assembly containing four advanced insulator materials was inserted into the Experimental Breeder Reactor-II (EBR-II) for irradiation at 400

and 800°C, and the irradiation of a low-temperature (below 150°C) assembly containing three of these materials was completed in the Engineering Test Reactor (ETR). The purpose of these irradiations is to determine whether any of these advanced materials is more stable than polycrystalline alumina in a fast flux.

An assembly containing bilayers and trilayers was irradiated in the ETR, and another assembly was inserted into the EBR-II.

17. CORROSION STUDIES OF ADVANCED REFRACTORY METALS

A T-111 forced-circulation loop (FCLLL-1) is being operated with Li at a maximum temperature of 1370°C and a temperature difference of 165°C. The test was interrupted after 1735 hr by a Li leak in a vent line leading to the hot leg. We are presently repairing the leak and parts of the system damaged by the release of Li.

PART III. GENERAL REACTOR TECHNOLOGY

FUELS

18. FISSION-GAS RELEASE AND PHYSICAL PROPERTIES OF FUEL MATERIALS DURING IRRADIATION

Data for the thermal diffusivity of UO_2 during irradiation was processed by means of a computer program to obtain values for thermal conductivity. The irradiation of the sol-gel $(U,Pu)O_2$ was completed. These specimens begin to release bursts of fission gas, characteristic of breakaway release, after 1.7% heavy-metal burnup.

19. DEVELOPMENT OF FUEL ELEMENT FABRICATION

Our studies of the irradiation performance of Al-base dispersion fuel elements is continuing along with an investigation of improved processing techniques for the fabrication of dispersion plates.

We examined 50% high-fired U_3O_8-Al dispersions irradiated to an average fission density of 2.24×10^{21} fissions/cm^3. Some evidence of

incipient failure was observed at the end of this plate, where the burnup corresponded to 2.5×10^{21} fissions/cm^3.

Dispersion plates that contain the burned grade of U_3O_8 appear to be more resistant to blistering after irradiation than those that contain the high-fired grade of oxide. Also, the presence of fines increases the temperature at which the plates that contain the high-fired grade of U_3O_8 blister after irradiation.

We continued our investigations of the use of scattered and fluorescent radiation for measuring the thickness of cladding with studies of the angle, intensity, and energy of scattered radiation.

20. TECHNICAL ASSISTANCE IN PROCUREMENT OF FUEL ELEMENTS

We assisted the Advanced Test Reactor (ATR) project by examining the problem of characterizing void volume for ATR fuel plates. We wrote a standard, general operating procedure for measuring fuel plates. We measured full-sized ATR plates of types 8 and 19 fabricated at ORNL. The results from both plates agreed with the results of previous measurements of miniature plates.

CLADDING AND OTHER STRUCTURAL MATERIALS

21. BEHAVIOR OF REFRACTORY MATERIALS UNDER IRRADIATION

A long-term, low-temperature (below 150°C) assembly containing carbides of Ti, Zr, Ta, Nb, and W was irradiated in the Engineering Test Reactor (ETR). The results are expected to be useful in defining damage mechanisms.

Specimens of depleted UN, $U^{15}N$, and UN-UC (50-50 mole %) were irradiated at about 150°C in the ETR to determine the effects of He gas generated through the $^{14}N(n,\alpha)^{11}B$ reaction. The results will be compared with those from a high-temperature (1000°C) assembly still being irradiated.

22. JOINING RESEARCH ON NUCLEAR MATERIALS

Data obtained at room temperature on the tensile properties of welds made in Incoloy 800 with commercial and experimental Incoloy 800 filler metals showed that an alloy nominally containing 0.02% P had the best reduction in area. The presence of nominally 0.015% S decreased both strength and ductility. All welds except that made with Inconel 82T, a commercial filler metal, failed in the weld metal.

An investigation of the experimental Incoloy 800 type of alloys by means of the Duffers Gleeble showed that the hot ductility during heating is impaired by the presence of S. Low levels (0.01 to 0.04%) of C tend to lower the zero ductility temperature of the alloy and somewhat reduce the recovery of ductility during cooling.

We began investigating the effect of certain minor elements on the ductility of Inconel 600 at intermediate temperature (about 650°C). Tensile tests are under way.

An extensive metallographic and electron-microprobe investigation is being conducted on experimental low-Ni alloys. Four alloys formulated to contain 0, 6, and 10% ferrite in an austenite matrix were examined after a homogenization treatment in H_2 for 1 hr at 1150°C. This study showed that the alloy designed to contain no ferrite (and containing Mn) did, indeed, contain measurable amounts of ferrite. The alloys with quite different levels of Ni and Cr that were designed to contain ferrite did contain it; however, the size and distribution were considerably different.

An electron-beam microprobe analysis revealed a ratio of Ni:Cr of 1.5 in the austenite matrix, regardless of the nominal composition of the alloy.

23. NONDESTRUCTIVE TESTING

Our analytical work in electromagnetic theory emphasized response to flaws in plate and design of coils for the phase-sensitive instrument. We further improved the accuracy, stability, and sensitivity of the phase-sensitive instrument.

We used polaroid filters in an attempt to improve the sensitivity of our ultrasonic schlieren system. An analytical model was developed to identify the size and orientation of flaws by ultrasonic frequency analysis. Correlation is good between calculated and measured sizes for reflection both in water and in metal. We developed techniques for accurately fabricating cylindrical reference discontinuities by means of electrodischarge machining.

We are continuing parametric studies on scattered radiation spectra as a function of the angles of incident and scattered radiation. For these studies, we use a precision goniometer and a multichannel analyzer.

24. IMPROVEMENT OF HASTELLOY N AND RELATED COMPOSITIONS

Laboratory melts and small commercial melts of Hastelloy N modified with Ti, Nb, and Hf were irradiated at 760°C to a thermal fluence of 3×10^{20} neutrons/cm^2. Several alloys had good properties after irradiation, and electron microscopy revealed the presence of finely dispersed carbides of the MC type in these alloys. The addition of Si causes the formation of large carbides of the M_6C type. If the concentration of Ti, Nb, and Hf is high enough, fine carbides of the MC type are also formed when Si is present.

25. ADVANCED MATERIALS FOR STEAM GENERATORS

A study is underway to investigate general and preferential corrosion of welds in steam at 595 and 650°C. Specimens have now experienced exposures of more than 10,000 hr. We used weight gains to predict the amounts of corrosion to be expected after 20 years. We also measured and tabulated scale thicknesses. We found that the depth of the scales on Inconel 625, Hastelloy X, and IN 102 at 595 and 650°C, when they were used either as base metal or filler metal, never exceeded 3 μm except in the case of the IN 102 alloy used as base metal at 595°C. The scales formed on Incoloy 800 used as base metal and on Inconel 82 used as filler metal were comparable in thickness to those of the foregoing alloys. Scale thicknesses were greater on Hastelloy W used as filler metal and on Inconel 600.

PART I

FAST REACTOR TECHNOLOGY

FUELS

1. DEVELOPMENT OF FAST-REACTOR OXIDE FUELS

P. Patriarca A. L. Lotts

The objective of this program is to obtain an economically optimized $(U,Pu)O_2$ fuel cycle for a liquid-metal fast breeder reactor (LMFBR) by extending the performance capability and advancing the fabrication technology of oxide fuels. These fuels have the most advanced technology and greatest potential for reliable operation in first-generation LMFBR's. They have been tested in fast-flux environments but as yet have not been exposed under actual prototypic conditions. Currently, the burnup and heat rate are limited to about 50,000 Mwd/metric ton and 16 kw/ft, respectively, based on irradiation experiments with fuels that are not necessarily optimized for thermal, chemical, and mechanical performance.

Preparation of $(U,Pu)O_2$ Fuel Materials

W. T. McDuffee[1]

Preparation of PuO_2 Sol

Five standard PuO_2 sols (150 g of Pu in each) were prepared. Two lots (a total of 300 g of Pu) were prepared for blending with enriched UO_2 sol and conversion into pellet fuel. One lot (150 g of Pu) was prepared for blending with enriched UO_2 sol and conversion into pellet fuel for the capsules for the series II irradiation in the Experimental Breeder Reactor-II (EBR-II). Two lots (a total of 300 g of Pu) were blended with enriched UO_2 sol and converted into dense microspheres for use in Sphere-Pac fuel for the capsules for the series II irradiation in the EBR-II.

Preparation of Enriched UO_2 Sol

We prepared a total of twelve lots of 93% enriched UO_2 sols, each containing 300 g of U, for use in studies of fuel fabrication. Two lots

were converted into dense $^{235}UO_2$ microspheres for fuel; ten lots (3.0 kg U) were blended with PuO_2 sol to produce a ratio of Pu:(U+Pu) of 0.2 and converted into $(^{235}U_{0.8},Pu_{0.2})O_2$ fuel. About 60% of the blended sol was to be fabricated into pellet fuel and the remainder into Sphere-Pac fuel for loading into the capsules for the series II irradiation in the EBR-II.

Formation of $(U,Pu)O_2$ Microspheres

We completed the preparation[2] of about 1.5 kg of dense $(^{235}U,Pu)O_2$ microspheres for loading by the Sphere-Pac technique into the capsules for the series II irradiation in the EBR-II. Autoradiographic examination of each sublot of the 210- to 600-μm-diam dense microspheres showed that in several sublots individual microspheres were of variable Pu:(U+Pu) ratio, in contrast to results of chemical analysis on samples of microspheres. Results of microprobe analyses of individual microspheres from these lots confirmed this finding. We believe this resulted from a failure to mix the $(U,Pu)O_2$ sol thoroughly after the blending step. This conclusion is supported by results of the second phase of the program completed this quarter in which we prepared 0.9 kg of dense 520- to 595-μm-diam microspheres with a uniform ratio of Pu:(U+Pu), being careful to blend each lot of mixed sol thoroughly before forming. The second phase of the program was necessary to prepare sufficient microspheres to replace those of variable Pu content. Characteristics of the microsphere products prepared in both phases of the program are given in Table 1.1.

Development of Fabrication Processes

J. D. Sease

Fast reactors that operate at high specific powers will require fuel pins of small diameter with fuel ranging from 80 to 90% of theoretical density and a high fissile loading. Our work is to develop procedures for Sphere-Pac and pelletization and for fabricating irradiation capsules.

Table 1.1. Dense $(^{235}U_{0.8},Pu_{0.2})O_2$ Microspheres for Sphere-Pac Loading into Capsules for the Series II Irradiations in the Experimental Breeder Reactor-II

Microsphere Diameter (μm)	Weight of Product[a] (g)	Yield (% oxide)	Ratio Pu:(U+Pu)	Tap Density (g/cm^3)	Density[b] (% of theoretical)	Carbon Content (ppm)	Mole Ratio of Oxygen to Metal
420–595	1280	60	0.203	6.3	> 95	< 50	2.0
< 44	364	57	0.204		> 99	< 150	
420–595	905	63	0.20	6.5			

[a] After classification.

[b] By Hg porosimetry (10,000 psi).

Sphere-Pac (R. A. Bradley)

The purpose of the Sphere-Pac development program is to provide the information required to load fuel pins to a specified density. In previous experiments, idealized ThO_2 microspheres were used to investigate the effects of process variables on the density of the fuel bed.[3–5] However, the limited availability of $(U,Pu)O_2$ microspheres will necessitate loading the series II fuel pins with available microspheres rather than an optimized size or distribution of sizes that might be predicted by the development work on ThO_2 microspheres. Therefore, we discontinued work on ThO_2 and began work on the $(U,Pu)O_2$ microspheres on hand.

We determined the density of the coarse bed and the loaded density of each batch of microspheres by loading the coarse microspheres into a 0.220-in.-ID fuel pin and then infiltrating fine microspheres less than 25 μm in diameter. The results of these experiments are given in Table 1.2.

Table 1.2. Summary of Loaded Densities for Microspheres for the Experimental Breeder Reactor-II

Batch Number	Density of Coarse Bed (% of theoretical)	Loaded Density (% of theoretical)
PUM-13-11/12	59.2	81.5[a]
PUM-13-13	59.7[a] 58.2[a] 59.6[b] 59.7[b]	83.4[a] 81.9[a] 84.5[b] 82.9[b]
PUM-13-4/5 PUM-13-6/7 PUM-13-8/9/10	57.2	80.6
PUM-13-16/17 PUM-13-18/19	62.0	84.6
PUM-13-14/15	67.9	85.1
PUM-13-20 PUM-13-21	60.0[a] 59.7[a]	83.6[a] 83.1[a]
PUM-13-21/22	60.7	80.6
PUM-13-23	61.8[a] 61.2[a]	83.4[a] 82.5[a]

[a]Duplicate determinations by Operator 1.

[b]Duplicate determinations by Operator 2.

We observed that the density of the coarse bed varied as much as 5% between batches, that the variation between duplicate loadings of the same batch by the same operator was 1.5%, and that there was about 1% variation between operators. It appears, therefore, that to obtain the densities required for the EBR-II fuel pins, it will be necessary to load a pin, check the density, and reload it if the density is not within the tolerances of the specification.

Pelletization of Sol-Gel $(U,Pu)O_2$ (R. A. Bradley)

The series II irradiation experiment in the EBR-II requires[6] $(U,Pu)O_2$ pellets 83, 88, and 93% of theoretical density with ratios of O:metal of 1.94 and 1.98. The purpose of the work reported here was to develop the fabrication procedures for producing pellets that meet these requirements.

Pellets with densities of 84 and 91% of theoretical and a ratio of O:metal of 1.98 were produced previously from sol-gel $(U,Pu)O_2$ for other irradiation experiments.[7,8] The 84% dense pellets were made from powder calcined in Ar–4% H_2, and the 91% dense pellets were made from powder that had been given an oxidation-reduction treatment. To produce powder suitable for making 83, 88, and 93% dense pellets, we calcined the powder to produce powder for pellets of either high or low density and then varied the forming pressure or sintering conditions slightly to obtain the exact density required.

The $(U_{0.80},Pu_{0.20})O_2$ fuel (93% enriched U) used in this work was prepared by the sol-gel process.[7,8] The results of various analyses used to characterize this batch of powder are summarized in Table 1.3. The powder was calcined in an Inconel boat with a gas supply tube along the bottom to allow introducing gas at the bottom of the powder bed. Powder was calcined and pellets were sintered in an alumina tube furnace by heating at 300°C/hr to the desired temperature.

Pellets 83% of Theoretical Density. – The results of sintering tests on powder calcined in Ar at 520°C for 4 hr are given in Table 1.4. Pellets pressed at 30,000 to 60,000 psi and sintered in Ar at 1450°C had densities about 81 to 87% of theoretical; those sintered in Ar–4% H_2 at 1550°C ranged from about 76 to 84% of theoretical. It appeared, therefore, that either sintering schedule would be suitable for making 83%

Table 1.3. Characterization of $(U,Pu)O_2$ Powder Batch BR1

Material Form	Ratio Pu:(U+Pu) × 100 (%)	Surface Area (m^2/g)	Bulk Density, g/cm^3	
			At Atmospheric Pressure[a]	At 10,000 psi[b]
Dried gel shards		74	5.3	5.4
Jet-milled powder	20.1	52		
Powder for 83% dense pellets[a]		16.4		
Powder for 88 and 93% dense pellets[b]		11.3		

[a]Calcined in Ar at 520°C for 4 hr.

[b]Calcined by oxidizing at 400°C and reducing at 520°C. Ball milled 116 hr.

Table 1.4. Results of Sintering Tests on Powder Calcined in Argon

Sintering Run Number	Sintering Conditions	Forming Pressure (psi)	Density, % of Theoretical	
			Green	Sintered
		× 10^3		
110	300°C/hr to 1450°C in Ar and hold 4 hr. Change to Ar–4% H_2 and hold 20 hr.	30	42.7	82.6
		40	44.3	84.8
		50	46.3	86.0
		60	48.3	86.6
113	300°C/hr to 1450°C in Ar and hold 4 hr. Change to Ar–4% H_2 and hold 10 hr.	30	42.5	80.9
		40	44.4	83.0
		50	46.1	85.5
		60	48.0	86.9
120	300°C/hr in Ar–4% H_2 to 1550°C and hold 6 hr.	25	41.8	76.2
		30	42.8	78.2
		35	43.6	80.0
		40	44.4	81.0
		50	46.1	83.5
121	300°C/hr in Ar–4% H_2 to 1550°C and hold 6 hr.	25	42.3	77.1
		30	43.0	78.0
		35	43.8	80.3
		40	44.8	81.4
		50	46.1	83.3

dense pellets. Six batches of 40 pellets each were sintered in Ar at 1450°C for 4 hr and then reduced in Ar–4% H_2 for 12 hr. The average density of the control pellets in the first two sintering runs was about 3% too high. In subsequent runs, the forming pressure was reduced to decrease the density; however, this was not very effective. The data in Table 1.5 show that the densities varied from 82.2 to 86.5% of theoretical and that only one of the six runs produced pellets with densities that met the specification of 83.0 ± 1.0% of theoretical density.

Table 1.5. Average Density of Control Pellets[a] Sintered in Argon

Sintering Run Number	Forming Pressure (psi)	Density, % of Theoretical	
		Green	Sintered
	× 10^3		
114	44.6	45.3	85.9
115	44.6	45.3	86.5
116	40	44.7	84.4
117	35	44.0	84.7
118	30	43.4	85.9
119	25	43.0	82.2

[a]Six pellets per 40-pellet batch (two adjacent pellets from the left, middle, and right sections of the boat).

Six additional batches were sintered in Ar–4% H_2 at 1550°C for 6 hr. The average density of the control pellets ranged from 82.1 to 84.4% of theoretical, and in four of the six batches the average density of the control pellets was in the desired range of 82 to 84% of theoretical. It appears, therefore, that the process is more reproducible when the material is sintered in Ar–4% H_2 than when it is sintered in Ar. The improved reproducibility is probably the result of the material reaching a common stoichiometry before significant densification occurs during sintering in Ar–4% H_2 and thereby minimizing the effect of day-to-day variations in powder stoichiometry.

Pellets 88 and 93% of Theoretical Density. – A sintering test on powder that had been oxidized in air at 400°C and reduced in Ar–4% H_2 at 520°C indicated that it would be difficult to produce pellets with densities greater than 87% of theoretical. Therefore, the powder was calcined by this oxidation-reduction technique and then ground in a rubber-lined steel ball mill with WC grinding cylinders. The results of sinterability tests on the ball-milled powder are summarized in Table 1.6. Pellets sintered in Ar–4% H_2 at 1550°C were about 93.5 to 94.5% of theoretical density; pellets sintered in Ar or Ar–10% CO_2 were 89 to 92% of theoretical density.

We attribute the lower density that resulted from sintering in Ar or Ar–10% CO_2 to either (1) the trapping of porosity during rapid

Table 1.6. Results of Sintering Tests on $(U,Pu)O_2$ Powder[a] for Pellets 88 and 93% of Theoretical Density

Sintering Run Number	Sintering Conditions	Forming Pressure (psi)	Density, % of Theoretical	
			Green	Sintered
		$\times 10^3$		
141	300°C/hr to 500°C, 125°C/hr to 1000°C, 300°C/hr to 1550°C in Ar–4% H_2 and hold 6 hr.	20	50.4	93.5
		30	51.9	93.9
		40	53.2	94.2
		50	53.9	94.5
		60	55.2	94.1
146	300°C/hr in Ar to 1550°C and hold 2 hr. Change to Ar–4% H_2 and hold 4 hr.	20	50.1	91.2
		30	52.0	92.5
		40	52.1	91.7
		50	53.7	91.5
		60	54.7	89.0
147	300°C/hr in Ar–10% CO_2 to 1550°C and hold 2 hr. Change to Ar and hold 2 hr. Change to Ar–4% H_2 and hold 2 hr.	20	50.5	91.9
		40	53.2	91.3
		60	55.2	88.1

[a]Powder calcined in air to 400°C and reduced in Ar–4% H_2 at 520°C. Ball-milled 116 hr.

densification of the hyperstoichiometric mixed oxide in the critical temperature range of 500 to 1000°C where most of the sintering occurs or (2) the introduction of porosity as O is removed from the lattice during the reduction in Ar–4% H_2 after densification is complete.

Series II Unencapsulated Fuel Pins for Irradiation in the Experimental Breeder Reactor-II (R. B. Pratt, R. A. Bradley)

During fiscal year 1970 we plan to fabricate 19 unencapsulated fuel pins for irradiation in a 37-pin reactor subassembly shared with the Babcock & Wilcox Company. We plan to produce 21 fuel pins to ensure that 19 are available for irradiation. Each site is responsible for design, fabrication, inspection, shipping, and postirradiation examination of its own fuel pins. Our test pins will be fueled with pelletized and Sphere-Pac fuel produced by the sol-gel process.

During the past quarter we were primarily concerned with fuel preparation, qualification of raw materials, welding development, fabrication and inspection of components and equipment, and writing of procedures. Analysis of activities listed by the critical path schedule shows that the project is 42% complete through the end of March.

Fuel Preparation. – The series II irradiation experiment for the EBR-II requires 13 fuel pins loaded with $(U_{0.80},Pu_{0.20})O_2$ microspheres (93% enriched U) for loading by the Sphere-Pac process, 8 fuel pins loaded with sol-gel pellets of the same composition, and 17 archive rods. The smear density of the fuel will be 80, 85, or 90% of theoretical for pellets and 80 or 85% for microspheres. The ratio of O:metal will be either 1.940 ± 0.005 or 1.980 ± 0.005. The requirements for these fuel pins are summarized in Table 1.7.

The pellets for these pins were fabricated by the processes described above.[9] For the pellets requiring a ratio of O:metal of 1.98 the stoichiometry was adjusted during the final stage of the sintering run by decreasing the temperature to 1450°C and holding in Ar–4% H_2 until the H_2O in the effluent gas decreased to 30 ppm. The pellets were cooled from 850°C in Ar to prevent retention of H_2 by the fuel. Previous studies[10] showed that fuel treated in this manner will have values for release of sorbed gas of less than 0.05 g/cm^2. The average density of

Table 1.7. Number of Fuel Pins, Densities, and Ratios of Oxygen to Metal Required for Series II Irradiations in Experimental Breeder Reactor-II

Fuel Form	Smear Density (% of theoretical)	Pellet Density[a] (% of theoretical)	Ratio of Oxygen to Metal	Number of Fuel Pins Required	Number of Archive Fuel Pins Required
Sphere-Pac	80		1.98	2	2
Sphere-Pac	85		1.98	7	2
Sphere-Pac	80		1.94	2	2
Sphere-Pac	85		1.94	2	2
Pellet	85	88.2	1.98	3	3
Pellet	90	93.4	1.98	2	2
Pellet	80	83.0	1.94	2	2
Pellet	85	88.2	1.94	1	1
TOTAL				21	16

[a]Based on diametral gap of 0.004 in.

six control pellets from each sintering run and the average O:metal ratio of each run are given in Table 1.8. The pellet pins with fuel 85 and 90% of theoretical density were ground on a centerless grinder, and samples were submitted for final characterization before loading.

The microspheres for the Sphere-Pac pins were received from the Chemical Technology Division. Examination by α-ray autoradiography revealed large variations in Pu content between microspheres in three out of five batches. The two batches that appear uniform in Pu content contain sufficient material to fabricate the seven Sphere-Pac fuel pins with fuel 85% of theoretical density. Additional microspheres were prepared for the remaining fuel pins, and α-ray autoradiography indicated that the Pu content was uniform between microspheres. These microspheres are ready to be heat treated to adjust the ratio of O:metal.

Hardware Preparations. — We have qualified the materials and then fabricated and inspected about 400 individual hardware components that will be used to assemble 21 fuel pins and 17 archive pins. Packages of

Table 1.8. Summary of Densities and Ratios of Oxygen to Metal in Control Pellets for Fuel Pins for Experimental Breeder Reactor-II

Fuel Form	Sintering Run Number	Pellet Density, % of Theoretical		Ratio of Oxygen to Metal
		Nominal Desired	Measured for Control Pellets[a]	
Pellet	151	88.2 ± 1.0	88.7	1.983[a]
	152		87.4	1.978[a]
	154		89.3	1.979[a]
	155		89.6	1.981[a]
	156		89.1	1.973[a]
	157		88.3	1.985[a]
Pellet	142	93.4 ± 1.0	95.0	1.970[b]
	143		93.3	1.963[b]
	144		94.5	1.974[b]
	145		93.4	1.968[b]
Pellet	122	83.0 ± 1.0	83.1	c
	123		82.1	c
	124		84.4	c
	125		84.4	c
	126		83.9	c
	127		83.2	c
Pellet	153	88.2 ± 1.0	89.1	c
	158		89.0	c

[a]Average of six pellets.

[b]Average of three pellets — additional analyses will be obtained.

[c]To be heat treated to adjust ratio of O:metal to 1.94.

cleaned and inspected hardware components were prepared and assigned to individual fuel and archive tubes.

To date, 10 of the 21 fuel tubes have had bottom end plugs welded in place and have been inspected and approved for loading. Fifteen capillary tubes were assembled, welded to top end plugs, and inspected.

Equipment Fabrication. — We assembled and installed equipment capable of measuring the void volume in fuel pins after fabrication. This information and equipment are used for loading fuel pins with a mixture of He and Xe. We load each experimental subassembly with a unique mixture of normal and isotopic Xe that can be identified easily so that we can identify failed fuel elements during irradiation. We installed this equipment and are calibrating and testing it.

Hardware Qualification. – Initially, thirty fuel tubes were introduced to our inspection and qualification program. To date, twenty-three of those have been accepted and seven rejected. Twenty-three tubes have bottom end plugs welded in place; ten of these welds passed inspection and were approved. The remaining welds are being inspected. Welds are inspected by radiography for thickness and porosity, by dye penetrant examination for surface defects, and by He leak checking.

Characterization of $(U,Pu)O_2$ Fuels

J. D. Sease C. M. Cox

The development of sol-gel fuel fabrication requires characterization of both the chemical composition and physical properties of the material to control the process and to interpret meaningfully the irradiation behavior. Thermodynamic studies will contribute to the development of the process for producing the fuel and will aid in predicting fuel performance for both irradiation testing and model studies.

Chemical Analysis of Ratio of Oxygen to Metal (W. H. Pechin, W. J. Lackey, R. A. Bradley)

We are trying to find how best to use analytical chemistry for the control of the fabrication process and for the qualification of the $(U,Pu)O_2$ fuel for irradiation testing. The factors of major interest are the relevance, precision, and accuracy of the various analyses.

We found that a drying step in the analysis for the ratio of O:metal seriously biased the results. This step, which was used from about November 1969 to January 1970, consisted of a 1-hr heat treatment in Ar–4% H_2 at 110°C before the normal gravimetric analysis for the O:metal ratio. We originally included this step because of concern that microsphere samples might be picking up moisture that would bias the O:metal ratio.

The amount of bias was estimated from a series of samples for which the O:metal ratio was determined with and without drying. The bias was positive and proportional to the hypostoichiometry of the fuel; all results are biased toward 2.00.

The combined uncertainties in the bias and in the reported ratio of O:metal make it impractical to determine what the ratio would have been if the drying step had not been included by simply subtracting the bias.

The only fuel pins affected by this bias are those for the Engineering Test Reactor (ETR) capsules 43-120 and 43-121. Subsequent experience in preparing fuel by the process conditions used for the ETR fuel indicates that the latter should have an O:metal ratio of 1.98. Archive material from the lots used to load the ETR pins will be analyzed to verify the ratio of O:metal.

The errors introduced by this drying step, however, did interfere with the development of the process for producing material with an O:metal ratio of 1.94 for use in the series II irradiations in the EBR-II.

We plan to submit a series of samples in accordance with an experimental design that will permit the separation of such effects as variation between sintering runs and variation with position in the sintering furnace from the random variation of the analysis.

Alpha-Ray Autoradiography of $(U,Pu)O_2$ Microspheres (R. A. Bradley, W. H. Pechin)

Five batches of $(U_{0.80},Pu_{0.20})O_2$ microspheres were examined by α-ray autoradiography to determine whether the ratio of Pu:(U+Pu) was uniform. The autoradiographs were made by placing a polished specimen in intimate contact with Kodak Type 106-01 autoradiography film for 5 sec and then etching the film in a solution of NaOH for 3 min. The etched film was then examined on a light microscope and photographed at a magnification of 29×. The limit of resolution of this technique is believed to be about 50 to 100 μm.

The autoradiographs showed no inhomogeneities within microspheres; but in three of the five batches (HT-117, HT-118, HT-121) there appeared to be wide variations in Pu content between microspheres. The other two batches (HT-119 and HT-120) appeared to be homogeneous. Photomicrographs and α-ray autoradiographs of typical inhomogeneous and homogeneous batches of microspheres are shown at the same magnification in Figs. 1.1 and 1.2, respectively. Several microspheres are numbered in Fig. 1.1(a) to aid in comparing the microspheres in the photomicrograph with those in the α-ray autoradiograph.

The microspheres in Fig. 1.1 were examined by means of the electron microprobe to determine the variation in the ratio of Pu:(U+Pu).

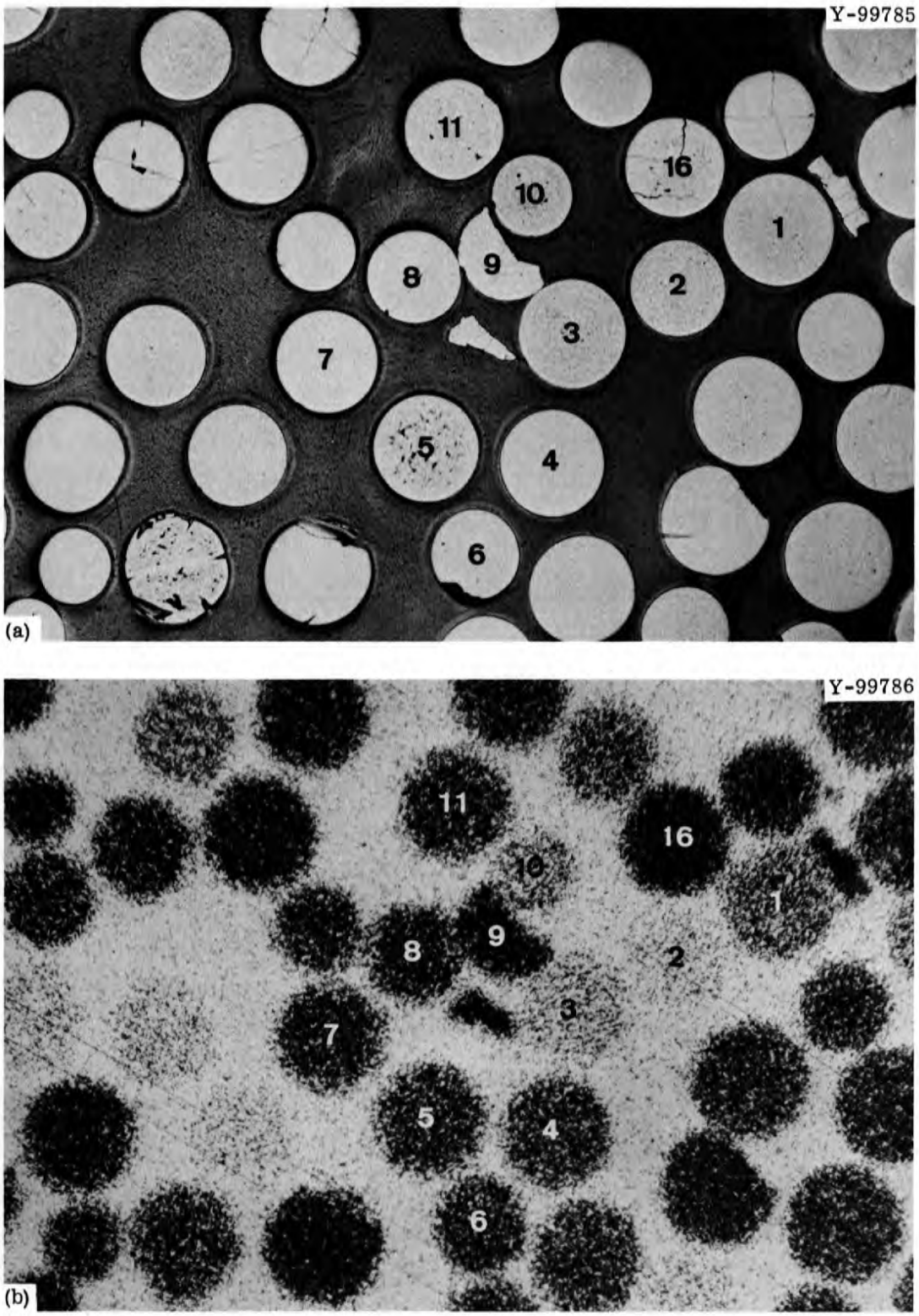

Fig. 1.1. Microspheres of $(U_{0.80},Pu_{0.20})O_2$ from Batch HT-117. (a) Photomicrograph, and (b) alpha-ray autoradiograph. 29×.

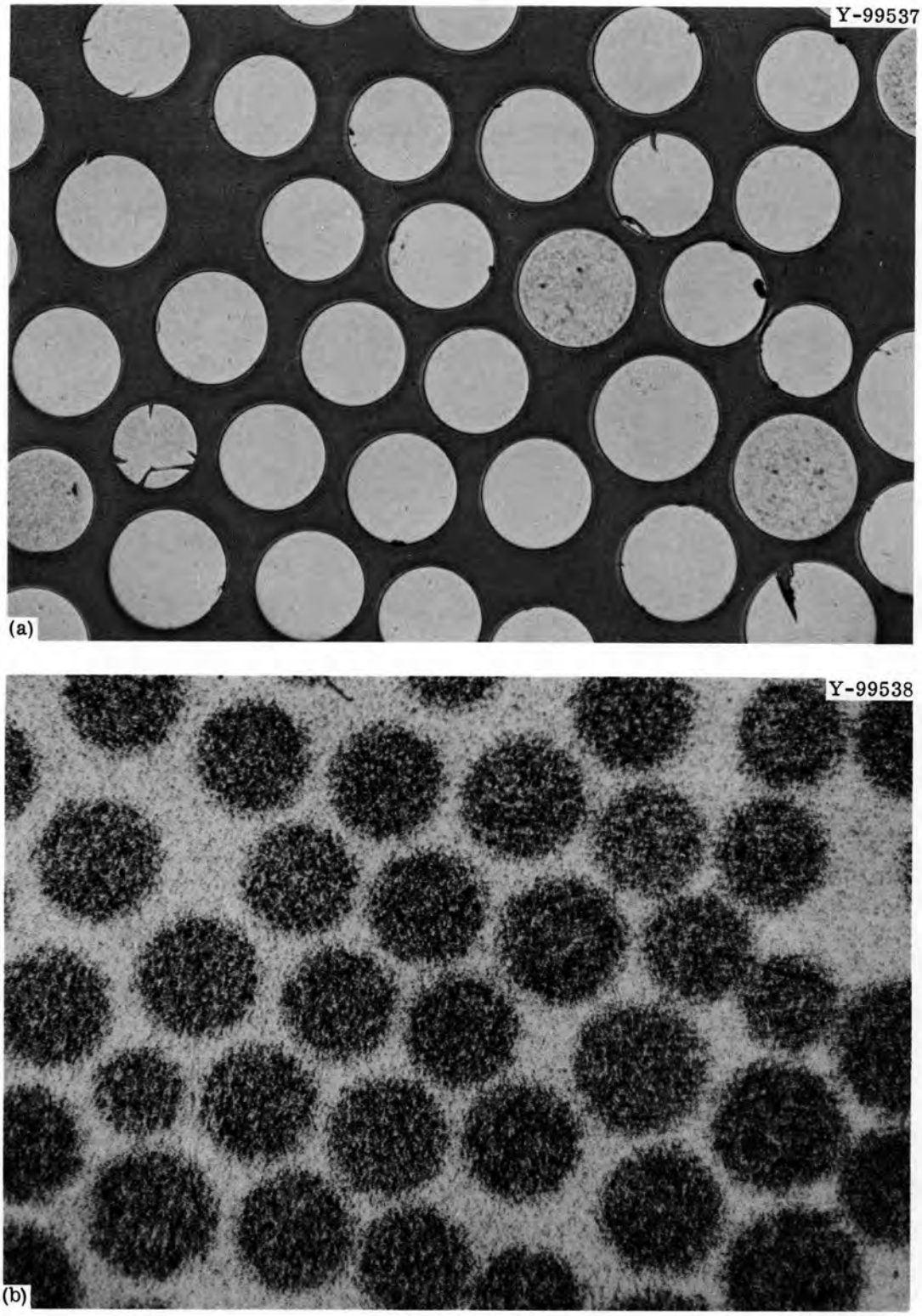

Fig. 1.2. Microspheres of $(U_{0.80},Pu_{0.20})O_2$ from Batch HT-119. (a) Photomicrograph, and (b) alpha-ray autoradiograph. 29X.

Microspheres from the batches shown in Figs. 1.1 and 1.2 were also analyzed by γ-ray spectroscopy.

Analysis of Mixed Oxide Microspheres by Electron Microprobe (R. S. Crouse, W. J. Lackey)

The batch of mixed oxide microspheres (HT-117) suspected of containing the widest variation in Pu content, as indicated by the α-ray autoradiograph,[11] was examined by electron microprobe analysis to determine quantitatively the atomic ratio of Pu:(U+Pu) for individual spheres. Simultaneous point counts for Pu and U were performed, in triplicate, on a total of ten spheres (those shown in Fig. 1.1). We monitored the Pu M_α and U M_β x rays and compared the intensities to those of a standard sample of $(U_{0.80},Pu_{0.20})O_2$ microspheres (Batch PM-11C) that appeared homogeneous in an α-ray autoradiograph and that was subsequently found to be homogeneous, within the limit of detection, by microprobe analysis.

The values obtained for the ratio Pu:(U+Pu) expressed in percent (i.e., the atomic percent of Pu in the heavy metal) are given below:

Sphere Number	Pu:(U+Pu) (at. %)
1	15.0
2	4.7
3	7.3
4	19.3
5	20.3
8	22.6
9	29.5
10	10.7
11	22.7
16	33.9
Average	18.6

The measured values frequently differed significantly from the 20.0% expected from the nominal composition. The minimum Pu content observed was 4.7%; the maximum was 33.9%. The Pu content within any given sphere was constant. The average Pu content for the ten spheres was 18.6%. Thus, while the Pu content varied extensively from sphere to sphere, there was not sufficient evidence to conclude that the average Pu content of the entire batch differed from the nominal composition.

Visual comparison of the darkness of the α-ray autoradiograph shown in Fig. 1.1(b) showed it to be highly correlated to the Pu content. This indicates that autoradiography would be valuable in future characterization of Pu homogeneity. Thus, considering both the autoradiograph and the microprobe results, we concluded that the Pu content of individual microspheres varied from about 5 to 34% of the heavy metal present.

Gamma-Ray Spectroscopy of $(U,Pu)O_2$ Microspheres (R. A. Bradley, W. J. Lackey, W. H. Pechin)

We used γ-ray spectroscopy to determine quantitatively the ratio of Pu:(U+Pu) in individual spheres from two batches of microspheres. Alpha-ray autoradiography had shown that one of these batches (HT-119) was homogeneous, but that the other (HT-117) contained large variations in Pu content between spheres.

We prepared samples for γ-ray spectroscopy by placing a microsphere on a 3/4-in. square plastic slide cover and covering it with plastic tape. The γ rays were counted for 2 hr by centering the encapsulated microsphere with respect to a 54-cm^3 coaxial Ge detector associated with a γ-ray spectrometer. A sheet of Cu was used to filter out x rays and low-energy γ rays. The ratio of Pu:U was determined by comparing the area under the curve of the 186-kev ^{235}U peak with that of a peak at 205 kev, believed to be ^{240}Pu. No verification could be found in the literature that the 205-kev peak was ^{240}Pu, but this peak was always present when the 414-kev ^{239}Pu peak was present and was always absent when the ^{239}Pu peak was absent. In addition, the ratio of the peak at 205 kev to the peak at 414 kev was always constant.

A standard was prepared by dissolving samples of the UO_2 and PuO_2 sols from which the microspheres were made, coulometrically analyzing the solutions for U and Pu, and putting measured amounts of U and Pu on plastic slides. Another standard was prepared by placing six microspheres from the homogeneous batch (HT-119) in a 3/8-in.-diam circle on a single plastic slide mount. This mount, which we termed the circle standard, was counted five times. Since we were concerned that there might be some variation in the results because the microspheres were spread out in a circle, we removed microspheres from the circle standard and

remounted them in a small group in the center of the slide. This mount, called the point standard, was counted three times. Using the standard prepared from the Pu and U solutions as a reference, we calculated the ratio of Pu:(U+Pu) in atomic percent for each analysis of the circle and point standards:

Circle Standard (at. % Pu)	Point Standard (at. % Pu)
20.6	20.8
20.9	21.0
20.8	20.2
20.4	
20.5	

An analysis of variance on these results indicated no significant difference between the circle standard and the point standard. Therefore, we combined the eight analyses and found that the average Pu content of these six spheres was 20.7% and that the standard deviation of the analytical technique when six spheres were counted simultaneously was 0.27. The 95% confidence interval for the mean of these eight analyses was 20.4 to 20.9.

Six other microspheres from this homogeneous batch (HT-119) were analyzed individually three times each, and the ratio of Pu:(U+Pu) was calculated as before. The results of these analyses are given in Table 1.9. Based on the average of three determinations for each sphere, the Pu content varied from 19.4 to 22.3%.

An analysis of variance for these data showed (1) that there was not sufficient evidence to say that there was a day-to-day variation in the analytical technique; (2) that we could say with 99% confidence that there was a variation in Pu content from sphere to sphere; and (3) that the standard deviation of the analytical technique when a single sphere was counted was 0.43.

The 95% confidence interval for the mean of each sphere was constructed and is shown in the last column of Table 1.9. These intervals make it apparent that the Pu content of the first four spheres differed significantly from that of the last two. The mean of all 18 observations (i.e., the average Pu content of the six microspheres) was 21.3% with a

Table 1.9. Results of Gamma-Ray Spectroscopy on Six Microspheres from Batch HT-119

Sphere Number	Analyses for Ratio of Pu:(U+Pu), at. %			Mean[a] of Analyses for Each Sphere	95% Confidence Interval for Mean
	Day 1	Day 2	Day 3		
1	21.4	22.4	22.0	21.9	21.3–22.5
2	22.6	22.0	22.2	22.3	21.7–22.9
3	21.3	21.4	21.7	21.5	20.9–22.1
4	22.1	21.6	22.7	22.1	21.5–22.7
5	20.6	20.7	19.8	20.4	19.8–21.0
6	19.5	19.3	19.3	19.4	18.8–20.0

[a]Mean of the means for all spheres = 21.3.

standard deviation due to variation between spheres of 1.2. Based on this standard deviation, we can say with 95% confidence that the Pu content of 95% of the spheres will be between 16.3 and 26.3%. This calculated interval is probably larger than the actual range of Pu content because we assumed that the spheres analyzed came from a single population with a normal distribution. Actually, the batch from which they came was composed of four subbatches; therefore, there are probably four populations with normal distribution instead of one.

We analyzed six individual microspheres from a nonhomogeneous batch (HT-117); the ratio of Pu:(U+Pu) ranged from 2.7 to 25.1%, as shown below:

Sphere Number	Ratio of Pu:(U+Pu) (at. %)
1	13.2
2	23.5
3	2.7
4	21.0
5	21.0
6	25.1

These results are in good agreement with those obtained qualitatively by α-ray autoradiography and with those obtained quantitatively by electron microprobe analysis. Based on these analyses, the following conclusions may be drawn:

1. Gamma-ray spectroscopy can be used to detect variations in Pu content of about 0.5% or greater between individual $(U,Pu)O_2$ microspheres that contain enriched U.

2. Six microspheres from a batch that appeared homogeneous when examined by α-ray autoradiography had small but real variations in the Pu content (19.4 to 22.3%).

3. Six microspheres from a batch that was shown by α-ray autoradiography to be nonhomogeneous had Pu contents ranging from 2.7 to 25.1%.

Galvanic Cell for Determination of Ratio of Oxygen to Metal (W. J. Lackey, W. H. Pechin)

As part of our continuing effort to improve the understanding of the chemical properties of mixed oxide fuels, we are making plans to design and construct a high-temperature, solid electrolyte, galvanic cell for use in determining the ratio of O:metal for $(U,Pu)O_{2\pm x}$. The theory and general usefulness of galvanic cells employing solid electrolytes for determining thermodynamic properties were first demonstrated by Kiukkola and Wagner,[12] and such cells have been used to determine the O potential, $\Delta\bar{G}_{(O_2)}$, for $(U,Pu)O_{2\pm x}$ as a function of the O:metal ratio.[13]

For determining the ratios of O:metal, an appropriate cell should be as follows:[14]

$$(U,Pu)O_{2\pm x} \mid Th_{0.85}Y_{0.15}O_{1.92} \mid Zr_{0.85}Ca_{0.15}O_{1.85} \mid Th_{0.85}Y_{0.15}O_{1.92} \mid Ni, NiO \ .$$

The $Th_{0.85}Y_{0.15}O_{1.92}$ and $Zr_{0.85}Ca_{0.15}O_{1.85}$ electrolytes are commercially available. Physically, the cell might consist of a flat-bottomed, calcia-stabilized zirconia tube with a $Th_{0.85}Y_{0.15}O_{1.92}$ disk in contact with both sides of the tube bottom. A disk composed of a mixture of Ni and NiO would be pressed against the $Th_{0.85}Y_{0.15}O_{1.92}$ on the inside of the tube while the unknown $(U,Pu)O_{2\pm x}$ pellet would be in contact with the other $Th_{0.85}Y_{0.15}O_{1.92}$ disk. The cell, with electrical leads attached, would then be placed in a furnace.

The equilibrium electromotive force (emf) developed by such a cell is

$$\text{emf} = \frac{\Delta\bar{G}_{(O_2)}\ \text{Ni,NiO} - \Delta\bar{G}_{(O_2)}\ \text{Mixed Oxide}}{4F}$$

where $\Delta\bar{G}_{(O_2)}$ is the O chemical potential, and F is Faraday's constant. Using tabulated values for the $\Delta\bar{G}_{(O_2)}$ terms,[14,15] we used this equation to calculate the relationship between the electromotive force and the O:metal ratio shown in Fig. 1.3. In practice, after experimentally determining the electromotive force of the cell containing the unknown specimen, the ratio of O:metal would be read from the curve in Fig. 1.3. Based on the slope of this curve over the range representing hypostoichiometric fuel, the expected error in the electromotive force, and the uncertainty in the thermodynamic data, we estimate that the error in the determination of the ratio of O:metal would be about 0.005 or less.

Such a cell will be used as a spot check on other analytical techniques used at ORNL to determine the ratio of O:metal or as a routine analysis technique, depending on the analysis time. One potential advantage of using the galvanic cell is that it will probably be nondestructive.

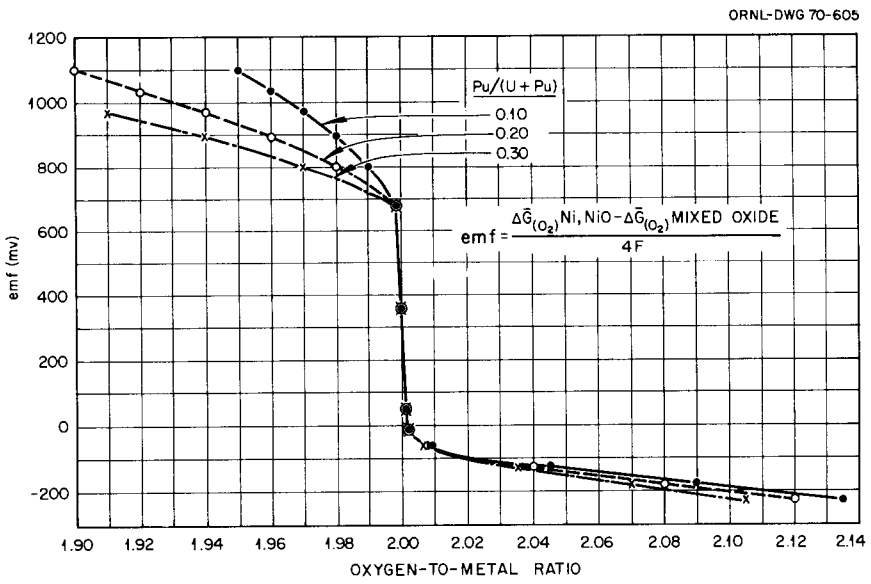

Fig. 1.3. Equilibrium Electromotive Force at 650°C from the Cell Ni,NiO[Electrolyte](U,Pu)$O_{2\pm x}$ Versus Ratio of Oxygen to Metal.

Irradiation Testing of $(U,Pu)O_2$ Fuels

C. M. Cox

The performance characteristics of mixed $(U,Pu)O_2$ fuels are being evaluated in a variety of irradiation tests for potential application in an LMFBR. We are now concentrating on comparative tests of sol-gel fuel fabricated as pellets or as microspheres compacted by the Sphere-Pac technique. The program includes thermal-flux experiments, which permit use of instrumented capsules and the achievement of high levels of burnup in relatively short periods of time, and fast-flux experiments, in which the fission rate distribution and radiation effects on the cladding are more typical of those for operating conditions anticipated in an LMFBR.

Uninstrumented Thermal-Flux Irradiation Tests (A. R. Olsen, D. R. Cuneo,[16] J. H. Goode[1])

A series of uninstrumented capsules is being irradiated in the X-basket facilities of the ETR. Each capsule contains four test pins arranged in tandem. The initial objective of these tests was to investigate the effects of fabrication form with extended burnup on release of fission gas, migration of fission products, and swelling of the fuel. Some capsules are now being irradiated specifically to provide short-cooled irradiated fuel for LMFBR reprocessing studies. The current status of these tests is given in Table 1.10.

Experiment 43-113, the only capsule currently under irradiation, is operating routinely in the ETR. It is scheduled to be removed from the ETR at the end of cycle 108 late in July or early in August of 1970. At that time it will have achieved a calculated average burnup level of 10% fissions per initial actinide metal atom (FIMA).

The metallographic examinations of capsules 43-103 and 43-115 continued. Additional data were also obtained for the burnup analysis of experiment 43-115. Although a final analysis of the fuel performance must be delayed until the results of examinations by α and β-γ autoradiography are available, there is sufficient information to permit preliminary analysis of thermal conditions and data for release of

Table 1.10. Uninstrumented Tests of $(U,Pu)O_2$ Fuels in a Thermal Flux

Experiment Number	Fuel		Number of Fuel Pins	Peak Burnup (% FIMA)[a]	Peak Linear Heat Rate (w/cm)	Temperature at Peak Inner Surface of Cladding (°C)	Status February 1970
	Form	Composition					
43-99	Sphere-Pac	$(^{235}U_{0.80},Pu_{0.20})O_{2.00}$	2	1.5[b]	1640[b]	1000	Examined
43-100	Sphere-Pac	$(^{235}U_{0.80},Pu_{0.20})O_{2.00}$	2	1.4[b]	1470[b]	900	Examined
43-103	Sphere-Pac Pellet	$UO_{2.02}$(20% ^{235}U) $UO_{2.00}$(20% ^{235}U)	3 1	5	690	530	Being examined
43-112	Sphere-Pac Pellet	$(^{238}U_{0.85},Pu_{0.15})O_{1.97}$ $UO_{2.02}$(20% ^{235}U)	3 1	0.7	500	360	Examined
43-113	Sphere-Pac Pellet	$(^{238}U_{0.85},Pu_{0.15})O_{1.97}$ $UO_{2.02}$(20% ^{235}U)	3 1	10[c]	500[c]	380[c]	In reactor, ≅ 9.2% FIMA
43-115	Sphere-Pac Pellet	$(^{238}U_{0.85},Pu_{0.15})O_{1.97}$ $UO_{2.02}$(20% ^{235}U)	3 1	6.5	600	460	Being examined
43-116	Sphere-Pac	$(^{238}U_{0.85},Pu_{0.15})O_{1.97}$	4	1.5[c]	600[c]	460[c]	Processed
43-117	FTR Pellets	$(^{238}U_{0.75},Pu_{0.25})O_{1.98}$	4	1.5	430[c]	360[c]	Being prepared
43-118	FTR Pellets	$(^{238}U_{0.75},Pu_{0.25})O_{1.98}$	4	4.0	430[c]	360[c]	Being prepared
43-119	FTR Pellets	$(^{238}U_{0.75},Pu_{0.25})O_{1.98}$	4	8.0	430[c]	360[c]	Being prepared
43-123	FTR Pellets	$(^{238}U_{0.75},Pu_{0.25})O_{1.98}$	4	4.0	350[c]	310[c]	Being prepared

[a] FIMA is fissions per initial actinide metal atom.

[b] Pins failed in reactor from overpowering.

[c] These are target design values.

fission gas. These data are reported in Table 1.11 along with information previously reported on the earlier low-burnup test capsules.[17] Typical transverse cross sections for the three types of fuel contained in these capsules are shown in Fig. 1.4. These sections clearly show the similarity in the microstructures of the irradiated fuel regardless of the initial fuel form (Sphere-Pac or pellet) and the effects of linear heat rate on the extent of restructuring.

The next four capsules to be irradiated in this series will contain mechanically blended UO_2-PuO_2 pellets of the type currently proposed[18] for fueling the Fast Test Reactor (FTR). Since these capsules are being irradiated to provide short-cooled fuel for LMFBR fuel reprocessing, the test conditions were selected to simulate operating conditions for the FTR fuel pins. A wide range of burnup levels and linear heat rates was chosen to determine the effects of these changing conditions on the volatility of fission products during shearing, oxidation, volatilization,[19] and dissolution and on the dissolution characteristics of the fuel pellets — this latter as a complement to the matrix of solubility experiments being performed on unirradiated fuels by investigators at Battelle Memorial Institute Pacific Northwest Laboratory (BNWL). The decision to operate capsules 43-117, 43-118, and 43-119 at a peak design linear heat rate of 14 kw/ft was based on the comparison of calculated[20] FTR and test pin temperatures shown in Fig. 1.5 and the 10% uncertainty associated with advertised fluxes in the ETR. All of the hardware for these tests is available and has been tested by the standard procedures for quality assurance. The fuel is scheduled to be delivered from BNWL early in April. The safety analysis for the irradiation is 90% complete, and irradiation of the first three capsules is currently expected to start with ETR cycle 108 in June 1970.

Instrumented Tests in Oak Ridge Research Reactor (R. B. Fitts, V. A. DeCarlo,[21] K. R. Thoms,[21] D. R. Cuneo[16])

The instrumented irradiations in the Oak Ridge Research Reactor[22] (ORR) are designed[23] to monitor the thermal performance of test fuel pins. The temperatures of the cladding and fuel center and the rates of heat generation are continuously measured and recorded. These data

Table 1.11. Fabrication and Operating Data for Tests of Prototypic Fuels in Thermal Flux

Fuel Pin[a]	Smear Density (% of theoretical)	Fuel Composition	Ratio $^{235}U/U$ (%)	Peak Linear Heat Rate[b] (kw/ft)	Peak Temperature at Inner Surface of Cladding (°C)	Fuel Center $\int$ kdT 400°C (w/cm)	Burnup (% FIMA)[c]		Equivalent Days at Full Power	Power Cycles[d]	Fission Gas Released (% ^{85}Kr)
							Peak	Average			
99-1	76	$(U_{0.80},Pu_{0.20})O_{2.00}$	93	34.6	730	56	1.4	1.2	18.9	11	24
99-3	76	$(U_{0.80},Pu_{0.20})O_{2.00}$	93	49.9	1000	84	2.8		18.9	11	NA
100-1	76	$(U_{0.80},Pu_{0.20})O_{2.00}$	93	29.3	650	48	1.2	1.1	18.9	11	NA
100-3	76	$(U_{0.80},Pu_{0.20})O_{2.00}$	93	44.9	900	75	2.5	2.3	18.9	11	NA
112-1	79	$(U_{0.85},Pu_{0.15})O_{1.97}$	0.6	8.4	220	18	0.5	0.45	27.8	11	2
112-2	74	$UO_{2.02}$	20.2	11.9	260	28	0.68	0.64	27.8	11	34
112-3	81	$(U_{0.85},Pu_{0.15})O_{1.97}$	0.6	13.6	320	31	0.68	0.67	27.8	11	27
112-4	80	$(U_{0.85},Pu_{0.15})O_{1.97}$	0.6	10.5	260	24	0.55	0.52	27.8	11	4
103-1	74	$UO_{2.02}$	20.2	16.4	380	34	4.2	3.8	126.3	73	30
103-2[e]	84	$UO_{2.00}$	19.8	25.9	540	64	4.9	4.4	126.3	73	47
103-3	73	$UO_{2.02}$	20.2	21.6	470	44	5.5	4.9	126.3	73	44
103-4	74	$UO_{2.02}$	20.2	17.9	400	38	4.5	4.0	126.3	73	41
115-1	80	$(U_{0.85},Pu_{0.15})O_{1.97}$	0.6	18	400	40	6.7	6.2	174.2	97	31
115-2	74	$UO_{2.02}$	20.2	17.0	390	39	5.9	5.8	174.2	97	47
115-3	82	$(U_{0.85},Pu_{0.15})O_{1.97}$	0.6	20.6	460	46	6.4	5.0	174.2	97	44
115-4	81	$(U_{0.85},Pu_{0.15})O_{1.97}$	0.6	13.4	370	32	4.2	4.1	174.2	97	38

[a] All fuel was in the form of microspheres vibratorily compacted by the Sphere-Pac process except for 103-2, which was pellets.

[b] Time averaged values based on the total exposure in equivalent days at full power.

[c] FIMA is fissions per initial actinide metal atom.

[d] Cycles from less than 50% full power to greater than 50% full power.

[e] Average cold diametral gap between fuel and cladding = 0.004 in.

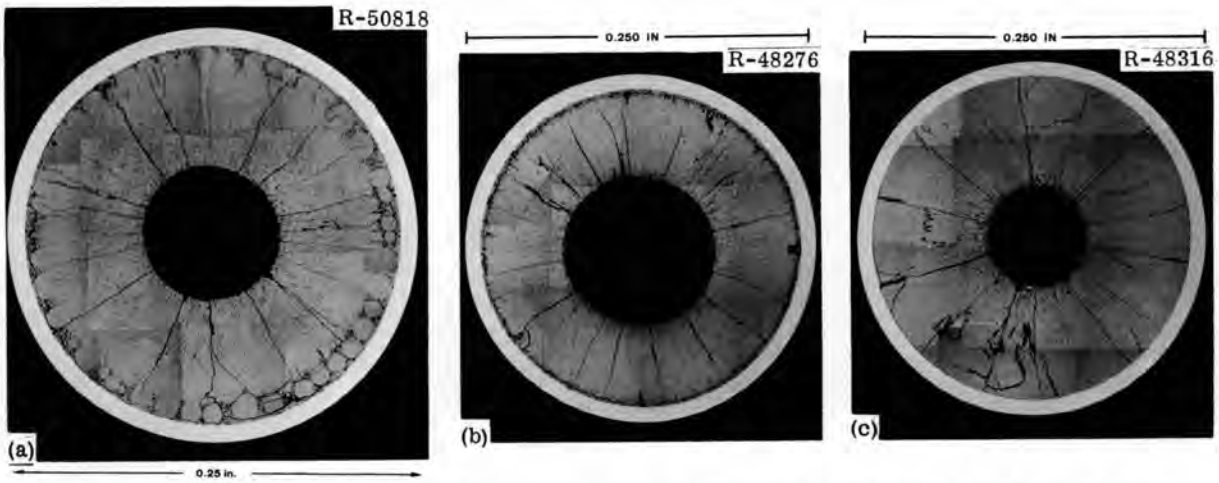

Fig. 1.4. Comparative Transverse Cross Sections of Fuel Pins After Irradiation to Moderate Burnup. (a) $(U_{0.85},Pu_{0.15})O_{1.97}$, 82% smear density, 20 kw/ft, to 6% FIMA; (b) Sphere-Pac $UO_{2.02}$, 73% smear density, 22 kw/ft, to 5.5% FIMA; and (c) pelletized $UO_{2.00}$, 84% smear density, 26 kw/ft, to 5.7% FIMA.

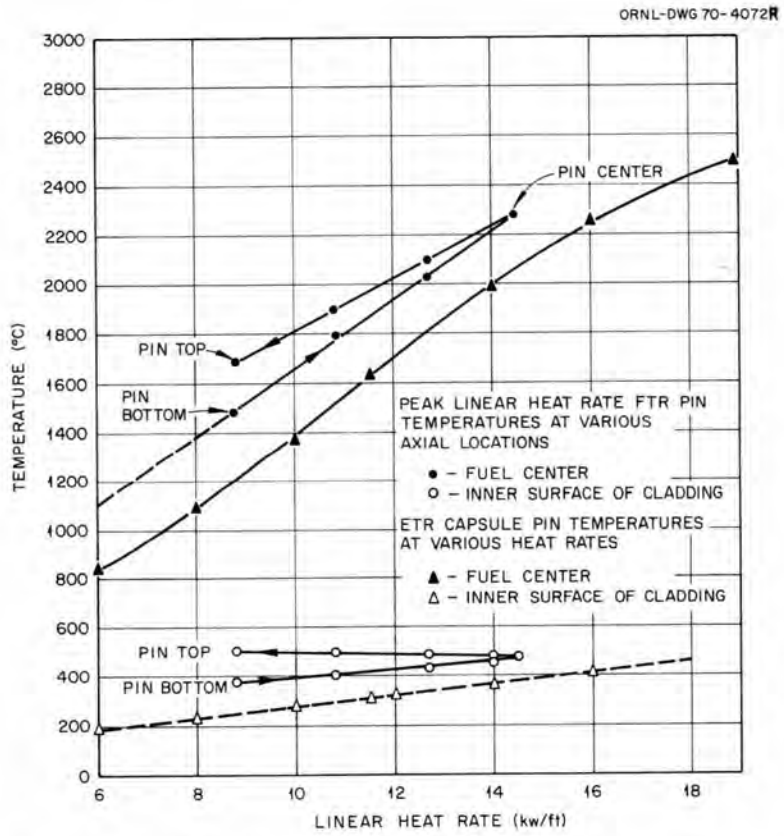

Fig. 1.5. Comparison of Temperatures of Fast Test Reactor (FTR) Fuel Pin with Those of Engineering Test Reactor (ETR) Capsule Pin.

are being used to evaluate the thermal characteristics of various fuels in-reactor and the effects of irradiation conditions upon the temperatures and rates of structural change within the operating fuels.

The irradiation of the third capsule in this series, SG-3, is nearing completion. This capsule contains one fuel pin of $(U_{0.8},Pu_{0.2})O_2$ Sphere-Pac[24] fuel at a smear density of 82% of theoretical and a second fuel pin of 83.5% dense sol-gel pellet[25] fuel of the same composition and smear density. This experiment will provide a direct comparison of these fuels to temperatures at the fuel center of near 2000°C and to heat rates of about 16 kw/ft.

The temperatures of the cladding, NaK, and center of the fuel are shown in Fig. 1.6 after about 60 days of operation with scheduled gradual increases in fuel temperature. These data were collected during a power decrease that lasted 1 1/2 hr after operation at temperatures in the pellet fuel that exceeded 1800°C for 120 hr, including 30 hr at 1935°C.

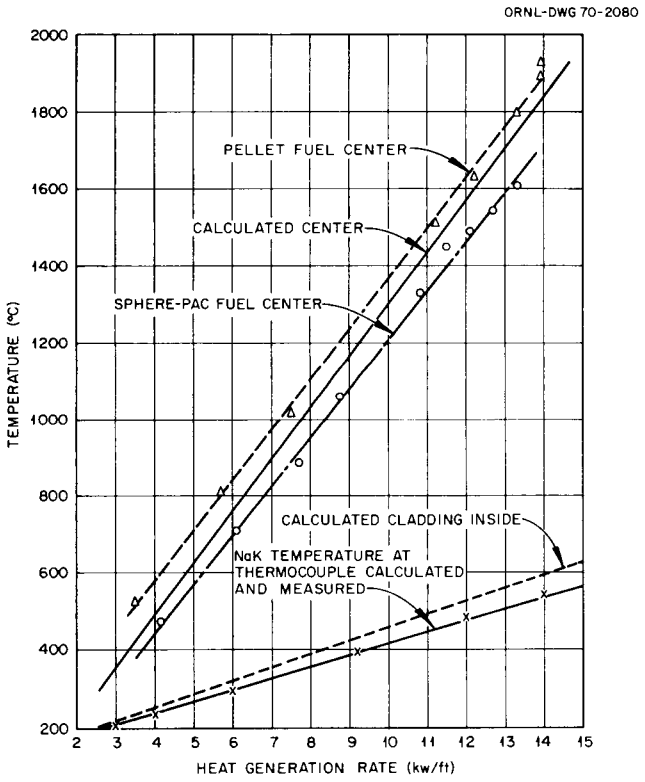

Fig. 1.6. Temperatures Versus Heat Generation Rate after 1000 hr of Operation of Capsule SG-3 Fueled with Sol-Gel $(U_{0.8},Pu_{0.2})O_2$ at 82% Smear Density.

The temperatures calculated for the center of the fuel were based on the measured temperatures of the cladding and the rates of heat generation, a fuel-to-cladding thermal resistance of 1 w/cm^2, the data of Baily et al.[26] for the thermal conductivity of $(U,Pu)O_2$ pellet fuels of this density, and an empirical model for fuel restructuring that was described previously.[27] The Sphere-Pac fuel has lower center temperatures than pellets at a given heat rate, indicating that the Sphere-Pac pins have a higher effective heat transfer coefficient between fuel and cladding. This difference is not large and may be insignificant with respect to experimental accuracy. After the data given above were collected, the thermocouple that measured the central temperature in the pellet fuel failed, and we placed a Cd shield around this pin to permit continued operation of the Sphere-Pac fuel. This shield limits the pellet fuel to heat generations below 5 kw/ft, while the Sphere-Pac fuel operates at full power. The fuel central temperature in this pin will be increased to near 2000°C before the experiment is terminated.

Instrumented Tests in Engineering Test Reactor (C. F. Sanders)

Two instrumented capsules were constructed to investigate fuel swelling and the chemical interaction between fuel and cladding for Sphere-Pac and pellet fuels under peak LMFBR conditions in the ETR. These capsules were completed during March and shipped to the ETR on March 25. The design data are given in Table 1.12.

Transient Tests (C. M. Cox, E. J. Manthos, D. R. Cuneo[16])

Six fuel pins containing unirradiated $(U_{0.80},Pu_{0.20})O_{1.98}$ produced by the sol-gel process were subjected to power transients at the Transient Reactor Test Facility (TREAT). No failures occurred even though two Sphere-Pac pins received a transient that probably melted 50 to 60% of the fuel.

Design, operating conditions, and postirradiation neutron radiographs were described previously.[28,29] Table 1.13 summarizes the present state of our evaluation of the data. Destructive examination of the fuel pins is in progress.

Table 1.12. Design Data for Instrumented Capsules for the Engineering Test Reactor

	Capsule Identification	
	43-120	43-121
Fuel composition	$(U_{0.80},Pu_{0.20})O_{1.98}$	$(U_{0.80},Pu_{0.20})O_{1.98}$
Fuel length, in.	3	3
Fuel smear density, % of theoretical	~ 81, pellet pins ~ 85, Sphere-Pac pins	~ 81, pellet pins ~ 85, Sphere-Pac pins
Fuel pins per capsule	2 pellet pins 2 Sphere-Pac pins	2 pellet pins 2 Sphere-Pac pins
Outside diameter of cladding, in.	0.250	0.250
Wall thickness of cladding, in.	0.016	0.016
Bond between fuel and cladding	He	He
Peak linear heat rate, kw/ft	18	18
Maximum cladding temperature, °C	640	640
Insulator composition	ThO_2	ThO_2
Maximum burnup, % FIMA	5	10
Instrumentation	Two cladding thermocouples per fuel pin	Two cladding thermocouples per fuel pin

Table 1.13. ORNL Data for Present Status of Capsules TR-1 and TR-2

	Fuel Pin					
	TR-1A	TR-1B	TR-1C	TR-2A	TR-2B	TR-2C
Fabrication Data						
Fuel fabrication form[a]	P	S	P	S	S	P
Fuel smear density, % of theoretical	0.88	0.82	0.79	0.82	0.81	0.80
Gas release, cm^3/g (STP) at 1600°C	0.07	0.14	0.23	0.14	0.14	0.19
Diametral gap between fuel and cladding, in.	0.005		0.005			0.005
Gas plenum volume,[b] cm^3 (STP)	1.1	1.3	1.5	1.3	1.3	1.4
Transient Data						
Initial sodium temperature, °C	410	449	414	400	436	410
Peak sodium temperature, °C	577	605	535	590	603	535
Peak instantaneous linear power, kw/ft[c]	140 to 170	130 to 170	110 to 130	140 to 170	140 to 170	100 to 120
Peak energy release, cal/g[c]	310 to 390	320 to 400	270 to 340	410 to 510	410 to 510	300 to 380
Reactor integrated power, Mwsec		140			172	
Fuel volume melt,[c] %	5 to 35	40 to 60	0 to 30	55 to 65	55 to 65	0 to 45
Postirradiation Examination						
Cladding maximum ovality, maximum diameter minus minimum diameter,[d] in.	< 0.0005	< 0.0005	0.0015	< 0.0005	< 0.0005	0.0018
Number of fuel column separations[c]	2	3	0	< 0.5	2	1
Total width of fuel column separations,[c] in.	0.140	0.160 to 0.250		0	0.120	0.060
Change in length of fuel column,[e,f] in.	−0.050	−0.180 to 0.270	−0.030	−0.060	−0.150	−0.020
Maximum diameter of central void,[e] in.	0	0.100	0	0.120	0.100	0

[a] P = solid pellets; S = Sphere-Pac.

[b] Including all porosity.

[c] Preliminary analysis, based on normalization to exterior flux monitor wires.

[d] Maximum diametral increase < 0.0005 in.

[e] Based on neutron radiographs; estimated accuracy ±0.020 in.

[f] Corrected for fuel column separations.

The activity of the exterior Co-Al flux monitor wires was measured for each capsule. Measurements of selected sections from one of the interior flux monitor wires in each capsule showed a considerable spread in the results. It appears that the results may have been influenced by contamination of the wires by γ radiation emitters during handling in the cell. We are attempting to remove one of the remaining wires from each capsule and decontaminate them before they are sectioned for activation analysis.

Profilometry data indicate no significant changes in pin diameter except for an ovality of 0.001 to 0.005 in. along pin TR-1C and a localized ovality of 0.0015 in. at the bottom of pin TR-2C.

Due to the low fuel burnup (about 3×10^{-6} %), γ-ray scanning was difficult. The fuel pins were removed from the HRLEL and scanned with a Ge detector. Although background noise was greatly reduced with this system, the scans are still not precise enough to determine fuel length and fuel separations. Gamma spectrum analysis identified ^{137}Cs and ^{140}Ba in the plenum region of most of the fuel pins. The data show a higher concentration of Cs for the TR-2C fuel pins, which operated at higher temperatures.

Gas was recovered from the plenum of each of the fuel pins. No Kr or Xe was detected by either γ-ray spectrometry or mass analysis. Helium was the predominant constituent of the gas in all of the pins except TR-1C and TR-2C, as shown in Table 1.14. These results seem consistent with those reported by Pechin[30] for the gas released from pins as fabricated. The high water content in the pellet pins with low density fuel may be due either to the water content of the pellets as loaded or to release of H_2 from the pellets during the transients. The latter problem was eliminated by changing the heat treatment.[31]

On the basis of available information, such as neutron radiography, the fuel pins were sectioned to obtain samples for metallography and burnup analysis. Samples were submitted for radiochemical analyses for those nuclides that may be suitable to allow calculations of burnup.

When these fuel pins were sectioned and subsequently examined with a stereomicroscope, we learned that the extremely short exposure in the reactor (2 to 4 sec) was sufficient to cause restructuring of the fuel in the microsphere pins. No obvious changes occurred in the pellet pins.

Table 1.14. Results of Analyses of Gas Removed from Fuel Pins TR-1 and TR-2 after Irradiation

Fuel Pin Number	Fuel Form	Composition of Gas, vol %								Total Gas Volume[a] (cm^3)
		H_2	He	CH_4	H_2O	N_2 + CO	O_2	Ar	CO_2	
TR-1A	Pellets	7	69	0.6	14	8	0.1	0.8	0.2	1.57
TR-1B	Microspheres	14	48	0.2	4	32	< 0.1		0.4	3.55
TR-1C	Pellets	6	42	2	44	6	0.2		0.1	3.99
TR-2A	Microspheres	18	55	0.4	10	16	< 0.1		0.4	2.89
TR-2B	Microspheres	20.6	70.5	7.1	< 0.1	0.9	< 0.1		0.2	3.93
TR-2C	Pellets	19	37	1	35	7	0.1		0.2	4.22

[a]At standard temperature and pressure.

Fast-Flux Irradiation Tests (A. R. Olsen)

The fast-flux irradiation tests in the EBR-II are designed to approximate conditions to be encountered in a commercial-scale LMFBR. The objective of these tests is to establish the effects of fuel fabrication form (Sphere-Pac or pellet), void distribution, and stoichiometry on the swelling of the fuel, mechanical and chemical interactions of fuel and cladding, release of fission gas, and distribution of fission products in a $(U,Pu)O_2$ fuel operating at typical heat rates to design levels of burnup.

The five series I encapsulated tests all contain Sphere-Pac fuels. They are still undergoing irradiation in EBR-II subassembly X050. It was previously reported[32] that this subassembly would be discharged following reactor cycle 39. However, the experimenters for the General Electric Company, who also have capsules in subassembly X050, asked for an extension of the exposure. This extension will extend the exposure through cycle 42. The extended irradiation will provide a peak calculated burnup for our pins of about 6.3% FIMA at discharge. Currently, the calculated burnup through cycle 41 is 5.6% FIMA. Three of the five capsules will be reinserted in another subassembly to continue their irradiation to a target burnup level of 10% FIMA.

The series II unencapsulated tests were described previously.[33] The safety analysis of these tests was begun. Since the subassembly will contain pins from both ORNL and Babcock & Wilcox Company, detailed fuel analyses are prepared by both installations. The design of the ORNL fuel pin was approved by personnel of the EBR-II project, and they have sent us preliminary design drawings for the three possible subassemblies (J-37, E-37, and N-37) that could be used for these tests. They have informed us that information on flow distribution for these subassemblies will be available early in April. As soon as this information is available, we shall begin the thermal analysis of the subassembly. In the interim, we have begun calculating the accumulation of fission product by means of the ORIGEN code.[34] These calculations, together with calculations of depletion, will permit us to establish irradiation times for the sequential removal and replacement of test pins and to establish the rates of decay heat for the various pins.

Notes

1. Chemical Technology Division.

2. W. T. McDuffee, Fuels and Materials Development Program Quart. Progr. Rept. Dec. 31, 1969, ORNL-4520, pp. 4–5.

3. C. R. Reese and W. L. Moore, LMFBR Fuel Cycle Studies Progress Report for October 1969, No. 8, ORNL-TM-2764, pp. 71–74.

4. C. R. Reese, LMFBR Fuel Cycle Studies Progress Report for November 1969, No. 9, ORNL-TM-2795, pp. 61–62.

5. C. R. Reese, LMFBR Fuel Cycle Studies Progress Report for December 1969, No. 10, ORNL-TM-2819, p. 61.

6. R. B. Pratt and R. A. Bradley, "Series II Unencapsulated Fuel Pins for Irradiation in the Experimental Breeder Reactor-II," pp. 11–14, this report.

7. R. A. Bradley, Fuels and Materials Development Program Quart. Progr. Rept. June 30, 1969, ORNL-4440, pp. 6–9.

8. R. A. Bradley and W. H. Pechin, Fuels and Materials Development Program Quart. Progr. Rept. Dec. 31, 1969, ORNL-4520, pp. 7–16.

9. R. A. Bradley, "Pelletization of Sol-Gel $(U,Pu)O_2$," pp. 7–11, this report.

10. W. H. Pechin and R. A. Bradley, Fuels and Materials Development Program Quart. Progr. Rept. Dec. 31, 1969, ORNL-4520, pp. 20–27.

11. R. A. Bradley and W. H. Pechin, "Alpha-Ray Autoradiography of $(U,Pu)O_2$ Microspheres," pp. 15–18, this report.

12. K. Kiukkola and C. Wagner, J. Electrochem. Soc. 104, 379–387 (1957).

13. T. L. Markin and E. J. McIver, "Thermodynamic and Phase Studies for Plutonium and Uranium-Plutonium Oxides with Applications to Compatibility Calculations," pp. 845–857 in Plutonium 1965, Proc. Int. Conf. 3rd, ed by A. E. Kay and M. B. Waldron, Chapman and Hall, London, 1967.

14. T. L. Markin et al., Proc. Brit. Ceram. Soc. 8, 51–66 (1967).

15. K. E. Spear, A. R. Olsen, and J. M. Leitnaker, Thermodynamic Applications to $(U,Pu)O_{2\pm x}$ Fuel Systems, ORNL-TM-2494 (April 1969).

16. On loan from Reactor Chemistry Division.

17. A. R. Olsen, C. M. Cox, and R. B. Fitts, Trans. Am. Nucl. Soc. 12(2), 605–606, 1969.

18. W. W. Little, Jr., and L. L. Maas, Nuclear Parameters and Parametric Studies for the Fast Test Reactor (FTR), BNWL-1067 (June 1969).

19. V.C.A. Vaughan et al., LMFBR Fuel Cycle Studies Progress Report for October 1969, No. 8, ORNL-TM-2764, pp. 16–18.

20. C. M. Cox, Oak Ridge National Laboratory, personal communication.

21. Reactor Division.

22. D. B. Trauger, Some Major Fuel Irradiation Test Facilities of the Oak Ridge National Laboratory, ORNL-3574 (April 1964).

23. R. B. Fitts and V. A. DeCarlo, Fuels and Materials Development Program Quart. Progr. Rept. June 30, 1968, ORNL-4330, pp. 20–23.

24. F. G. Kitts, R. B. Fitts, and A. R. Olsen, "Sol-Gel Urania-Plutonia Microsphere Preparation and Fabrication into Fuel Rods," pp. 195–210 in Intern. Symp. Plutonium Fuels Technol., Scottsdale, Arizona, 1967, Nucl. Met. 13, ed. by K. E. Horton, R. E. Macherey, and R. J. Allio, American Institute of Mining, Metallurgical, and Petroleum Engineers, New York, 1968.

25. R. A. Bradley, Fuels and Materials Development Program Quart. Progr. Rept. Sept. 30, 1969, ORNL-4480, pp. 7–8.

26 W. E. Baily et al., "Thermal Conductivity of Uranium-Plutonium Oxide Fuels," pp. 293–308 in Intern. Symp. Plutonium Fuels Technol. Scottsdale, Arizona, 1967, Nucl. Met. 13, ed. by K. E. Horton, R. E. Macherey, and R. J. Allio, American Institute of Mining, Metallurgical, and Petroleum Engineers, New York, 1968.

27. C. M. Cox, R. B. Fitts, and F. J. Homan, Fuels and Materials Development Program Quart. Progr. Rept. March 31, 1969, ORNL-4420 pp. 33–36.

28. C. M. Cox and R. E. Adams, Fuels and Materials Development Program Quart. Progr. Rept. March 31, 1969, ORNL-4420, pp. 30–31.

29. E. J. Manthos and D. R. Cuneo, Fuels and Materials Development Program Quart. Progr. Rept. Dec. 31, 1969, ORNL-4520, pp. 45–50.

30. W. H. Pechin, Fuels and Materials Development Program Quart. Progr. Rept. Sept. 30, 1969, ORNL-4480, pp. 11–15.

31. W. H. Pechin and R. A. Bradley, Fuels and Materials Development Program Quart. Progr. Rept. Dec. 31, 1969, ORNL-4520, pp. 20–27.

32. A. R. Olsen, Fuels and Materials Development Program Quart. Progr. Rept. Dec. 31, 1969, ORNL-4520, pp. 50–51.

33. A. R. Olsen, Fuels and Materials Development Program Quart. Progr. Rept. Sept. 30, 1969, ORNL-4480, pp. 29–33.

34. M. J. Bell, LMFBR Fuel Cycle Studies Progress Report for November 1969, No. 7, ORNL-TM-2748, p. 45.

2. DEVELOPMENT OF HIGH-PERFORMANCE LMFBR FUELS

P. Patriarca J. L. Scott

The goals of this program are to investigate the properties and behavior of those U- and Pu-based ceramic fuels that we term conductors — such as the mononitrides, carbonitrides, and monocarbides — and to compare their potential as liquid-metal fast breeder reactor (LMFBR) fuel with that of $(U,Pu)O_2$, which by comparison is an insulator. Since the thermal conductivity of the ceramic conductors is about ten times that of $(U,Pu)O_2$, it is theoretically possible to operate a conductor at ten times the power density with the same temperature at the center of the fuel. In practice, heat-transfer limitations, thermal stresses in the cladding, and high rates of swelling at high temperatures limit the power density that can be achieved with thermal conducting fuels to about two or three times that of $(U,Pu)O_2$ — still a challenging improvement. Additionally, the margins for transient overpower in the ceramic conductors are much higher than those for $(U,Pu)O_2$.

We seek to provide the information necessary for evaluating the true potential of nitrides, carbonitrides, and carbides in comparison to each other and to mixed oxides. We need to define the structures, composition, and quality control required to achieve 150,000 Mwd/metric ton at peak linear heat ratings of 30 to 50 kw/ft. We must also demonstrate the possibility of a low-cost fuel cycle for manufacturing fuel with the needed properties. And since austenitic stainless steel is a poor conductor of heat, we seek to establish the physical and thermodynamic criteria for the new cladding material that will probably be required to exploit the conducting fuels.

Our work is oriented primarily toward demonstrating the irradiation performance of $(U,Pu)N$ at high burnups and high heat ratings. Therefore, much of our effort is devoted to fabricating and characterizing fuel for irradiation testing. Two fabrication routes are being pursued, physical mixing of UN and PuN and fabrication of $(U,Pu)N$ from prealloyed metal ingots. Type 316 stainless steel will be used as cladding in near-term irradiation tests. Finally, some effort is being expended to develop

economical methods of fabricating high-performance fuels. Since carbothermic reduction of oxide followed by nitriding appears attractive, we are generating basic kinetic data for evaluation of this process.

Synthesis, Fabrication, and Characterization of Nitride Fuels

V. J. Tennery

The purposes of this portion of our program are to develop methods for preparing (U,Pu)N powders of high purity, to characterize them, and to fabricate pellets of variable but controlled density for use in irradiation test capsules.

Synthesis and Fabrication of Mixed Nitrides (E. S. Bomar)

Fabrication by Hot Pressing. — Work on this portion of our program was deferred temporarily for lack of manpower. A single pellet of (U,Pu)N was prepared, however, using powder made from prealloyed metal. The structure of this sample confirmed the presence of metal in the nitride powder as synthesized.

Fabrication by Sintering. — We experimented further with (U,Pu)N powder made from prealloyed U and Pu metals preparatory to selecting a schedule for fabricating the pellets required to fuel two capsules to be tested in the Engineering Test Reactor (ETR). The results of initial experiments with (U,Pu)N prepared from prealloyed metal, reported and illustrated previously,[1] showed that free metal was present in the microstructure of some sintered pellets. Evidence of the presence of a liquid phase during sintering is shown on a macroscopic scale in Fig. 2.1. Pellets prepared from ground powders wet the W plate on which they were set for sintering more than those that were not ground, presumably because grinding would break the envelope of nitride that would surround the metal particles if present in the synthesized powder. Wetting increased whether the powder was ground in a small steel mill or in a mullite mortar.

We determined that free metal in the sintered pellets was due to incomplete conversion of metal to nitride in the synthesis step. A

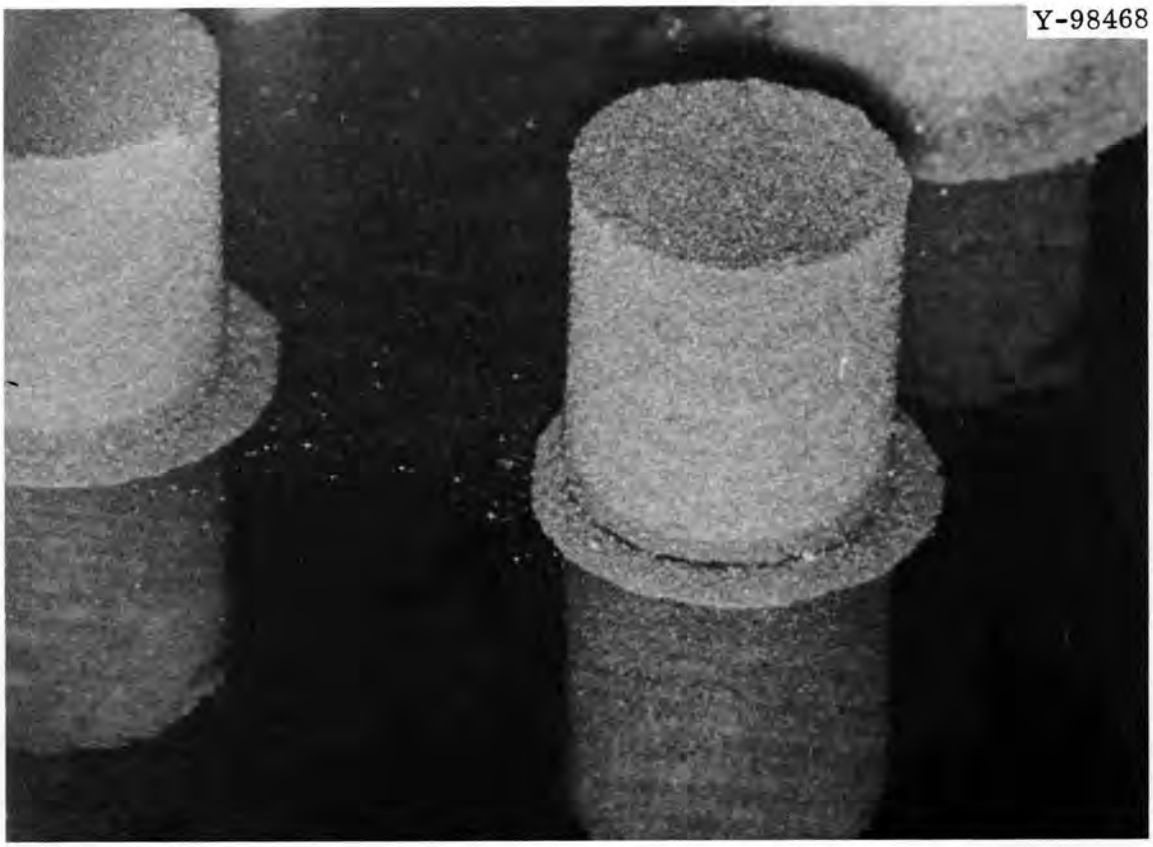

Fig. 2.1. Pellet of $(U_{0.8},Pu_{0.2})N$ Prepared by a Single Hydride-Nitride Cycle from Prealloyed Metal. Powder was cold pressed at 40 tsi and then sintered for 3 1/2 hr at 2100°C on a tungsten sheet in an atmosphere of nitrogen. A ring formed at the base of the pellet due to wetting of the tungsten sheet by a molten phase that was present during sintering. The lower portion of the image is a reflection of the pellet from the tungsten sheet. Sintered pellet is about 1/4 in. in diameter by 1/4 in. high.

minimum of three cycles of hydriding and nitriding is necessary in our equipment to completely convert prealloyed U mixed with Pu to the nitride.

We prepared five batches totaling about 400 g of mixed nitride from the prealloyed metal by means of multiple hydride-nitride cycles. This powder was then used to fabricate 185 pellets, 1/4 in. in diameter by 0.209 in. long, in 13 lots by cold pressing and sintering. Three pellets from each lot will be used for chemical analyses, metallographic examination, x-ray diffraction, and archive samples; the balance of 146 pellets, which provide a total length of 30.51 in. of fuel pellets, will be used to prepare 10 irradiation pins. Eight pins are required to load two irradiation capsules for the ETR; two pins will be left in reserve.

We also fabricated 45 UN pellets, 1/4 in. in diameter by 1/4 in. long, to serve as end spacers for the (U,Pu)N fuel column in the ETR pins.

The fabrication sequence selected for the (U,Pu)N pellets included the following steps:

1. Convert an 80- to 90-g charge of U-Pu alloy to nitride by first forming the hydride by exposure to gaseous H_2 at about 760 torr and 150 to 250°C.

2. Introduce gaseous N_2–1% H_2 at 50 torr of Hg, raise the temperature in 50°C increments, pump down to a partial vacuum, and reintroduce N_2–1% H_2 before increasing temperature.

3. Continue incrementally increasing temperature to 1050°C, pump down to about 10^{-5} torr, and hold for 30 min to reduce the amount of residual sesquinitride.

4. Cool to about 125°C and repeat steps 1 through 3 two additional cycles to convert any residual metal to nitride.

5. Load 5 g of nitride powder into each of six small steel mills and grind for 15 min on the "Shatterbox" grinder.

6. Cold press at 40 tsi in a steel die lubricated with stearic acid.

7. Heat to 1400°C under vacuum of 10^{-5} to 10^{-7} torr in a W-resistor furnace; then, backfill with N_2 to 635 torr.

8. Heat to 2100°C and hold for 165 min; then heat to 2250°C and hold for 15 min.

9. Cool to 1400°C and evacuate; then cool to room temperature.

Dimensional and density measurements for 159 mixed nitride pellets containing 19.3 metal atom % Pu are summarized in Table 2.1. The tabulation shows a dependence of sintered density on powder batch that implies a relationship between some variation in the synthesis process and the subsequent sintering behavior. Pellets pressed from the A-5-C powder had the lowest density and also shrank less longitudinally than those from the other powders. Pellets pressed from the A-6-C powder sintered more longitudinally and less diametrically than did pellets made from four other powders.

Samples representative of the first five lots of pellets were examined metallographically and found to be fine grained and to have a

Table 2.1. Sintering Results for $(U_{0.806},Pu_{0.183})N$ Pellets[a]

Powder Code	Sintering Lot	Number of Pellets	Average Measured Values for Sintered[b] Pellets			
			Diameter (in.)	Height (in.)	Density (g/cm^3)	Density (% of theoretical, 14.32 g/cm^3)
A-4-C	1	13	0.243	0.210	12.48	87.3
A-5-C	2	13	0.242	0.216	12.29	85.8
	3	13	0.242	0.215	12.25	85.8
	4	13	0.242	0.215	12.33	86.1
A-6-C	5	13	0.246	0.203	12.58	87.8
	6	13	0.247	0.204	12.49	87.2
	7	13	0.248	0.204	12.43	86.8
A-7-C	8	13	0.242	0.207	12.77	89.2
	9	13	0.242	0.206	12.91	90.2
	10	9	0.243	0.205	12.79	89.3
A-8-C	11	13	0.243	0.208	12.64	88.3
	12	13	0.242	0.210	12.62	88.1
	13	7	0.243	0.208	12.61	88.1

[a]Each pellet weighs 2 g.

[b]Sintering cycle in N_2 atmosphere: 165 min at 2100°C plus 15 min at 2250°C.

single-phase microstructure. A representative pellet is shown in Fig. 2.2. No evidence of melting was found in the form of beads on any of the 185 pellets fabricated for the irradiation pins. The microstructures contained only single-phase nitride. The bright particles that appear in the porosity shown in Fig. 2.2(c) are artifacts caused by small bits of stainless steel worn from the side of the bowl on the vibratory polisher. One pellet made from A-4-C powder was partially chemically analyzed; it contained 720 ppm O_2, 460 ppm C, and 100 ppm Fe. The Fe content was essentially unchanged from that found in the U-Pu alloy used to prepare the nitride powder. We are holding the balance of the samples until several problems in the analytical procedures for U, Pu, and N_2 are

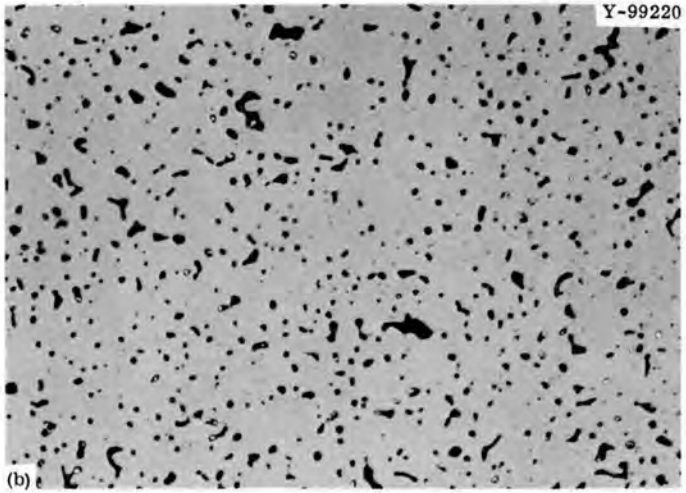

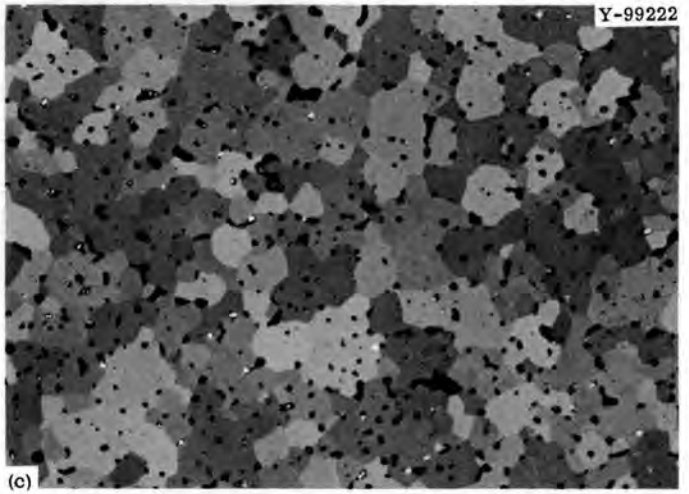

Fig. 2.2. Pellet from Set for Irradiation Pins. (a) Macrophotograph. (b) Microstructure as polished. 500×. (c) Microstructure as etched. 500×. Nitride powder was prepared from prealloyed metal by three hydride-nitride cycles. Pellet was cold pressed at 40 tsi and then sintered for 3 hr at 2100°C and 15 min at 2250°C in an atmosphere of nitrogen. A slight discoloration of the tungsten can be seen at the base of the pellet, but the pellet did not stick to the tungsten sheet. The lower portion of the image is a reflection of the pellet from the tungsten sheet.

resolved. The isotopic content of the U-Pu alloy was obtained, however, and the results are presented elsewhere in this report.[2]

Since preparing the pellets for the ETR capsules required that our technicians use the glove boxes 4 or 5 hr a day for several weeks, we supplemented the routine check of gamma activity on the gloves with a check of hand exposures by means of finger rings. Previous surveys with finger rings several months earlier revealed acceptable hand dosage. Our most recent checks of daily exposure showed that the accumulative dosage would exceed the limit of 1.5 rem/week for extremities. A gamma scan of a sample from our current stock of Pu identified the principal source of hand exposure to be the 59.5 kev gamma from ^{241}Am. We provided a temporary solution to our problem by reducing the box inventory as much as practical, providing additional shielding for nitride powders and pellets located in the glove boxes, and adding another man to share the glove-box work. Our long-range plan is to thoroughly clean the interior of our boxes and request that Pu supplied for future work on fuel development have a lower ^{241}Pu content.

Fabrication Equipment. — A contract was placed with the CVI Corporation to design and fabricate a purifier with a capacity of up to 160 cfm for recirculation of the inert gas to our glove boxes. The purifier will operate on the principle of cryogenic adsorption on charcoal refrigerated with liquid N_2 to purify He gas. Design of the purifier is nearly complete, and delivery is expected the latter part of this summer.

Characterization of Nitride Fuels (V. J. Tennery)

X-Ray Diffraction Studies of Uranium-Plutonium Nitrides. — We are studying the x-ray lattice parameter of $(U_{0.80},Pu_{0.20})N$ and PuN as a function of the state of the starting material and the thermal history of the specimens. Most of our effort was concentrated on measurements of the lattice parameters of synthesized (U,Pu)N powders and the changes that occur in the lattice parameter when the powder is pressed into pellets and sintered at high temperatures in N_2. We found free metal in the microstructure of several pressed-and-sintered pellets that were intended to have a nominal composition $(U_{0.80},Pu_{0.20})N$. It was

imperative that the origin of the metal be identified (i.e., was it present in the nitride powder as synthesized or was it being generated by decomposition of the mononitride during sintering at high temperature?). All available phase data on the U-Pu-N system indicated that sintering temperatures of about 2150°C and 1 atm N_2 would not lead to gross decomposition of the mononitride. X-ray powder diffraction patterns of the nitride powders prepared from U-Pu alloy by the hydride-dehydride-nitride process indicated that these powders consisted solely of the U-Pu mononitride phase. In order to clarify this situation, we used nitride powder made from the alloy to fabricate a specimen of the nominal composition $(U_{0.8},Pu_{0.2})N$ and hot pressed this specimen at 1750°C, a temperature far below that at which decomposition of the mononitride could occur. The microstructure of this specimen contained several percent of free metal at the grain boundaries, and the x-ray pattern indicated the presence of a low-symmetry phase or phases in addition to the mononitride. The extraneous phases were apparently U and Pu. Therefore, it was apparent that this free metal was present in the powders initially, even though x-ray patterns of the powders indicated the presence of only the mononitride phase. This discrepancy is apparently due to the free metal being present in the center or core of the nitride powder particles as synthesized and thus being screened from the x rays during the diffraction process. Reexposure of these powders to H_2 at high temperature resulted in small but perceptible reactions with the gas that confirmed that small amounts of free metal had been present in the powders. A modification of the synthesis procedure for producing the (U,Pu)N powders solved the problem of free metal in the sintered pellets.

We examined several samples of $(U_{0.8},Pu_{0.2})N$ by x-ray diffraction to establish the reproducibility of the computed lattice parameters and correlations of the parameters with powder comminution, sample sintering conditions, and other variables. Several of these results are presented in Tables 2.2 and 2.3. The variations between the lattice parameters for various specimens are quite small, if they are real. The causes for these small variations are not yet understood. An

Table 2.2. Fabrication Conditions and Lattice Parameters Determined by X-Ray Diffraction for Sintered Pellets of Nominal Composition $(U_{0.80},Pu_{0.20})N$

Sintered Pellet Sample Designation	Sintering Conditions[a]		Lattice Parameter (A)	Comments
	Time (min)	Temperature (°C)		
96	30	1750[b]	4.89005 ± 0.00014	
S-99	220	2100	4.89153 ± 0.00022	A-2 powder from BNWL[c] alloy, ground 15 min in rotating mill, no magnetic cleanup
S-57	240 plus 252	2100 2200	4.89040 ± 0.00062	Powder from ORNL 80% U–20% Pu alloy
S-53	210 plus 252	2100 2200	4.89049 ± 0.00020	Specimen from mechanically mixed UN and PuN powders
S-102	240	2100	4.89072 ± 0.00019	A-2-B alloy powder, hand ground before fabrication
S-103	240	2100	4.89084 ± 0.00015	A-2 powder from BNWL[c] alloy, ground 15 min in rotating mill, magnetic cleanup
S-119	188	2150	4.89117 ± 0.00037	A-4-C alloy powder as synthesized, no grinding
S-121	188	2150	4.89108 ± 0.00020	A-4-C alloy powder, ground 5 min in rotating mill

[a]All samples except 96 were sintered in N_2 at 760 torr.

[b]Sintered by hot pressing at 6 tsi in a N_2-Ar atmosphere.

[c]Battelle Memorial Institute Pacific Northwest Laboratory.

Table 2.3. Fabrication Process and Lattice Parameters Determined by X-Ray Diffraction for Nitride Powders of Nominal Composition $(U_{0.80},Pu_{0.20})N$

Nitride Powder Sample Designation	Synthesis Procedure, cycles		Lattice Parameter (A)	Comments
	Hydride-Dehydride	Nitride		
A-2	1	1	4.89158 ± 0.00028	As synthesized: later found to contain traces of free metal, −325 mesh fraction
A-4-B	2	2	4.89176 ± 0.00051	+325 mesh fraction
A-4-B	2	2	4.89111 ± 0.00011	−325 mesh fraction
A-4-C	3	3	4.89106 ± 0.00026	−325 mesh fraction

increase in the number of hydride-dehydride-nitride cycles in powder synthesis may cause a slight decrease in the measured lattice parameter of the powder. Also, the fractions of the powders with larger particle sizes exposed to only one or two synthesis cycles may exhibit slightly larger parameters than do the smaller size fractions. If this apparent behavior is real, it may be related to the "cores" of free metal that are apparently present in the larger particles when only one or two hydride-dehydride cycles are used in the synthesis of powder.

As noted above,[3] a large number of fuel pellets were produced for irradiation. We are determining and shall report the lattice parameter of an x-ray control specimen from each sintering run.

Chemical Analyses for Studies of Uranium-Plutonium Nitrides (V. J. Tennery, J. L. Botts,[4] J. P. De Luca)

We concentrated our efforts on establishing analytical procedures that will allow accurate, quantitative, chemical analyses of specimens of U-Pu nitrides. We also obtained the spectrographic and isotopic analyses needed to characterize the specimens to be used in irradiation experiments in the ETR.

The techniques that have been developed or are being developed for analyzing these materials are listed below:

Element	Analytical Technique
U	Coulometry
Pu	Coulometry
N	Microkjeldahl
O	Inert-gas fusion
C	Combustion

Early analyses for U and Pu in sintered mononitride specimens indicated periodic perturbations in the results that could not be rationally correlated with any of the variables of synthesis or fabrication. A study by the Analytical Chemistry Division showed that the use of coulometric techniques for control samples of either U or Pu alone in solution produced the expected results but that the presence of both together in

ratios relevant to LMFBR applications apparently can lead to significant errors in some of the analyses. We prepared several standard solutions that contained U or Pu alone or mixtures of the two. Coulometric titrations of those solutions that contained U or Pu alone gave results that typically agreed with the expected results within about 0.2%, but results from solutions that contained both elements in concentrations relevant to the LMFBR repeatedly indicated a Pu content that was lower than expected by about 0.5 to 0.8%. It appeared that the negative bias for Pu may have been due to the presence of some Pu^{+6} ions in those solutions that contained both U and Pu. We added a reducing agent to determine if this step would remove the negative bias for Pu in the control samples.

After we confirm that no negative bias occurs for either U or Pu, we shall determine if such problems also exist due to the methods used to place sintered mononitride samples into solution for analysis.

Our analyses for N are plagued with the classical problems associated with the Kjeldahl technique. However, we developed techniques for transferring and digesting samples that apparently have removed much of the negative bias usually observed in analyses of mononitride samples.

We analyze for O by inert-gas fusion of mononitride samples and by vacuum fusion of metal samples. These analyses presently provide results with acceptable precision. The analysis for small amounts (< 600 ppm) of C in the mononitride sample is a routine procedure.

The analyses for U and Pu in the U-Pu alloy and in a sintered (U,Pu)N pellet made from the alloy are shown in Table 2.4.

The O and C contents of the alloy noted in Table 2.4 were determined to be about 600 and 500 ppm, respectively. The spectrographic analysis of the alloy indicated that there were no other significant contaminants present. If no Pu or U bias is assumed and the concentrations of these elements are combined, one obtains 99.69%. If approximately 0.11% of O plus C is added to this value, one obtains 99.80%, which indicates that at least one of the analyses is exhibiting some negative bias. If a 3% Pu negative bias is assumed, a mass balance of 100.27% is obtained.

For the sintered pellet S-151, if we average the two U analyses and assume no bias and stoichiometric mononitride, a negative bias for Pu is

Table 2.4. Results of Analyses for Uranium and Plutonium in Uranium-Plutonium Alloy and in Sintered Pellet Made from the Alloy

Sample	Uranium Content (%)	Plutonium Content, %		Remarks
		Unadjusted	Adjusted[a]	
Alloy	80.37	19.32	19.90	Mass balance 99.69% if no bias is assumed, 100.27% if 3% negative Pu bias assumed
Sintered pellet S-151	74.98	17.94	18.48	Two separate aliquots
	75.34	17.96	18.50	

[a]Plutonium concentrations adjusted for the negative bias observed in U-Pu standard solutions.

indicated. The average for the U analyses is 75.16%. The percentage of U plus Pu by weight in a stoichiometric mononitride sample, $(U_{0.8},Pu_{0.2})N$, is 94.45% if we assume ^{238}U and ^{239}Pu to be present. Thus, 94.45 − 75.16 = 19.29%, the expected concentration of Pu. As shown in Table 2.4, the measured value was about 17.95%. Assuming a 3% bias correction leads to about 18.50% Pu, a difference of about 0.8% from the expected value. Microstructural analysis, the analyses for N, and the measurements of lattice parameter to date indicate that the samples are a single mononitride phase, and all thermodynamic data to date indicate that these compounds do not exhibit significant deviations from the stoichiometric composition. Therefore the analytical data should be reasonably close to the expected values for the various elements.

After all bias effects observed in the control samples have been removed from the analyses, we shall determine what bias effects occur when a dense mononitride specimen is dissolved.

The U-Pu alloy used for producing the nitride powders and a typical sintered specimen of nominal $(U_{0.8},Pu_{0.2})N$ were analyzed spectrographically, and the results are given in Table 2.5. The isotopic content of the sintered mononitride was determined, and the results are given in Table 2.6.

Table 2.5. Results of Spectrographic Analysis of Uranium-Plutonium Alloy and a Sintered Specimen

Element	Specimen Content, ppm by Weight	
	U-Pu Alloy	Sintered Specimen S-152
Al		130
B		
Cr	4	10
Cu	5	
Fe	100	80
Mn		
Mo		
Nb		
Ni	8	30
Pb		
Si		
Sn		
Ti		
V		
Zr		

Table 2.6. Isotopic Content of Mononitride Fuel for Irradiation Experiments

Isotope	Concentration (%)
^{238}Pu	< 2
^{239}Pu	93.21
^{240}Pu	6.19
^{241}Pu	0.58
^{242}Pu	< 0.022
^{244}Pu	0.0002
^{233}U	0.0012
^{234}U	0.0015
^{235}U	0.273
^{236}U	0.0048
^{238}U	99.72

We investigated the source of the problems that hinder the analysis of mononitride samples for U, Pu, and N. For comparison, two different laboratories of the Analytical Chemistry Division conducted duplicate analyses for U and Pu, and two different techniques were used to dissolve the specimens. These methods varied basically in the technique used to fume the dissolved sample to remove traces of nitrate ions from the solutions. One method was found to provide more consistent mass balances and was selected to be used henceforth.

The results obtained by laboratories A and B for analyses of the U and Pu in a sintered specimen (S-147) of the nominal composition $(U_{0.8},Pu_{0.2})N$ and for the alloy from which the powder was made are given in Table 2.7. Specimen S-147 was produced from the same nitride powder as was S-151 and was sintered identically.

Only one laboratory analyzed for N content in specimen S-147; values of 5.38, 5.39, and 5.15% were found. The latter value is thought to be low due to some loss of sample during analysis. If we assume a N content of 5.39% and a measured content of O plus C in these sintered samples of 0.07 + 0.04% = 0.11%, the average of the U (76.08%) and Pu (18.23%) values added to the O and C contents, produces a mass balance of 99.81%. Neglecting the difference of the mass balance from 100.00%, we calculated the molar composition of the specimen by two methods.

If we assume that the sample was basically a stoichiometric mononitride phase that contained ^{238}U and ^{239}Pu, 0.806 mole fraction of U and 0.193 mole fraction of Pu were present, based on 252.2 g as the molecular weight of the stoichiometric mononitride. These assumptions and the results of the analyses indicate that the composition of sample S-147 was $(U_{0.806},Pu_{0.193})N_{0.9926}$, where the O plus C is assumed to substitute for N and to be equivalent to N in the crystal structure of the mononitride. The sum of the mole fractions of U and Pu is 0.999 (the theoretical value is 1.000).

On the other hand, the molar composition of the specimens can be calculated by another route that involves no assumptions as to the actual molecular weight of the final composition. If the analyzed N content (5.39%) is added to the sum of the O and C contents (0.11%) the total nonmetallic content is 5.50%, which is 0.05% below the theoretical

Table 2.7. Results of Comparative Analyses[a] for Uranium and Plutonium in Sintered Uranium-Plutonium Nitride Sample S-147 and in the Uranium-Plutonium Alloy from Which it was Made

Material	Specimen Number	Uranium Content, wt %		Plutonium Content, wt %		Sum of Metal Actinides[b] (wt %)
		Measured	Average	Measured	Average	
			Laboratory A			
S-147	1	76.154 76.084	76.12	18.085 18.058	18.07	94.21
	2	76.169 76.216	76.19	18.313 18.320	18.31	94.53
	3	75.689 75.742	75.71	18.097 18.118	18.11	93.84
Alloy[c]	1	80.484 80.425	80.45	19.361 19.328	19.34	99.81
	2	79.728 79.825	79.78	19.680 19.666	19.67	99.47
			Laboratory B			
S-147	1	76.108 76.198 76.153	76.15	18.31 18.27	18.29	94.443
	2	76.202 76.222 76.188	76.20	18.30 18.34	18.32	94.524
	3	76.192 75.987 75.951	76.04	18.22 18.11 18.15	18.16	94.283
Alloy[c]	1	80.44 80.42 80.48	80.45	19.38 19.30 19.21	19.30	99.745
	2	80.02 79.88 79.93	79.94	19.34 19.42	19.38	99.32

[a]Samples were dissolved in laboratory A and analyzed in laboratories A and B.

[b]Weight percentage of uranium plus nitrogen in $(U_{0.8},Pu_{0.2})N$ is 94.45% when sample contains only ^{238}U and ^{239}Pu.

[c]Oxygen plus carbon content of the alloy was about 0.10 wt %.

value. The O and C are now assumed to have an average atomic weight equal to that of N. The mole fraction of ^{238}U present is 76.08/238 = 0.3196, that of ^{239}Pu is 18.23/239 = 0.0763, and that of ^{14}N is 5.50/14 = 0.3929. The fact that the mass balance for this sample was 99.82% rather than 100.00% was neglected. The molecular composition of the specimen can then be calculated if one of the elemental constituents is selected for normalization. The N was selected for normalization to allow a straightforward comparison with the composition calculated by the first method. The molar composition obtained for specimen S-147 by this technique is $(U_{0.809},Pu_{0.194})N$. In this case, the mole fractions of U plus Pu give a sum of 1.003 (the theoretical value is 1.000). This result is essentially identical to that of the first method of calculation.

From these studies it appears that the negative bias noted in the analyses for Pu may not be due to the presence of Pu^{+6} ions in the U-Pu solutions but may actually be due to the fact that the sample sizes used previously were somewhat too small for the coulometer cells being used. These small samples may have resulted in solution concentrations that did not take full advantage of the inherent accuracy of the solid-state coulometers being used. This possibility is now being investigated by means of analyses of larger samples.

This dependence on the size of the sample is reflected in the data in Table 2.7 for the U-Pu alloy analyzed in laboratories A and B. Sample 1 of the alloy had a mass of about 170 mg, whereas sample 2 had a mass of about 75 mg. In both laboratories, the values for U obtained from sample 2 were smaller than those from sample 1.

Compatibility of Mixed-Nitride Fuels with LMFBR Cladding Alloys

J. M. Leitnaker

Our approach to compatibility in high-performance fuel systems is to characterize interactions that can occur between the fuel and cladding material. A basic understanding of these reactions may point to methods for tailoring the fuel so that the reactions cannot occur and perhaps to methods for hindering these reaction kinetics.

The U-Pu-Cr-N System (J. P. De Luca, K. E. Spear)

A mixed-nitride fuel pellet Na-bonded to a cladding of type 316 stainless steel is a potential advanced fuel pin for the LMFBR. To determine what constituents of the fuel and cladding can cause compatibility problems and to find solutions to these problems, one needs a minimum amount of thermodynamic and phase data on the system.

We hope to follow a three-step procedure in evaluating and solving these compatibility problems. First, we shall investigate the phase behavior in (U,M)N systems, where M will be Cr, Fe, Ni, V, and Mo (V and Mo were added because both are possible backup cladding materials; V can be used to buffer the fuel, and Mo is a major fission product and thus should be investigated in any fuel-cladding system). Second, we shall use these results to guide experiments involving Pu instead of U and the different metal components. This procedure will take advantage of the thermodynamic similarity between U and Pu nitrides and will enable us to do the minimum number of experiments with Pu to gain a maximum amount of information. Third, we shall investigate the phase relationship between the metal components, N, and alloys of U and Pu.

Pu-Cr-N System

We fabricated Cr metal and PuN powder in a ratio of 2:1 into a 1/4-in.-diam pellet.

Malfunction of the Venco high-vacuum valve delayed heat treatment of this pellet. We removed the glass on the glove box and repaired the valve. The induction unit also failed and was repaired. The window for the optical pyrometer in the induction furnace, the right-angle prism, and the window of glove box 9 were calibrated for temperature correction.

We made an initial run in this glove-box system with a well-characterized sample of V_2N. This sample is now being examined with x rays. The Cr-PuN pellet sample will be heat treated when time permits.

Thermodynamic Investigations of High-Performance Fuel Systems

J. M. Leitnaker

The goal of our thermodynamics program for high-performance fuels, the carbides, nitrides, and carbonitrides, is to be able to predict the limiting equilibrium behavior of fuel and cladding in fast-reactor environments. Our experiments, though limited to measurements out-of-reactor, are of value for defining and understanding the factors that affect fuel performance.

Thermodynamics of Plutonium Nitride (K. E. Spear, J. P. De Luca)

For our study of the compatibility of mixed nitride fuels with cladding materials, we are building a system for measuring N_2 pressures over the nitrides and carbonitrides of Pu to define the effects of temperature, pressure, and composition on the behavior of the fuel toward cladding materials. The system was described previously.[5]

This quarter we assembled the apparatus. The services (electricity, air, water, Ar) to the glove box and vacuum system were completed. The vacuum system is 90% completed; only the vacuum microbalance remains to be put in place. Initial check-out procedures were started on the vacuum system.

Thermophysical Properties

D. L. McElroy

Measurement of the Physical Properties of (U,Pu)N Alloys (S. C. Weaver, T. G. Kollie)

We began a study of the thermal conductivity of (U,Pu)N alloys, since this property largely determines the temperature distribution and irradiation behavior of the fuel. Irradiation effects, such as fuel swelling, release of fission gas, and distribution of fission products, depend on the temperature distribution. We plan to study the effects of fuel density, impurity content (C and O), and ratio of U:Pu in these alloys.

The two glove boxes for measuring electrical resistivity, thermal conductivity, and thermoelectric power arrived from the manufacturer.

Minor modifications must be made to these boxes due to manufacturing defects. In the meantime, the box for measurements of electrical resistivity has been set up temporarily in the physical properties laboratory so that we may install the equipment and develop assembly techniques for the experiments. We are simulating our experimental problems by using (U,Th)N alloys because they oxidize rapidly in air and must therefore be assembled in an inert atmosphere. Consequently, the problems associated with assembly of (U,Th)N samples should be nearly identical to those of Pu materials. As a result of these tests, we made a large number of changes in equipment design and experimental techniques for glove-box operations.

We are in the process of connecting the existing apparatus for measurements of thermal conductivity and electrical resistivity at low temperatures into the PDP-8 computer-recorder system (CODAS). If the data taken by this technique are sufficiently accurate, the time required to obtain and calculate the data should be reduced significantly. As a result of our success with UN — with recent refinements we obtained values reproducible to ±0.02% — we plan to use CODAS to evaluate the electrical resistivity of (U,Pu)N alloys at high temperatures.

Irradiation Testing of Nitride Fuels for LMFBR Applications

T. N. Washburn

The objective of this program is to establish the irradiation performance of the U-Pu nitrides and carbonitrides. The nitrides and carbonitrides have a thermal conductivity about 5 times higher, a theoretical density 30% higher, and a metal content in the compound 7% higher than the oxides. These properties make the nitride and carbonitride strong contenders as advanced fuel for a LMFBR.

Thermal-Flux Tests (C. F. Sanders)

For the first series of tests, two uninstrumented capsules that each contain four fuel pins will be irradiated in the ETR. These screening tests will allow us to evaluate the performance of (U,Pu)N fuel synthesized from metal.

In these tests, the ratio of the fuel column length to the pellet diameter (L:D) is 10 or greater. With this ratio, we can use one-dimensional analyses to calculate the rates of heat transfer and heat generation. With ratios of L:D significantly less than 10, the value of temperatures calculated from mathematical models becomes questionable.

The fuel will be cold-pressed-and-sintered (U,Pu)N pellets with densities from 86 to 91% of theoretical. The fuel pins will have a 0.010-in. radial gap between the fuel pellet and the inside surface of the type 316 stainless steel cladding. The gap will be filled with NaK-19 (Na–19 wt % K) to enhance heat transfer. The fuel pins will operate at a peak linear heat rating of 30 kw/ft to burnups of 30,000 and 60,000 Mwd/metric ton. These capsules are being fabricated and will be inserted into the ETR at the beginning of cycle 107 on May 17, 1970.

We began conceptual design of an instrumented capsule for the irradiation of mixed nitride fuel. The outer capsule wall is 3/4-in.-OD stainless steel tubing with 1/2-in.-OD stainless steel tubing as the inner sleeve. The design of the fuel pin is the same as that of the one used in experiments ORNL 43-N1 and 43-N2. Figure 2.3 shows the

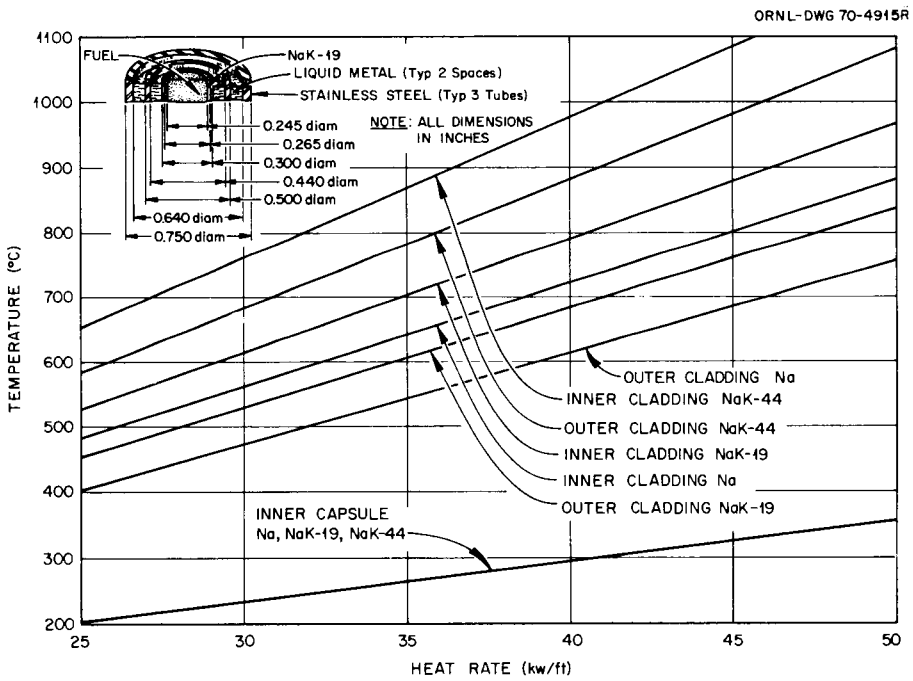

Fig. 2.3. Temperature Versus Heat Rate for $(U_{0.8},Pu_{0.2})N$.

temperatures of the cladding as a function of heat rates that result from the use of NaK-44 (Na–44 wt % K), NaK-19, or Na in the annulus. If we select 700°C as a maximum temperature for the inside surface of the cladding, then the maximum heat rates for this capsule design will be 27, 35, and 38 kw/ft for NaK-44, NaK-19, and Na, respectively.

If we position a thermocouple on each side of the 1/2-in.-OD sleeve, we can use the indicated temperature to calculate the temperature of the cladding. By calculating the system before the irradiation test, we can use the temperature differences of the thermocouples to calculate rates of heat generation.

Liquid-Metal Bonding of Fuel to Cladding (C. F. Sanders, J. D. Sease)

In the initial tests in a thermal flux, the (U,Pu)N pellets will be thermally bonded to the stainless steel cladding with NaK-19. Due to the uncertainty in the delivery date of the glove box for loading NaK, we developed an alternate loading procedure. Since the NaK-19 is a paste at room temperature, we

1. load a tube with NaK-19 at elevated temperature,
2. freeze the liquid metal inside the tube,
3. cut out a predetermined length of the tubing,
4. load this NaK-filled section of tube into the fuel pin in an inert atmosphere,
5. weld the fuel pins, and
6. centrifuge the fuel pins at elevated temperature to force the NaK into the gap between the fuel pellets and the cladding.

The initial check of this procedure showed that the NaK-19 separated into Na and NaK-35 if it was at room temperature for a few days. The liquid metal recombined and formed NaK-19 if it was heated to 400°C and maintained at this temperature for 2 or 3 hr. Loading by this technique in the welding box increased the O content of the NaK-19 by 20 to 100 ppm, depending on the time (5 to 20 min) required for loading. Since we would like to keep the O content to less than 100 ppm, we changed from loading NaK-19 in the welding glove box, which has an atmosphere of about 90 ppm O_2, to loading in a glove box that has an atmosphere of less than 10 ppm O_2.

Notes

1. E. S. Bomar, Fuels and Materials Development Program Quart. Progr. Rept. Dec. 31, 1969, ORNL-4520, pp. 58–66.

2. See Table 2.5, p. 52, this report.

3. E. S. Bomar, "Fabrication by Sintering," pp. 40–45, this report.

4. Analytical Chemistry Division.

5. J. P. De Luca, Fuels and Materials Development Program Quart. Progr. Rept. Sept. 30, 1969, ORNL-4480, p. 52.

3. EFFECT OF POWER CYCLING ON LMFBR FUEL-CLADDING BEHAVIOR

P. Patriarca O. Sisman[1]

This program investigates the effects of power cycling and transients on fuel behavior and the mechanical interaction of fuel and cladding for a liquid-metal-cooled fast breeder reactor (LMFBR), first for mixed oxide fuel and stainless steel cladding and later for other fuels and claddings. The objectives of this study are to compare the mechanical interactions of fuel (flat-ended pellets, dished pellets, and particulate fuel) and cladding during thermal-cycling conditions typical of those to be expected in an LMFBR. The mechanical interactions between $(U,Pu)O_2$ fuel and stainless steel cladding will affect both the safety and economic characteristics of LMFBR's. Axial separations in the fuel column tend to make the reactor power coefficient more positive. In addition, concentrations of stress in the cladding due to fuel "hourglassing," cracking, and ratchetting combine with power cycling and reduced cladding ductilities to decrease the lifetime of the fuel elements. These mechanical interactions are quite important in defining allowable schemes of fuel management and reactor operating conditions and thus have a significant effect on the reactor economy.

Power Cycling Irradiation Tests

C. M. Cox

The intent of our program is to measure in-reactor the axial extension of the fuel column and cladding during operation under carefully controlled conditions, which include programmed power cycles and an occasional overpower cycle. The irradiation capsules will be designed so that the fuel pin operates at LMFBR prototypic power and temperature conditions. The irradiation tests will last 1 to 2 years and will give burnup levels of 5 to 9%.

Power Cycling of Mixed Oxide Fuel with Stainless Steel Cladding to Moderate and High Burnup (R. B. Fitts, V. A. DeCarlo,[2] J. G. Morgan[1])

We surveyed the literature on mechanical interactions of fuel and cladding for metal-clad oxide fuel pins. Nineteen sets of irradiation tests, consisting of 238 uninstrumented and 104 instrumented fuel pins, were conducted over the last ten years. Our survey indicated a severe lack of tests under LMFBR conditions and a poor definition of the influences of the major variables that affect interactions of fuel and cladding.

Since there are almost no pertinent data for LMFBR systems, our first experiments will be aimed at near-term application for the Fast Flux Test Reactor (FTR). The first of these will operate with an FTR prototypic design for about 3% burnup at 10 kw/ft and an additional 4% burnup at 16 kw/ft. Superimposed on these heat rates will be a daily power transient and an occasional 20% overpower transient. The second experiment will be operated to 8% burnup at nominally 16 kw/ft but with a small diametral gap between fuel and cladding and a fuel smear density of 90%, which represents the upper density range of the specifications for the FTR fuel element. These experiments should indicate whether it is practical to manage the FTR fuel by moving the peripheral fuel into the center of the core to obtain a higher average burnup. We intend to aggravate mechanical interaction in the second capsule to determine whether this is, indeed, a problem.

The Poolside Facility[3] in the Oak Ridge Research Reactor (ORR) is well equipped for this type of program in that (1) the neutron flux is sufficiently high to provide the desired peak heat rates of 16 to 19 kw/ft, (2) a symmetrical axial flux profile can be obtained over at least a 10-in.-long fuel column, (3) the mechanism for horizontal translation of the capsule can be used to give power transients that closely simulate a reactor power transient, (4) instrumentation is available, and (5) we have had previous experience with five instrumented $(U,Pu)O_2$ fuel pin capsules in this facility.

Temperature distributions for a typical poolside capsule design are compared with the peak FTR fuel pin in Fig. 3.1. An earlier analysis[4] showed that prototypic LMFBR temperature distributions could be obtained

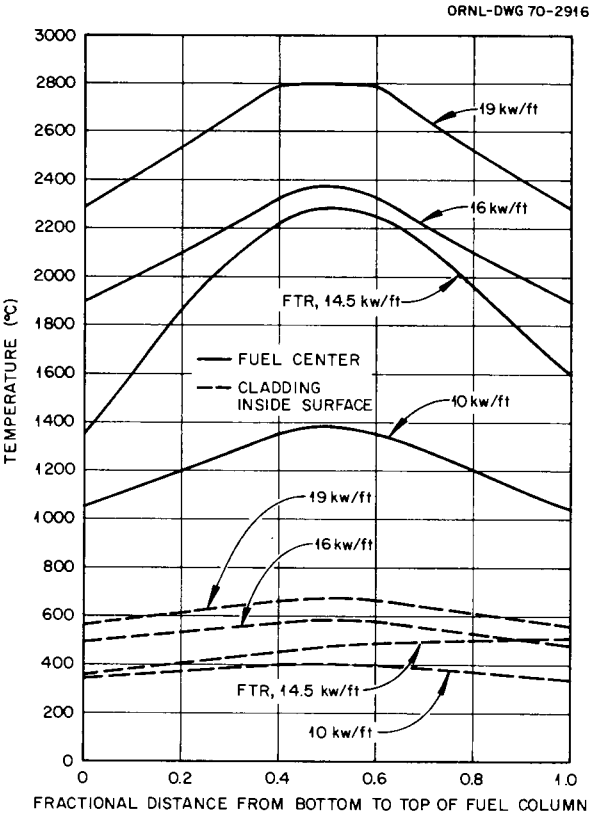

Fig. 3.1. Temperatures at Fuel Center and Inside Surface of Cladding for Power Cycling Capsule with 0.230-in.-OD Fuel Pin.

in a thermal-flux environment. A capsule that was used successfully to measure changes in the length of a fuel column in a test of stainless steel clad UO_2 fuel pins at lower power[5] is being used as the basis of the initial design. This earlier design is being modified to yield the desired fuel and cladding temperatures and to include an improved length transducer.

A sketch of the capsule with preliminary revisions is shown in Fig. 3.2. The fuel column is nominally 10 in. long, although neutron physics calculations have been initiated to determine the length that will provide an optimized power distribution along the axis of the pin. The push rod shown transmits the motion of the fuel to the position transducer. The transducer illustrated is an air-gage device that has been used successfully in-reactor. In an effort to obtain an alternate device with more rapid response and continuous readout to replace the air gage, we are testing a resistor for use as a position transducer.

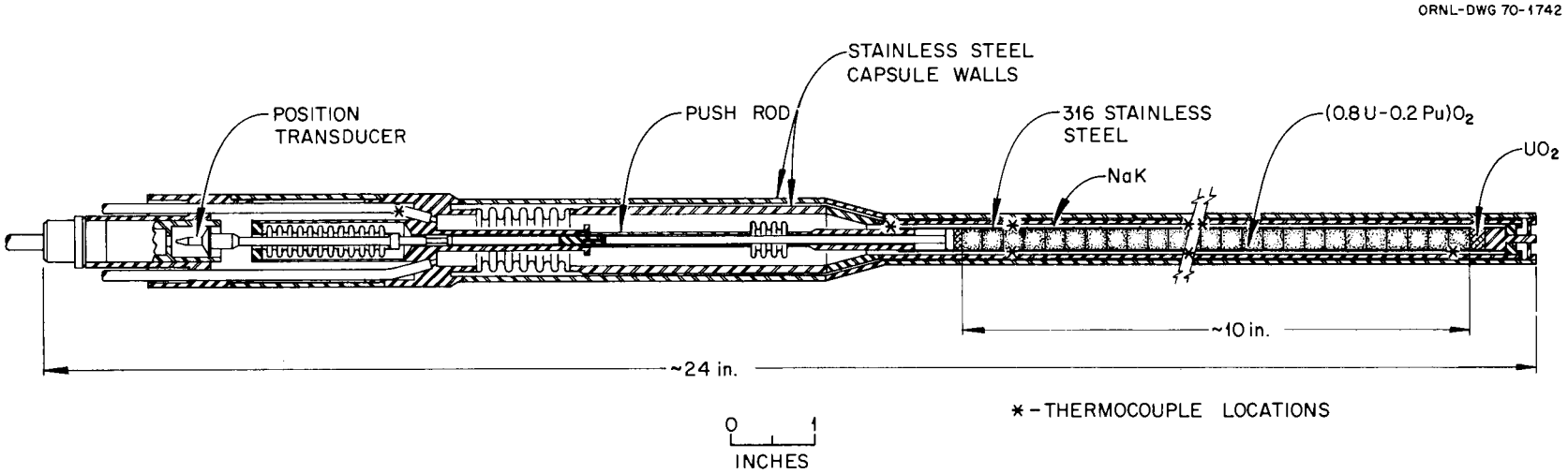

Fig. 3.2. Capsule for Tests of Mechanical Interactions of Fuel and Cladding.

The first capsule, designated MINT-1, is scheduled for insertion into the reactor during shutdown of the ORR on September 13, 1970.

Notes

1. Reactor Chemistry Division.

2. Reactor Division.

3. D. B. Trauger, Some Major Irradiation Test Facilities of the Oak Ridge National Laboratory, ORNL-3574 (April 1964).

4. A. R. Olsen, R. B. Fitts, and C. M. Cox, "Analysis of the Validity of Fast Reactor Fuel Tests in Existing Test Facilities," pp. 127–150 in National Symposium on Development in Irradiation Testing Technology, held at Sandusky, Ohio, September 9–11, 1969, CONF-690910.

5. S. C. Weaver, V. A. DeCarlo, R. B. Fitts, R. L. Senn, K. R. Thoms, and J. L. Scott, Results from Irradiation Testing of UO_2 Fuel Pins Designed for the Medium Power Reactor Experiment, ORNL-TM-2859, in press.

4. LMFBR FUEL ELEMENT DESIGN AND MODEL DEVELOPMENT

P. Patriarca A. L. Lotts C. M. Cox

The objective of this program is to develop analytical methods to predict and evaluate the performance of fuel pins and fuel elements for the liquid-metal-cooled fast breeder reactor (LMFBR). This work is closely coordinated with the related programs for development of fuel and cladding. It provides methods for designing and systematically evaluating irradiation tests, evaluating the influences of materials properties on the performance of fuel elements, and identifying specific areas in which experimental research needs to be intensified.

The program is divided into three areas: model integration, fuel performance, and cladding performance. The fuel and cladding performance tasks are oriented toward mathematical description of the various phenomena of the fuel and cladding under irradiation such as swelling, gas formation, and mechanical, thermal, and chemical behavior. These individual models are incorporated into a generalized computer program that simulates the performance of an operating fuel pin.

Fuel Performance

We worked toward normalizing our current analytical models for swelling and release of fission gas for $(U,Pu)O_2$ and characterizing the behavior of fission gas and microstructural changes in irradiated $(U,Pu)O_2$.

Normalization of Current Models for Swelling and Release of Fission Gas for $(U,Pu)O_2$ (C. M. Cox)

Many of the models currently used in the FMØDEL code are of a semi-empirical nature, and it is important to normalize and verify their predictions with experimental data. We have established a basis for the adjustable parameters used to describe fuel swelling and release of fission gas for $(U,Pu)O_2$ pellet fuels.

The basic cause of fuel swelling is the buildup of solid fission products and bubbles of fission gas. Anselin and Baily[1] calculated that the contribution of solid fission products to the swelling of

$(U_{0.8},Pu_{0.2})O_2$ amounts to maximum swelling rates of 0.32 to 1.3% fractional volume increase ($\Delta V/V$, or change in volume divided by original volume) per percent fissions per initial actinide metal atom (FIMA). Experiments[2] with high density $(U_{0.75},Pu_{0.25})O_2$ with the fuel subjected to very strong radial restraint indicated minimum swelling rates of 0.3 to 0.4% $\Delta V/V$ per percent FIMA. The range depends on one's interpretation of an apparent incubation period during which the swelling is presumably being accommodated in some of the fabricated porosity. This lowest swelling rate corresponded to an estimated temperature of 1400°C at the fuel center; and, if one assumes that most of the fission gases are in solution at this temperature and under the large hydrostatic pressure arising from the radial restraint, then the swelling should be representative of solid fission products. Although specific cases would depend on temperature and the thermodynamic properties of the fission products, we assume that the swelling from solid fission products can be estimated at 0.32% $\Delta V/V$ per percent FIMA.

For swelling from gaseous fission products we use the Greenwood-Speight model[3] with modifications similar to those of Goldberg et al.[4] Since this model does not account for the effects of large temperature gradients and such defects as grain boundaries, its use for oxide fuels is primarily as a pseudoempirical fit to data.

The model for swelling caused by gas is strongly influenced by release of fission gas. Irradiation tests of $(U,Pu)O_2$ fuel in a fast reactor typically show gas releases of 50 to 80%, as described previously.[5] Although release of fission gas seems to depend on burnup, fuel fabrication form, and power cycling, measured gas releases vary fairly uniformly with the calculated average temperature of the fuel.[5] This indicates that, to a first approximation, gas releases may be empirically represented as a function of temperature distribution. We have assumed a three-zone model, similar to our empirical model for restructuring, in which 98% of the gas is released from fuel above 1800°C, 50% from fuel between 1400 and 1800°C, and 30% at lower temperatures. These values arise from our analysis of data on the microstructure and gas release of irradiated fuel. A comparison with data[5] for pellets tested to moderate burnup is shown in Table 4.1.

Table 4.1. Comparison of Predicted and Measured Release of Fission Gas from Fast-Flux Tests with Pelletized $(U,Pu)O_2$

Fuel Smear Density (% of theoretical)	Peak Heat Rate (kw/ft)	Fuel Average Burnup (% FIMA)[a]	Fission Gas Released, %	
			Measured	Calculated
96.7	16.7	5.3	47	52
94.5	9.9	3.2	32	30
96.7	17.5	5.5	55	58
87.2	16.1	5.1	58	62
94.0	16.1	5.1	49	53
94.4	16.7	5.3	50	55
92.6	16.6	5.3	50	55
94.6	16.4	5.3	48	53
72.4	9.8	6.8	44	30

[a]FIMA is fissions per initial actinide metal atom.

The total volumetric swelling predicted by these combined models at 10% FIMA is shown as a function of temperature in Fig. 4.1. In this application of the Greenwood-Speight model, we used the UO_2 physical constants suggested by Goldberg et al.[4] Several experimental points are included for comparison. Data from Bettis Atomic Power Laboratory of the Westinghouse Electric Corporation[6] for UO_2 plate fuels operating at temperatures of 500 to 1000°C indicated bulk swelling rates of the order of 1.7% $\Delta V/V$ per percent FIMA. These data have wide scatter and could be half or twice this value.

The higher temperature points shown in Fig. 4.1 were taken from tests with high burnup and high radial restraint.[2] The temperatures shown are nominal temperatures at the fuel center. Average fuel temperatures were several hundred degrees lower. These data were adjusted as shown by the arrows in the figure to include an estimate of the swelling that was accommodated in fabricated porosity. More precise data are needed to establish the swelling characteristics; however, the data plotted in Fig. 4.1, with the exception of the datum point at 1400°C

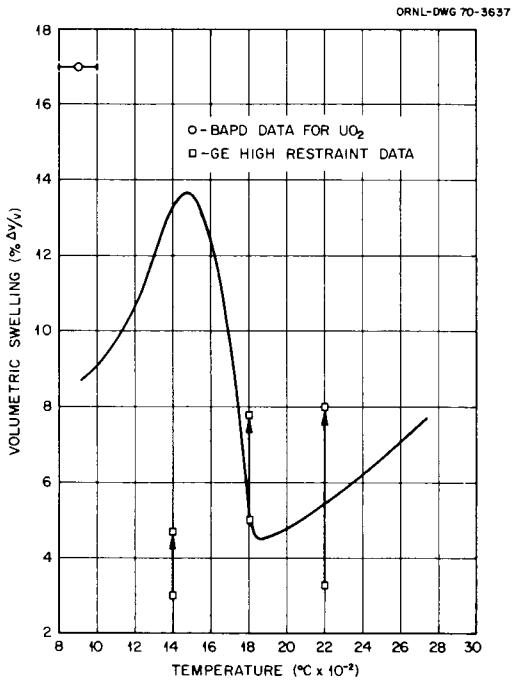

Fig. 4.1. Calculated Swelling of 100% Dense $(U,Pu)O_2$ at 10% Fissions per Initial Actinide Metal Atom. [Data from R. C. Daniel et al., Effects of High Burnup on Zircaloy-Clad, Bulk UO_2, Plate Fuel Element Samples, WAPD-263 (September 1962); E. L. Zebroski et al., "Review of Status of Technology of Fast Reactor Fuels," pp. 2-63-2-80 in Fast Reactors National Topical Meeting, San Francisco, April 10-12, 1967, American Nuclear Society, San Francisco, 1967.]

indicate that the results predicted by these empirical models will at least be reasonable.

The incubation period during which swelling is accommodated in some of the fabricated porosity depends on the fuel porosity after restructuring, temperature, stress, and time. Karsten et al.[7] summarized data that indicate that about 80% of the porosity of fuel above 1700°C, 50% at 1300 to 1700°C, and up to 30% below 1300°C should be available to accommodate swelling. We modified the temperature ranges to correspond to our empirical model for gas release and used this model to correct the data shown in Fig. 4.1. Fuel swelling is assumed to be accommodated in the porosity left after initial restructuring until these minimum values are reached.

While these models can be expected to give reasonable results, the data from which they have been normalized are neither precise nor tied

to well-known operating conditions. We have thus begun microscopic examinations of $(U,Pu)O_2$ from well-characterized irradiation experiments to improve our understanding of the behavior of fission gas and microstructural changes.

Microscopic Examinations of $(U,Pu)O_2$ Fuel (W. J. Lackey)

Since improved models describing fuel behavior are needed for incorporation into the FMØDEL code, irradiated $(U,Pu)O_2$ is being studied by means of light and electron microscopy to improve our knowledge of fuel swelling, release of fission gas, and restructuring. We examined an irradiated mixed oxide fuel pin, fabricated from coarse and fine microspheres produced by the sol-gel process, by means of light microscopy, conventional replica electron microscopy, and scanning electron microscopy.

For the conventional electron microscopy we used the two-stage C replica and selected area techniques developed by Padden;[8] for the scanning electron microscopy we used a Au-coated polyvinyl chloride replica. Particular attention was given to the size distribution and location of bubbles of fission gas, since these factors are expected to influence fuel swelling and release of fission gas considerably.

A metallographically polished transverse section (43-112-3C) of the fuel pin was examined after irradiation in a thermal reactor at a linear heat rate of 13.6 kw/ft to a burnup of 0.7% FIMA. A portion of the transverse section is shown in Fig. 4.2. Bubbles of fission gas up to 1.5 μm in diameter were observed on surfaces at boundaries between columnar grains, as shown in Fig. 4.3. The bubbles were elongated in the direction of the thermal gradient, and, in some cases, they were quite aspherical. The fuel temperature at a radius corresponding to the location of the bubbles was about 1850°C. The standard deviation of the calculated temperatures is estimated to be 100°C.

We occasionally observed in the coarse spheres rows of voids, which we believe to be bubbles of fission gas. The lowest temperature at which these occurred was 1450°C, which corresponded to 0.19 cm from the thermal center. The voids (Fig. 4.4) were 0.1 to 0.2 μm in diameter and occurred in rows, which we believe represent grain boundaries. Even in those areas

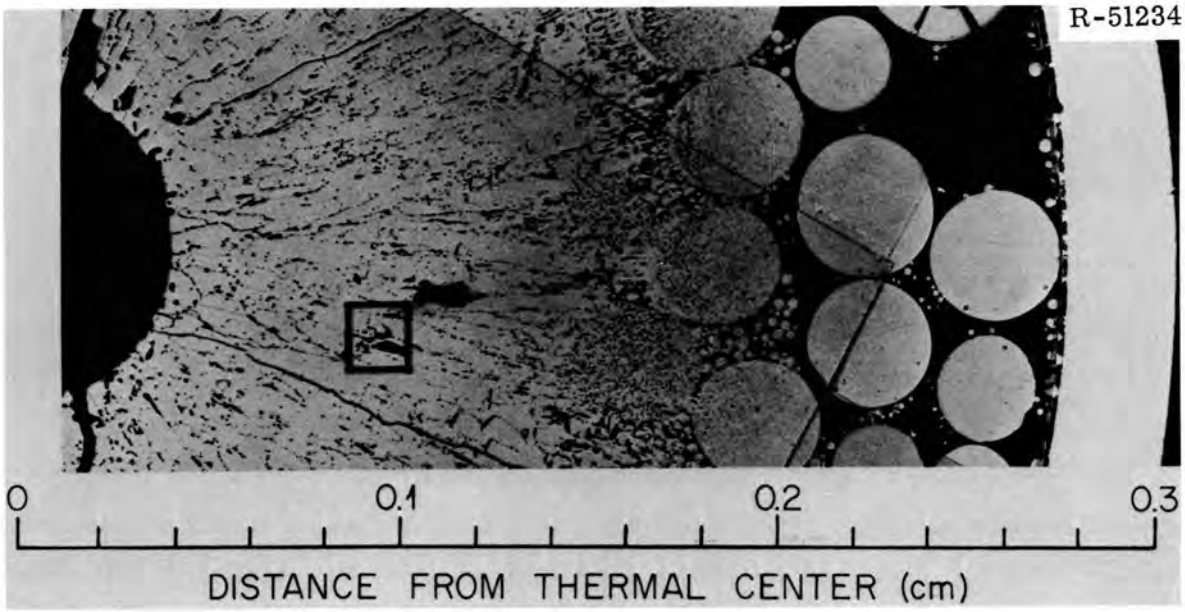

Fig. 4.2. Transverse Section of $(U_{0.85},Pu_{0.15})O_2$ Fuel Pin 43-112-3 After 0.7% Burnup at a Linear Heat Rate of 13.6 kw/ft. The dark regions enclosed by the square are cavities caused by intergranular fracture and subsequent pullout. These are shown at higher magnifications in Fig. 4.3. 50×.

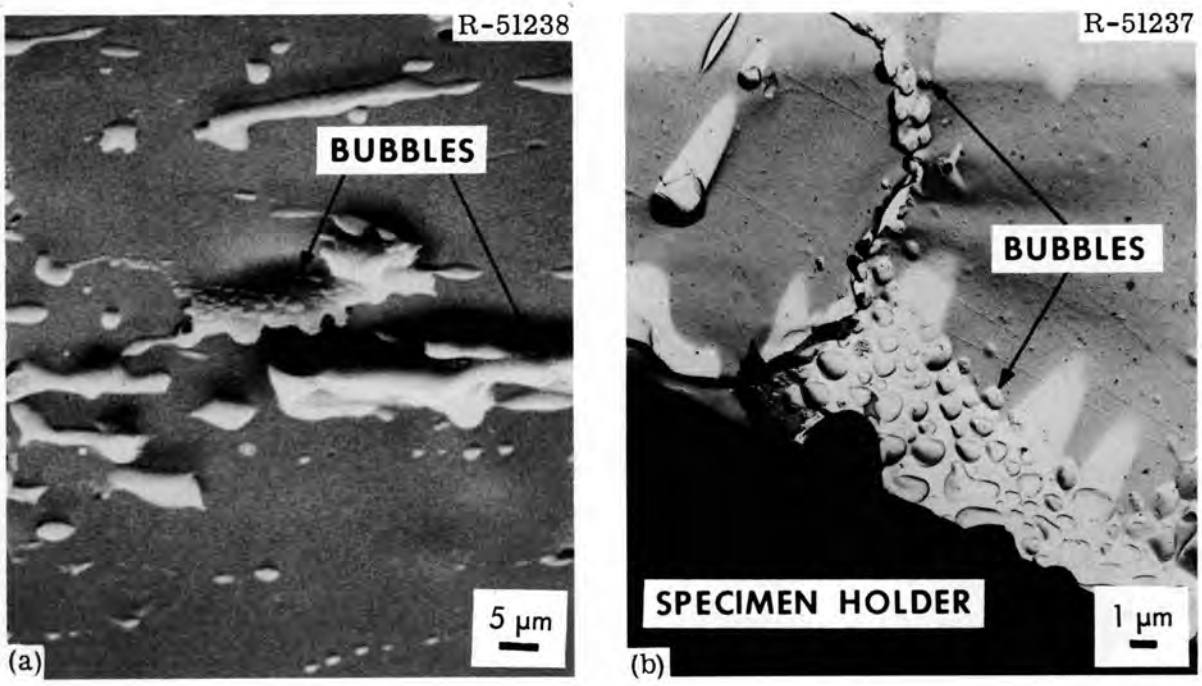

Fig. 4.3. Fission Gas Bubbles Located on Grain Boundaries. The grain-boundaries are at the bottom of the cavities shown in Fig. 4.2. (a) Scanning electron microscopy. 1000×. (b) Conventional electron microscopy. 3200×.

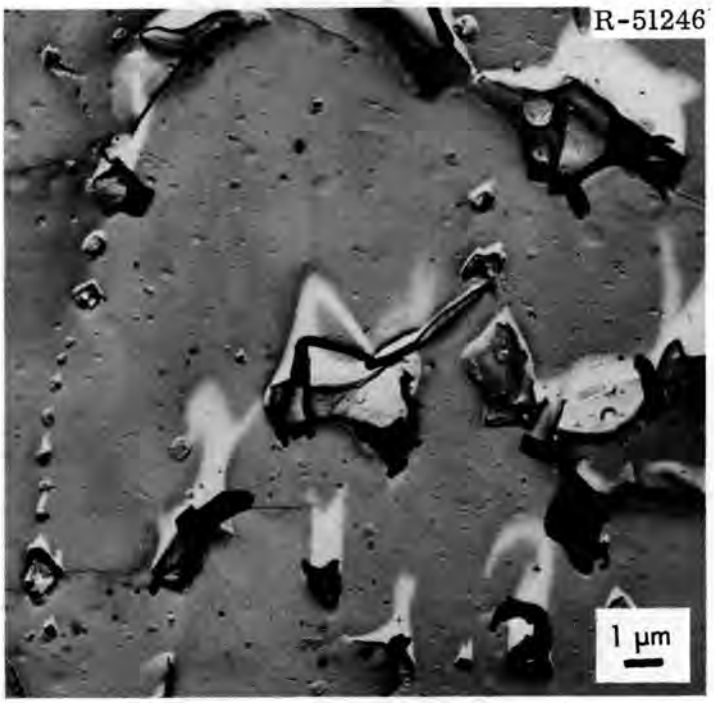

Fig. 4.4. Row of Voids, Presumed to be Bubbles of Fission Gas Located at a Grain Boundary. The large white areas are shadows cast by relatively large voids. Conventional electron microscopy. 4800×.

where these voids did occur, they were rare. The rows of voids did not appear to be aligned preferentially in any direction.

We observed numerous larger voids at temperatures above about 1200°C (which corresponds to 0.22 cm from the thermal center) but less than that capable of producing columnar grains. These pores are just visible in Fig. 4.2 but are clearly visible in Fig. 4.4. Archive samples of unirradiated microspheres will be examined by electron microscopy to determine if these pores are agglomerated fabrication pores or an irradiation effect.

Near the cladding there was essentially no indication of fuel transport, and the spheres maintained their original shape. Figure 4.5 shows the microstructure of an irradiated coarse microsphere typical of those irradiated below about 1200°C in that the structure is essentially featureless except for an occasional relatively large pore with faceted surfaces such as that shown here. The facets are grain-boundary surfaces of surrounding grains.

Fig. 4.5. Essentially Featureless Surface of a Coarse Microsphere Irradiated at Less than 1200°C. The small black specks are artifacts. A faceted pore is shown in the lower left corner of the photomicrograph. Conventional electron microscopy. 4800×.

The inner surface of the cladding was observed by electron microscopy at several locations. There was no indication of cladding reaction, which is not surprising because of the low burnup and low cladding temperature (about 320°C). We do not yet know whether a gray material observed by both light and electron microscopy near the boundary between the regions of columnar and equiaxed grains is truly a second phase or whether it is mounting material. It appears that electron microprobe analysis will be necessary to identify this material.

Cladding Performance

Our development of a model for cladding performance was concentrated on the effects of intrinsic cladding swelling, the development of a failure analysis, and evaluation of the mechanical behavior of type 316 stainless steel tubing, the current reference cladding material.

Effect of Cladding Swelling on Kinetics of Gap Closure (F. J. Homan)

The size of the gap between fuel and cladding is important in the treatment of fuel temperature and mechanical interaction of fuel and cladding. In the analysis of the performance of a typical mixed oxide LMFBR fuel pin presented previously,[9] we used a function for swelling of the cladding suggested by Appleby.[10] Appleby suggested that the swelling effect reached saturation at about 12% $\Delta V/V$. The fuel pin selected for study (as shown in Fig. 4.1 of the previous report[9]) received a high fast-neutron flux approaching 10^{16} neutrons cm^{-2} sec^{-1}. For this high flux, Appleby's equation predicts that saturation will be reached about halfway through the irradiation lifetime of the fuel pin (as shown in Fig. 4.3 of the previous report[9]). When saturation is reached, there is an abrupt change in the kinetics of closure of the gap between fuel and cladding.

Bloom[11] suggested that the combination of tensile stresses in the cladding and buildup of the He concentration due to (n,α) reactions may actually lead to accelerated swelling of the cladding. Not enough is known about this effect to allow speculation, except in qualitative terms; but it suggests that the assumption of swelling saturation is not appropriate.

Without swelling saturation, the gap between fuel and cladding in a typical LMFBR fuel pin appears to grow without bound (see Fig. 4.3 of the previous report[9]). A more recent correlation, suggested by Biancheria,[12] predicts this sort of behavior at high cladding temperatures and neutron fluxes. Biancheria's swelling equation for type 316 stainless steel with 20% cold work relates the volume change to neutron fluence raised to a power of 1.69; however, use of his equation for LMFBR fuel pins requires extrapolation of the swelling equation far beyond its range of validity. This is demonstrated in Fig. 4.6. The fluence necessary to achieve 10% average burnup for a typical LMFBR pin is about 2.2×10^{23} neutrons cm^{-2} sec^{-1}; but swelling data are not available past about 7×10^{22} neutrons cm^{-2} sec^{-1}. From the solid curves in Fig. 4.6 it can be seen that cladding with temperatures above 500°C would have extremely large diametral expansions at fluences commensurate with 10%

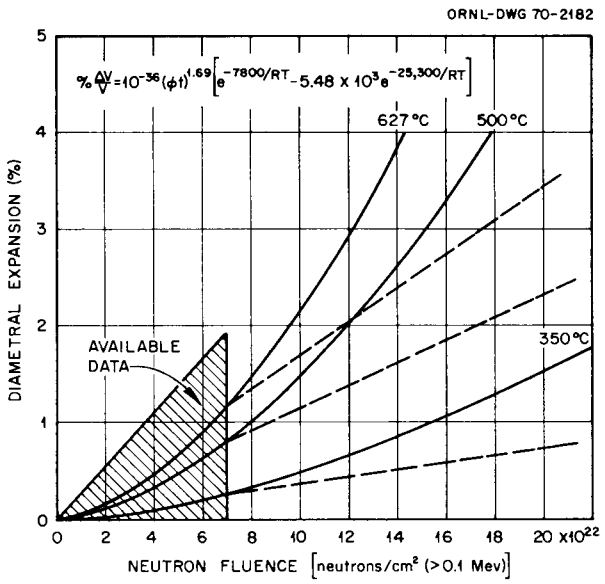

Fig. 4.6. Swelling of Cladding as a Function of Fluence.

average burnup. The extrapolated predictions of cladding swelling are intolerable from a design standpoint and probably are not realistic. Bloom[13] thinks that part of the problem may lie in the data selected for the curve. He independently analyzed the available data for swelling and concluded that a fluence exponent of unity might be more appropriate.[13] We have modified Biancheria's[12] equation for swelling to use his correlation within the range where there are data and have used a fluence exponent of one for extrapolation. This change is represented by the dashed curves in Fig. 4.6. The modified curves for swelling represent a more acceptable situation from the design standpoint; however, cladding exposed to high temperatures and neutron fluxes still swells faster than the fuel. It appears that an accurate analytical investigation of the kinetics of gap closure in this case must wait for additional data on swelling at higher fluences.

Effect of Cladding Swelling on Stress-Strain Distributions (F. J. Homan)

We previously reported[14] our technique for calculating cladding stresses and strains. The variables involved in the calculation are the physical and mechanical properties of the cladding, its creep and yield characteristics, temperature gradient, boundary conditions

(internal and external pressures), and time. An LMFBR fuel pin operating at about 16 kw/ft would have temperature gradients of about 50°C across the 0.015-in.-thick cladding wall. Temperature gradients of this magnitude (over 3000°C/in.) would be expected to cause initial compressive stresses at the inner cladding surface and tensile stresses at the outer surface that would relax with time. The rate of relaxation would increase with average cladding temperature. We studied the relaxation of initial stresses for our typical LMFBR fuel pin cladding.[9] This pin was divided into nine axial regions for purposes of calculation. Pertinent data for each of these nine regions are given in Table 4.2. Figure 4.7 indicates the relaxation of the inner compressive stresses and outer tensile stresses with time for the top, bottom, and center axial regions of the typical LMFBR fuel pin. As noted in Table 4.2, the average cladding temperature increases from 475°C for region 1 to 644°C in region 9. As expected, stress relaxation for the cladding in axial region 9 is much more rapid than that for regions 1 or 5. For this calculation, we used literature data[15–18] for the physical and mechanical properties. Pressures on the outside of the cladding are given in Table 4.2; the pressures on the inside of the cladding were assumed to vary linearly from 100 to 1500 psi in 10,000 hr.

The results presented in Fig. 4.7 are based on the assumption that the geometry of the cladding is changed only by the initial deformation and by creep. However, if the effect of cladding swelling due to formation of voids is superimposed on the changes in geometry due to creep, a different set of conditions results. To model this situation we assumed that cladding swelling can be included in the calculation by adjusting the linear coefficient of thermal expansion to include the volume changes due to formation of voids in the cladding:

$$\alpha = \alpha_T + \frac{\% \, \Delta V/V}{300 \, T} \, , \tag{1}$$

where

α = the effective coefficient of linear thermal expansion,

α_T = the coefficient of linear thermal expansion due to thermal considerations alone,

Table 4.2. Reference Data for a Typical LMFBR Fuel Pin

Axial Region Number	Coolant Temperature (°C)	Average Cladding Temperature (°C)	External Pressure on Cladding (psi)	Neutron Flux (neutrons cm^{-2} sec^{-1})	Temperature Rise Across Cladding (°C)	Temperature of Fuel Center (°C)	Rate of Heat Generation (kw/ft)
				$\times 10^{15}$			
1	440	475	95	7.26	44	2238	13.36
2	462	498	88	7.79	46	2399	14.32
3	484	523	81	8.43	48	2587	15.45
4	506	547	73	8.75	50	2708	16.09
5	528	568	66	8.75	49	2735	16.09
6	549	588	59	8.51	48	2689	15.61
7	570	607	51	8.05	44	2597	14.80
8	592	625	44	7.26	40	2417	13.36
9	614	644	37	6.74	37	2309	12.40

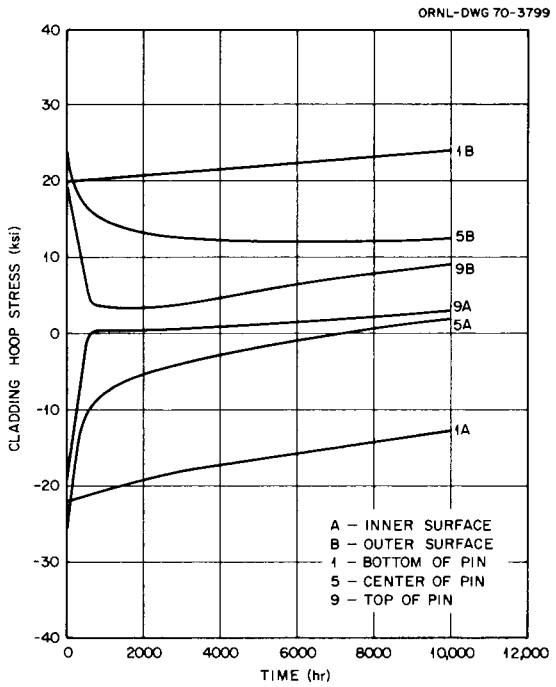

Fig. 4.7. Changes in Cladding Stresses with Time. Swelling of the cladding was not considered.

$\% \Delta V/V$ = the amount of cladding swelling due to void formation, as calculated from the equation given in Fig. 4.6 (for type 316 stainless steel cold worked 20%), and

T = temperature (°C).

This approach has also been suggested by other investigators.[19]

When swelling of the cladding is considered in the calculation for stress relaxation, we find that relaxation is retarded at the cool end of the pin because the inner surface of the cladding expands faster than the outer surface due to the formation of voids. At the hot end of the fuel pin, the outer surface of the cladding expands faster than the inner surface (a recent equation[12] for swelling of 20% cold-worked type 316 stainless steel cladding predicts peak swelling at about 627°C; therefore, for cladding hotter than this temperature, the cooler surface will expand faster than the hotter surface) and relaxation is enhanced. This effect is summarized by the results plotted in Fig. 4.8 for our typical fuel pin. The same physical and mechanical properties and the same boundary conditions used for the calculations presented in Fig. 4.7 were

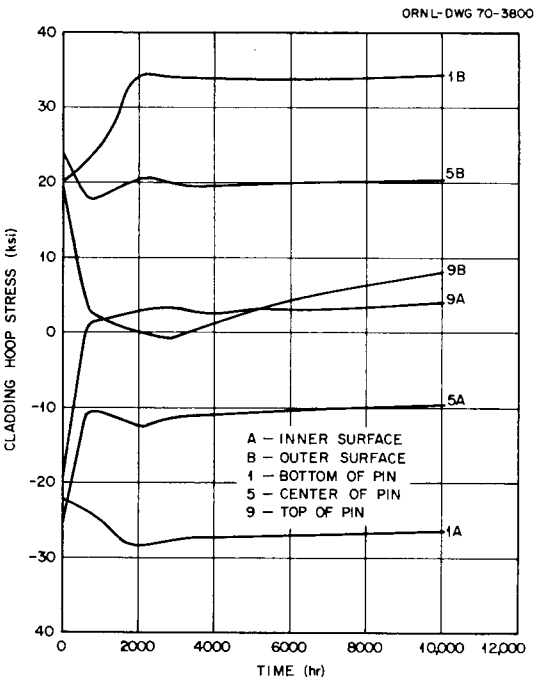

Fig. 4.8. Changes in Cladding Stresses with Time Using Modified Equation for Swelling of Cladding.

used for the plot in Fig. 4.8. The modified equation for cladding swelling shown in Fig. 4.6 was used for the results in Fig. 4.8.

The effect of cladding swelling on stress relaxation is demonstrated by comparison of Figs. 4.7 and 4.8. Figure 4.9 indicates the effect of swelling of the cladding due to formation of voids on the calculated diametral expansion of the cladding for axial regions 1, 5, and 9 of the typical LMFBR fuel pin. Three cases are presented in Fig. 4.8 based on the assumptions of (1) no cladding swelling, (2) swelling according to Biancheria's equation[12] (solid curves in Fig. 4.6), and (3) swelling according to our modification of Biancheria's equation (dashed curves in Fig. 4.6). The dangers associated with gross extrapolation beyond the range of experimental data are demonstrated graphically by the results of the assumption of swelling according to Biancheria's equation. This suggests strongly the need for data for cladding swelling at higher fluences. Even our modifications of the equation for swelling result in calculated diametral expansions that would probably be unacceptable to designers.

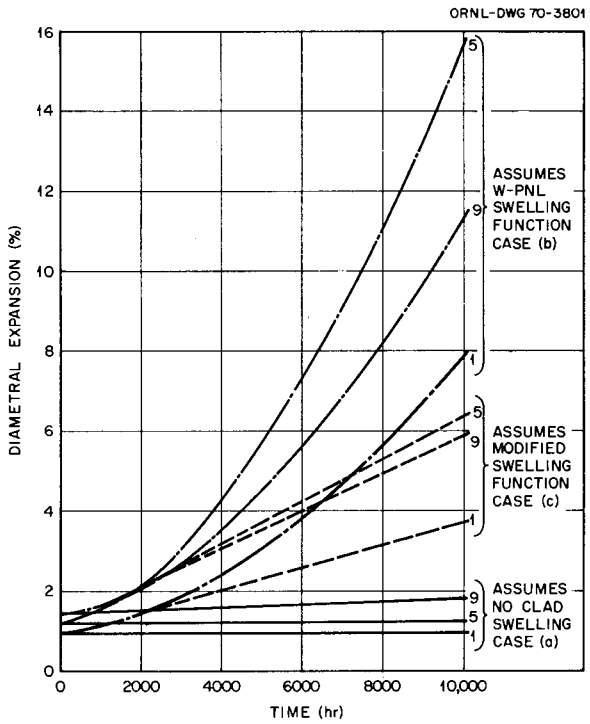

Fig. 4.9. Effect of Cladding Swelling on Diametral Expansion.

Thermophysical and Mechanical Properties of Type 316 Stainless Steel (W. H. Bridges)

A review of the physical and mechanical properties of type 316 stainless steel is in preparation. The section on thermophysical properties[20] covers density, melting range, specific heat, thermal expansion, thermal conductivity, thermal diffusivity, emissivity, and electrical resistivity. The influence of environment, particularly neutron irradiation, is given when such data are available. The section on tensile properties is undergoing review before issuance as an internal memorandum.

Tensile Yield Data for Type 316 Stainless Steel Tubing (R. W. Swindeman)

The data we obtained on type 316 stainless steel tubing fabricated at ORNL are summarized here for use in modeling studies for LMFBR fuel pins. Four-inch segments were tested longitudinally on an Instron machine. Both cold-worked (20%) and annealed (1065°C for 15 min) conditions were studied at room temperature and 650°C. Of primary concern were the shape

of the yield curve and the effect of strain rate at 650°C. Some data regarding the ultimate strength and elongation were also obtained.

Yield curves at room temperature are shown in Fig. 4.10. Annealed tubes exhibit a slightly higher modulus of elasticity than expected (about 30.5×10^6 psi) and a well defined yield stress at 43,000 psi. The cold-worked tubes exhibited little, if any, truly elastic behavior. Between 0 and 10,000 psi the value for Young's modulus averages about 28.4×10^6 psi. Based on this value, the yield stress appears to be 114,000 ± 7,000 psi. One yield curve shown in Fig. 4.10 corresponds to a test after prestraining at 650°C. It is apparent that this treatment produced some recovery, inasmuch as the elastic behavior has been restored and the yield stress significantly reduced.

Yield curves for annealed material tested at 650°C are shown in Fig. 4.11. The value for the modulus of elasticity, 21.3×10^6 psi, is in fair agreement with the range of recognized values and shows little if any effect of strain rate. Discontinuous yielding occurs at the

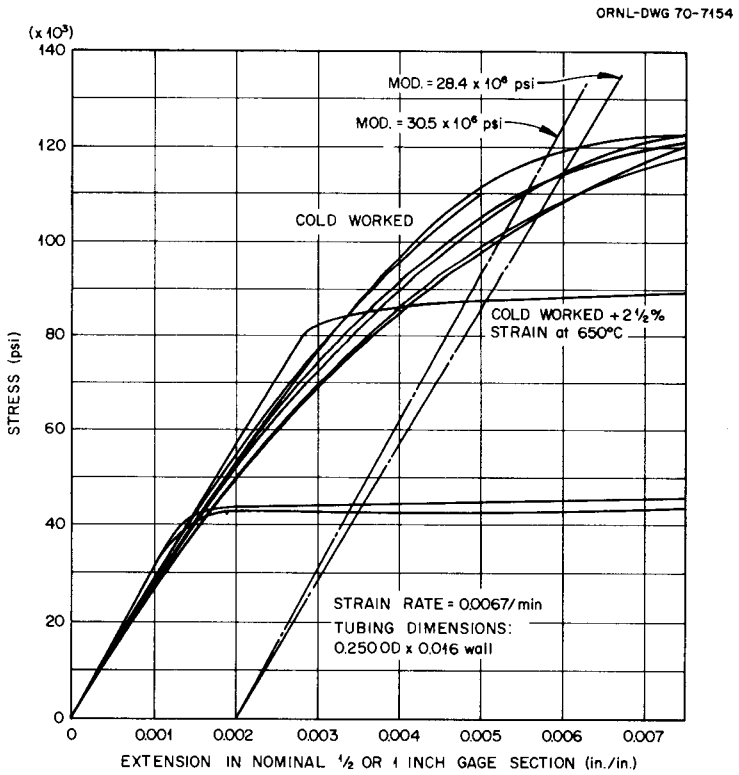

Fig. 4.10. Tensile Strength of Type 316 Stainless Steel Tubing at Room Temperature.

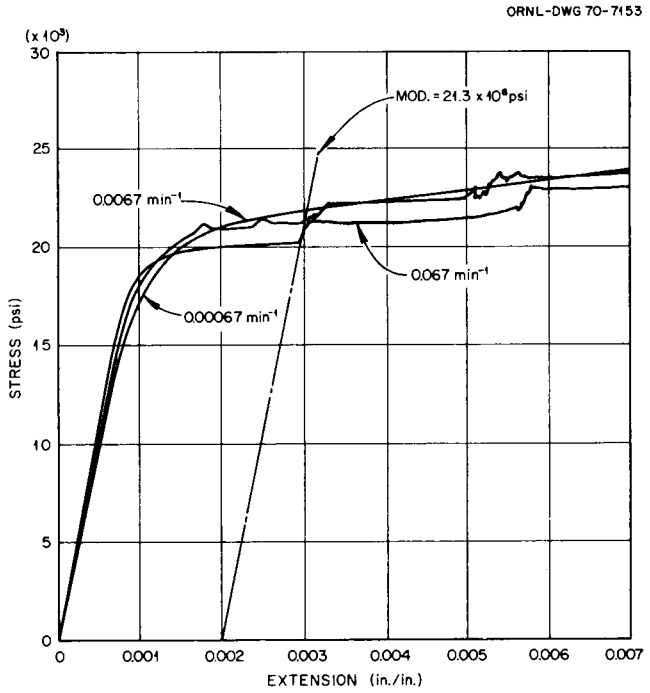

Fig. 4.11. Yield Curves for 0.250-in.-OD × 0.016-in.-wall-thickness Annealed Type 316 Stainless Steel Tubing at 650°C.

higher strain rates, and it appears that the 0.2% offset yield strength is slightly higher at the lower strain rate, 0.00067 min^{-1}. The yield stress is about 21,000 psi.

The yield curves for cold-worked material tested at 650°C are shown in Fig. 4.12. There appears to be a significant effect of the strain rate on Young's modulus. At 0.067 and 0.0067 min^{-1} the value of the modulus of elasticity, 21.6 × 10^6 psi, is close to the range of accepted values. At 0.00067 min^{-1}, and even more so at 0.000067 min^{-1}, nonelastic behavior is apparent. The yield stress is also reduced by a significant amount. Although not shown in the figure, the elongation at the maximum load decreases with decreasing strain rate from about 5% at 0.067 min^{-1} to less than 1% at 0.000067 min^{-1}.

Other data are summarized in Table 4.3.

Creep of Cold-Worked Modified Type 316 Stainless Steel (R. W. Swindeman)

We have reviewed data on the creep behavior of the British cold-worked modified type 316 stainless steel. There is evidence that this

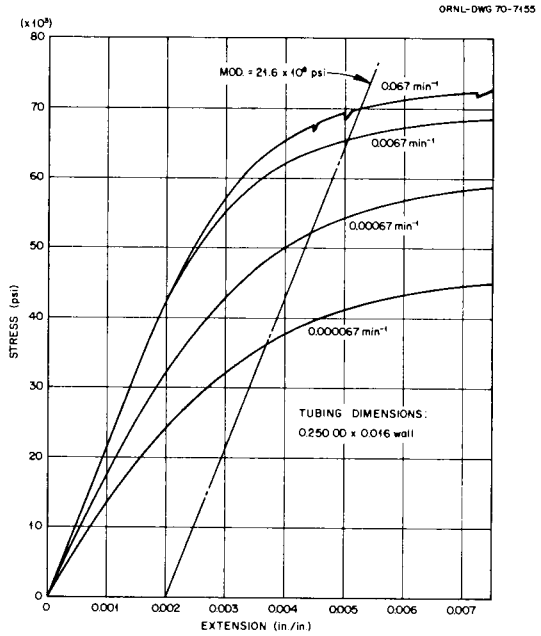

Fig. 4.12. Tensile Strength of 20% Cold-Worked Type 316 Stainless Steel Tubing at 650°C.

Table 4.3. Tensile Data for Type 316 Stainless Steel Tubing[a]

Test Temperature (°C)	Extension Rate[b] (in./min)	Young's Modulus of Elasticity (psi)	Strength, psi		Elongation (%)	Reduction in Diameter (%)
			Yield	Ultimate		
		× 10^6	× 10^3	× 10^3		
		Annealed at 1065°C				
Room	0.2	30.5	44	98	c	20
Room	0.02	30.5	43	98	c	21
650	0.2	21.6	21	60	40	20
650	0.02	21.3	21.5	d	d	d
650	0.002	20.4	22	d	d	d
		20% Cold Worked				
Room	0.005	28.4	114	124	c	21
Room	0.2	21.6	70	77	15	12
650	0.02	21.6	65	71	25	18
650	0.002		52	60	42	21
650	0.0002		37	47		

[a]All tubing was produced at Oak Ridge National Laboratory and was 0.250 in. in outside diameter and 0.016 in. in wall thickness.

[b]Actual strain rate (inches per inch per minute) is about one-third of extension rate.

[c]Failed outside gage mark.

[d]Failed at extensometer clamp.

material undergoes "creep softening" at low stresses, which makes it difficult to describe both primary and secondary creep analytically.

To what extent the creep softening is a real and reproducible effect is questionable. For the purposes of developing models for the behavior of cladding for fuel pins, it is probably best to assume some extremes and determine how performance is affected.

One possible equation for creep rate ($\dot{\epsilon}$) for the stress range 0 to 20,000 psi, which assumes no strain softening, is

$$\dot{\epsilon}_s = A\sigma^n ,$$

where

$A = 2.5 \exp(-89{,}000/RT)$, and

$n = 4$.

Another equation, which assumes softening at all stress levels and strength decreasing to that of modified type 316L stainless steel, is

$$\dot{\epsilon}_s = A(\sinh \alpha\sigma)^n ,$$

where

$A = 1.3 \times 10^{17} \exp(-83{,}000/RT)$,

$\alpha = 1/15{,}800$, and

$n = 3.9$.

The Search for the Mitra-McLean Effect in Type 316 Stainless Steel
(R. W. Swindeman)

We have prepared a number of creep curves for annealed stainless steel that show the performance after reductions in stress to establish whether significant recovery occurs as described by Mitra and McLean[14] for Ni and Al. This effect has also been observed[15] for W.

Figure 4.13 shows schematically what we would expect if recovery occurred after a stress reduction. A period, Δt, should occur during which there should be no creep. Since, within the limits of sensitivity of our extensometer, no such effect was observed, there was either very rapid recovery or very sluggish recovery. We are inclined to believe that recovery was sluggish. In either event, primary creep is not pronounced for this specific heat of material, and recovery is of little

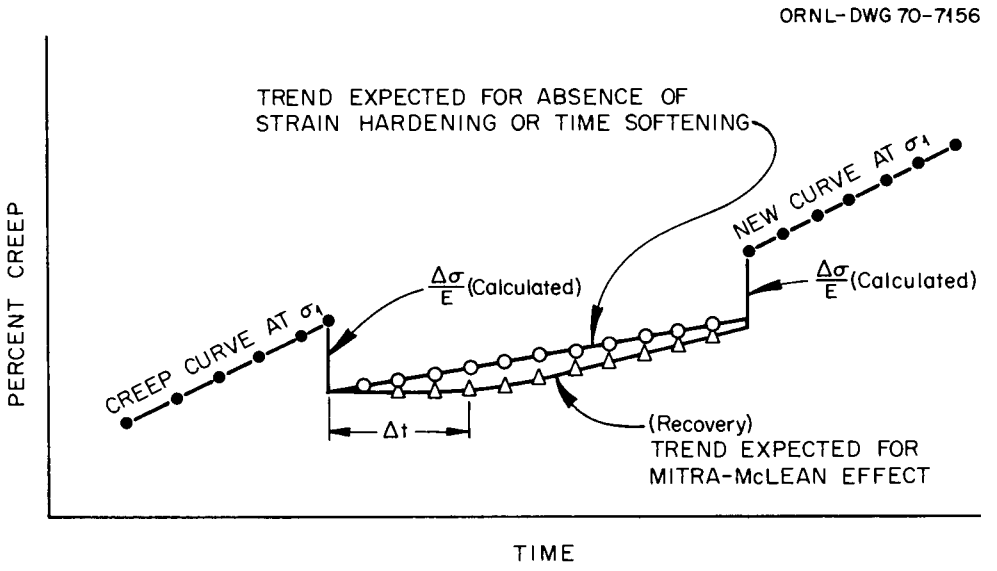

Fig. 4.13. Illustration of the Mitra-McLean Effect.

practical importance. This is not necessarily true for cold-worked type 316 stainless steel. Even other heats of type 316 stainless steel, in the annealed condition, could behave differently. We consider it prudent to continue such studies on other materials, preferably LMFBR-grade tubing, since the existence of such a phenomenon could have a pronounced effect on the performance of fuel pins during power cycling.

Notes

1. F. Anselin and W. E. Baily, Trans. Am. Nucl. Soc. 10(1), 103–104 (1967).

2. E. L. Zebroski et al., "Review of Status of Technology of Fast Reactor Fuels," pp. 2-63–2-80 in Fast Reactors National Topical Meeting, San Francisco, April 10–12, 1967, ANS-101, American Nuclear Society, San Francisco, 1967.

3. G. W. Greenwood and M. V. Speight, J. Nucl. Mater. 10(2), 140–144 (1963).

4. I. Goldberg, L. L. Lynn, and C. D. Sphar, FIGRØ – FORTRAN IV Digital Computer Program for the Analysis of Fuel Swelling and Calculation of Temperatures in Bulk Oxide Cylindrical Fuel Elements, WAPD-TM-618 (December 1966).

5. C. M. Cox, R. B. Fitts, and F. J. Homan, Fuels and Materials Development Program Quart. Progr. Rept. March 31, 1969, ORNL-4420, pp. 33–39.

6. R. C. Daniel et al., Effects on High Burnup on Zircaloy-Clad, Bulk UO_2, Plate Fuel Element Samples, WAPD-263 (September 1962).

7. G. Karsten et al., Fabrication of Fast Reactor Fuel Pins for Test Irradiations, KFK-577 (April 1967).

8. Thomas R. Padden, Polyvinyl Chloride Replica Technique for High Burnup Reactor Fuels, WAPD-T-1595 (August 1963).

9. F. J. Homan, W. E. Stillman, and B. R. Dewey, Fuels and Materials Development Program Quart. Progr. Rept. Dec. 30, 1969, ORNL-4520, pp. 85–91.

10. W. K. Appleby et al., Oxide Fuel Element Development Quart. Progr. Rept. June 30, 1969, WARD-3791-39, p. 4.

11. E. E. Bloom, Oak Ridge National Laboratory, personal communication, February 1970.

12. A. Biancheria et al., Oxide Fuel Element Development Quart. Progr. Rept. Sept. 30, 1969, WARD-4135-1, pp. 6–9.

13. E. E. Bloom and J. O. Stiegler, Fuels and Materials Development Program Quart. Progr. Rept. Sept. 30, 1969, ORNL-4480, pp. 76–85.

14. C. M. Cox and F. J. Homan, Fuels and Materials Development Program Quart. Progr. Rept. Sept. 30, 1969, ORNL-4480, pp. 63–64.

15. Pipes and Tubes for Elevated Temperature Service, USS Bull. 26, ed. 59, p. 62, National Tube Division, United States Steel Corporation, Pittsburgh, Pennsylvania, 1959.

16. T. Lyman (ed.) Metals Handbook, 8th ed., p. 423, vol 1, American Society for Metals, Metals Park, Novelty, Ohio, 1961.

17. E. C. Bishop et al., Stainless Steel Cladding Development Quart. Progr. Rept. June 30, 1969, WARD-3791-41, p. 13.

18. A. Biancheria et al., Oxide Fuel Element Development Quart. Progr. Rept. Sept. 30, 1969, WARD-4135-1, p. 19.

19. W. E. Bailey, Sodium-Cooled Reactors Fast Ceramic Reactor Development Program, Thirty-First Quarterly Report, May–July 1969, GEAP-10028-31. pp. 7-22–7-23.

20. W. H. Bridges, The Physical and Tensile Properties of Type 316 Stainless Steel, ORNL-TM-3037, in press.

CLADDING AND OTHER STRUCTURAL MATERIALS

5. MECHANICAL PROPERTIES OF ALLOYS IN REACTOR ENVIRONMENTS AND DEVELOPMENT OF LMFBR CLADDING AND STRUCTURAL MATERIALS

J. R. Weir, Jr. H. E. McCoy, Jr.

This program is concerned with the effects of irradiation on the mechanical properties of various metals of potential use in nuclear reactors. The materials of primary concern are types 304 and 316 stainless steel, both materials of interest for liquid-metal fast breeder reactors (LMFBR). These alloys are being exposed to high neutron fluences, and the resulting changes in density, microstructure, and mechanical properties are being measured. Other materials under study include Incoloy 800 and V. Some attention is also being given to the use of particle accelerators to simulate neutron damage.

Austenitic Stainless Steels

Irradiation Damage to Type 304 Stainless Steel at 370 to 800°C
(E. E. Bloom, J. O. Stiegler)

The effect of irradiation temperature from 370 to 800°C on the immersion density and microstructural changes in type 304 stainless steel at a fluence of about 4×10^{22} neutrons/cm^2 (> 0.1 Mev) was determined. Materials irradiated at 370 to 380°C and 430 to 440°C were obtained by examining portions of the safety-rod thimble (flat C of the 3-D-1 thimble) from the Experimental Breeder Reactor-II (EBR-II). Irradiation temperatures along the length of the thimble were calculated at Argonne National Laboratory.[1] Materials irradiated at 570 to 630°C and at 770 to 840°C were obtained by examining specimens of types 304 and 304L stainless steel irradiated in EBR-II subassembly XO-34. In all cases, the irradiation temperatures were calculated with the lower and upper temperatures in each case based on gamma heating rates of 3 and 4 w/g at the reactor midplane of row 2 at a reactor power of 50 Mw. The calculated heating rate for this position is about 3.6 w/g. The

ranges on the irradiation temperature are believed to be the largest possible.

Changes in immersion density for these specimens are listed in Table 5.1. These results show that the density decrease (at this fluence) for type 304 stainless steel reaches a maximum at 450 to 500°C and then decreases rapidly with increasing irradiation temperature.

Table 5.1. Density Decrease of Types 304 and 304L Stainless Steel Irradiated at 370 to 800°C

Type Stainless Steel	Unirradiated Density (g/cm^3)	Irradiation Temperature (°C)	Fluence [neutrons/cm^2 (> 0.1 Mev)]	Change in Density (%)
			$\times 10^{22}$	
304[a]	7.8875	370–380	4.3	−0.60
	7.8875	430–440	4.2	−1.33
304[b]	7.8724	570–630	4.0	−0.19
	7.8724	770–840	4.0	+0.01
	7.9724	770–840	4.0	−0.01
304L[a]	7.8911	570–630	4.0	−0.06
	7.8911	570–630	4.0	−0.07

[a]Safety rod thimble, EBR-II.

[b]EBR-II subassembly XO-34.

Transmission electron microscopy of these specimens showed that irradiation temperature markedly influenced both dislocation and void structures. Below 470°C, faulted dislocation loops like those shown in Fig. 5.1(a) formed during irradiation. During irradiation at 570 to 630°C, a structure consisting of a dislocation network and a few unfaulted dislocation loops formed [Fig. 5.1(b)] in types 304 and 304L stainless steel. The transition in dislocation structure appears to be governed primarily by irradiation temperature rather than composition or other variables. At irradiation temperatures of about 400°C, these same heats of stainless steel contained faulted dislocation loops. At 770 to 840°C no dislocation structure was produced by irradiation.

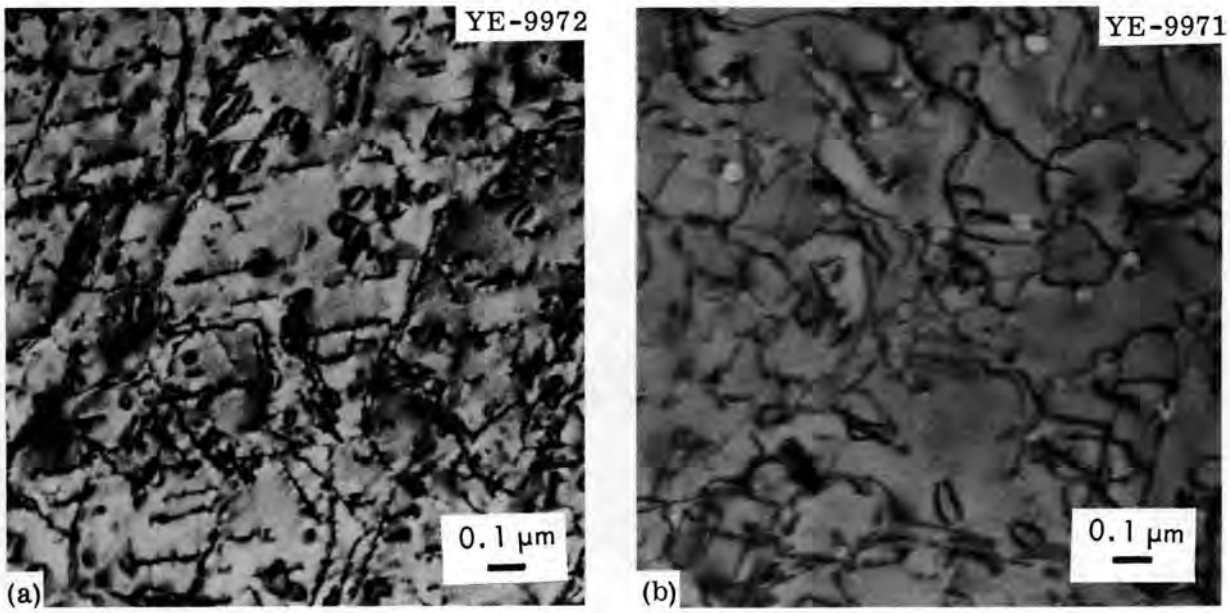

Fig. 5.1. Effect of Irradiation Temperature on the Dislocation Structure in Type 304 Stainless Steel. (a) Faulted dislocation loops formed during irradiation below 470°C; (b) unfaulted dislocation loops and dislocation network formed during irradiation at 570 to 630°C.

The void structures produced by irradiation are shown in Fig. 5.2. Several qualitative observations can be made. With increasing irradiation temperature to 570 to 630°C, the concentration of voids decreases, the size increases, and the shape becomes more polyhedral. In agreement with previous observations[2] made on specimens irradiated to relatively low fluences at 370 to 470°C (which, thus, contained low concentrations of voids), a large fraction of the voids in the specimen irradiated at 570 to 630°C were associated with dislocation lines and precipitate particles. The specimen irradiated at 770 to 840°C contained cavities both within the matrix and at the grain boundaries. The cavities within the matrix had maximum diameters of about 100 A and those at grain boundaries had maximum diameters of about 275 A. The lack of dislocation structure, the presence of cavities at grain boundaries, and the fact that the cavities are smaller than the voids in the corresponding specimen irradiated at 570 to 630°C suggest that the cavities present after irradiation at high temperatures are bubbles of He. Experiments are in progress to determine the behavior of these cavities during annealing after irradiation.

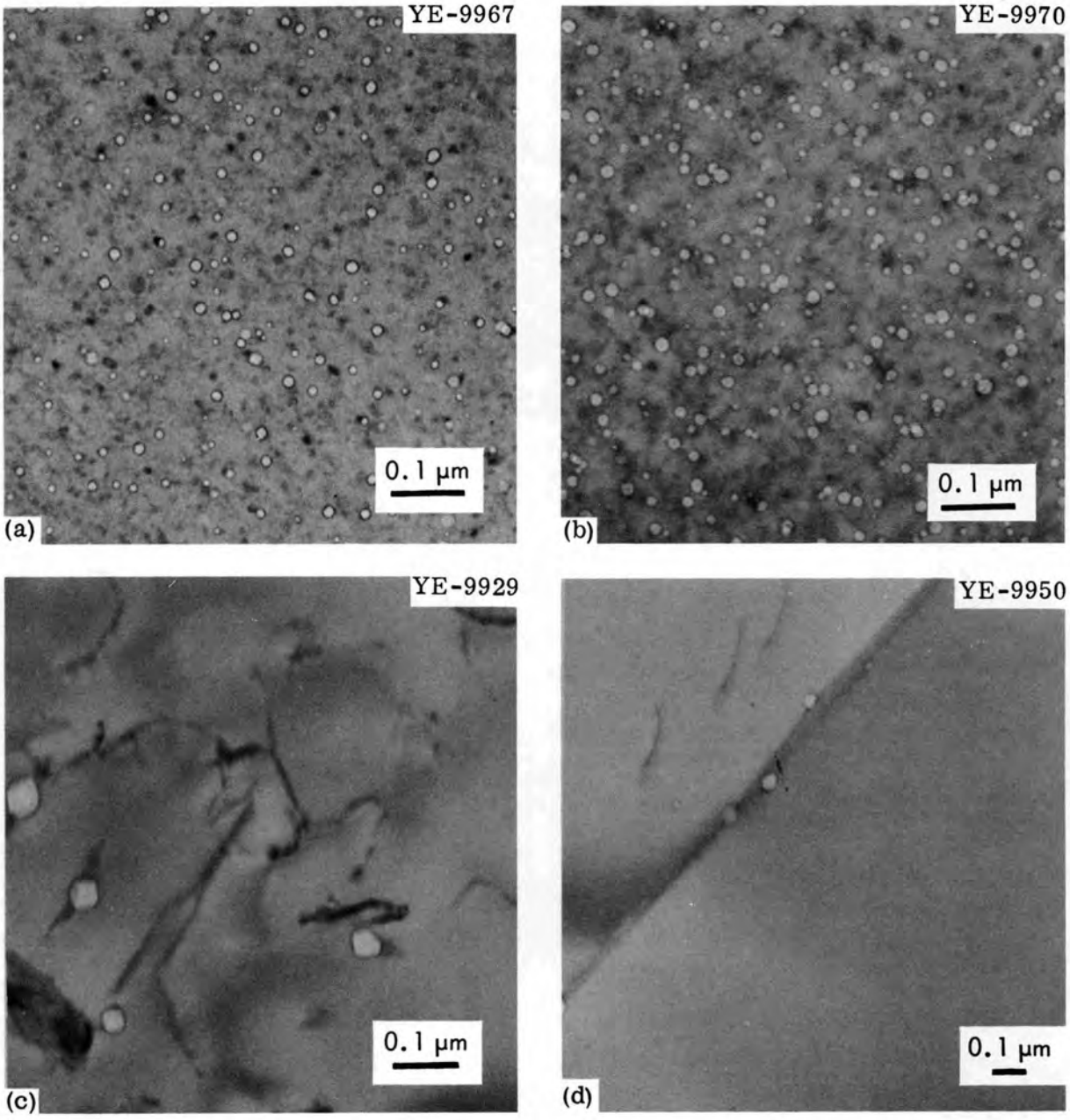

Fig. 5.2. Effect of Irradiation Temperature on the Concentration and Size of Voids in Type 304 Stainless Steel Irradiated to 3.7×10^{22} neutrons/cm^2 (> 0.1 Mev). The irradiation temperatures were (a) 370 to 380, (b) 430 to 440, (c) 570 to 630, and (d) 770 to 840°C.

The concentration of voids is shown as a function of irradiation temperature in Fig. 5.3. At each fluence level, the concentration of voids decreases with increasing irradiation temperature. The curves also reflect the previous observation that the concentration of voids increases at a faster rate at 460 to 470°C than at 370 to 380°C.

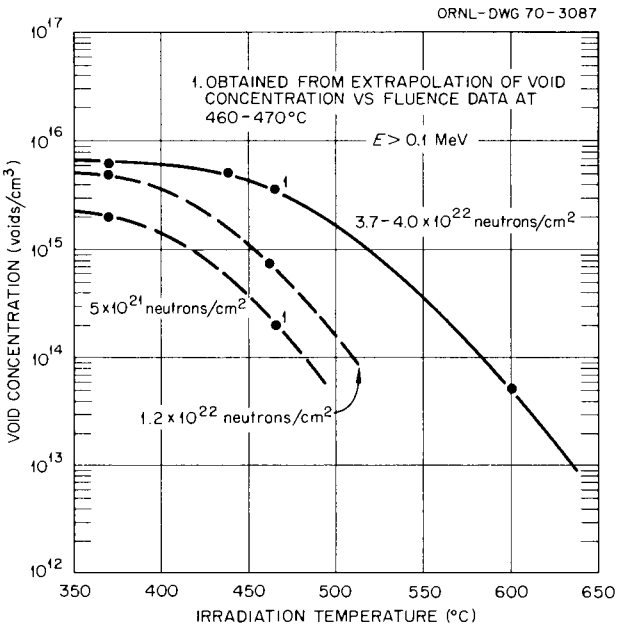

Fig. 5.3. Void Concentration as a Function of Irradiation Temperature for Type 304 Stainless Steel.

Previous results showed that the maximum diameter of the voids is essentially independent of the fast-neutron fluence for fluences greater than about 1×10^{22} neutrons/cm^2 (> 0.1 Mev). Figure 5.4 shows that the maximum diameter of the voids is a sensitive function of the irradiation temperature: it increases as the temperature increases.

The Development of Concentration Gradients Around Voids in Irradiated Stainless Steel (J. O. Stiegler, E. E. Bloom, B.T.M. Loh)

Although macroscopic swelling due to the formation of microscopic voids is a common feature of metals and alloys irradiated at elevated temperatures, the nature of the void population depends greatly on the material under consideration. For example, the fluence at which voids

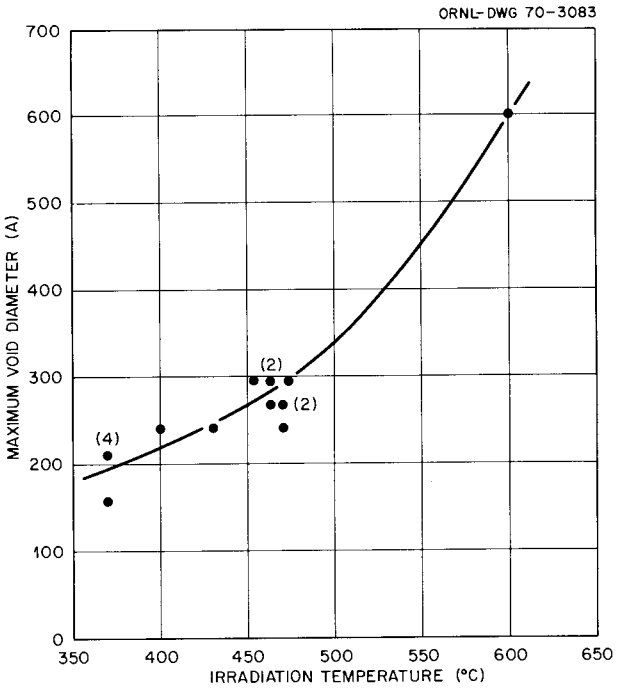

Fig. 5.4. Maximum Diameter of Voids as Function of Irradiation Temperature for Specimens Irradiated to Fluences Above 1×10^{22} neutrons/cm^2. The numbers in parentheses indicate the number of observations.

are first observed in Al of commercial purity is three orders of magnitude higher than that at which they are first seen in high-purity (99.9999%) Al (ref. 3). A similar difference exists between Ni and type 304 stainless steel.[4,5] There are significant differences in the concentration and size of voids even among stainless steels of similar composition irradiated under identical conditions.

A description of these differences is of both fundamental and applied interest. Such observations may guide our development of theoretical models that describe the process, and, of course, existing models must explain the differences to remain under consideration. Practically, an understanding of the factors that influence the concentration and size of voids will aid in the development of materials that are more resistant to swelling.

The striking contrast between the dependence of void concentrations and sizes on fluence in stainless steel and in Ni is illustrated in Figs. 5.5 and 5.6. The transmission electron photomicrographs of

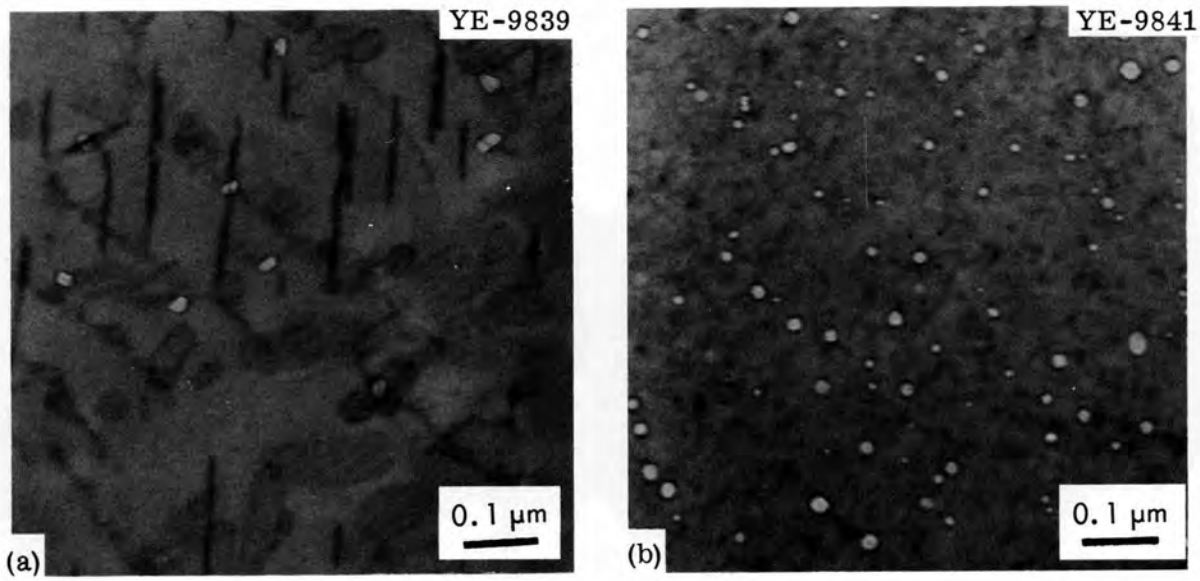

Fig. 5.5. Void Structure in Type 304 Stainless Steel Irradiated in the Experimental Breeder Reactor-II at About 470°C to a Fluence of (a) 3×10^{21} and (b) 2×10^{22} neutrons/cm^2.

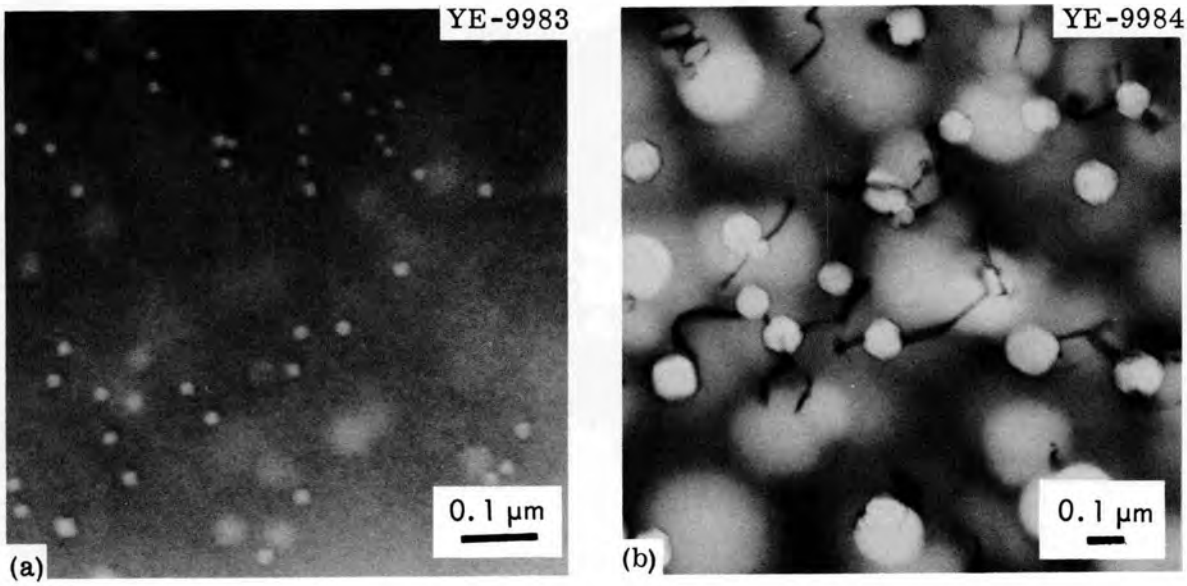

Fig. 5.6. Void Structure in Nickel 270 Irradiated in the Experimental Breeder Reactor-II at About 470°C to a Fluence of (a) 1.4×10^{20} and (b) 1.5×10^{22} neutrons/cm^2.

stainless steel irradiated at 470°C to fluences of 3×10^{21} and 2×10^{22} neutrons/cm^2 (> 0.1 Mev) in Fig. 5.5 show that in this material the concentration of voids increases with increasing fluence but that the maximum void size, reached at 3×10^{21} neutrons/cm^2, increases little, if any, as the fluence is increased by nearly an order of magnitude. Measurements of the concentration and maximum size of voids as functions of fluence for irradiation temperatures of 370 and 470°C, shown in Figs. 5.7 and 5.8, confirm this observation. Identical behavior was noted for material irradiated at intermediate temperatures to fluences as high as 7×10^{22} neutrons/cm^2. Over the temperature range in which voids have been observed (350 to 650°C), the concentration of voids increases with increasing fluence, and the maximum size

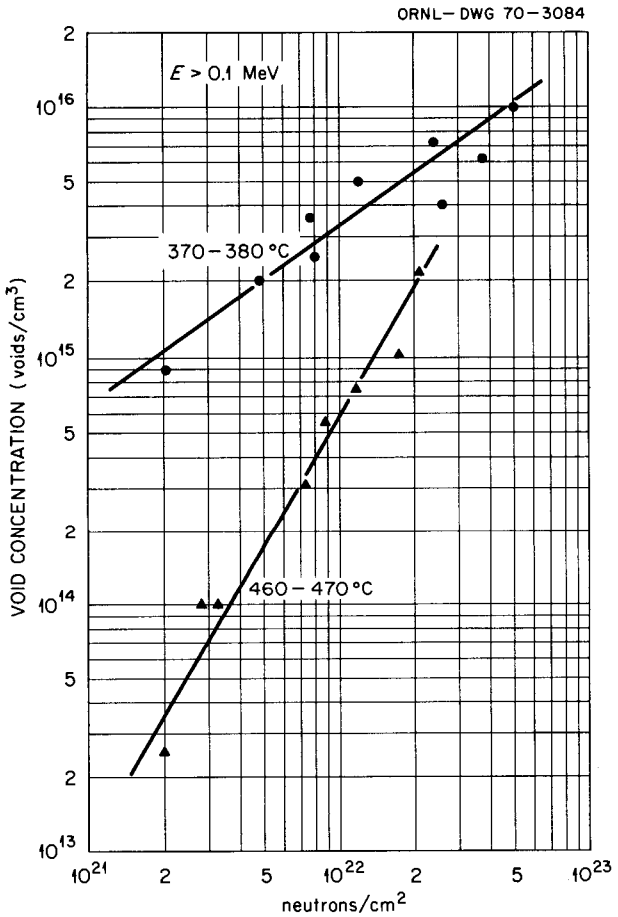

Fig. 5.7. Concentration of Voids as a Function of Fluence for Type 304 Stainless Steel Irradiated in the Experimental Breeder Reactor-II at 370 to 470°C.

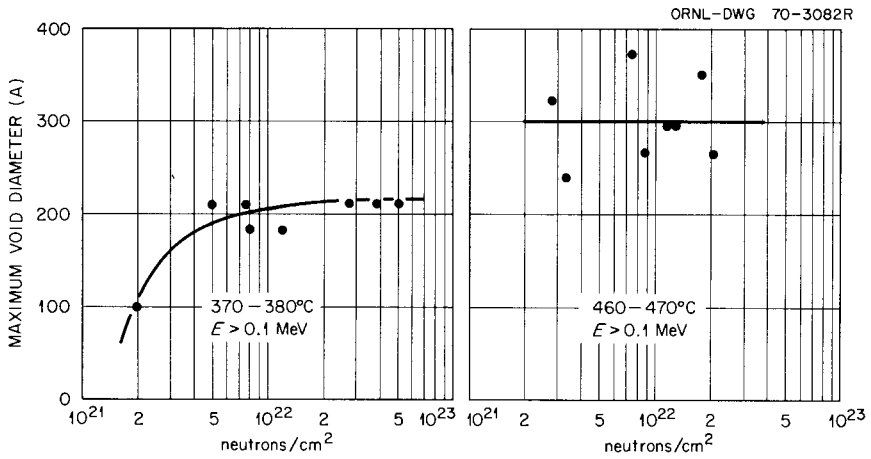

Fig. 5.8. Maximum Size of Voids as a Function of Fluence for Type 304 Stainless Steel Irradiated in the Experimental Breeder Reactor-II at 370 to 470°C.

of the voids varies little with fluence but increases with increasing irradiation temperature.

Photomicrographs of Nickel 270, shown in Fig. 5.6, illustrate essentially the opposite behavior; that is, the concentration of voids seems to become saturated at a relatively low fluence, but the size of the voids appears to increase without limit. In fact, in Fig. 5.6(b) a large fraction of the voids have diameters larger than the foil thickness and result in the circular, indistinct images. An increase in fluence from 1.4×10^{20} to 1×10^{22} neutrons/cm^2 at 470°C results in no appreciable change in void concentration (about 10^{14}/cm^3) but does cause an increase from 225 to about 1500 A in the maximum size of the voids.

Lauritzen et al.[6] recently reported significant differences in swelling and in the concentrations and sizes of voids in types 304 and 347 stainless steel irradiated in the EBR-II to a fluence of 3.4×10^{22} neutrons/cm^2 (total) at about 660°C. The voids in the type 347 stainless steel were significantly smaller, although slightly more numerous, than those in type 304 stainless steel. In addition, the type 347 stainless steel swelled less. Bloom and Steigler[7] compared swelling and microstructures in a standard type 304 stainless steel and a similar alloy modified by the addition of 0.18 wt % Ti.

They found for irradiation to a fluence of about 1.6×10^{22} neutrons/cm^2 (> 0.1 Mev) at 450 ± 50°C that the Ti-modified alloy swelled less due to a decreased concentration of voids; the distributions of void sizes were equivalent in the two alloys.

These observations show that, even within the austenitic stainless steels, minor variations in composition can significantly change void concentrations and maximum and average sizes. A model describing void formation must be sensitive to these changes in composition and explain the apparent occurrence of a limiting void size in stainless steel and the lack of a limiting void size in Ni. It must also predict the saturation of void concentration at low fluences in Ni but not in stainless steel. We shall attempt to rationalize these effects by examining some of the factors that influence the growth of voids.

Growth of voids has been considered to be limited by diffusion of vacancies to the void or by adsorption of vacancies onto void surfaces or other locations.

Bullough et al.[8] derived an expression for the growth rate of voids when that growth is limited by absorption of vacancies at steps on the surface of the void. Their equation for growth rate is independent of the void radius. That is, if growth is limited by this process, a small void will experience the same change in radius as a large void during a given radiation increment. The curve for the distribution of the void sizes, then, reflects the nucleation rate. The shape of that end of the curve that represents the large void sizes should not change as the irradiation proceeds but rather should be translated as a unit to larger void sizes. The newly generated voids make up the portion of the curve that represents small void-size range.

Such a translation of the curve for distribution of void sizes is not observed experimentally as the irradiation progresses. In stainless steel, the maximum void size does not increase (for fluences greater than 3×10^{21} neutrons/cm^2), but the concentration of voids in the largest size interval continually increases. In high-purity Al, the maximum void size increases during the irradiation, but the curve changes shape.[9] We conclude that in these materials surface absorption does not

limit void growth. Studies of the annealing of dislocation loops[10] and voids[11,12] in thin foils have shown that dissolution is governed by diffusion of vacancies and not surface emission. Accordingly, we shall treat void growth as a process limited by diffusion of vacancies to the void and examine the factors that might account for the limiting void size.

For the case in which void growth is controlled by diffusion and the vacancy concentration, N_v, is much greater than that in equilibrium with a cavity of radius, r, we may write $dr/dt = (N_v D_v)/r$, where D_v is the coefficient for diffusion of vacancies and t is the time. We expect that N_v will vary with time since concentrations of voids and loops (i.e., sink concentrations) change with time:

$$rdr = D_v N_v dt \tag{5.1}$$

$$\frac{r_2^2}{2} - \frac{r_1^2}{2} = D_v \int_{t_1}^{t_2} N_v(t)dt \ .$$

Without knowing the time variation of N_v we cannot integrate the expression on the right. We can, however, evaluate it for a given fluence increment by examining the change in radius of certain voids.

At a fluence of 4.8×10^{21} neutrons/cm^2 at 370°C, we observed 2×10^{15} voids/cm^3 greater than 50 A in diameter (our limit of resolution) and a maximum void size of 200 A. At a fluence of 5×10^{22} neutrons/cm^2, we counted 10×10^{15} voids/cm^3 greater than 50 A in diameter and 2×10^{15} voids/cm^3 greater than 150 A in diameter. The maximum void size was again 200 A. Therefore, during this fluence increment, an appreciable number of voids were nucleated or grew from an invisible size to a diameter of 150 A. If we evaluate the integral in Eq. (5.1) for the most conservative case in which a void grows from just below the limit of visibility to 150 A (r_1 = 25 A and r_2 = 75 A), Eq. (5.1) then becomes

$$(7.5 \times 10^{-7})^2 - (2.5 \times 10^{-7})^2 = 2 D_v \int_{t_1}^{t_2} N_v(t)dt \tag{5.2}$$

$$= 50 \times 10^{-14} \text{ cm}^2 \ .$$

A void that was 100 A in radius at the beginning of this increment should grow to a final size given by

$$r_2^2 - (10 \times 10^{-7})^2 = 50 \times 10^{-14}$$

$$r_2^2 = 150 \times 10^{-14} \qquad (5.3)$$

$$r_2 = 122 \text{ A} .$$

That is, a void that was 200 A in diameter at 4.8×10^{21} neutrons/cm^2 should grow to a diameter of 244 A at 5×10^{22} neutrons/cm^2. We are capable of clearly detecting this amount of growth. Since we do not observe it, we conclude that the apparent limiting void size observed in stainless steel is not due solely to a depletion of the supersaturation of vacancies as a result of an increase in sink concentration. The only other term in Eq. (5.1) that can vary is the coefficient for diffusion of vacancies.

Variation of the coefficient for diffusion of vacancies is not inconceivable in an alloy in which solute segregation may be induced by a vacancy flow. Segregation will change local solute concentrations and, consequently, coefficients for diffusion of vacancies. This situation is the inverse of the well-known Kirkendall effect, which occurs when two dissimilar metals or alloys are joined together in a temperature range at which diffusion can occur. The different atomic species generally diffuse at different rates, and, since diffusion occurs by a vacancy process, a vacancy flow also occurs to counter the flow of the faster moving component. That is, a concentration gradient induces a vacancy flow. In a homogeneous alloy, the inverse process occurs during neutron irradiation at temperatures at which vacancies are mobile. Early in the irradiation, the lattice becomes supersaturated with vacancies, the concentration depending on the flux, temperature, and mechanisms of their annihilation. The situation changes, however, when a void is nucleated; the void acts as a vacancy sink and results in a vacancy concentration gradient around it. This sets up a net flow of vacancies into the void, which in turn induces a flow of atoms away from the void. If the different atoms in the alloy diffuse at different rates, as is generally the case, a shell of material with lower

diffusivity will gradually build up around the void. This is, in a sense, an inverse Kirkendall effect.

Such segregation as a result of a vacancy flow may also occur during heating, cooling, or sintering. The general aspects of the problem were treated theoretically by Anthony,[13] and experimental evidence for segregation during sintering was obtained by Kuczyuski et al.[14] By metallographic examination of the necked regions of sintered wires of a Cu–8% In alloy in which vacancy currents were induced by differences in radius of curvature, Kuczyuski et al. observed precipitation of an In-rich phase that could have occurred only by movement of the faster moving In atoms into the necked region.

Anthony pointed out that segregation may be induced by vacancy flow by two processes: (1) the reverse flow of atoms, mentioned above, which is a consequence of vacancy flow, and (2) the dragging of solute atoms by vacancies. The latter occurs when the energy of attraction between a vacancy and solute atom is much greater than the thermal energy. Following Anthony, we shall consider the distribution of solute around a void for the former (weak binding) case.

Consider a thin shell of material surrounding a void in a binary alloy composed of A and B atoms. The composition in the shell will change until the fluxes of solute and solvent atoms (J_A and J_B) entering and leaving the shell are proportional to their atom fractions in the shell (C_A and C_B); that is, until $J_A/J_B = C_A/C_B$. Anthony showed that, for a dilute solution of B in A and a weak interaction between solute atoms and vacancies, the solute concentration for a one-dimensional gradient (direction X) can be described by

$$\frac{\partial \ell n C_B}{\partial X} = \frac{\partial \ell n C_V}{\partial X} \frac{(D_B - D_A)}{D_B} \qquad (5.4)$$

where C_V is the concentration of vacancies and D_B and D_A the diffusion coefficients for B and A atoms, respectively. If the diffusivity of the solute is less than that of the solvent ($D_B < D_A$), the region in the vicinity of the void will be enriched in solute, the degree of enrichment depending on the vacancy concentration gradient and the

difference in diffusivities of the elements. If $D_B > D_A$, the region in the vicinity of the void will be enriched in solute, the degree of enrichment depending on the vacancy concentration gradient and the differences in diffusivities of the elements. If $D_B > D_A$, the region adjacent to the void will be depleted of solute. In either case the diffusion coefficient near the surface of the void will be lower than that in the original alloy.

The difference between D_B and D_A must necessarily decrease with increasing temperature. This would require a larger void before sufficient segregation could occur to reduce the growth rate to a negligible level. The increase in the apparent limiting void size with increasing temperature is consistent with this interpretation.

Such a process could, of course, occur only in an alloy, not in a pure metal. It should significantly slow the void growth rate but not totally stop it. It is possible that the greatly reduced rate of void growth observed in stainless steel results from a combination of the vacancy depletion effect, discussed earlier, and solute segregation.

It is interesting to consider the observations of Lauritzen et al.[6] in this light. They found that voids formed in type 347 stainless steel were considerably smaller than those formed in type 304 stainless steel. It is difficult to make any meaningful calculations of the nature and extent of segregation in an alloy as complex as stainless steel, but we can speculate that differences in composition lead to buildup of a layer of sufficiently low diffusivity at a smaller void size in the type 347 stainless steel.

It is also possible that this process may explain the saturation of void concentration observed in Ni and the apparent lack of saturation observed in stainless steel. If He atoms generated by (n,α) reactions are involved in the nucleation of voids, the rate of nucleation will be related to the concentration of gas dissolved in the lattice. If the gas is mobile during irradiation, the void population will serve as effective sinks, at least in the case of Ni, where there is no barrier to diffusion of gas atoms into the voids. In the case of stainless steel, however, the development of a layer of low diffusivity around

voids could reduce their effectiveness as sinks and thereby increase the rate of void nucleation because of the enforced solution of the gas.

We suggest that the differences in the irradiation behavior of stainless steel and Ni may be due in part to the development of a layer of low diffusivity around voids in the stainless steel as a result of solute segregation induced by vacancy flow. Such a layer would reduce the rate of growth of existing voids and reduce the effectiveness of the voids as sinks for He atoms. The increased He concentration in the lattice would tend to increase the rate at which voids were nucleated. The increased concentration of voids would, in turn, further deplete the vacancy supersaturation and further decrease the rate of growth.

We believe that solute segregation should occur as a result of vacancy flow. Whether or not it is the cause of the observed behavior is a matter of speculation. More careful experiments on simpler binary alloys may provide the proof. In situ measurements of the annealing kinetics of voids by means of the electron microscope may show anomalous behavior that can be related to the concentration gradient. That is, the coefficient for diffusion of vacancies may appear to increase with decreasing void size. We believe that it is important to understand the effect, for compositional modifications that decrease the limiting void size in alloys may prove useful in controlling the swelling of reactor materials.

Void Distributions as Monitors of Irradiation Temperature and Fluence

(J. O. Stiegler, E. E. Bloom)

A preliminary survey of the concentrations and sizes of voids formed in type 304 stainless steel irradiated in EBR-II at 370 to 650°C and to fluences of 2 to 70×10^{21} neutrons/cm^2 (> 0.1 Mev) indicated that the configuration of voids is a unique function of the irradiation temperature and fluence. Specifically, at constant fluence, the concentration of voids decreases and the maximum size of the voids increases with increasing irradiation temperature. At constant temperature, the concentration of voids increases with increasing fluence, but the maximum size of the voids changes little at fluences above about 1×10^{22} neutrons/cm^2.

Quantitative plots of void concentrations and maximum void sizes as functions of fluence for irradiation temperatures of 370 and 470°C are shown in Figs. 5.7 and 5.8. A curve depicting the maximum size of voids as a function of irradiation temperature for fluences above 1×10^{22} neutrons/cm^2 is given in Fig. 5.4. In order to use microstructural characteristics as monitors of temperature and fluence one must first determine the maximum size of the voids as an indication of the irradiation temperature. Once the temperature is known, the concentration of voids can be read directly from the plots developed by Straalsund et al.[15] for void concentration, temperature, and fluence, since the concentration of voids is a unique function of fast-neutron fluence. The maximum size of the voids must be used, since the average size of the voids increases with increasing fluence, but the maximum size does not. As an additional temperature reference we observe that interstitials precipitate as faulted dislocation loops at irradiation temperatures below about 550°C and as unfaulted loops at higher temperatures.

Present data are not extensive or accurate enough to permit quantitative determinations of irradiation conditions, but they do allow evaluation of reported conditions and at least a qualitative determination of temperature and fluence for cases where no monitors were present. As additional data become available, the accuracy of estimates based on microstructural characteristics should improve.

We can illustrate the use of this technique by evaluating some observations made by Lauritzen et al.[6] on type 304 stainless steel irradiated in the EBR-II to a total fluence of 3.4×10^{22} neutrons/cm^2 at 660°C, as determined by fusible-metal thermometry. Unfortunately, the specimens were taken from gage and grip regions of a tensile specimen that had been tested at 704°C; therefore, no evidence was retained of the original dislocation-loop structure. A maximum void diameter of 550 A was observed in the gage sections and in one specimen taken from a grip region.[16] In a second grip specimen, a similar distribution of void sizes was obtained with the exception that a few voids were as large as 900 A in diameter.[16] The average concentration of voids was about 1×10^{15} voids/cm^3.

On the basis of our observation that the maximum size of voids is a function of irradiation temperature, we suggest that this material was irradiated at 550 to 600°C. The presence of some very large voids in one region of the grip may signify that part of the specimen ran at an appreciably higher temperature, perhaps as high as 660°C, for at least part of the irradiation. We conclude from the microstructural characteristics that the bulk of the specimen was not irradiated at 660°C but rather at a temperature 50 to 100°C lower. A local hot spot or transient heating effect may have been responsible for the higher irradiation temperature established by fusible-metal thermometry.

Notes

1. J. P. Bacca et al., Reactor Development Program Progress Report, January 1969, ANL-7548, pp. 73–75.

2. E. E. Bloom and J. O. Stiegler, Fuels and Materials Development Program Quart. Progr. Rept. Sept. 30, 1969, ORNL-4480, pp. 76–89.

3. J. O. Stiegler, K. Farrell, C.K.H. DuBose, and R. T. King, "High-Fluence Neutron-Irradiation Damage in Aluminum," pp. 215–232 in Radiation Damage in Reactor Materials, Vol. II, International Atomic Energy Agency, Vienna, 1969.

4. E. E. Bloom and J. O. Stiegler, Trans Am. Nucl. Soc. 12, 116 (1969).

5. B. Mastel and J. L. Brimhall, J. Nucl. Mater. 28, 115 (1968).

6. T. Lauritzen et al., Nucl. Engr. Design 9, 265 (1969).

7. E. E. Bloom and J. O. Stiegler, "A Comparison of Irradiation Induced Swelling and Void Formation in Two Austenitic Stainless Steels," to be published in the Journal of Nuclear Materials.

8. R. Bullough et al., Trans. Am. Nucl. Soc. 12, 523 (1969).

9. N. H. Packan, Oak Ridge National Laboratory, private communication.

10. P. S. Dobson et al., Phil. Mag. 16, 9 (1967).

11. T. E. Volin and R. W. Balluffi, Phys. Status Solidi 25, 163 (1968).

12. K. Westmacott et al., Metal Sci. J. 2, 177 (1968).

13. T. R. Anthony, Acta Met. 17, 603 (1969).

14. G. C. Kuczyuski et al., Acta Met. 8, 209 (1960).

15. J. L. Straalsund et al., Quarterly Progress Report October, November, December 1969, Reactor Fuels and Materials Development Program for Fuels and Materials Branch of USAEC Division of Reactor Development and Technology, BNWL-1279, p. 4.52.

16. U. E. Wolff, General Electric Company, Vallecitos Nuclear Center, Pleasanton, California, private communication.

6. FABRICATION DEVELOPMENT FOR LMFBR STAINLESS STEEL TUBING

W. O. Harms W. R. Martin

This program for the development of techniques for fabricating cladding for fast reactors involves manufacturing thin-walled tubing of high quality. Our studies are designed to show the relationships among processing variables, mechanical properties at elevated temperature, and the physical defects of the tubing.

Effect of Fabrication Variables During Mandrel Plug Drawing on the Quality and Properties of Type 316 Stainless Steel

A. C. Schaffhauser H. E. McCoy, Jr.

Fabrication of Ultrafine Grain Size in Stainless Steel Tubing (G. A. Reimann)

We attempted to refine still further the grain size of type 316 stainless steel produced from Allegheny-Ludlum Steel Corporation heat 65808. We split tubing lengthwise and rolled it flat from the original 0.016-in. wall thickness to 0.008-in. sheet. This rolling, coupled with the 20% cold work already in the finished tube, produced the equivalent of 60% total cold work. Samples of this strip were annealed 1 hr at 750, 760, and 775°C. The three structures that resulted were substantially identical, and the grain size was not appreciably smaller than that of the original structure.[1] We conclude that neither variations in the temperature of heat treatments between 750 and 775°C nor cold working above 50% significantly alters the grain size in this heat of material.

Biaxial Stress-Rupture Properties at 650°C of Type 316 Stainless Steel Tubing (R. T. King)

Techniques for producing ultrafine grain structure and a uniform distribution of a fine carbide precipitate[1] in type 316 stainless steel tubing and early results from biaxial stress-rupture testing of this material at 650°C in the 20% cold-worked condition[2] were described

previously. The balance of the results of these tests at 650°C on the 20% cold-worked material and the results of tests at 650°C on specimens that were stress-relieved for 1 hr at 700°C before testing are reported here.

The stress-relieved specimens were prepared from tube 1A2-C (from Allegheny-Ludlum Steel Corporation heat 65808 of type 316 stainless steel) and tested as described previously.[2] Ultrasonic inspection for responses greater than those produced by a standard 0.002-in.-deep × 0.030-in.-long reference notch revealed no longitudinal or transverse discontinuities.

Eight specimens of 20% cold-worked material and six specimens of stress-relieved material were tested at circumferential hoop stresses of 10,000 to 50,000 psi. The rupture times from these tests are plotted versus circumferential hoop stress in Fig. 6.1, and standard least-squares straight lines were calculated from

$$\ell n\ t_r = a + b\ \ell n\ \sigma \quad ,$$

where t_r is the rupture time, σ is the hoop stress, and a and b are constants. These test results indicate that, although the stress-relief annealing treatment had little or no effect on the short-term rupture times at high stresses, the rupture times at low stresses were increased by stress-relief annealing.

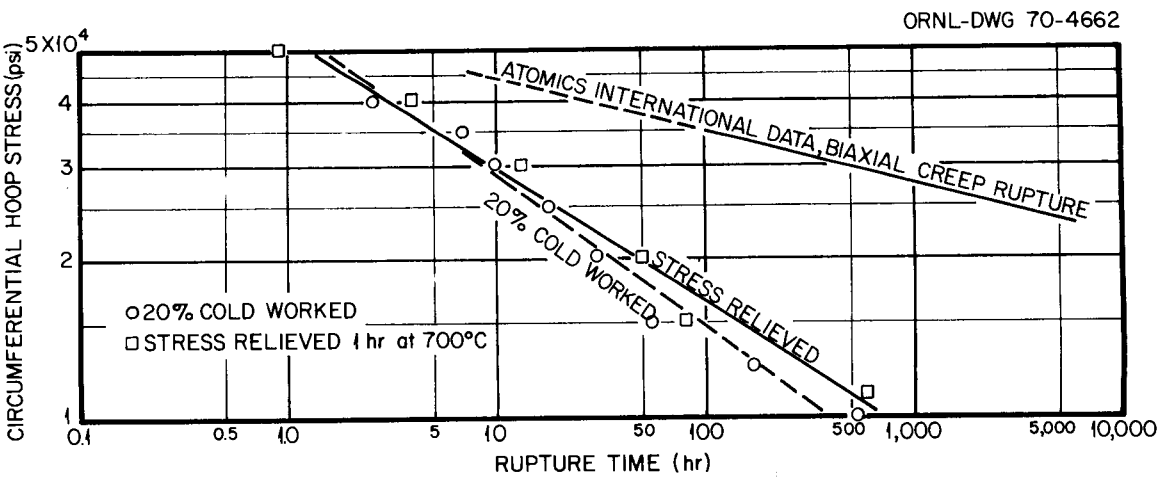

Fig. 6.1. Biaxial Stress-Rupture Characteristics of Ultrafine Grained Type 316 Stainless Steel Tubing at 650°C.

Date[3] obtained from Atomics International on conventional 0.275-in.-OD × 0.010-in.-wall-thickness, 20% cold-worked type 316 stainless steel tubing (also from Allegheny-Ludlum Steel Corporation heat 65808) that had a grain size of ASTM 7 are plotted in Fig. 6.1 for comparison. The longer rupture times of this tubing may be primarily due to the presence of dissolved C, which strengthens the alloy by precipitation of carbide on dislocations during testing. Barnby[4] showed that strain aging by the precipitation of $(Fe, Cr)_{23}C_6$ on dislocations in solution-annealed type 316 stainless steel caused creep rates 20 to 30 times lower than those observed when the C is precipitated before testing. Since the C in both the 20% cold-worked and stress-relieved material with ultrafine grain size is in the form of carbide precipitates, the relatively short rupture times observed are reasonable.

Both the maximum uniform circumferential strain measured about 0.25 in. from the point of failure and the total circumferential strain measured at the point of failure are plotted versus rupture time in Fig. 6.2. A single scatterband is drawn to include all data for both

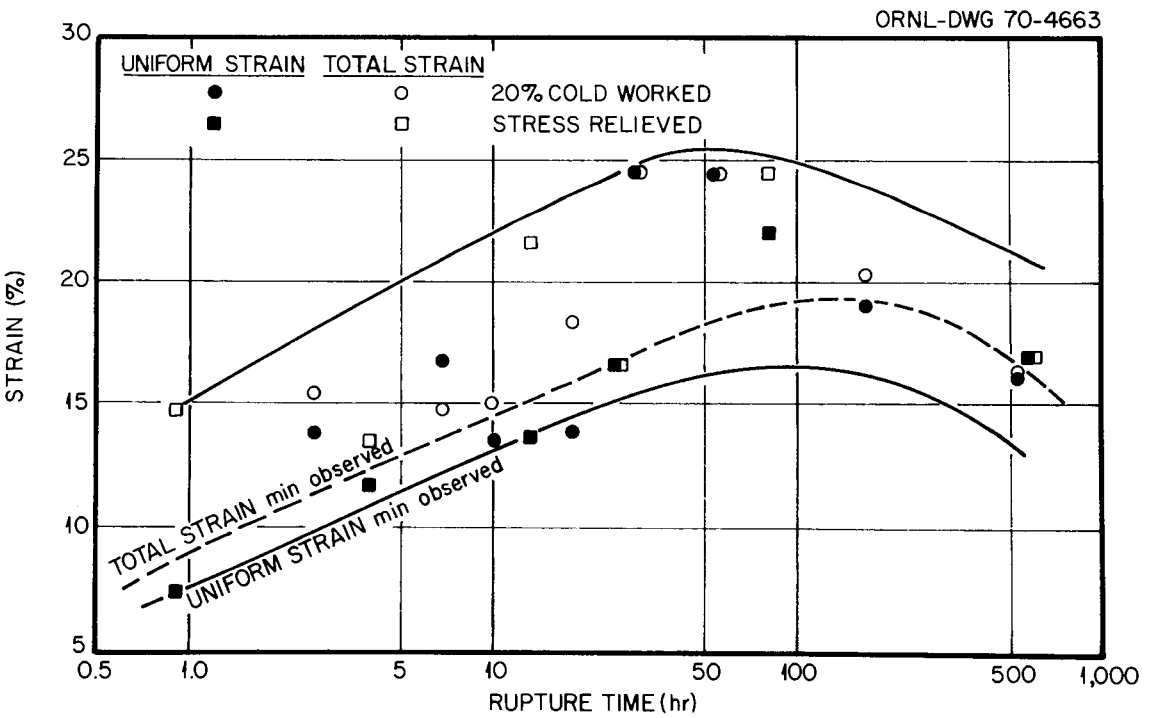

Fig. 6.2. Ductility of Ultrafine Grained Type 316 Stainless Steel Tubing at 650°C.

material conditions, since there is no significant difference between the ductility of the 20% cold-worked material and that of the stress-relieved material. The data indicate that the minimum uniform and total strains increase from about 7 and 9%, respectively, for tests that last 1 hr to about 17 to 19%, respectively, for tests that last 100 hr. Rupture ductility may decrease at longer times.

Specimens of the material cold worked 20% were examined by transmission electron microscopy to determine whether extensive recrystallization occurred during testing. A typical photomicrograph is shown in Fig. 6.3. We found that only limited recrystallization occurred in either long- or short-time rupture tests. Voids formed at old grain boundaries, suggesting that the mode of failure was intergranular. The mode of failure of these tubes will be studied in more detail next quarter.

Fig. 6.3. Typical Microstructure for Cold-Worked Type 316 Stainless Steel Tubing with Ultrafine Grain Size after Stress-Rupture Testing at 650°C. 10,000×. Reduced 30%.

Evaluation of Artificial Defects (K. V. Cook)

Our study of artificial defects in tubing is continuing. One phase of our study is to determine the effect of artificial defects at known orientations and locations on the mechanical properties at elevated temperatures.

Forty-two tube burst specimens were sectioned from tubes BA1-2A-26 and BA1-3-28. These tubes of type 316 stainless steel with ultrafine grain size are 0.250 in. in outside diameter by 0.016 in. in inside diameter and contain about 20% cold work. Both tubes had been nondestructively tested and found to conform to Fast Flux Test Facility (FFTF) tubing specifications. The specimens were divided into two series, each containing 21 tubes. We notched 18 of the first series by electrodischarge machining to simulate defects 0.030 in. long by 0.0023 in. wide on the thin portion of the wall of the tube at depths of 10, 35, and 65% of the wall thickness. Because of the need for multiple mechanical tests, we divided these 18 tubes into triplicate samples, each of which contained a notch of one of the specified depths on either the outer or inner surface. Each tube is somewhat eccentric but within the allowable limit set by the FFTF specification. The depths of the notches on the outer surfaces were measured directly, but the depths of the notches on the inner surface were measured from rubber replicas. We measured the wall thicknesses of the first series of tubes by means of ultrasonic resonance with display techniques that showed variations in wall thickness as a function of tube rotation and notch location.

This first series of specimens, 3 without defects and 18 with artificial defects are now being prepared for stress-rupture testing at 650°C. The second series of 21 tubes will be used for a similar study of 0.125-in.-long notches.

Notes

1. G. A. Reimann, Fuels and Materials Development Program Quart. Progr. Rept. Dec. 31, 1969, ORNL-4520, pp. 134–141.

2. R. T. King, Fuels and Materials Development Program Quart. Progr. Rept. Dec. 31, 1969, ORNL-4520, pp. 141–146.

3. J. J. Gill and D. F. Athins, Atomics International, personal communication, January 1970.

4. J. T. Barnby, J. Iron Steel Inst. (London) 204, 23 (January 1966).

7. WELDING DEVELOPMENT FOR LMFBR VESSELS AND COMPONENTS

J. R. Weir, Jr. G. M. Slaughter

We are evaluating the behavior of weldments in austenitic stainless steel at 370 to 650°C as a function of both the welding process and the variables within a process for application to liquid-metal fast breeder reactor (LMFBR) vessels and components. The solidification substructure (the finest structural detail that can be resolved by an optical microscope) markedly influences the mechanical properties of a weldment at elevated temperatures. Since the size and type of substructure in a weldment are significantly influenced by factors that the welder can control, our approach is to determine the effects of different welding processes and of the variables within each process (current, voltage, travel speed, etc.) upon mechanical properties.

The research for this program is closely interrelated with that for Shielded Metal-Arc Welding for LMFBR Components.[1] For example, the mechanical-properties and metallographic studies on the two programs directly complement each other, and occasional cross referencing of information is useful.

Study of Submerged-Arc Process

Preparation of Weldment Specimens (G. M. Goodwin, D. G. Harman, Nancy C. Cole)

Based on the results of the bead-on-plate study reported previously,[2] we prepared multipass weldments in 1-in.-thick plate to investigate the effect of heat input on mechanical properties at elevated temperatures. The following conditions were used:

Heat input	Low	Medium	High
Current, amp	600	600	600
Voltage, v	34	34	34
Travel speed, in./min	30	18	4.5
Energy input, kJ/in.	40.8	68	272

All other welding variables were identical for each of the welds and were the same as reported for the submerged-arc test weldment.[2]

To study the effect of variations in flux composition, we prepared welds with each of the four fluxes available commercially: Arcos S-4, Hobart HS-300, Linde 709-5, and Lincoln ST-100. Each weld was prepared in 1-in.-thick plate under conditions identical to those used for the submerged-arc test weld; flux composition was the only intentional variable.

Six submerged-arc welds, each 32 in. long, were prepared in 1-in.-thick plate for a study at the Naval Research Laboratory (NRL). The welds were prepared under full restraint in the equipment shown in Fig. 7.1. Note that ten 2-in.-thick "C" clamps were required on a

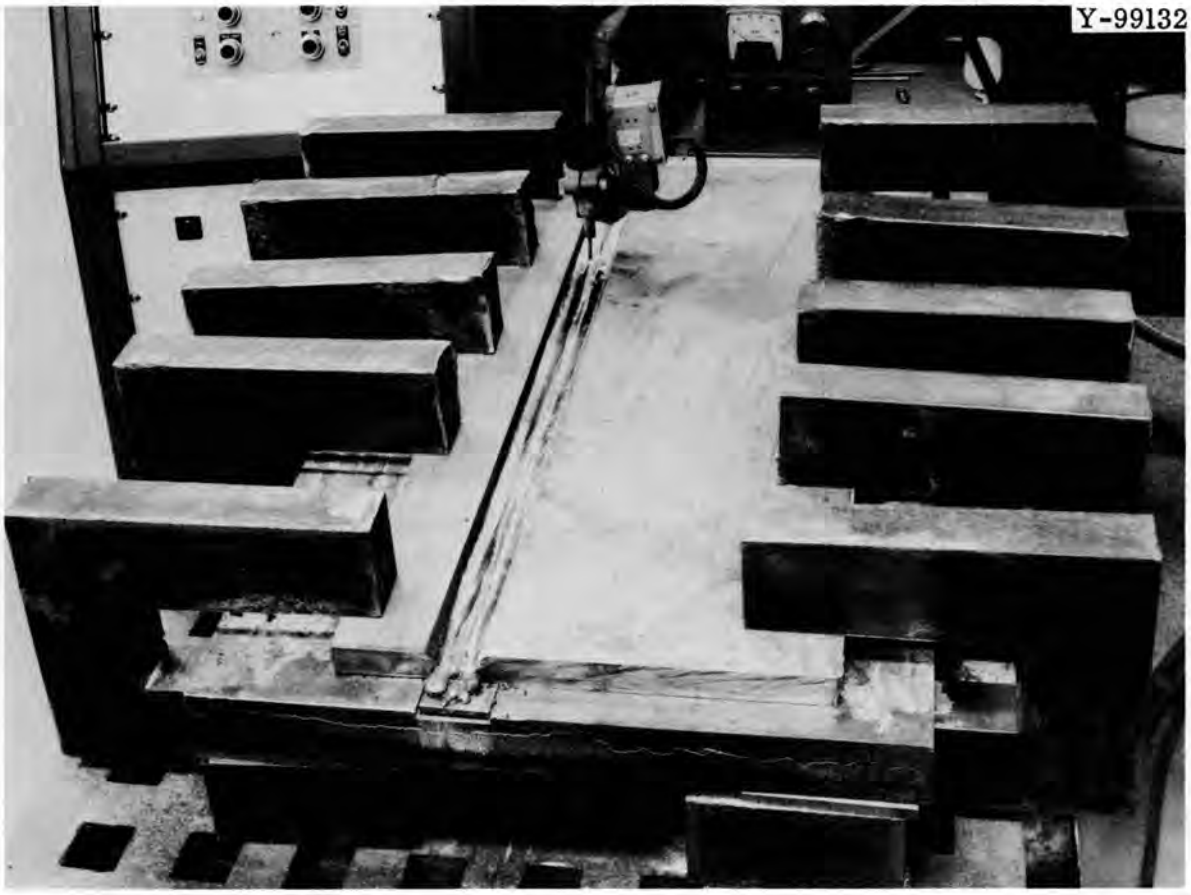

Fig. 7.1. Equipment Used to Produce Submerged-Arc Test Weldments for Naval Research Laboratory.

2-in.-thick strongback to minimize distortion. Five of the weldments were shipped to NRL for fracture-mechanics tests, and one was retained for study here.

Portions of two electroslag welds were obtained for incorporation into our program for testing mechanical properties. The welds were produced in both cast and wrought stainless steel plates, 4 in. thick by 24 in. long, at the ESCO Corporation, Portland, Oregon. Wafers 1/2 in. thick were removed from each of the welds and will be machined into specimens for tests of mechanical properties.

Evaluation of Weldments (G. M. Goodwin, D. G. Harman, Nancy C. Cole)

Several specimens machined from a submerged-arc weld made under "prototypical" conditions were creep-rupture tested. The test results show strengths much lower than those of the shielded metal-arc welds.[3] Figure 7.2 compares the stress-rupture properties of the two welding processes; the data for the shielded metal-arc process are from the weld made with commercial electrodes with lime TiO_2 coatings. We

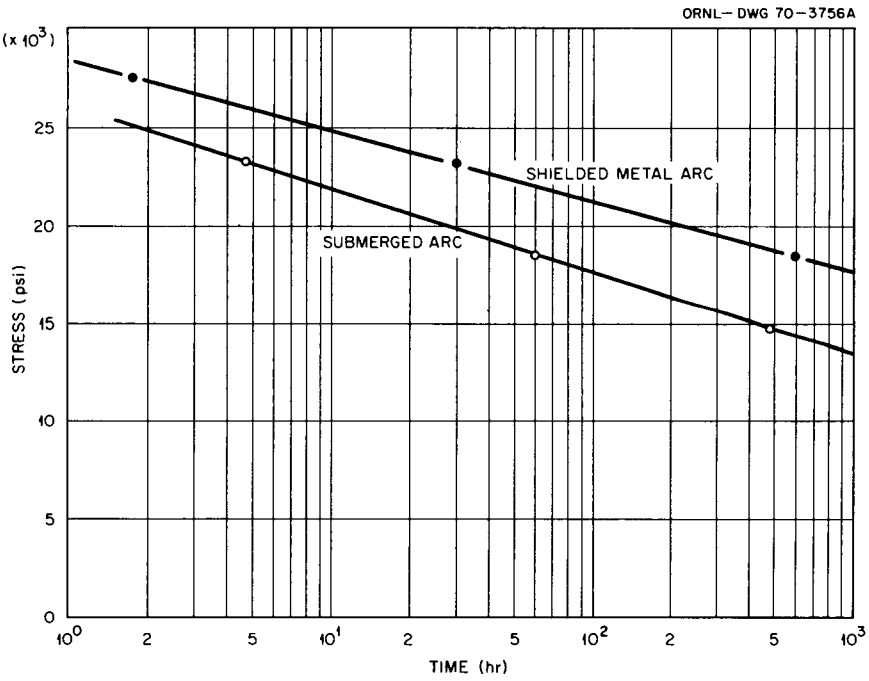

Fig. 7.2. Comparison of Creep-Rupture Properties of Submerged-Arc and Shielded Metal-Arc Welds in Stainless Steel. Base metal is type 304 stainless steel; filler metal is type 308 stainless steel. Specimens were tested as welded at 650°C (1200°F).

tested transverse specimens of all weld metal at 650°C (1200°F) as welded. The shielded metal-arc weld was significantly stronger than the submerged-arc weld.

We also tested specimens from the submerged-arc weldment that were heat treated either by a solution anneal at 1065°C or a solution anneal at 1065°C (1950°F) followed by a 10-hr aging treatment at 800°C (1470°F). The treatment at 800°C is designed to agglomerate carbides and avoid subsequent sensitization. The creep-rupture strengths at 650°C (1200°F) for these two conditions along with that for the as-welded condition are shown in Fig. 7.3, and the creep elongations are shown in Fig. 7.4. Figure 7.4 shows that all submerged-arc weld specimens had much better long-time creep ductilities than did the shielded metal-arc weld specimens. Both treatments after welding improved the creep ductility of the submerged-arc specimens without lowering the rupture strength. Examination of the data for creep from the tests at 14,000 psi showed an extension of third-stage creep due to annealing after welding with no change in deformation characteristics in the first or second stages. Similar tests are now under way at 595°C (1100°F).

Examination of the fracture surfaces of specimens from the submerged-arc weldment with a scanning electron microscope showed that a smaller portion of these was composed of the fracturing between different phases than in similar specimens from the shielded metal-arc weldment. Annealing after welding further reduced the amount of fracturing between phases. Figures 7.5 and 7.6 show the fracture surface of a test specimen as welded, and Fig. 7.7 shows that of a test specimen annealed after welding. We are using studies of this type to determine the mechanical behavior of the different types of welds and to enable us to predict the most favorable welding processes and conditions.

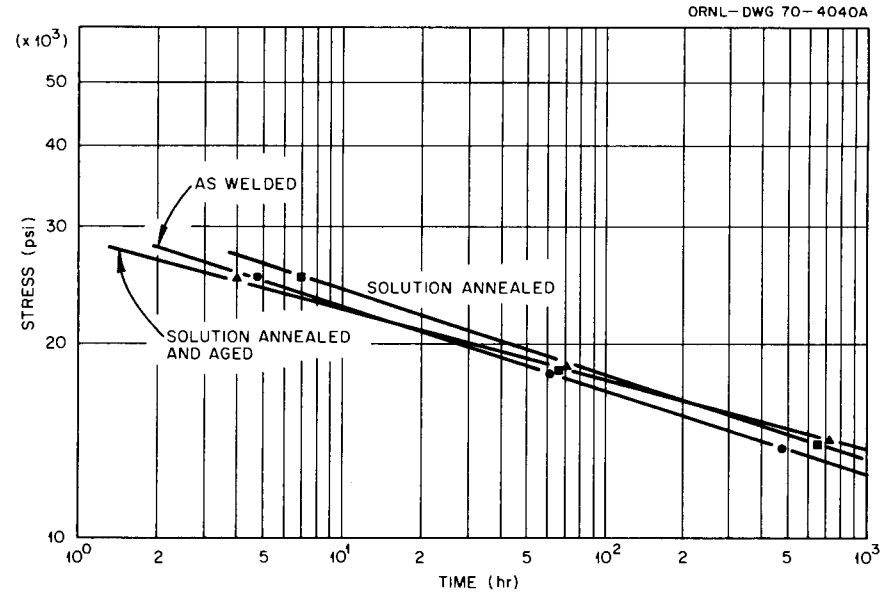

Fig. 7.3. Effect of Heat Treatment after Welding on Creep-Rupture Properties of Submerged-Arc Welds. Specimens of all weld metal were machined transverse to the weld direction and tested at 650°C (1200°F). Annealing was at 1065°C (1950°F) and aging was at 800°C (1470°F).

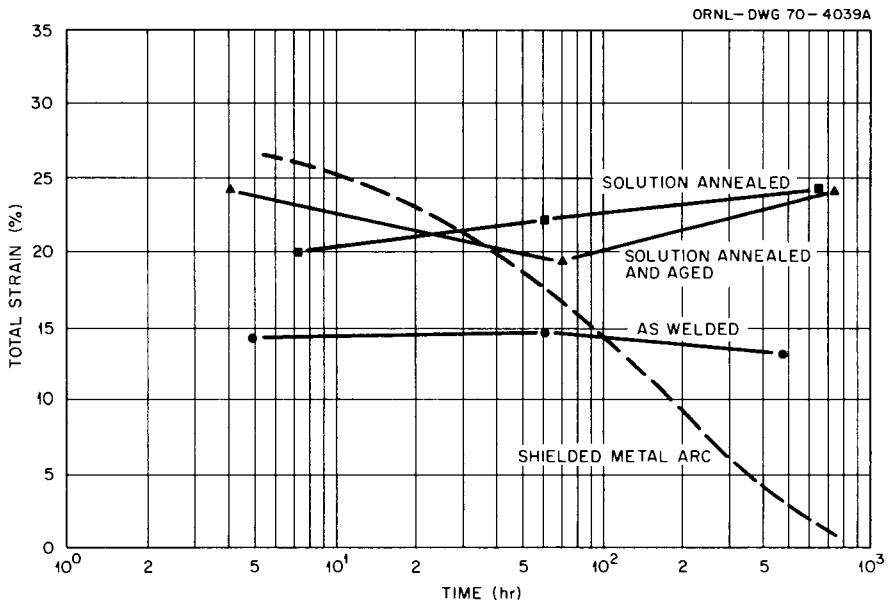

Fig. 7.4. Effect of Heat Treatment after Welding on Creep Ductility of Submerged-Arc Welds at 650°C (1200°F).

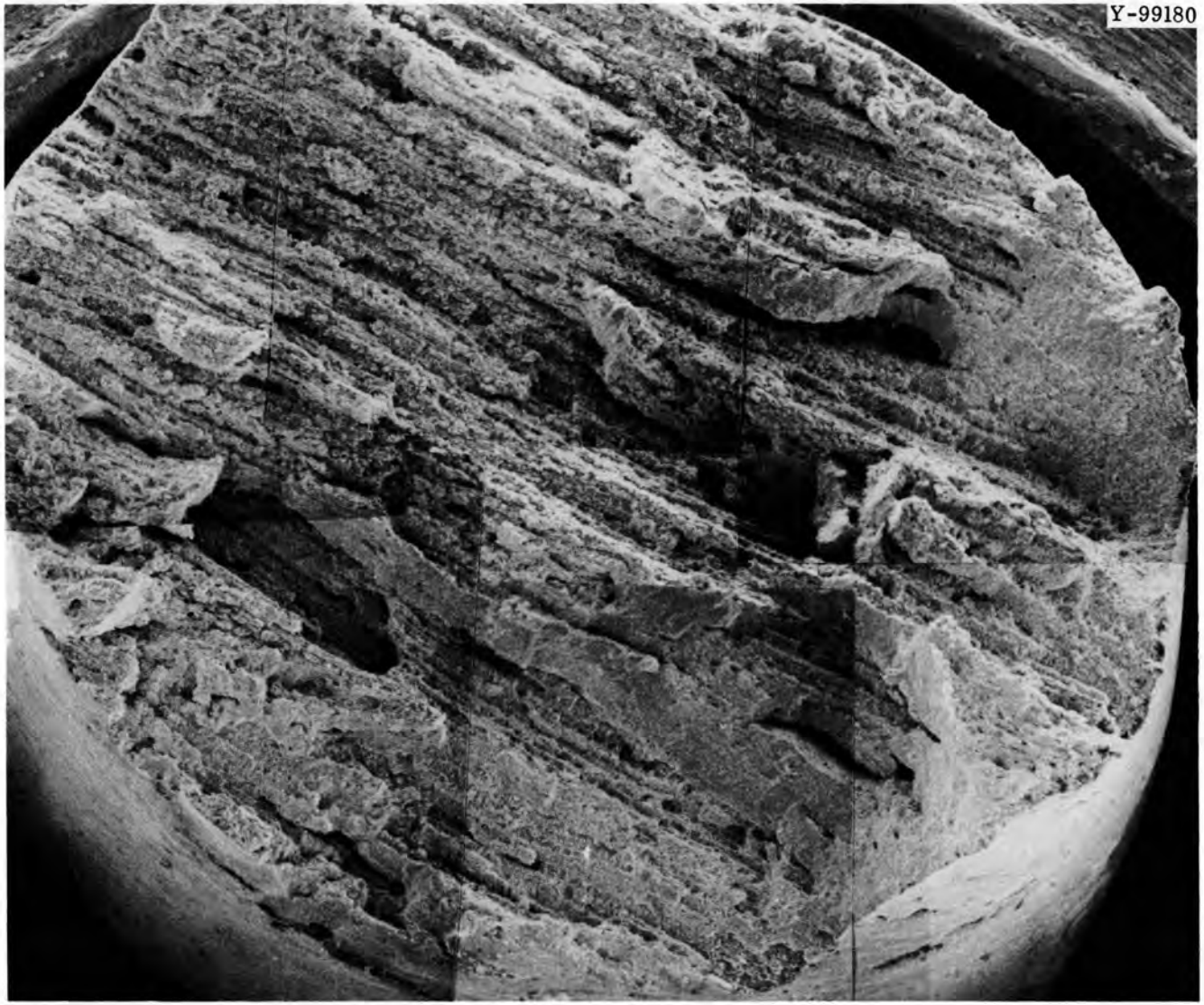

Fig. 7.5. Fracture Surface of Submerged-Arc Weld Metal. Specimen was tested at 650°C (1200°F) as welded. 100×.

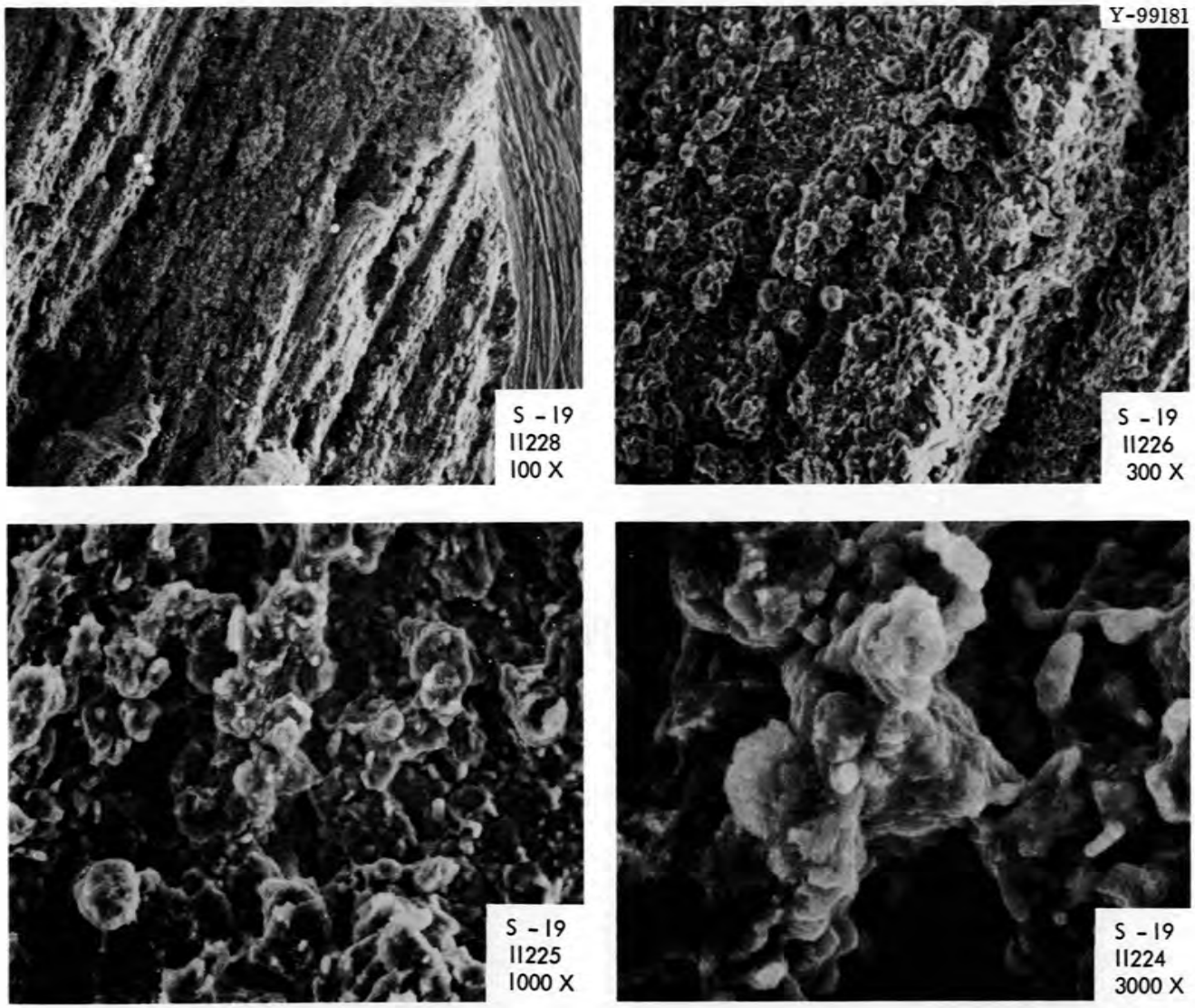

Fig. 7.6. Portions of Surface Shown in Fig. 7.5 that Fractured Between Phases.

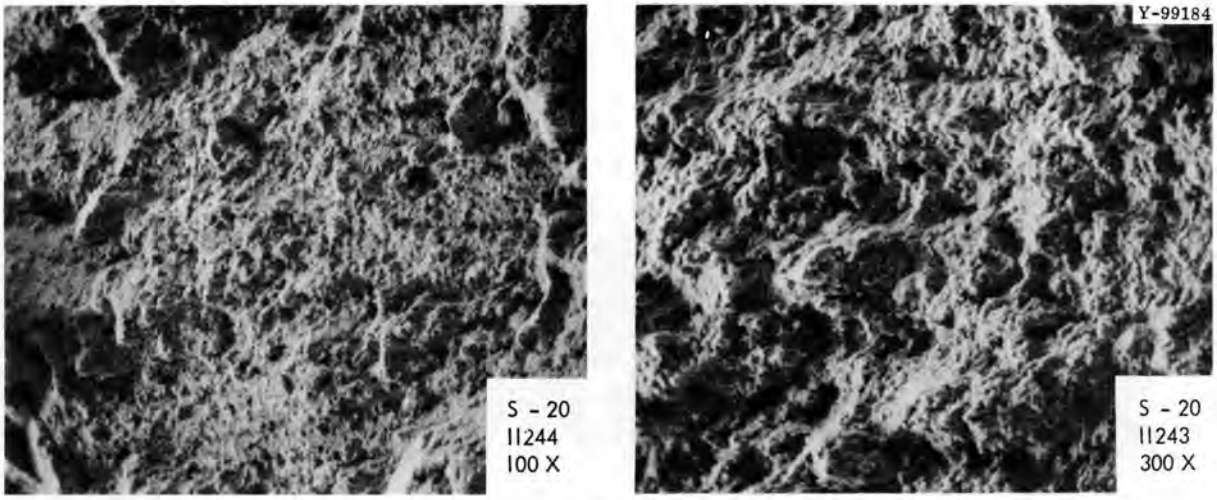

Fig. 7.7. Fracture Surface of Submerged-Arc Weld Tested Transverse to Weld Direction at 650°C (1200°F) after Solution Anneal at 1065°C (1950°F). This area of fracture surface reveals the suggestion of interphase fracture mode, but the specimen fractured in a ductile mode.

Notes

1. W. O. Harms and G. M. Slaughter, "Shielded Metal-Arc Welding for LMFBR Components," pp. 119–126, this report.

2. G. M. Goodwin, D. G. Harman, and Nancy C. Cole, Fuels and Materials Development Program Quart. Progr. Rept. Dec. 31, 1969, ORNL-4520, pp. 153–163.

3. N. C. Binkley, G. M. Goodwin, and D. G. Harman, Fuels and Materials Development Program Quart. Progr. Rept. Dec. 31, 1969, ORNL-4520, pp. 165–172.

8. SHIELDED METAL-ARC WELDING FOR LMFBR COMPONENTS

W. O. Harms G. M. Slaughter

The objective of this program is to evaluate the shielded metal-arc (stick electrode) welding process for fabricating and repairing certain stainless steel components for liquid-metal fast breeder reactors (LMFBR). We very slightly modified the flux coatings of electrodes and are determining the influence of minor elements on the mechanical properties of the weld metal at elevated temperature. Flux coatings traditionally have been evaluated and selected by the relative ease with which weld metal can be deposited, and bead contour, arc stability, and deposition efficiency are usually prime considerations. The effect of the coating on the properties at elevated temperatures has not been seriously considered.

As part of this effort, we are also providing weld specimens to Battelle Memorial Institute Pacific Northwest Laboratory (BNWL) for a program of irradiations for the Fast Flux Test Facility (FFTF).

Preparation of Weldment Samples for Irradiation and Control

Procurement and Machining of Samples for FFTF Irradiation Program (G. M. Goodwin)

The "prototypic" FFTF submerged-arc weldments[1] were completed and are now being examined nondestructively. The welds were prepared in 2-in.-thick plate under conditions identical to those used for the test welds previously made for BNWL. A double-welded joint eliminated the need for massive mechanical restraint. After inspection, these welds will be sectioned, heat treated, and machined into specimens for tests of mechanical properties and sent to BNWL for irradiation testing.

Effect of Variations in Flux Coating

Preparation and Creep-Rupture Testing of Weldments (N. C. Binkley, G. M. Goodwin, D. G. Harman)

Fractography and tests of mechanical properties were continued on the 14 stainless steel shielded metal-arc weldments made with type 308

stainless steel electrodes containing controlled minor differences in the type or composition of the coating. A simplified reference guide to the type of electrode coating and chemical anaysis of the weld deposit was presented previously.[2]

Optical metallography of welds 4 through 14 completed this phase of the study. Examination of both the weld metal and the fusion lines in these welds revealed virtually no difference from one weldment to the other. All attempts to find any unique microstructural features in one weldment as compared to the others were unsuccessful. It is very significant, therefore, that there are major differences in the creep-rupture behavior of the various welds at 650°C (1200°F).

We previously reported[2] results of creep-rupture tests at 650°C (1200°F) of welds made with electrodes that had the three standard types of coatings — lime, lime-TiO_2, and TiO_2. We had found that the weld made with the lime-coated electrode was consistently weaker than welds made with the other two types of electrodes. All three welds showed significant reductions in creep elongation with increasing rupture time, but the weld made with the electrode coated with lime-TiO_2 was the worst.

We conducted additional experiments to gain more information concerning the low ductility. We held a specimen from the weld made with the electrode coated with lime-TiO_2 in the test furnace at 650°C for 700 hr before applying a stress of 25,000 psi. Figure 8.1 shows the creep curve for this specimen compared with that for an identical specimen that was not held 700 hr at 650°C before testing. The aged specimen lost significantly in both rupture time and elongation. Table 8.1 lists the rupture life, elongation, and minimum creep rate for both specimens. Note that only the third stage of creep was significantly affected. Both specimens entered third-stage creep after about 0.5% elongation, but the aged specimen accelerated more quickly to high strain rates and fractured after only 2.8% third-stage deformation. The specimen that was not aged, on the other hand, survived to 9.7% third-stage elongation.

In these tests, the third stage of creep is essentially a fracturing process, and a significant percentage of the fracture occurs along the boundaries between austenite and ferrite.[3] The effect of thermal aging on the third-stage deformation, therefore, indicates a metallurgical

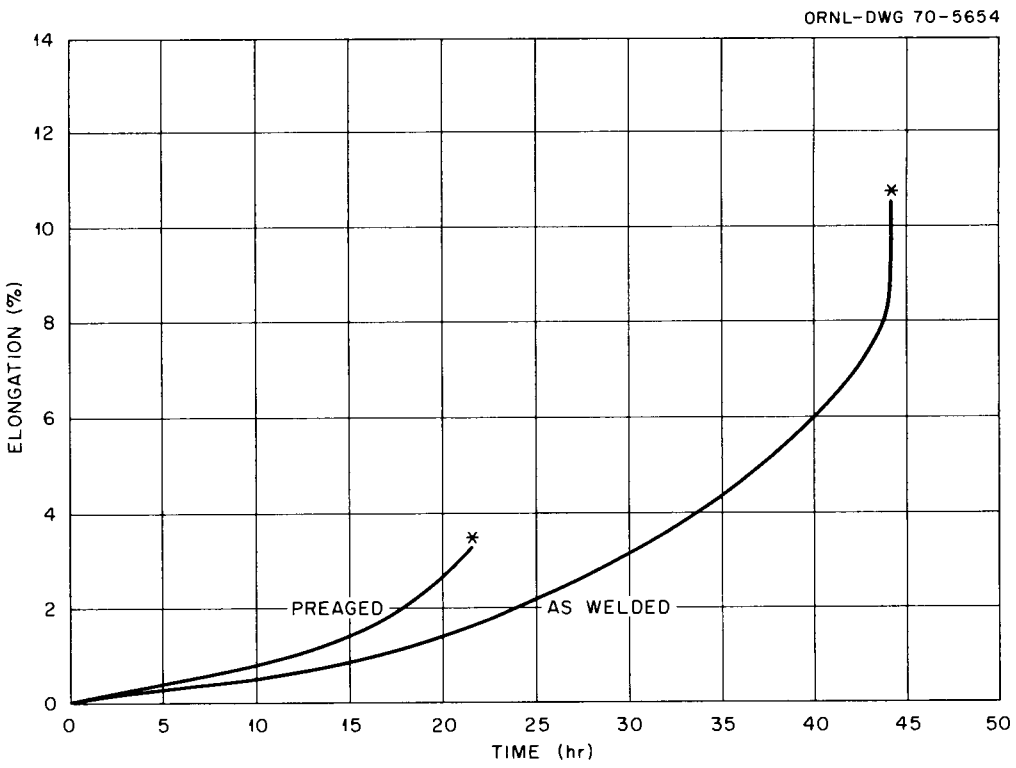

Fig. 8.1. Effect of Aging Before Testing on the Creep Behavior of Type 308 Stainless Steel Weld Metal at 650°C. Both specimens were from the standard weldment made with an electrode coated with lime-titania, had their axes parallel to the weld direction, and were tested at 25,000 psi. The aged specimen was held 700 hr at 650°C before loading.

Table 8.1. Effect of Aging Before Testing on Creep of Shielded Metal-Arc Weld Made with an Electrode with Commercial Lime-Titania Coating

	Creep Properties at 650°C (1200°F), 25,000 psi		
	Rupture Life (hr)	Total Elongation (%)	Minimum Creep Rate (%/hr)
Tested as welded	44	10.2	0.034
Held 700 hr at 650°C (1200°F) before test	22	3.3	0.034

instability of the ferrite at the substructure boundaries. Microprobe analyses[4] show that the ferrite typically contains about 26% Cr and is, therefore, susceptible to transformation to sigma phase at 650°C (1200°F), as shown by the Fe-Cr phase diagram. This has always been a problem in stainless steels, and its embrittling effect is well documented.[5]

Our fracture studies have also demonstrated the effect of longer rupture times on the percentage of fracture along substructure boundaries. Figure 8.2 compares the appearance of two specimens of weld metal after fracturing at 27 and 490 hr, respectively. The specimen that failed at the shorter rupture time showed a considerable amount of shear fracture connecting short segments of fracture between phases, while the specimen that failed after 490 hr fractured almost entirely along the phase boundaries. The fracture surface of a weld specimen that ruptured after 575 hr with only 0.14% elongation is shown in Fig. 8.3. Essentially the entire fracture surface was comprised of phase-boundary surface area.

Figure 8.4 shows the fracture surface of the aged specimen discussed above. We see that large portions of the surface fractured between phases. The comparable specimen that was not aged showed only small areas of this fracture mode.

We are also comparing the creep-rupture behavior of specimens machined from several of the welds made with electrodes that had controlled variations in the composition of their coatings. Table 8.2 lists the results from the tests conducted at 650°C (1200°F) and 18,000 psi The largest strengthening effects were caused by B, P, C, and Si, in that order. The S content, from 0.006 to 0.027%, had no apparent effect on creep properties. Lowering the level of C or Si improved creep ductility under these test conditions.

The significant effect of some compositional variables is illustrated by the case of C; Fig. 8.5 compares the creep curves obtained when weld specimens containing 0.035, 0.044, and 0.074% C are tested at 650°C (1200°F) and 18,000 psi. All three specimens entered third-stage creep after about the same amount of strain. The compositional effects on minimum creep rate and third-stage deformation, however, provide appreciable contributions to overall creep properties. Fractography showed

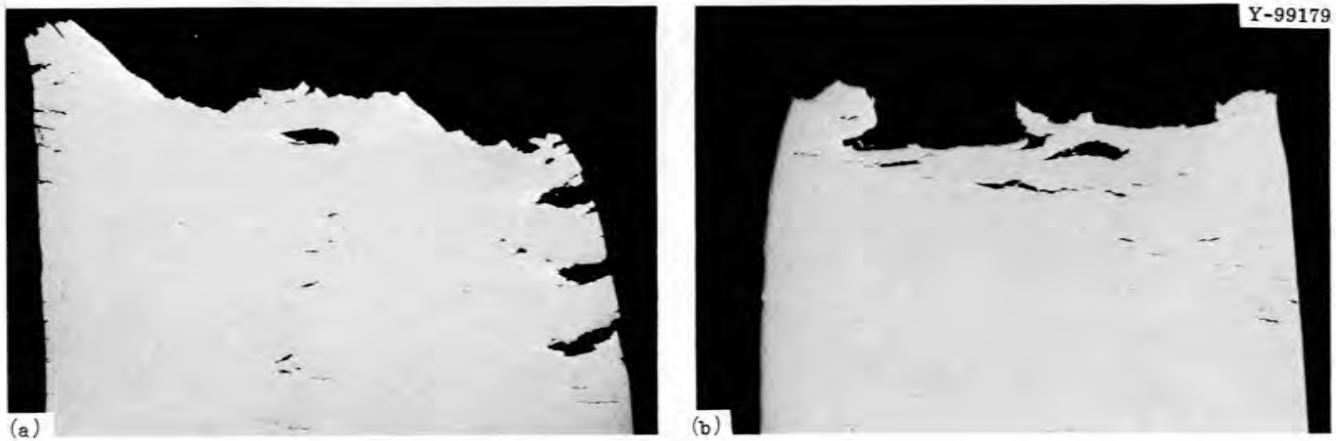

Fig. 8.2. Effect of Stress Level on Appearance of Fracture in Shielded Metal-Arc Weld Specimens Tested at 650°C (1200°F). (a) Specimen stressed 27 hr at 25,000 psi. (b) Specimen stressed 490 hr at 18,000 psi.

Fig. 8.3. Fracture Surface of Specimen of Shielded Metal-Arc Weld Metal Tested at 650°C (1200°F) that Failed after only 0.14% Elongation.

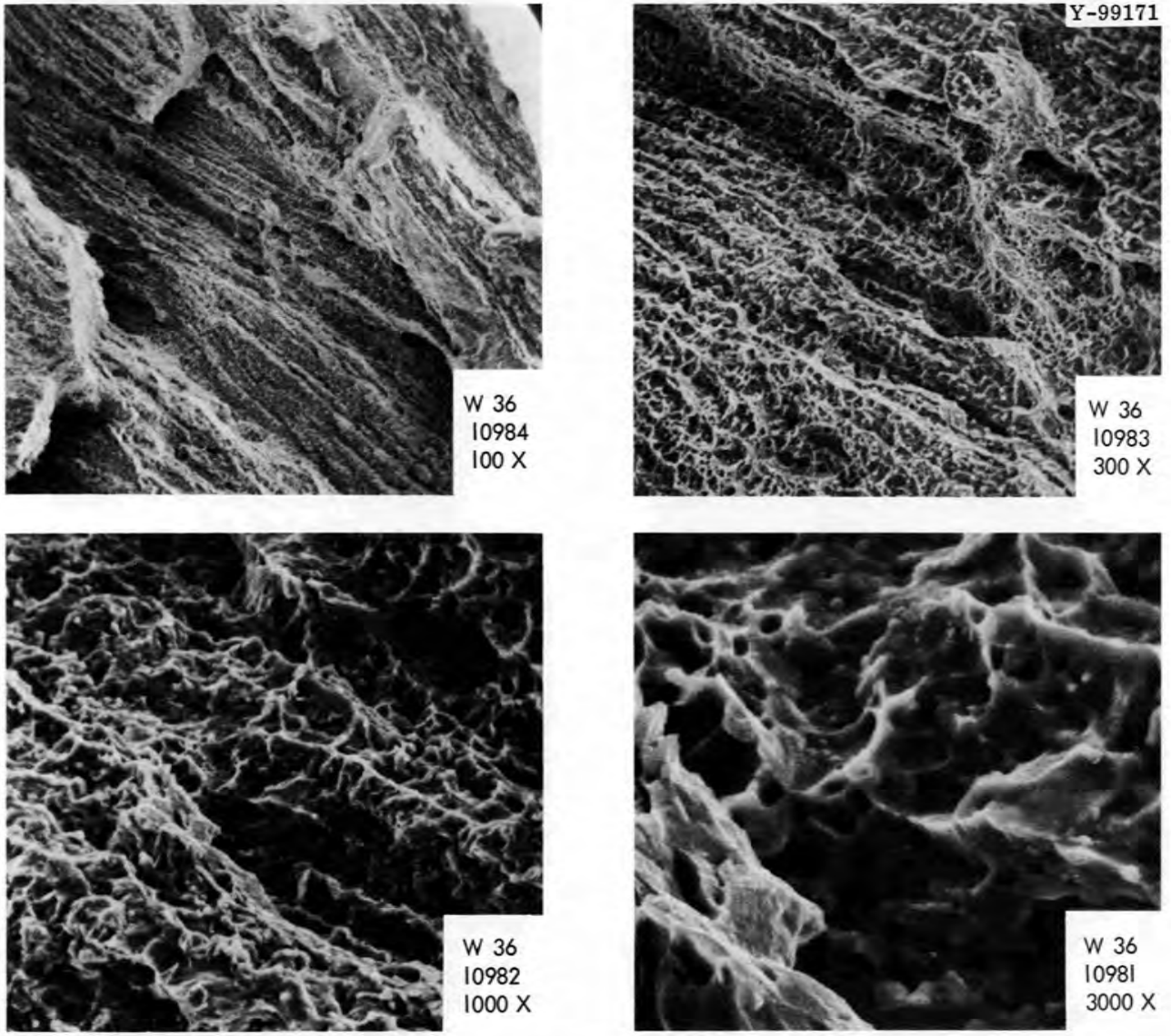

Fig. 8.4. Fracture Surface of Weld Specimen Aged 700 hr at 650°C Before Testing at 650°C (1200°F). A significant amount of fracture between phases is evident.

Table 8.2. Effect of Variation in Composition of Electrode Coating on Creep Properties of Shielded Metal-Arc Welds in Stainless Steel

Coating Variation	Creep Properties at 650°C (1200°F) and 18,000 psi		
	Rupture Life (hr)	Total Elongation (%)	Minimum Creep Rate (%/hr)
			$\times 10^{-4}$
Commercial lime-TiO_2 coating[a]	576	0.50	1.9
Low C (0.35%)	490	4.5	10
High C (0.74%)	1004	0.46	< 0.5
Low Si (0.29%)	592	3.2	
High Si (0.73%)	710	1.3	
Low P (0.009%)	b	b	b
Medium P (0.023%)	b	b	b
High P (0.034%)	1655	0.97	
Low S (0.006%)	526	0.75	8.3
High S (0.027%)	548	0.67	3.9
Medium B (0.004%)	2250+	c	
High B (0.006%)	b		

[a]The commercial lime-TiO_2 coating contains the following amounts of the elements considered in this study: 0.044% C, 0.47% Si, 0.012% P, 0.016% S, and 0.001% B.

[b]To be tested.

[c]Test in progress.

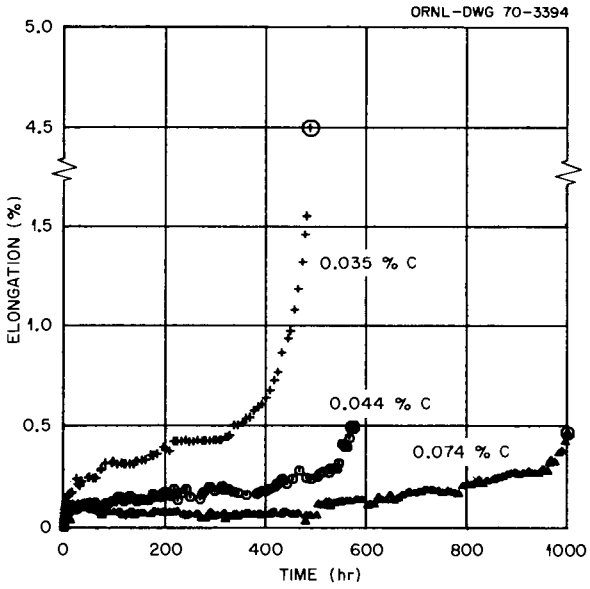

Fig. 8.5. Effect of Carbon Content on the Creep of Type 308 Stainless Steel Weld Metal at 650°C (1200°F) and 18,000 psi.

an increasing amount of shear fracture with decreasing C content for these three tests.

Mechanical testing of the remaining welds is continuing.

Notes

1. G. M. Goodwin, Fuels and Materials Development Program Quart. Progr. Rept. Dec. 31, 1969, ORNL-4520, p. 164.

2. N. C. Binkley, G. M. Goodwin, and D. G. Harman, Fuels and Materials Development Program Quart. Progr. Rept. Dec. 31, 1969, ORNL-4520, pp. 165–172.

3. We commonly refer to "fracture between phases" when the fracture path follows the boundaries between austenite and ferrite. It should be noted, however, that the solidification substructure boundaries represent regions of substantial solute segregation and will influence the fracture mode whether or not the degree of solute segregation is sufficient to promote the formation of the ferrite phase.

4. G. M. Goodwin and Nancy C. Cole, Fuels and Materials Development Program Quart. Progr. Rept. Sept. 30, 1969, ORNL-4480, pp. 109–110.

5. T. Lyman (ed.) Metals Handbook, 8th ed., pp. 591–592, vol I, American Society for Metals, Metals Park, Novelty, Ohio, 1961.

9. NONDESTRUCTIVE TESTING TECHNIQUES FOR LMFBR

W. O. Harms R. W. McClung

We are developing new methods, techniques, and equipment for nondestructively evaluating materials or components related to the liquid-metal fast breeder reactor (LMFBR). Among the methods studied are electromagnetic induction, ultrasonics, and penetrating radiation. Special emphasis is being given to developing techniques for measuring the degree of cold work in stainless steel tubing with a small diameter.

Development of Advanced Nondestructive Testing

Development of Eddy-Current Instrument (C. V. Dodd)

We are continuing the development of an eddy-current instrument for measuring both the size of defects and their depth below the surface. Construction of the modular phase-sensitive eddy-current instrument, whose modulues will be used in the new instrument, was completed.

Ultrasonic Schlieren Techniques for Evaluation of Welds (H. L. Whaley, Jr., K. V. Cook)

We are using the schlieren technique to study the interaction of ultrasonic pulses with discontinuities (flaws) in welds in 1-in.-thick butt-welded Al and stainless steel plates. The stainless steel welds are being examined and compared with the Al welds. Results for both sets of weld samples will then be compared to those obtained using conventional techniques of ultrasonic inspection of welds.

Measurement of Cold Work in Stainless Steel Tubing

Design and Construction of Impedance Bridge (C. V. Dodd, W. A. Simpson)

We are investigating methods for nondestructively measuring the degree of cold work in stainless steel tubing that has a small diameter. We emphasize the use of electromagnetic induction for detecting the changes in magnetic permeability produced by cold work.

We are now ordering or constructing components for the bridge circuits of the instrument. We have ordered an ac source and bridge resistor. We constructed a pair of coils with very low drift in inductance. They are mounted inside quartz tubes that are in turn mounted inside a large Al block to ensure that they have the same temperature. The total drift (resistive and inductive) was 0.0012%/°C as measured over a 36°C temperature change. We constructed a circuit to measure the difference between two ac signals to within an accuracy of 0.01% with a response from dc to 400 Hz. This will allow this technique to be applied to the high-speed testing of tubing (on the order of 200 fpm). We constructed an amplifier that seems to have the desired stability, although we cannot test it until we receive the ac source.

To aid in the initial adjustment of the bridge, we calculated both the magnitude and the phase of the anticipated coil voltages. We calibrated the phase-sensitive eddy-current instrument to measure these phase differences.

10. SODIUM CORROSION STUDIES

W. O. Harms J. H. DeVan

The purpose of this program is to investigate the chemical and metallurgical effects produced in structural materials during exposure to molten Na. The program is designed to guide the selection of container materials for liquid-metal-cooled fast breeder reactor (LMFBR) systems and provide guidelines for specifying insulating materials for use with stainless steel components in the Fast Flux Test Facility (FFTR).

Comparative Corrosion Tests on Refractory Alloys

J. H. DeVan

Although V alloys are highly resistant to dissolution by Na, they are quite reactive with nonmetallic impurities in Na, particularly with C, N, and O. Accordingly, we are investigating the mechanisms by which V alloys are attacked in Na at impurity levels typical of service conditions in a reactor. Our program is concerned with four basic aspects of the oxidation process for V alloys in Na: (1) the partitioning of O between V alloys and Na; (2) the effects of alloying additions of Cr and Zr on the diffusion coefficient of O in V; (3) the effects of Cr and Zr in V on the oxide formed and on the dissolution of the alloys in Na; and (4) the solubility of V in Na as affected by the presence of O in either metal. We are also examining the kinetics of the transfer of C, N, and O between V alloys and types 304 and 321 stainless steel in a Na circuit.

Effect of Oxygen on the Compatibility of Vanadium and Vanadium Alloys with Sodium (R. L. Klueh)

Static capsule tests are being used to study the effects of alloying additions on the oxidation behavior of V alloys in impure Na. Tests have now been completed on V–5% Cr, V–10% Cr, V–15% Cr, V–20% Ti, V–15% Cr, 5% Ti, Vanstar 7 (V–9% Cr–3% Fe–1.3% Zr–0.05% C), Vanstar 8 (V–8% Cr–10% Ta–1.3% Zr–0.05% C), and Vanstar 9 (V–6% Fe–5% Nb–1.3% Zr–0.05% C). Each alloy was encapsulated individually with an unalloyed V specimen

in a type 304 stainless steel container and exposed to Na with 2000 ppm O (added as Na_2O) for 100, 200, 300, and 600 hr at 600°C. As reported earlier,[1] all specimens after test had black surface scales of varying thicknesses and had gained weight.

Table 10.1 shows the change in O concentrations, as determined by fast-neutron activation analysis, for each alloy and its companion specimen of pure V. In all cases, the change in O concentration was commensurate with the observed change in weight, indicating that there was little or no mass transfer from the stainless steel capsule. Surface scales were scraped from several of the specimens and analyzed by neutron activation; V and Na were detected but not O. Several of the specimens will be checked further for changes in C and N.

The changes in O concentration with time confirmed our previous interpretation[1] of the change in weight; that is, there was migration of O from the V-Cr alloys to the V at longer test times. In the case of the V–20% Ti and V–15% Cr–5% Ti alloys, the movement of O was in the opposite direction, from the alloy to the V specimen.

Based on the diffusion rate of O in V and V-Cr alloys at 600°C, our calculations indicate that the redistribution of O should be essentially complete after 600 hr, at which time both alloys should have the same O activity. Therefore, the results for 600 hr can be used to compare the equilibrium distribution coefficients for O between Na and the V-Cr alloys with the O distribution coefficient for unalloyed V. We define the O distribution coefficient for the V-Cr alloys to be

$$\kappa^{V\text{-}Cr} = \frac{C_O^{(V\text{-}Cr)}}{C_O^{(Na)}} \qquad (10.1)$$

and that for unalloyed V to be

$$\kappa^{V} = \frac{C_O^{(V)}}{C_O^{(Na)}} \ , \qquad (10.2)$$

Table 10.1. Oxygen Concentration of Vanadium and Vanadium Alloys Exposed to Sodium Containing 2000 ppm of Oxygen at 600°C

Alloy	Time (hr)	Oxygen Concentration, ppm		
		Vanadium	Vanadium Alloy	
		After[a]	Before	After
V–5% Cr	100	5010	106	3850
	200	4630	130	3470
	300	4760		3280
	600	5060		3580
V–10% Cr	100	5390	89	2890
	200	5820	82	2840
	300	5310		2320
	600	6030		2810
V–15% Cr	100	6250	147	2280
	200	6360	123	1950
	300	6830		1740
	600	7080		1560
V–20% Ti	100	6220	840	3620
	200	5580		3640
	300	5200		4020
	600	4990	970	5070
V–15% Cr–5% Ti	100	6170	970	2780
	200	6220	1040	2950
	300	4150		2790
	600	4880		3100
Vanstar 7	100	5850	940	3010
	200	6790	980	2800
	300	5230		2930
	600	7540		3110
Vanstar 8	100	4930	750	4340
	200	4780	800	3390
	300	5100		3520
	600	4430		3690
Vanstar 9	100	6240	1040	5010
	200	5330	1120	4360
	300	4650		4110
	600	6050		4230

[a]Oxygen concentration before test was approximately 80 ppm.

where $C_O^{(V\text{-}Cr)}$, $C_O^{(V)}$, and $C_O^{(Na)}$ are the equilibrium concentrations of O in the V-Cr, V, and Na, respectively. It then follows that

$$\frac{\kappa^{V\text{-}Cr}}{\kappa^{V}} = \frac{C_O^{(V\text{-}Cr)}}{C_O^{(V)}} \quad . \tag{10.3}$$

Figure 10.1 shows the effect of Cr composition on the ratio of distribution coefficients in Eq. (10.3). The decrease in the ratio of $\kappa^{V\text{-}Cr}:\kappa^{V}$ with increasing Cr content can be attributed to the effect of Cr on the solubility of O in V (that is, Cr decreases the solubility of O in V). Figure 10.1 also compares our data with distribution coefficient ratios reported by Argonne National Laboratory.[2] We have not attempted to calculate distribution coefficient ratios for the alloys containing Ti or Zr, since the O content in these alloys undoubtedly is above the limit of solubility.[3]

Vanadium alloys with 1.3% Zr, 5% Zr, and 20% Mo were melted, cast, and rolled to 0.04-in. sheet, and these alloys are now being tested in capsules similar to those reported above.

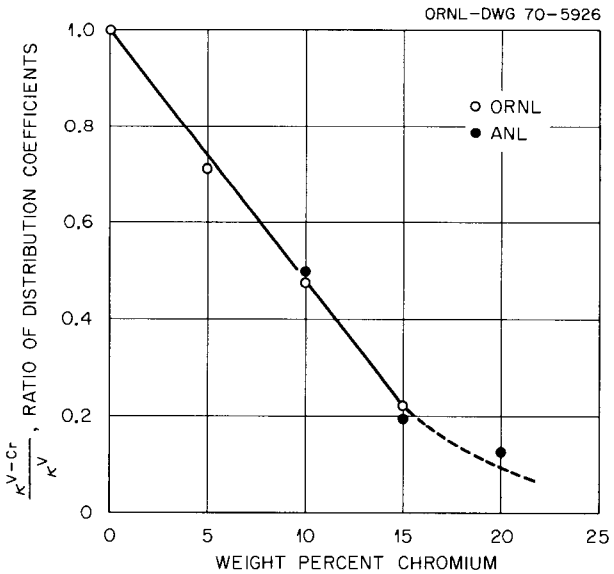

Fig. 10.1. The Effect of Chromium Concentration in Vanadium on the Distribution Coefficient for Oxygen Between Sodium and Vanadium at 600°C. (Ref. T. F. Kasnerr and D. L. Smith, Progress Report December 1969 Reactor Development Program, ANL-7655, p. 53.)

Interstitial Contamination of Vanadium and Its Alloys (H. Inouye)

An apparatus for determining the effects of O, C, and N on the creep properties of V alloys was placed into operation this quarter. The ion-pumped apparatus is capable of base pressures of 10^{-10} torr. The desired interstitial contaminant is added to the creep specimen during the test at a constant gas pressure by means of a controlled leak.

Sheet specimens of unalloyed V, 0.021-in. thick, were creep tested at 600°C under a load of 11,000 psi. The specimens before test contained 70 ppm C, 8 ppm N, and 130 ppm O and had been annealed for 1 hr at 900°C. Figure 10.2 shows the creep behavior (a) in vacuum of 3×10^{-9} torr, (b) in 5×10^{-7} torr O, and (c) after exposure to 5×10^{-7} torr O for 210 hr in the unstressed condition and then creep tested at 3×10^{-9} torr. The 210-hr exposure to 5×10^{-7} torr O before stressing was calculated to add about 340 ppm O, based on the assumption of a contamination rate of 1.6 ppm hr^{-1} (ref. 4).

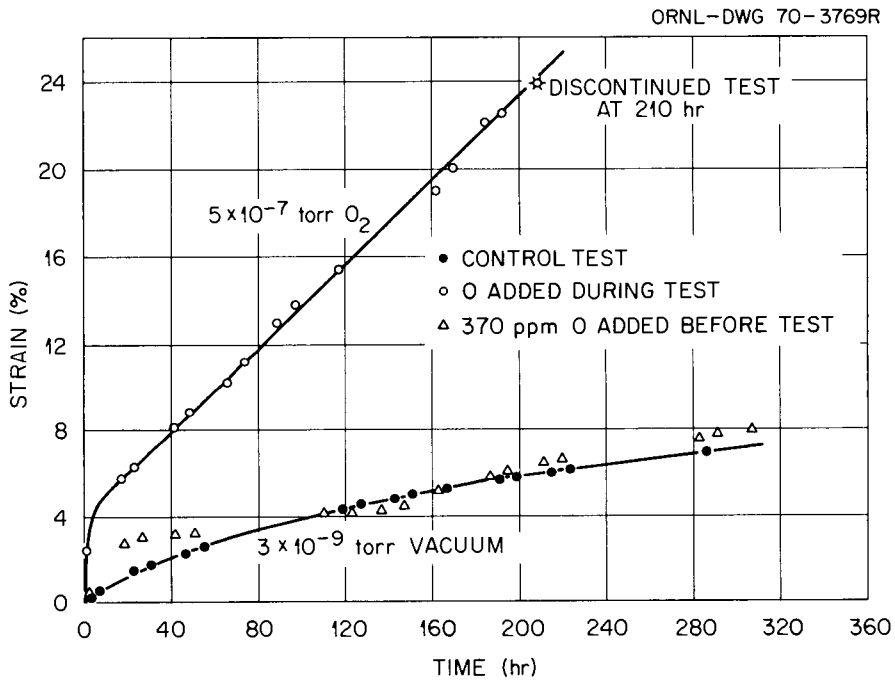

Fig. 10.2. Creep Behavior of 0.021-in.-thick Vanadium Sheet in Vacuum and Low-Pressure Oxygen. Specimens were creep tested at 600°C at a stress of 11,000 psi.

The results in the vacuum environment show that the addition of O to the V before test had little effect on the creep properties after the first 100 hr of test. However, if O is added to the specimen during the creep test, the creep rates in O are higher than in vacuum by a factor of 7.5, and the time required to produce 2% strain decreases by a factor of about 28. A creep strain of 24% without fracture indicates that 470 ppm O (340 + 130) does not impair the rupture ductility.

Mass Transfer of Interstitial Impurities Between Vanadium Alloys and Type 304 Stainless Steels (D. H. Jansen)

We are operating a series of thermal convection loops to determine the extent of interstitial mass transfer between V and stainless steel in Na. The heated portion of each loop is constructed of V, and the cooled portion is of either type 304L or type 321 stainless steel. Two tests of 3000 hr were completed, and the results are being evaluated. A third loop is in operation under the conditions shown below:

Temperature, °C	
Heater inlet	610
Heater outlet	710
Rate of Na flow	
fpm	7.7
g/min	370
Chamber pressure, torr	2×10^{-8}
Surface area of V tubing, in.^{2}	67
Surface area of type 304 stainless steel tubing, in.^{2}	102
Surface area of specimens, in.^{2}	
V + V–10% Cr	9
Type 304 stainless steel	9
Scheduled operation, hr	3000

In the first bimetallic loop[5] in this test series, one-fifth of the loop surface was V and four-fifths was type 304L stainless steel. Seven V inserts and three stainless steel inserts (pictured in Fig. 10.3) were stacked end to end along the heated V leg. This pattern was reversed in

ORNL-DWG 70-6525

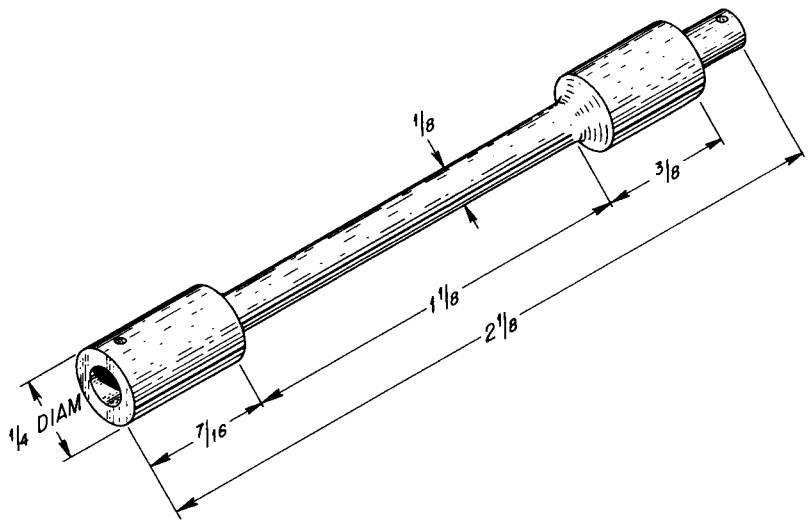

Fig. 10.3. Schematic Drawing of Buttonhead Inserts Used to Study Corrosion and Tensile Properties in Bimetallic Thermal-Convection Loop Test.

the cooled, stainless steel leg to include seven stainless steel inserts and three V inserts.

The temperatures and weight changes of these insert specimens are compared in Fig. 10.4. All V specimens gained weight with increasing temperature. The stainless steel specimens lost weight at the higher loop temperatures and gained a slight amount of weight at lower temperatures. The distance traveled by the Na appeared to have little effect on the weight gained by the V specimens; specimens at equivalent temperatures gained the same weight whether they were located in the heated (V tubing) or cooled (stainless steel tubing) leg.

As expected, the changes in the weights of the V inserts correlated closely with changes in the concentration of interstitial impurities. Small cylindrical slices were cut from the gage section (Fig. 10.3) of selected specimens and were analyzed by vacuum fusion for changes in O, C, N, and H. As shown in Table 10.2, the O, N, and C contents of each V specimen increased during test. The change in C concentration was nearly the same at all insert positions, while the changes in O and N concentrations increased with increasing loop temperature.

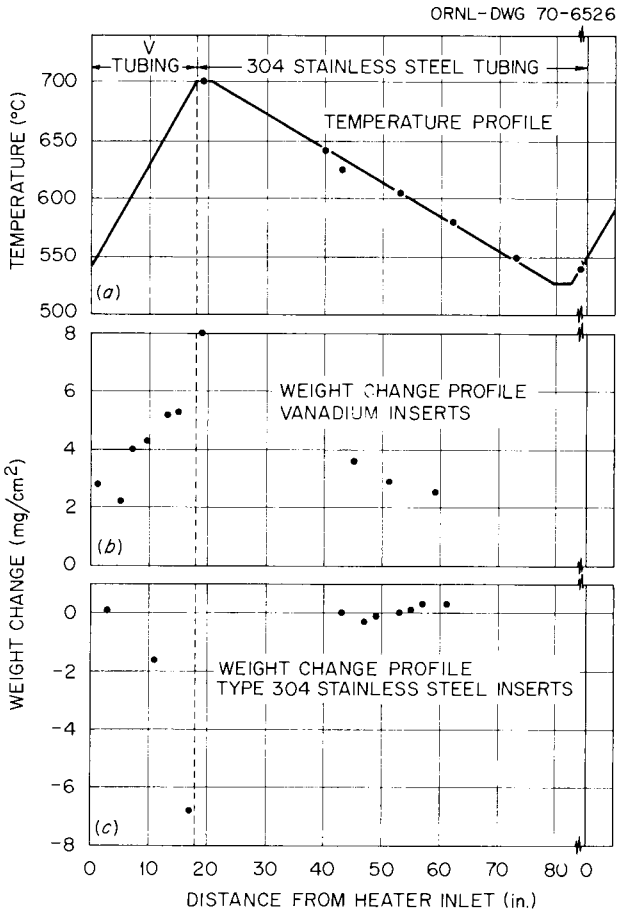

Fig. 10.4. Loop Temperatures and Specimen Weight Changes as Functions of Loop Position. (a) Loop temperatures as determined by Chromel-P vs Alumel Thermocouples, (b) weight changes of vanadium specimens, and (c) weight changes of stainless steel specimens.

Table 10.2. Interstitial Content and Tensile Properties at Room Temperature of Vanadium Specimens After Exposure to Sodium for 3000 hr

Specimen Temperature, °C (in Sodium)	Elongation (%)	Strength Properties, psi		Interstitial Content, ppm		
		Yield[a]	Tensile	O	N	C
		× 10^3	× 10^3			
550	30.0	18.1	29.9	270	120	250
587	35.5	22.4	31.6	390	150	250
603	25.5	30.4	41.4	870	140	220
630	34.0	24.4	34.8	530	180	280
700	25.0	28.7	45.6	630	240	290
As-received	40.0	13.6	29.6	140	7	110

[a]At 0.2% offset.

The results of similar chemical analyses of the stainless steel specimens are shown in Table 10.3. The O and N contents of the stainless steel inserts changed very little, but the C content decreased at all insert positions. The weight losses experienced by the stainless steel inserts near the heater exit are larger than can be ascribed to interstitial changes. Furthermore, the slight weight gains of the stainless steel specimens in cooler regions are counter to the interstitial changes. Thus, in the case of stainless steel, movement of interstitial impurities appears to have been accompanied by mass transfer of metallic elements.

Table 10.3. Interstitial Content and Tensile Properties at Room Temperature of Type 304L Stainless Steel Specimens Exposed to Sodium for 3000 hr

Specimen Temperature, °C (in Sodium)	Elongation (%)	Strength Properties, psi		Interstitial Content, ppm		
		Yield[a]	Tensile	O	N	C
		$\times 10^3$	$\times 10^3$			
567	47.0	56.8	99.4	170	270	220
580	45.0	57.0	99.4	170	290	250
600	49.5	55.8	99.4			
635	47.0	55.8	99.4	110	260	330
695	46.0	55.8	101.1	150	280	270
Control	49.0	55.0	99.1	180	280	300

[a]At 0.2% offset.

The increase in the O content of the V specimens was too high to be attributed to O impurities in the Na, which was hot trapped before test. It is likely that O was partitioned between the V heater tube, which initially contained 1300 ppm O, and the V specimens, which initially contained only 140 ppm O.

Selected insert specimens were tensile tested at room temperature to determine the effects of interstitial concentration changes on mechanical properties. Results for the V specimens are shown in Table 10.2. In the case of the maximum interstitial change, which occurred nearest the heater outlet, the elongation at fracture was 25%

after test compared to 40% before test, and the yield strength was 28,700 psi compared to 13,600 psi before test. Table 10.3 shows the corresponding tensile properties of selected stainless steel inserts. The elongations and yield strengths of these specimens changed very little from the values obtained before test.

Interactions of Sodium with Nonmetallic Materials

J. H. DeVan

Compatibility of Stainless Steel and Insulation for LMFBR Systems (C. D. Bopp[6])

The service temperatures of Na-cooled fast breeder reactors are considerably above those of present-generation power reactors. Among the potential problems associated with higher operating temperatures are the possible interaction of thermal insulation with reactor construction materials and the oxidation of the construction materials in the event of a Na leak. Accordingly, we are studying the reaction of commercial insulating materials with austenitic stainless steels between 370 and 760°C. A related study deals with the effect of Na on the oxidation of stainless steels, both insulated and uninsulated.

Oxidation of Insulated Stainless Steel. — We are evaluating the resistance of couples of stainless steel and insulation to oxidation at 760°C in an atmosphere of 99% N_2, 1% O_2, and 100 ppm (by weight) moisture. Table 10.4 compares recent experiments in this N_2 atmosphere with low moisture content to earlier experiments[7] in moist air. After 2700 hr at 760°C, the oxidation of type 316 stainless steel is greater by almost a factor of 10 in moist air than in the N_2 mixture. In contrast, type 304L stainless steel shows an oxidation rate in both environments which is comparable to that of type 316 stainless steel in the N_2 mixture. Because of their high Cr contents, both stainless steels form scales that are normally protective at the 760°C test temperature. During prolonged heating, however, the metal in the vicinity of grain boundaries may become depleted of Cr because of precipitation of carbides and other Cr-rich phases. Data obtained in boiling nitric acid[8]

Table 10.4. Comparison of Oxidation of Stainless Steel in Impure Nitrogen and in Moist Air After 2700 hr at 760°C

Type Stainless Steel[a]	Metal Loss After Descaling,[b] mg/cm^2	
	Low Moisture N_2 Atmosphere[c]	Moist Air[d]
304L	0.83	1.3
304	0.82	
304H	0.80	
316L	1.4	
316	1.7	12–15

[a]The specimens were pipe or tubing that had been annealed by the fabricator. The surfaces of the specimens were chemically polished before test.

[b]The alkaline permanganate descaling method was used [Ref. Materials Protection 6(7), 69–72 (July 1967).]

[c]The composition of this atmosphere was 99% N_2, 1% O_2, and 100 ppm (by weight) moisture.

[d]Air saturated with water vapor at 20°C.

indicate that 760°C is above the range of sensitizing temperatures for type 304L but not for type 316 stainless steel. Thus, one explanation for the lower resistance to oxidation of the type 316 stainless steel at 760°C may be associated with precipitation of Cr-rich phases and the attendant depletion of Cr from regions that adjoin the grain boundaries.

Effect of Sodium on the Oxidation of Stainless Steel. — We are conducting experiments to determine the effect of a Na leak on the oxidation behavior of austenitic stainless steels.[9,10] Currently we are evaluating the effect of leak size on the rate at which Na escapes and on the interaction of Na with type 304L stainless steel and thermal insulation. The tests are conducted at 760°C in an atmosphere of 99% N_2, 1% O_2, and 100 ppm (by weight) H_2O.

In the first two tests in this series, the Na leaks were small, circular holes drilled in the 1/4-in.-diam tube that served as our test specimen. Sodium was ejected through the hole after the tube had reached the desired temperature. In the third test the leak was a small, transverse

crack formed by repeatedly bending the specimen. The tube with the defect was filled with Na and brought to the test temperature with Na on the inside edges of the crack. We recently completed a fourth test under conditions similar to those of the third test but with a much smaller crack. Before testing, pressurization of the fourth test specimen with Ar produced a leak rate of only 0.0002 atm cm^3/sec (compared to 0.7 atm cm^3/sec for the third test).

As we had observed in the third test, no leakage of Na occurred as the fourth test was heated to 760°C. We attribute this to the formation of solid Na_2O within the crack. After reaching temperature, the Na in the tube was pressurized to 250 psig under a static head of Ar. We observed no evidence of Na leakage for 200 hr; then the O_2 and H_2O concentrations of the external, enclosed atmosphere decreased sharply. Leakage of Na continued for about 20 hr. The 250-psi internal pressure was maintained for an additional 10 hr, and, when no further leakage occurred, the test was discontinued.

The appearance of the defected tube after the test is shown in Fig. 10.5(b) and (c). The defect was covered by a ball of Na_2O about 1 in. in diameter [Fig. 10.5(b)]. The thermal insulation (colloidal silica) surrounding the tube had been pushed back by the ball, and there appeared to be little if any reaction of the insulation with the Na. Removal of the Na_2O residue revealed that the original defect had enlarged greatly, as may be seen by comparing Fig. 10.5(a) and (c), and there was evidence of heavy oxidative attack over the entire area of the tube that had been covered by Na_2O.

There are striking differences between the results of the third and fourth tests. As would be expected, the larger crack in the third test resulted in a quicker release of Na and allowed a greater mass of Na to escape (6 vs 1.5 g). However, despite the greater leakage in the third test, there was almost no interaction of Na or Na_2O with the wall of the tube, and essentially all of the Na reacted with the surrounding insulation. Thus, it would appear that slow seepage of Na can be more damaging in terms of external oxidation than rapid expulsion of Na through a crack and into a "sink" such as thermal insulation.

Photo 99623

Fig. 10.5. Fourth Sodium Leak Test. (a) Defect before test. 30×. (b) Sodium oxide ball on tubing (the defect was approximately at the center of the ball.) 1.5×. (c) Defect after test (sodium oxide ball removed). 7×.

Notes

1. R. L. Klueh, Fuels and Materials Development Program Quart. Progr. Rept. Dec. 31, 1969, ORNL-4520, pp. 176–177.

2. T. F. Kasnerr and D. L. Smith, Progress Report December 1969 Reactor Development Program, ANL-7655, p. 53.

3. R. L. Klueh and J. H. DeVan, The Oxidation of Vanadium and Vanadium Alloys in Sodium, ORNL-TM-2827 (March 1970).

4. R. L. Wagner, Fuels and Materials Development Program Quart. Progr. Rept. Dec. 31, 1969, ORNL-4520, pp. 179–180.

5. J. H. DeVan and D. H. Jansen, Fuels and Materials Development Program Quart. Progr. Rept. March 31, 1969, ORNL-4420, pp. 90–92

6. On loan from Reactor Chemistry Division.

7. C. D. Bopp, Fuels and Materials Development Program Quart. Progr. Rept. March 31, 1969, ORNL-4420, pp. 92–100.

8. H. F. Ebling and M. A. Scheil, "Time-Temperature-Sensitization (TTS) Diagrams for Types 347, 304L, and 316L Stainless Steels," pp. 275–284 in Advances in the Technology of Stainless Steels and Related Alloys, ASTM Spec. Tech. Publ. 369, American Society for Testing and Materials, Philadelphia, 1965.

9. C. D. Bopp, Fuels and Materials Development Program Quart. Progr. Rept. Sept. 30, 1969, ORNL-4480, pp. 125–128.

10. C. D. Bopp, Fuels and Materials Development Program Quart. Progr. Rept. Dec. 31, 1969, ORNL-4520, pp. 183–185.

11. DEVELOPMENT OF FAST-REACTOR NEUTRON-ABSORBER MATERIALS

G. M. Adamson, Jr. W. R. Martin

The prime candidate material for the safety and shim rods in the Fast-Flux Test Reactor (FTR) and liquid-metal-cooled fast breeder reactor (LMFBR) is boron carbide pellets in a stainless steel cladding. In spite of the widespread use of boron carbide as a neutron absorber in thermal reactors, basic data have never been obtained. The material has never been fully characterized for structure, homogeneity range, effect of fabrication variables, and the effects of varying composition. The objective of our work is to characterize the material sufficiently to provide measurable control parameters to properly evaluate fabrication techniques, compatibility experiments, and the effects of irradiation. The irradiation studies will emphasize basic effects of materials variables in both thermal and fast-reactor environments. A secondary effort of this program will be the preliminary characterization of alternate materials that possess possible advantages over boron carbide for use in fast reactors.

Characterization of Boron Carbide

Structural Changes that Result from Annealing of Powders (G. L. Copeland)

A series of powder samples was vacuum annealed at temperatures from 1300 to 2000°C for 1 hr to determine the amount of voids produced in the Norbide 325F powder at these temperatures. In order to minimize errors, a large sample (4 g) was used. The toluene pycnometer density of each sample was determined before and after annealing; a graphite boat was used to minimize contamination. The density before annealing ranged from 2.498 to 2.510 g/cm^3, but the average of 2.506 g/cm^3 was used for the starting density in each case. The results are shown in Table 11.1. A little over 6% voids was produced by 1 hr at 1500°C, and there was a very small increase in voids at 2000°C. These results indicate that the density increases previously reported[1] for high-temperature annealing may have been due to contamination by the crucible material. A sample

Table 11.1. Void Volume Created in Norbide 325F Boron Carbide Powder During Annealing at Various Temperatures

Annealing Temperature[a] (°C)	Powder Density After Annealing		Void Volume Created During Annealing[c] (%)
	(g/cm^3)	Percent of Original[b]	
1300	2.449	97.7	3.3
1500	2.348	93.7	6.3
1850	2.347	93.7	6.3
2000	2.340	93.4	6.6

[a]Optical pyrometer reading. The 4-g samples were annealed in 10^{-5} torr air for 1 hr in a graphite crucible.

[b]Based on the average toluene pycnometer density of 2.506 g/cm^3 before annealing.

[c]Percent void volume equals 100% minus percent of original density.

of the earlier material was submitted for mass spectrographic analysis to check this.

We attempted to determine the density of boron carbide powder by use of heavy liquids. Mixtures of tribromomethane ($CHBr_3$) and carbon tetrachloride (CCl_4) were prepared to densities of 2.375, 2.464, 2.495, and 2.514 g/cm^3. The results of experiments with some annealed and as-received Norbide 325F are shown in Table 11.2. Since the individual powder particles have different densities, the heavy-liquid technique cannot be used to determine the density of a powder sample. The results do confirm what metallography indicated, that only a portion of the particles form voids during annealing. We did not attempt to determine quantitatively the fractions of powder that floated and sank. However, since in most cases there was a very distinct segregation of the powders in the heavy liquid, this should be a good technique for separating the particles that contain voids (or attached carbon) if this is desirable.

The powders that were vacuum annealed for the density measurements were vacuum hot pressed at 2000°C to 0.020-in.-thick disks for thinning

Table 11.2. Density Checks of Boron Carbide Powders Using Heavy Liquids

Liquid Density[a] (g/cm^3)	Powder[b]		Results
	Annealing Temperature (°C)	Toluene Pycnometer Density (g/cm^3)	
2.375	1300	2.449	Some floated, some sank.
	1500	2.348	Some floated, some sank.
	1850	2.347	Some floated, some sank.
2.464	As received	2.506	Most floated, some sank.
	1300	2.449	All floated.
	1500	2.348	Most sank, some floated.
	1850	2.347	Most sank, some floated.
2.495	1300	2.449	Sample strung out from top to bottom.
	1500	2.348	Most floated, some sank.
	1850	2.347	Most floated, some sank.
2.514	1300	2.449	All floated.
	1500	2.348	All floated.
	1850	2.347	All floated.

[a] Mixtures of $CHBr_3$ and CCl_4. Density determined by pycnometer.

[b] Norbide 325F boron carbide vacuum annealed in graphite crucible for 1 hr at given temperature.

experiments for transmission electron microscopy. The powders were heated to 2000°C, immediately pressed, and then allowed to cool. The disks were examined metallographically to determine if the void sizes produced by the anneals at lower temperatures were stable. The microstructures in Fig. 11.1 show that the voids produced by annealing were not stable at higher hot-pressing temperatures. This behavior was expected. The powders as received and after annealing at 1300°C show the same void size and distribution after hot pressing. The powders annealed at 1500 and 1850°C show a larger void size. The powders annealed at 2000°C show larger voids after hot pressing and a much lower number of voids. This may indicate that the voids are coalescing, migrating to the interparticle voids, or both. The white particles in the disks are from a zirconia wash that was applied to the punches but that mixed with the thin layer of loose powders. Because of the low density of these disks, we are using slices from a larger pellet with higher density for electron transmission microscopy.

We annealed blends of B and C with Norbide 325F powder at 1500 and 2000°C to produce powders with ratios of B:C of 5.0 and 3.0. Microstructures of the powders are shown in Fig. 11.2. The B and C appear to have reacted completely with the boron carbide. The void formation confirms our previous conclusion.[2] The B essentially eliminated void formation during annealing, while the C increased void formation. The pore size is greater after annealing at 2000°C than at 1500°C.

Irradiation Behavior of Boron Carbide

X-Ray Diffraction Study of Irradiated Boron Carbide (V. J. Tennery, G. L. Copeland)

We refined a technique for producing Debye-Scherrer x-ray patterns of irradiated boron carbide material. Although the residual activity of the irradiated boron carbide is low, the long exposures normally required to produce the patterns darkened the film. This residual gamma level required careful tailoring of the intensity of the x-ray beam in order to produce the diffraction lines on the film before the residual activity severely blackened the film and resulted in loss of weak lines

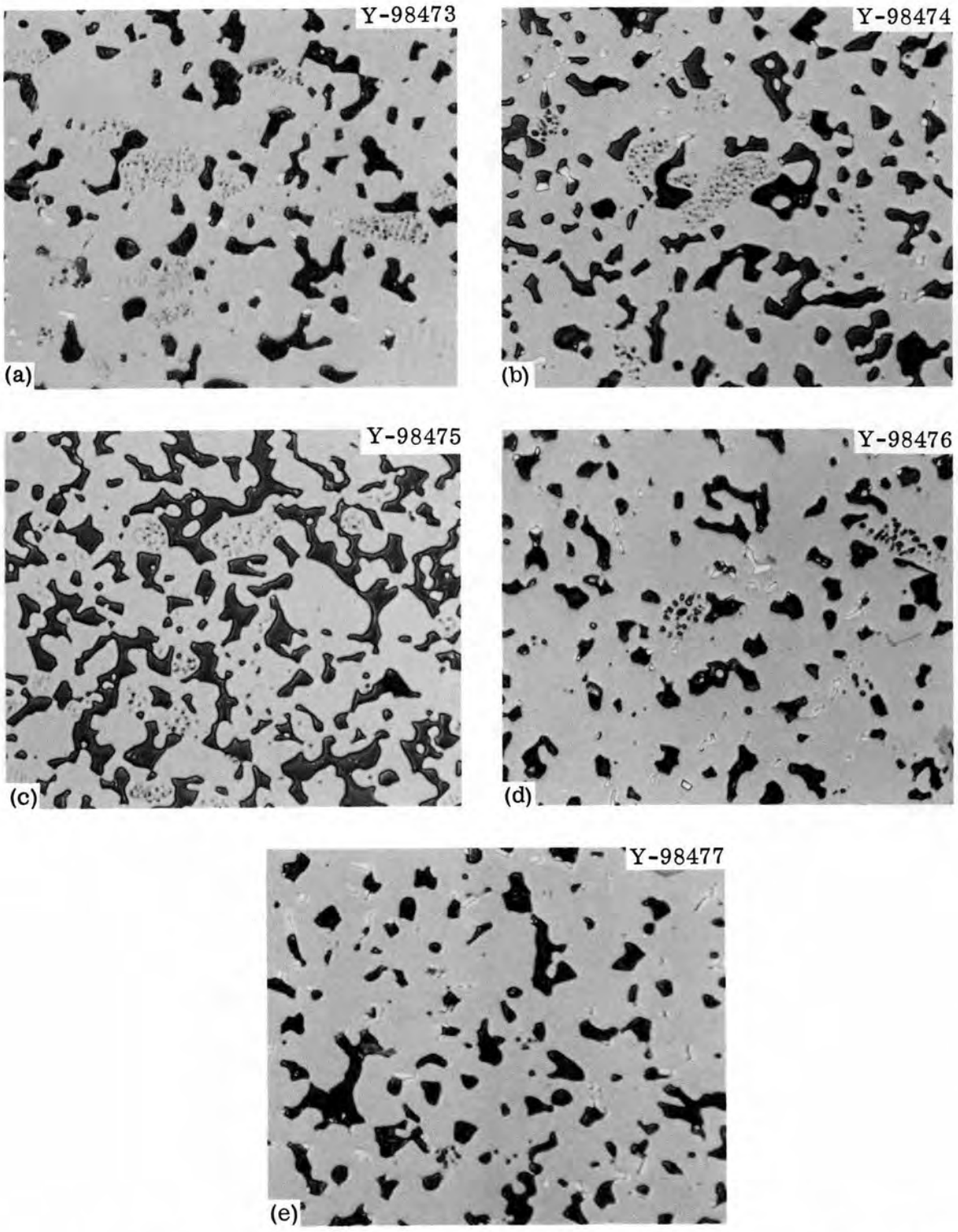

Fig. 11.1. Microstructure of Boron Carbide Hot Pressed at 2000°C from Norbide 325F Powder. (a) As received, (b) annealed at 1300°C, (c) annealed at 1500°C, (d) annealed at 1850°C, and (e) annealed at 2000°C. As polished. 500×.

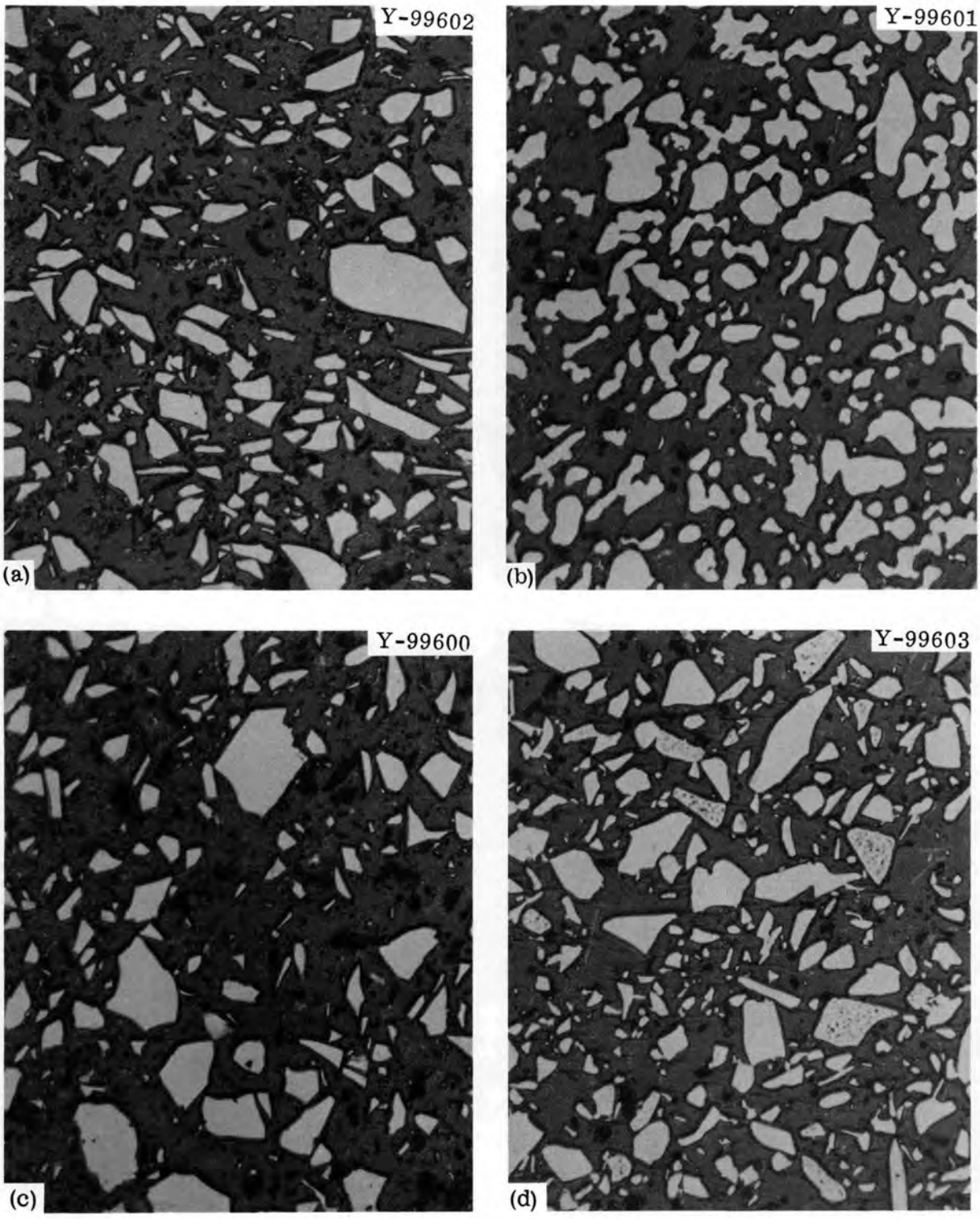

Fig. 11.2. Microstructure of Norbide 325F Boron Carbide Blended with Boron or Carbon to the Composition B_5C or B_3C and Annealed 1 hr at 1500 or 2000°C. (a) B_5C annealed at 1500°C, (b) B_5C annealed at 2000°C, (c) B_3C annealed at 1500°C, and (d) B_3C annealed at 2000°C. As polished. 500×.

in the film background. We obtained patterns of both unirradiated and irradiated material in which there were sufficient diffraction lines to permit identification of phases. Due to the low x-ray scattering factors for both B and C, extreme care had to be taken in filling the Lindemann glass capillaries to ensure that they actually were well filled with the sample.

The specimens consisted of unirradiated and irradiated samples of boron carbide material as received, as vacuum annealed at 1500°C for 1 hr, and as vacuum annealed at 2000°C for 1 hr. The irradiated specimens produced x-ray patterns in which the diffraction lines were considerably more diffuse than those for the unirradiated material. The three samples were irradiated at about 350°C to about 9% burnup of ^{10}B.

The diffraction pattern of the as-received sample (0-3-A) contained 54 lines, including α_2 lines. The pattern for the sample annealed at 1500°C (0-1-A) contained 51 lines, but the irradiated sample (0-1) produced only about 30 readable lines due to poor filling of the capillary. Future work will include the use of a capillary metering rod to ensure proper placement of the samples. The pattern for the specimen annealed at 2000°C (0-2-A) contained 68 readable lines, but after irradiation (0-2) there were only 36 readable lines.

We worked toward identifying the phases in all of the samples before and after irradiation. Some unresolved questions remain that should be answered by future experiments. The as-received material contained some free C in the form of graphite. The data for specimens 0-1-A, 0-2-A, and 0-3-A are given in Table 11.3, where some of the observed d spacings are given along with all of those noted in reference data for boron carbide and some of those noted for graphite. Within the range of the data shown in Table 11.3, specimen 0-1-A exhibited four unidentified spacings at 2.639, 1.850, 1.315, and 1.2096 A. Specimen 0-2-A exhibited 12 unidentified spacings at 5.39, 4.21, 2.90, 2.69, 2.497, 2.428, 2.207, 2.163, 1.885, 1.6002, 1.3110, and 1.206 A. Specimen 0-3-A exhibited five unidentified spacings at 4.201, 2.639, 1.572, 1.3142, and 1.2093 A. Either a complicated phase change occurred in the 0-2-A sample as a result of the anneal at 2000°C or it was inadvertently contaminated during the experiment.

Table 11.3. Spacings and Relative Intensities[a] of X-Ray Diffraction Lines for Unirradiated Boron Carbide Samples

Experimental Data						Reference Data[b]			
Sample 0-1-A		Sample 0-2-A		Sample 0-3-A		Boron Carbide		Graphite	
d Spacing (A)	Relative Intensity	d Spacing (A)	Relative Intensity	d Spacing (A)	Relative Intensity	d Spacing (A)	Relative Intensity	d Spacing (A)	Relative Intensity
		5.39	m						
4.51	m	4.49	m	4.50	m	4.49	m		
		4.21	vvw	4.201	vvw				
4.04	m	4.03	m	4.03	m	4.02	m		
3.79	s	3.77	s	3.80	s	3.79	s		
3.39	vw	3.39	m	3.37	vw			3.35	s
		2.90	w						
2.81	w	2.79	w	2.81	w	2.81	m		
		2.69	vw						
2.639	vvw	2.624	vw	2.639	vw				
2.573	s	2.557	s	2.569	s	2.57	s		
		2.497	vw						
		2.428	vw						
2.384	s	2.371	s	2.381	s	2.38	s		
2.309	w	2.292	w	2.305	w	2.30	w		
		2.207	w						
		2.163	vw						
2.126	m	2.123	vw	2.126	w			2.13	m
				2.046	vvw	2.02	vw	2.04	m
		1.885	vw						
1.850	vw	1.840	vvw						
1.818	w	1.8105	w	1.817	vw	1.82	w	1.80	m
1.715	m	1.7090	m	1.713	m	1.714	m		
								1.675	m
						1.637	w		
1.6310	vw	1.6250	vw	1.629	vw	1.628	w		
		1.6002	vw						
				1.572	vvw				
		1.5300	m	1.5450	vvw			1.541	m
1.5040	m	1.4983	m	1.501	m	1.505	m		
1.4630	m	1.4593	m	1.462	m	1.463	m		
1.4447	m	1.4403	m	1.4415	m	1.446	m		

Table 11.3. (Continued)

Experimental Data						Reference Data[b]			
Sample 0-1-A		Sample 0-2-A		Sample 0-3-A		Boron Carbide		Graphite	
d Spacing (A)	Relative Intensity	d Spacing (A)	Relative Intensity	d Spacing (A)	Relative Intensity	d Spacing (A)	Relative Intensity	d Spacing (A)	Relative Intensity
1.4037	m	1.4000	m	1.4020	m	1.407	m		
						1.403	m		
1.3402	w	1.3347	w	1.3377	w	1.345	w		
						1.342	w		
1.3273	w	1.3217	w	1.3233	w	1.326	w		
1.3155	w	1.3110	w	1.3142	w				
1.2844	vw	1.2798	w	1.2823	vw	1.286	vw		
1.2606	w	1.2573	w	1.2588	w	1.261	w		
								1.230	s
1.2096	vw	1.2060	vw	1.2093	vw				
1.1921	vw	1.1888	w	1.1900	w	1.191	w		

[a]Relative intensities are indicated by s = strong, m = medium, w = weak, vw = very weak, vvw = very very weak.

[b]ASTM Data Cards 6-055 (boron carbide) and 13-148 and 12-212 (graphite), Inorganic Index to the Powder Diffraction File, 1969, ASTM Publ. PDIS-19i, American Society for Testing and Materials, Philadelphia.

The Norbide 325F material as received from the commercial vendor was designated 0-3-A in the unirradiated condition and designated 0-3 after irradiation. Both samples were examined to determine if significant changes had occurred as a result of irradiation. The major change noted was that the graphite phase was not detectable on the x-ray patterns of the 0-3 specimen. It had apparently disappeared during the irradiation experiment. A part of sample 0-3-A is being heat treated for three weeks at 350°C to determine if this time and temperature are sufficient to cause the C to disappear. The 1.572 A line of 0-3-A also disappeared during irradiation, and lines appeared at 1.763 and 1.242 A. Many of these lines had very low intensity and were difficult to measure accurately.

Irradiation of sample 0-2-A led to the apparent disappearance of free graphite and the disappearance of the extraneous lines that had spacings of 5.39, 4.20, 2.90, 2.69, 2.497, 2.428, 2.207, 2.163, 1.885, 1.8105, 1.6002, and 1.3112 A. These data are summarized in Table 11.4.

Irradiation of sample 0-1-A led to essentially the same qualitative changes as were noted for sample 0-3-A. Since there was not enough of sample 0-1 to provide a filled x-ray capillary, the diffraction pattern was weak and judged not to be sufficiently resolved to permit meaningful measurements. Again, however, irradiation of this material led to the apparent disappearance of the graphite phase.

Compared to the unirradiated samples, samples 0-1 and 0-2 exhibited a sizable increase in the intensity of the line at about 2.08 A. This line is presumably the (006) line of the boron carbide. This line supposedly has a relative intensity of about 10% of the (021) line (about 2.38 A), which is the most intense line in unirradiated boron carbide. Sample 0-3 did not exhibit this increase in the intensity of the (006) line during irradiation. This phenomenon will be investigated in more detail in conjunction with the future irradiation tests.

Thermal-Reactor Tests (G. L. Copeland)

Evaluation of the first three capsules in this series was completed. The capsule design was shown previously.[3] The experiment is summarized in Table 11.5. The boron carbide powder used was Norbide 325F, both

Table 11.4. Spacings and Relative Intensities[a] of X-Ray Diffraction Lines for Irradiated Boron Carbide Samples

Experimental Data				Reference Data[b]			
Sample 0-2		Sample 0-3		Boron Carbide		Graphite	
d Spacing (A)	Relative Intensity	d Spacing (A)	Relative Intensity	d Spacing (A)	Relative Intensity	d Spacing (A)	Relative Intensity
4.51	s	4.50	s	4.49	m		
4.002	m	4.02	m	4.02	m		
3.63	s	3.79	s	3.79	s		
						3.35	s
2.788	w	2.805	w	2.81	m		
2.634	vw	2.638	vw				
2.549	s	2.559	s	2.57	s		
2.370	s	2.382	s	2.38	s		
2.291	vw	2.311	vw	2.30	w		
						2.13	m
						2.04	m
2.074	s	2.084	vvw	2.02	w		
1.795	m	1.816	vw	1.82	w		
						1.801	s
		1.763	vvw				
1.700	w	1.711	w	1.714	m		
						1.675	s
				1.637	w		
		1.625	vw	1.628	w		
1.613	vw						
		1.549	vvw				
						1.541	m
1.493	w	1.503	w	1.505	w		
1.451	w	1.461	w	1.463	w		
1.431	w	1.440	w	1.446	w		
		1.406	w	1.407	w		
1.393	w			1.403	w		
1.332	w	1.341	w	1.345	w		
				1.342	w		
1.317	w	1.325	w	1.326	w		
1.270	m	1.281	vvw	1.286	w		
1.251	vw	1.263	vw	1.261	w		
		1.242	vw			1.23	m
1.183	m	1.193	vw	1.191	vw		

[a]Relative intensities are indicated by s = strong, m = medium, w = weak, vw = very weak, vvw = very very weak.

[b]ASTM Data Cards 6-055 (boron carbide) and 13-148 and 12-212 (graphite), Inorganic Index to the Powder Diffraction File, 1969, ASTM Publ. PDIS-19i, American Society for Testing and Materials, Philadelphia.

Table 11.5. Summary of Irradiation Test of Boron Carbide in the Oak Ridge Research Reactor

	Capsule		
	0-1	0-2	0-3
Material	Norbide 325F	Norbide 325F	Norbide 325F
Ratio, B:C	3.62	3.62	3.62
Heat treatment	1500°C, 1 hr	2000°C, 1 hr	None
Irradiation temperature,[a] °C	340	b	360
Burnup,[c] % of ^{10}B	8.8	9.4	6.6
Helium release, %	5.8	5.2	5.0

[a]Based on evaluation of SiC temperature monitors by sequential annealing and by measurements after irradiation. The temperature at which the irradiation damage begins to anneal out of the SiC is taken as the irradiation temperature.

[b]The SiC temperature monitor broke, and no accurate measurements could be obtained. The temperature should have been close to those of the other two capsules.

[c]Based on analysis for Li after irradiation.

as received and after annealing in vacuum for 1 hr at 1500 and 2000°C. Pycnometer measurements of density indicated that 2.6 and 4.9% voids were formed by the 1500 and 2000°C anneals. Since the rates of gas release were essentially the same for the three powders, the voids apparently did not affect the release of He from the particles.

The typical metallographic appearance of the particles before and after irradiation is shown in Fig. 11.3. The powders do not appear to have been changed by the irradiation. The increase in size and volume of the internal voids at higher annealing temperatures is apparent from comparing the powders annealed at 1500°C (0-1) and 2000°C (0-2).

Using the scanning electron microscope, we observed no change in the appearance of the powders after irradiation at 350°C. Typical views of the powders are shown in Figs. 11.4 through 11.6. A thorough search was made for evidence of pores such as those shown metallographically in Fig. 11.3. The fact that none were found indicates that there was

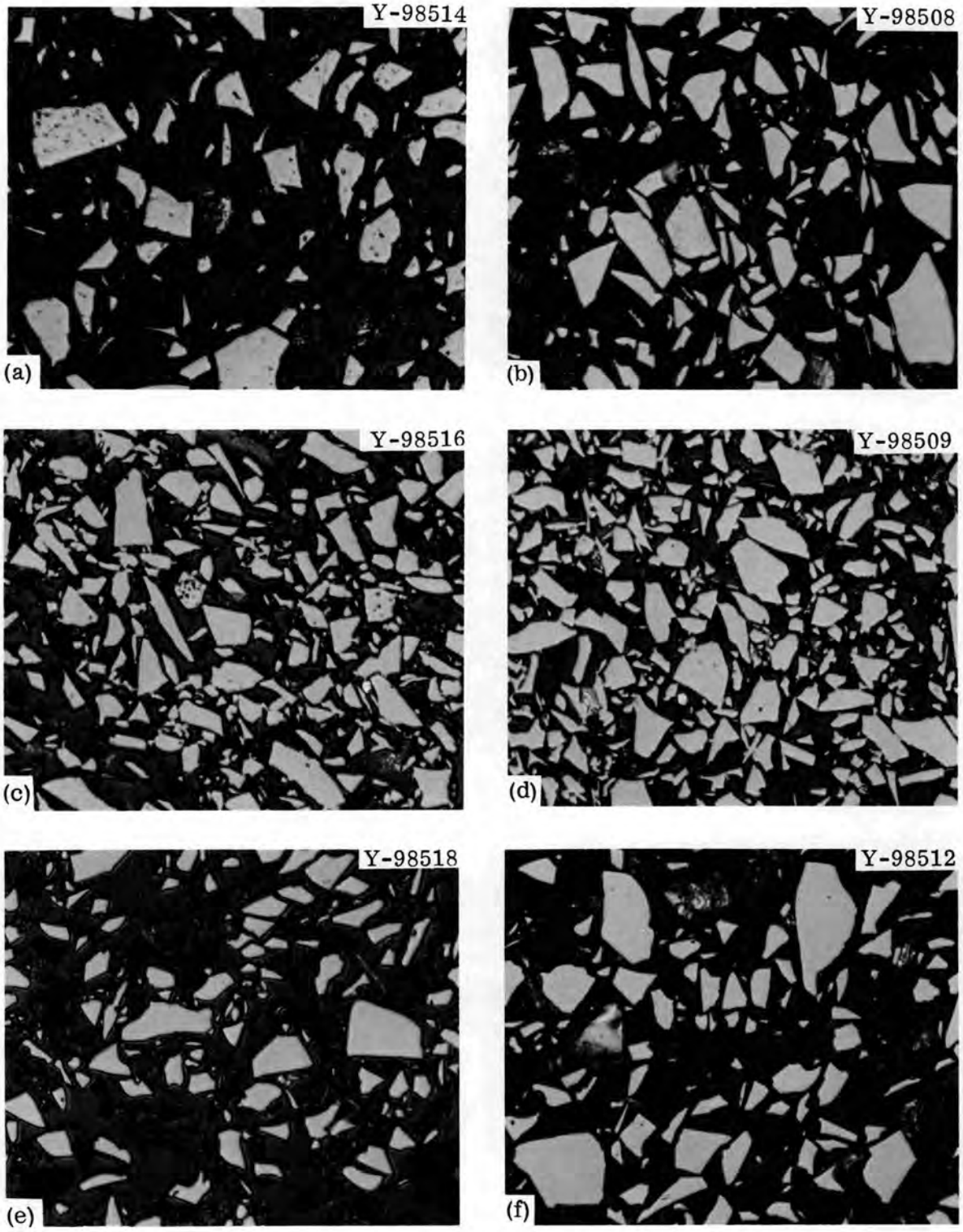

Fig. 11.3. Microstructures of Boron Carbide Powders Before and After Irradiation in the Oak Ridge Research Reactor. (a) Sample 0-1 before irradiation, (b) sample 0-1 after irradiation, (c) sample 0-2 before irradiation, (d) sample 0-2 after irradiation, (e) sample 0-3 before irradiation, and (f) sample 0-3 after irradiation. As polished. 500×.

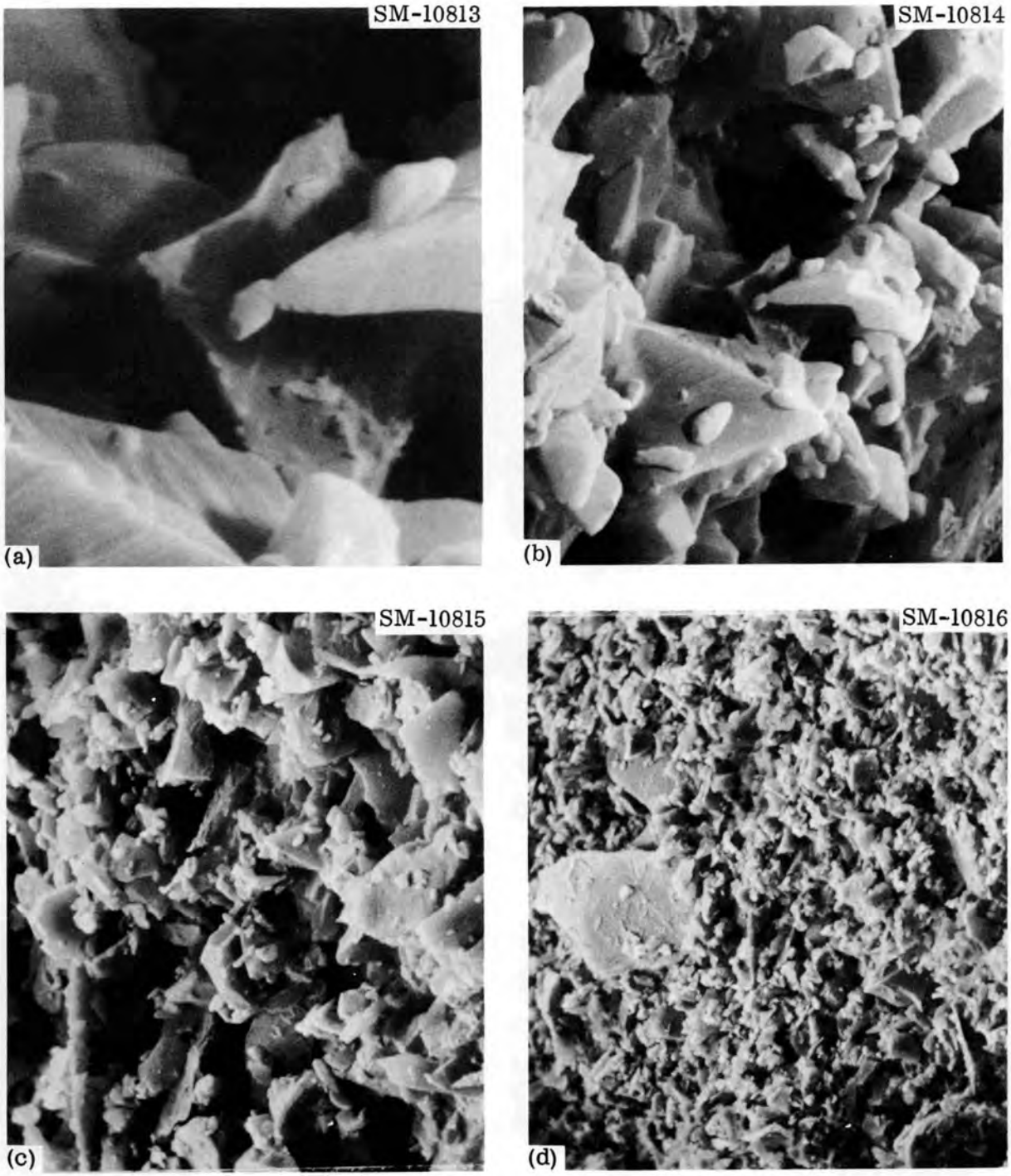

Fig. 11.4. Scanning Electron Micrographs of Boron Carbide Powders for the 0-2 Capsule Before Irradiation. Particles were gold plated to improve conductivity. (a) 10,000×. (b) 3000×. (c) 1000×. (d) 300×.

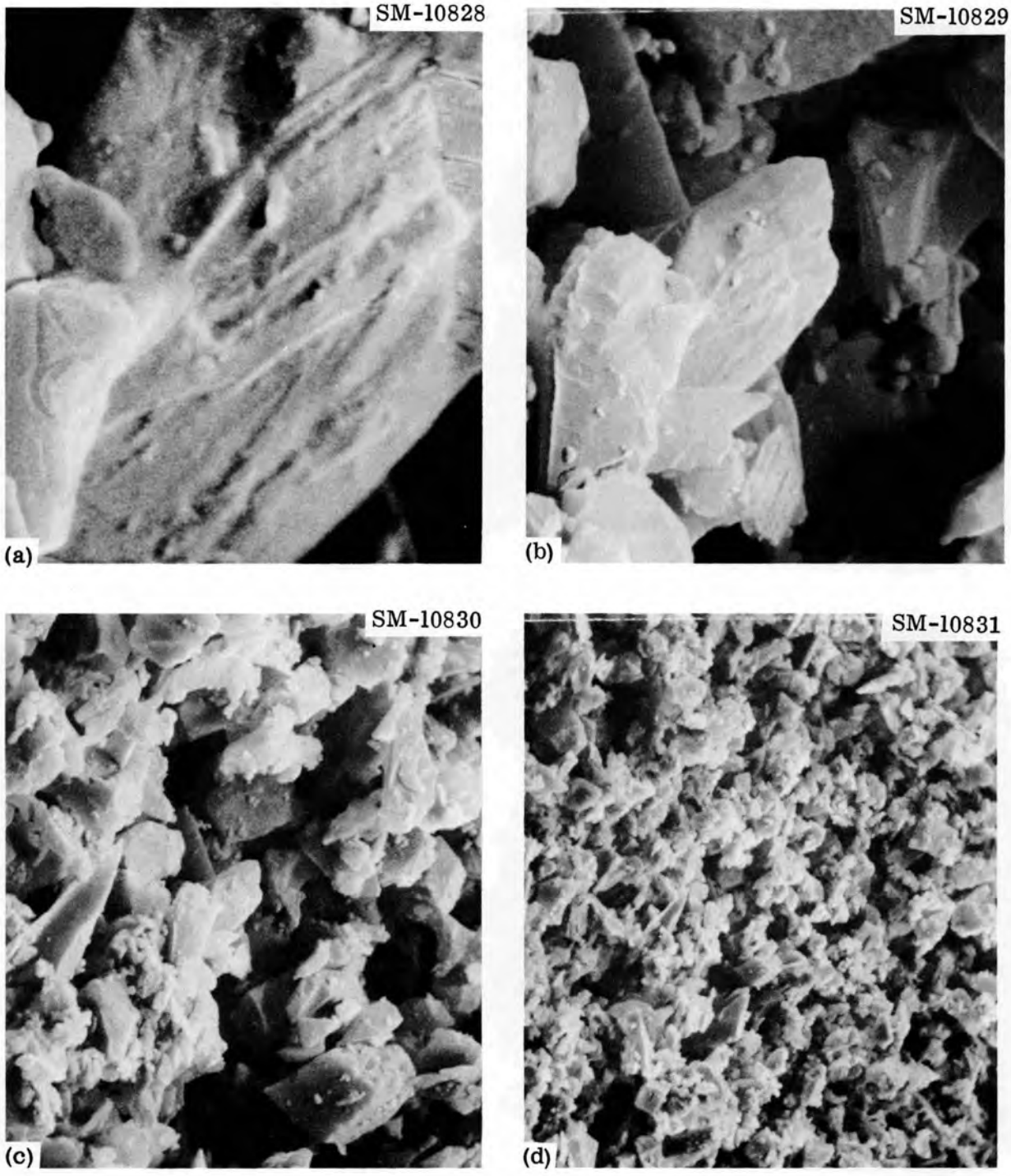

Fig. 11.5. Scanning Electron Micrographs of Boron Carbide Powders from the O-2 Capsule After Irradiation. Particles were gold plated to improve conductivity. (a) 10,000×. (b) 3000×. (c) 1000×. (d) 300×.

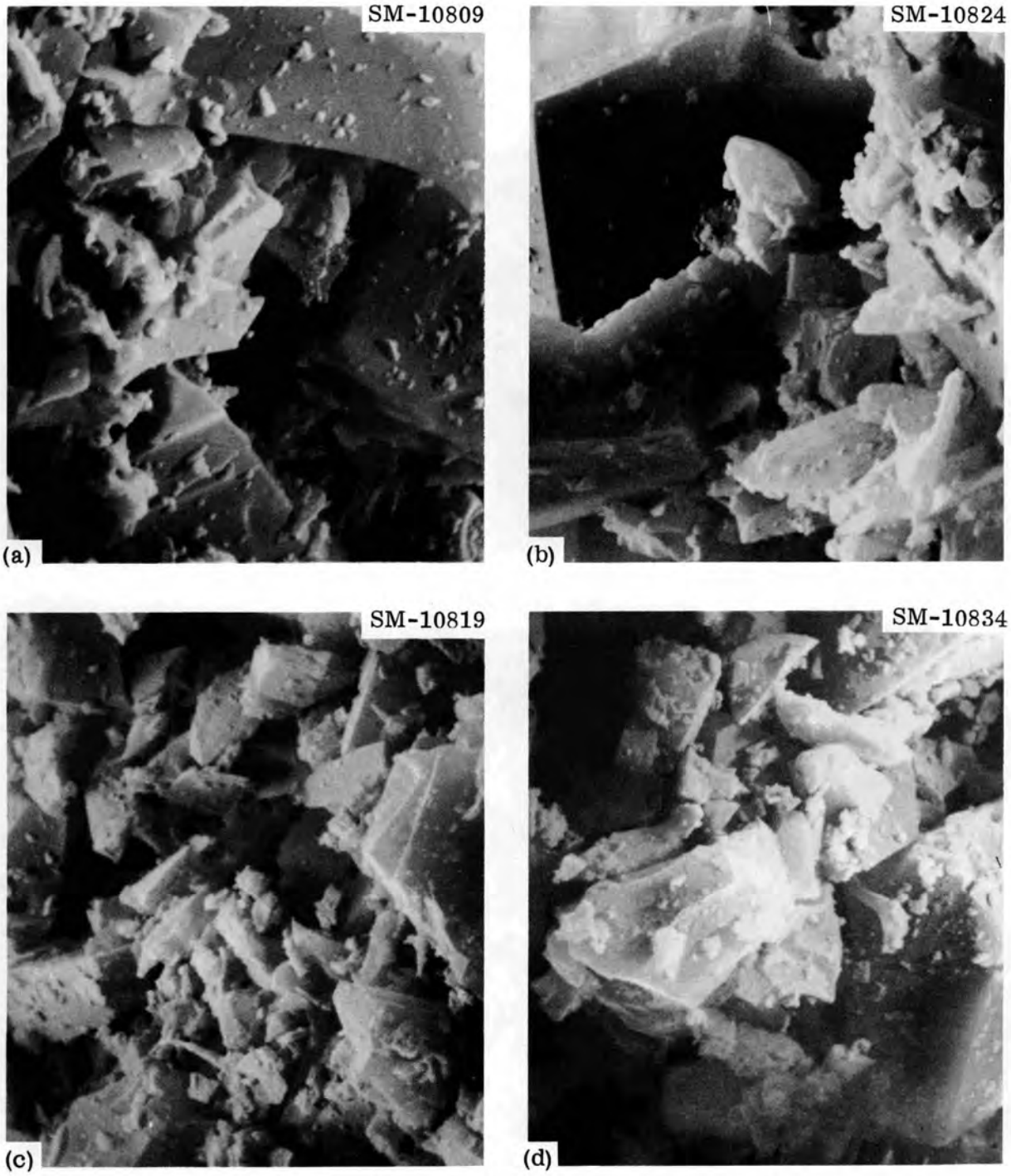

Fig. 11.6. Scanning Electron Micrographs of Boron Carbide Powders from 0-1 and 0-3 Capsules Before and After Irradiation. Particles were gold plated to improve conductivity. 3000×. (a) 0-1 before irradiation. (b) 0-1 after irradiation. (c) 0-3 before irradiation. (d) 0-3 after irradiation.

no significant breakup of the particles; otherwise, the pores would be visible on fractured surfaces.

We were unable to measure density by pycnometer to determine swelling since there was insufficient powder after the other samples had been taken. On future tests we plan to measure the density of the entire sample by pycnometer before we make the other evaluations.

We are preparing to repeat this experiment at a higher temperature and also test materials that have higher ratios of B:C.

Fast Reactor Tests (G. L. Copeland, G. W. Keilholtz[4])

Irradiation tests in a fast-reactor environment are necessary to correlate basic test results to expected performance in a fast reactor. We received approval-in-principle from the Division of Reactor Development and Technology for an irradiation test of six capsules in row 7 of the Experimental Breeder Reactor-II (EBR-II). Each capsule consists of two pellet pins, as shown schematically in Fig. 11.7. The variables included in the 12 pellet pins are summarized in Table 11.6. The test is designed to determine the effects on performance of (1) irradiation temperature, (2) pellet density, (3) ratio of B:C, (4) size and volume of intraparticle voids, (5) particle size of the powder used for the pellets, and (6) hot-pressing temperature during the fabrication of pellets. Final design of the capsules and fabrication of the boron carbide pellets are now proceeding.

Investigation of Materials Other than Boron Carbide

Mixtures of Boron Carbide and Tantalum (G. L. Copeland)

We are beginning to investigate the fabrication of alternate control materials. One system that offers the potential of increased control worth and possibly longer lifetime and better performance is a dispersion of a B compound (enriched in ^{10}B content) in Ta. We blended and cold pressed Ta and boron carbide mixtures of 0, 5, 10, 20, 30, 40, and 50 vol % boron carbide. After vacuum sintering at 2000°C, the compacts that contained 20% or more boron carbide expanded rather than shrank. The compacts that contained 0, 5, and 10 vol % boron carbide reached

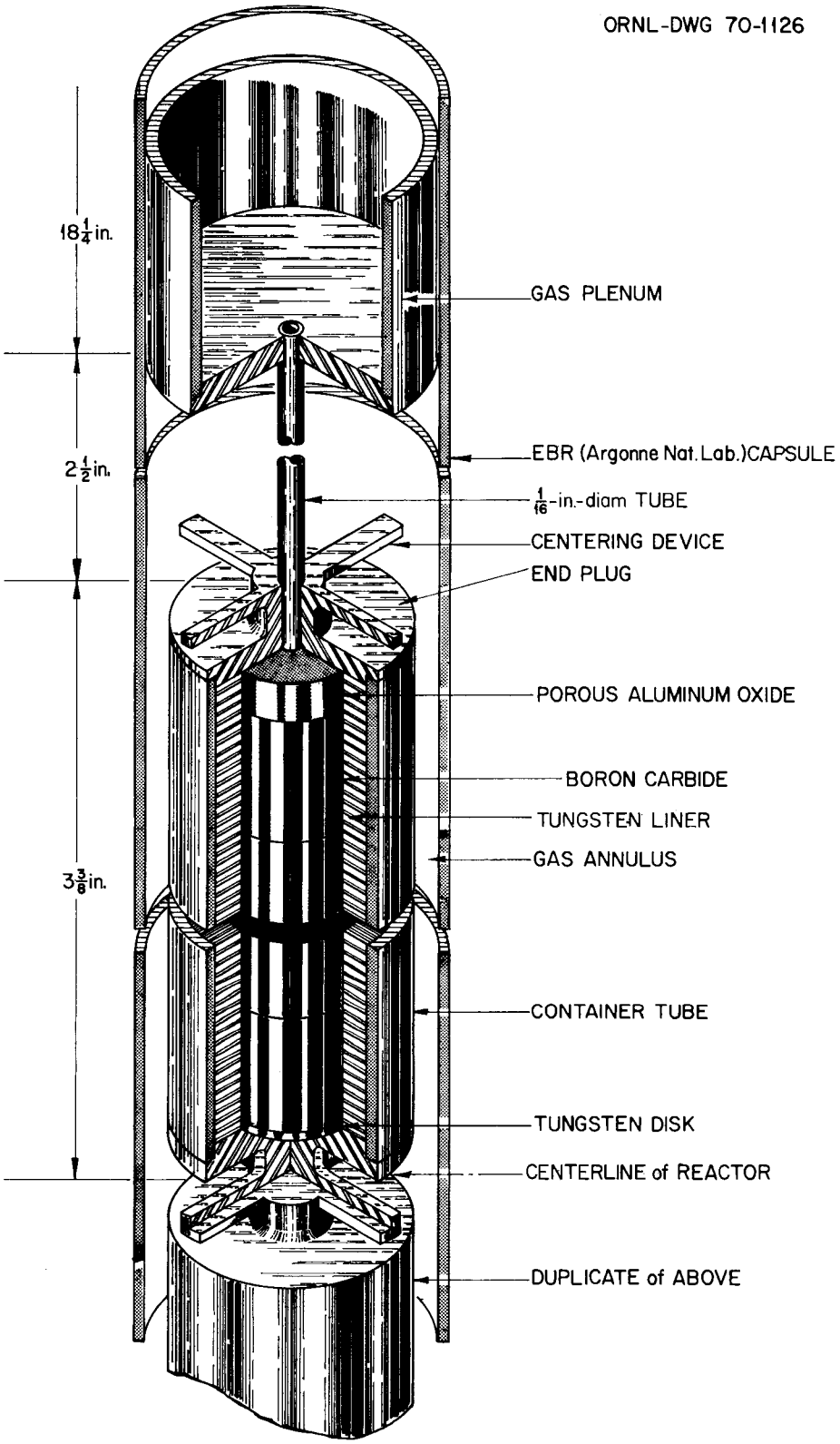

Fig. 11.7. Assembly for Irradiation of Boron Carbide at High Temperatures in the Experimental Breeder Reactor-II.

Table 11.6. Summary of ORNL Irradiation Test of Boron Carbide in Experimental Breeder Reactor-II

Pellet Pin Number	Irradiation Temperature (°C)	Atom Ratio B:C	Particle Size (U.S. Standard Mesh)	Density (% of Theoretical)	Hot-Pressing Temperature (°C)	Notes
1-T	427	3.62	−325	> 98	2300	a
1-B	427	3.62	−325	90	2300	a
2-T	427	4.50	−325	> 98	2300	b
2-B	427	4.50	−325	90	2300	b
3-T	427	4.50	−325	90	2300	c
3-B	427	4.50	−80 +325	90	2300	c
4-T	427	3.62	−325	90	1800	d
4-B	427	3.62	−325	90	1800	e
5-T	700	3.62	−325	> 98	2300	a
5-B	700	3.62	−325	90	2300	a
6-T	700	4.50	−325	> 98	2300	b
6-B	700	4.50	−325	90	2300	b

[a]Intraparticle voids held constant, but more interparticle voids in B pins. Powder is −325 mesh fraction of a commercial boron carbide.

[b]Boron powder blended with powder from the same batch used for pins 1 and 5 will decrease the amount of intraparticle voids.

[c]Ratio of B:C is obtained by selecting a size fraction of a crushed ingot that contains proeutectic boron carbide rich in B with no free C. The selected size fraction will then be ground to different sizes for 3-T and 3-B. Hot pressing of this powder should yield no intraparticle voids.

[d]Powder from the same batch used in pins 1 and 5. Hot pressing in vacuum at a lower temperature will result in decreased intraparticle void size.

[e]Powder from the same batch used in pins 1 and 5. The powder will be vacuum annealed at 2300°C to provide the same intraparticle void size as in pins 1 and 5. The pellet will then be hot pressed in vacuum at 1800°C.

about 65% of theoretical density. There is evidently a reaction between the Ta and boron carbide at the 2000°C sintering temperature. No further examination has yet been made to determine the type or degree of the reaction.

Notes

1. R. S. Mateer and G. L. Copeland, Fuels and Materials Development Program Quart. Progr. Rept. Sept. 30, 1969, ORNL-4480, p. 135.

2. R. S. Mateer and G. L. Copeland, Fuels and Materials Development Program Quart. Progr. Rept. Sept. 30, 1969, ORNL-4480, pp. 140–143.

3. G. L. Copeland, Fuels and Materials Development Program Quart. Progr. Rept. Dec. 31, 1969, ORNL-4520, p. 189.

4. Reactor Chemistry Division.

PART II

SPACE POWER TECHNOLOGY

FUELS

12. DEVELOPMENT OF URANIUM MONONITRIDE FUELS

P. Patriarca J. L. Scott

Uranium mononitride (UN) is potentially attractive as fuel for space-nuclear reactors because of its excellent stability at high temperatures, high thermal conductivity, and good irradiation stability up to 1000°C. The purpose of this program is to determine the basic mechanisms of fuel swelling and gas release at temperatures above 1000°C. Results will be used to develop a model for predicting the performance of UN as a function of temperature, burnup, and cladding restraint.

Irradiation Testing

T. N. Washburn

The basic objective of the ORNL program[1] for irradiation testing of UN is to investigate the performance capability of this fuel material at high temperatures and low heat ratings. Fuel temperatures of interest are 1000 to 1500°C, with temperatures of 900 to 1400°C at the outside surface of the cladding and linear heat ratings from 5 to 10 kw/ft. Fuel properties of most interest are swelling rate, release of fission gas, and compatibility with the cladding materials. The irradiation tests are conducted in the poolside facilities of the Oak Ridge Research Reactor (ORR). These facilities allow adjustment of the position of the test capsule relative to the reactor face and thereby make it possible to maintain a constant temperature at a selected reference point on the test specimen as the reactor flux profile changes or as the fissile content of the test fuel is diminished.

Postirradiation Examination of Capsule UN-3 (D. R. Cuneo,[2] E. L. Long, Jr.)

The nondestructive portion of the postirradiation examination of the three fuel pins of capsule UN-3 was reported previously.[3]

The middle fuel pin, which failed in test, was destructively examined after irradiation. The ends of the fuel pin were cut off adjacent to the end plugs, and the cladding was then slit longitudinally.

The UN fuel pellets were intact and in intimate contact with the cladding. Unreacted NaK was found in the plenum space above the fuel column, and white oxide was evident throughout the interior of the pin. The large cracks seen on the outside surface of the T-111 cladding were visible on the inside surface of the W barrier. In addition, there were also numerous finer cracks on the inside surface as well as at areas where small portions of the fuel pellets were bonded to the cladding. Close examination of the surface of the fuel pellets showed that fine scratches on the inner surface of the cladding as well as the much larger cracks had been replicated on the surface of the fuel. It is obvious from the data obtained to date that the UN fuel was in intimate contact with the W barrier and that the T-111 cladding increased little in diameter before it failed.

Several transverse sections were taken along the length of the cladding; the location of each metallographic section is shown in Fig. 12.1. Examination of section A, taken through the gas plenum region, showed no evidence of grain growth nor any gross changes in the microstructure of either the T-111 or W, relative to the unirradiated control specimen of cladding. The only significant change noted was what appeared to be

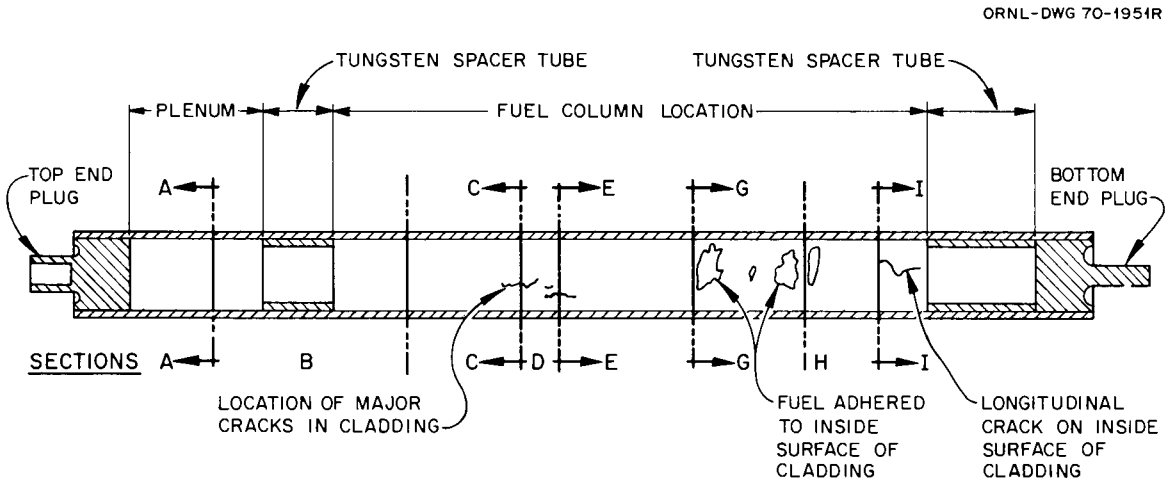

Fig. 12.1. Sectioning Diagram for Cladding of Middle Fuel Pin from Capsule UN-3.

very fine, intermittent precipitates on grain boundaries and grain corners, and these were revealed only after etching. Specimens will be examined by electron microscopy to determine the nature of the grain-boundary decorations.

The results of the examination of sections through two failed regions (sections C and E) are shown in Figs. 12.2 and 12.3. All fractures observed in the T-111 cladding were primarily intergranular; a few short transgranular fractures were noted in the T-111 in a 0.002 to 0.003-in.-long region parallel to the interface between the W and T-111. Measurements of microhardness in this region reflected a marked increase in hardness there as compared to the remainder of the wall. As can be seen in these figures, the intergranular fractures in both the W and T-111 appear to be preceded by spherical voids. These voids also collected at the interface between W and T-111 and partially separated the two materials. The nature of the voids is unknown at this time.

Metallographic examination of a section from an unfailed region (section G) revealed intergranular separations in the T-111 that originated at the inner surface and extended through half the wall thickness, as shown in Fig. 12.4(a). Numerous voids collected at the interface between W and T-111 and preceded the intergranular separations in the T-111. Many intergranular separations were noted in the W liner. The results of an examination of a region where the fuel had adhered to the W liner are shown in Fig. 12.4(b). We noted that not only had the UN formed a metallurgical bond with the W, but in some regions the UN had penetrated the W to a depth of about 15 μm. We also noted the occasional presence of a gray phase in some of the grain-boundary separations in the T-111 and in some of the voids at the interface between W and T-111. This gray phase can be seen in Fig. 12.4(b).

We determined microhardness values across the wall of the T-111 cladding for four sections: the unirradiated control, sections A (gas plenum region), C (failed region), and I (near bottom of fuel column). The results are shown in Fig. 12.5. If the unirradiated control is used as a reference, both sections A and C increased in microhardness about 5 and 15% near the inner and outer surfaces, respectively. The failed

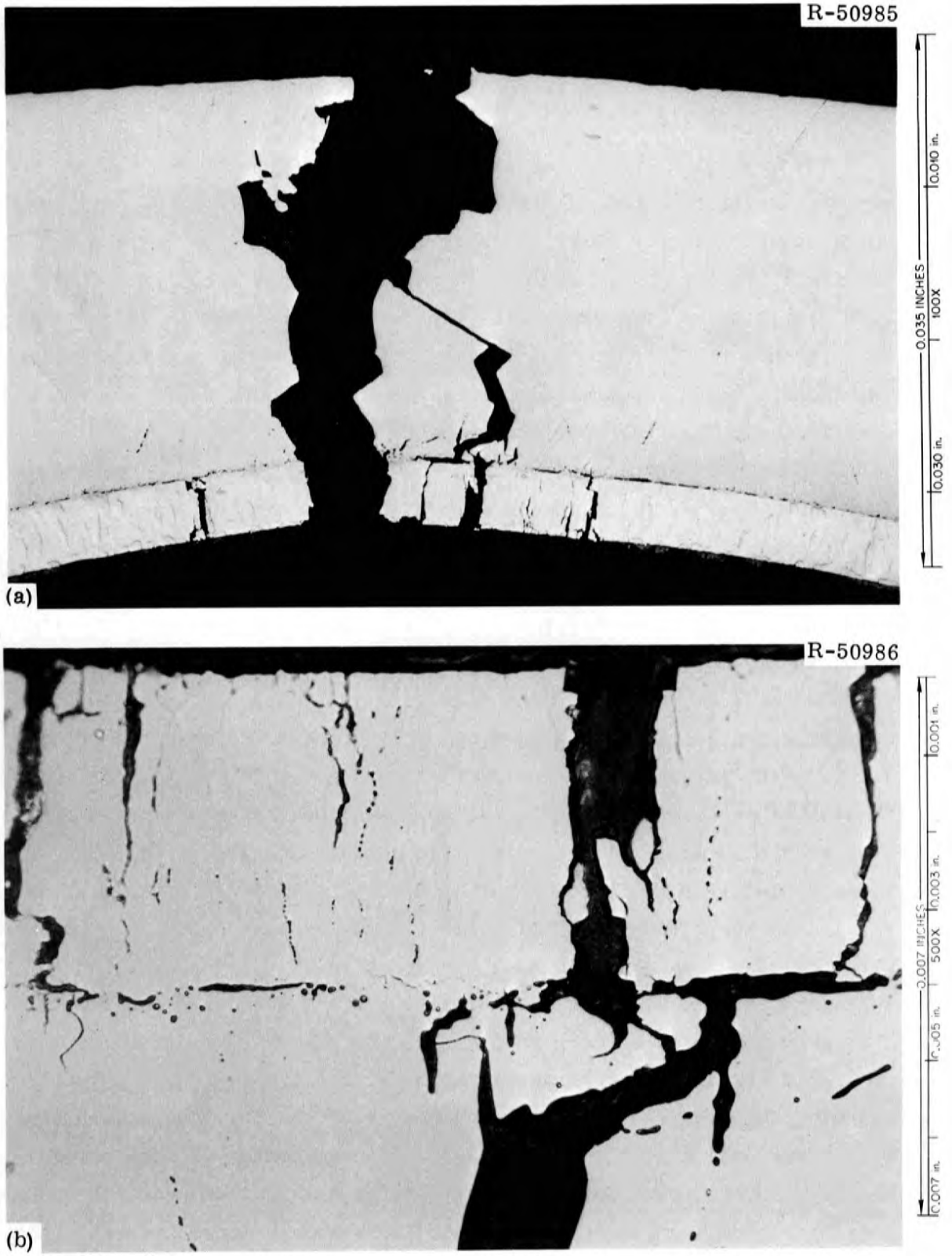

Fig. 12.2. Appearance of a Failed Region in the T-111 Cladding and Tungsten Liner. (a) Low and (b) high magnification. As polished.

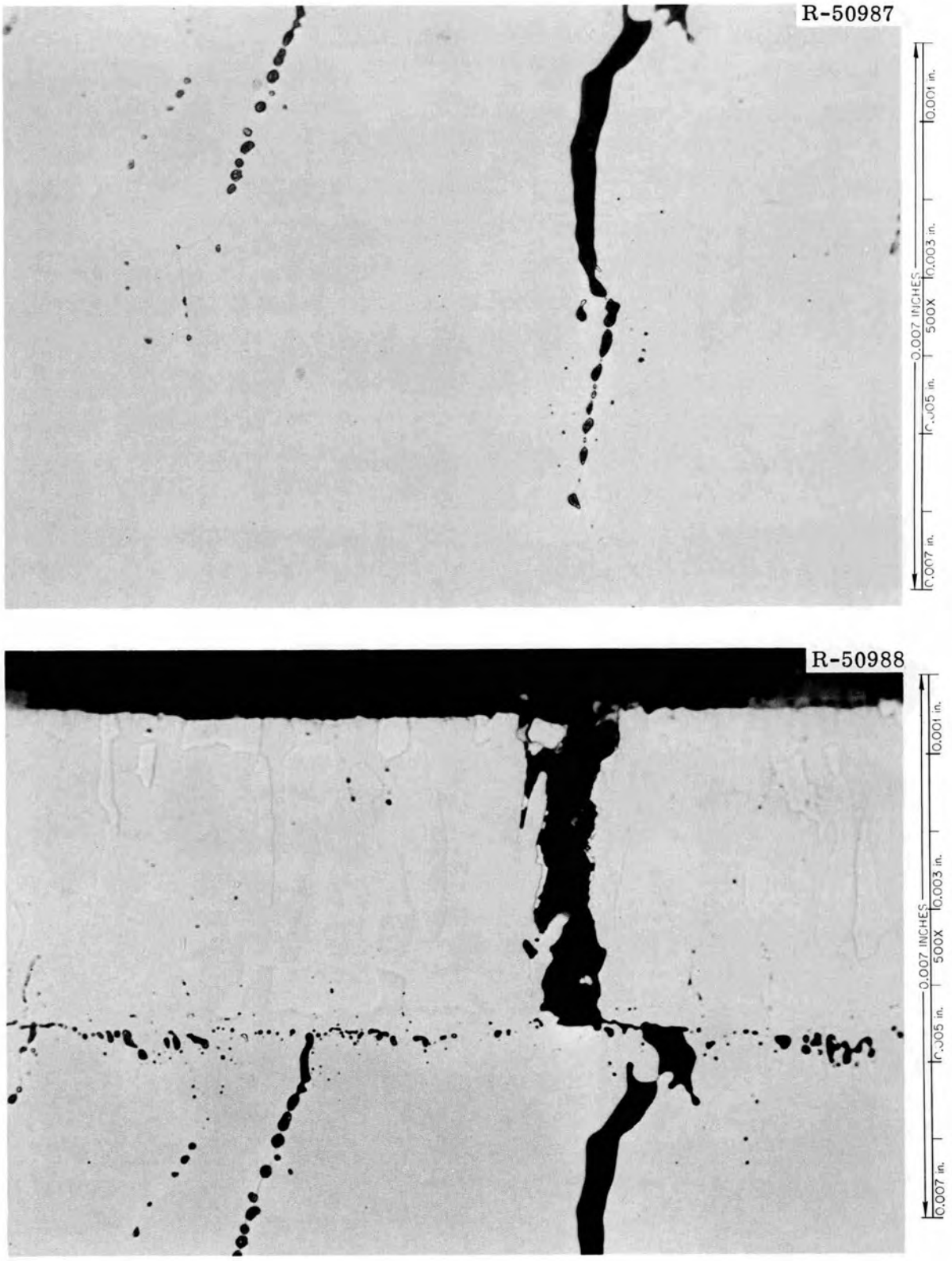

Fig. 12.3. Appearance of an Area from Section C. Note the series of voids that precede the intergranular separation of the T-111 cladding. As polished.

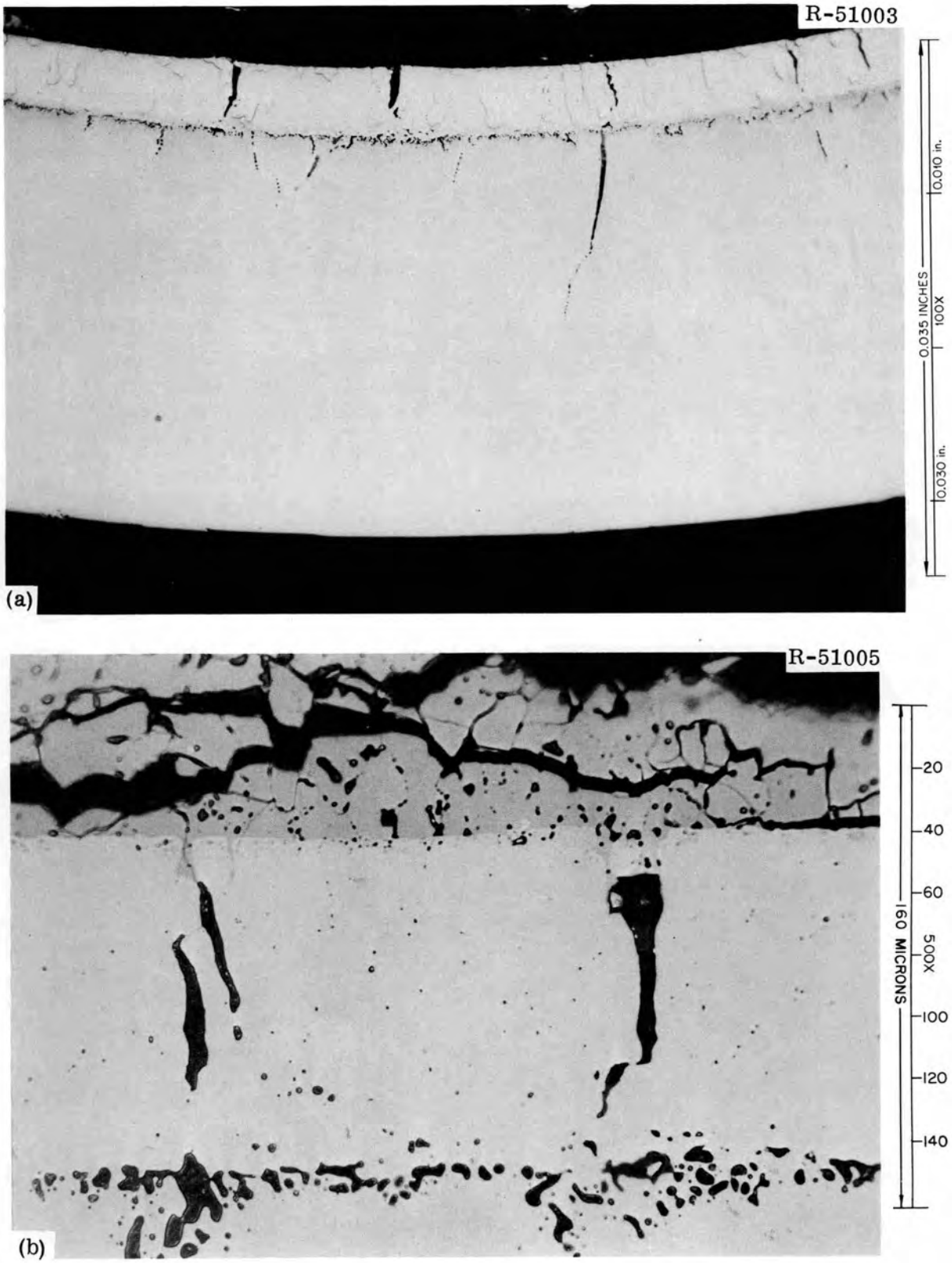

Fig. 12.4. Appearance of T-111 Cladding and Tungsten Liner from Section G. (a) Low and (b) high magnifications. As polished.

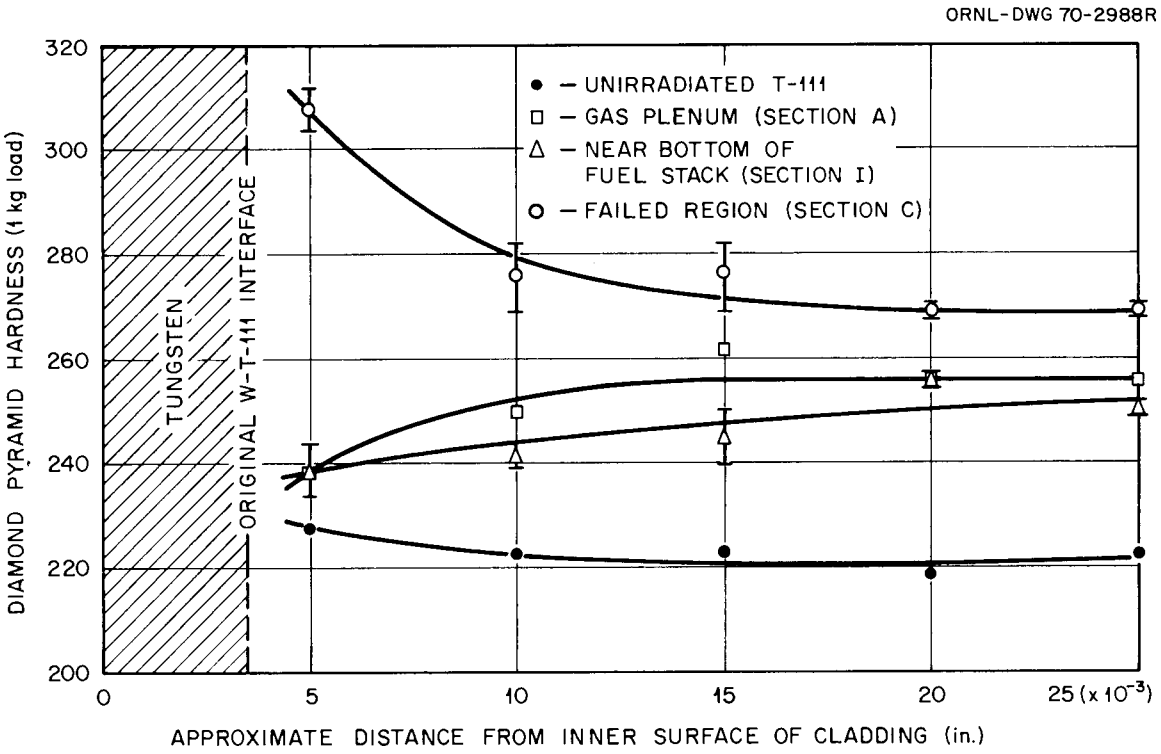

Fig. 12.5. Microhardness of Fuel Cladding of Middle Pin from Capsule UN-3.

region increased by about 35 and 21% near the inner and outer surfaces, respectively. The microhardness of the T-111 in the unfailed regions increased gradually from the inner to outer surfaces, but the microhardness near the inner surface in the T-111 from the failed region showed a marked increase that decreased as the outer surface was approached. Grain size was six times larger in the failed region of the T-111 than in the gas plenum region. There was an average of only seven grains across the cladding in the failed region. The grain diameters were as follows: unirradiated control, 0.022 mm; section A, 0.017 mm; section C, 0.102 mm; section I, 0.022 mm.

Electron microprobe analysis of a metallographic section taken through a failed region of the cladding (sample E) revealed no evidence of U in either the W liner, the T-111 cladding, or the interface between liner and cladding. If U is present in the grain boundaries of the cladding, it is in the form of an extremely thin film that would be below the limit of detection of the microprobe. Additional microprobe work is planned on fractured cladding surfaces. The two fuel pins from

capsule UN-3 that did not fail were removed from the hot cell and neutron radiographed. We could not detect any change in the diameter of the fuel by examining these radiographs. The most notable difference between the two fuel pins is that distinct pellet interfaces can be seen in the top pin, while the fuel column of the bottom pin appears continuous. We presume this difference to be due to the difference in fuel operating temperature of the two pins. The fuel length increased 2.3% in each fuel pin during irradiation.

Postirradiation examination of these fuel pins is continuing.

Notes

1. The current program includes work sponsored by the AEC, and work sponsored by NASA under Interagency Agreement 40-184-69, NASA Order C-54536-B. Specifically, capsules UN-1, UN-2, UN-3, and UN-6 are funded by AEC, and capsules UN-4 and UN-5 are funded by NASA. Details of these capsule tests were reported previously.

2. On loan from Reactor Chemistry Division.

3. D. R. Cuneo, Fuels and Materials Development Program Quart. Progr. Rept. Dec. 31, 1969, ORNL-4520, pp. 195–201.

CLADDING AND OTHER STRUCTURAL MATERIALS

13. CLADDING MATERIALS FOR SPACE ISOTOPIC HEAT SOURCES

P. Patriarca R. G. Donnelly

The purpose of this program is to develop new cladding materials for containment of radioisotopes in power systems for use in space. We are attempting to develop a single alloy with an optimum combination of strength at high temperature, fabricability, environmental stability, and resistance to oxidation in air to take the place of the layered combination of strength member, diffusion barrier, and oxidation resistant cladding used in present devices. We are also evaluating back extrusion as an improved method of fabricating capsules of various materials.

Development of Improved Alloys

H. Inouye

The material for fuel capsules for space thermoelectric systems should (1) be useful in the range 1000 to 1600°C; (2) be resistant to oxidation, evaporation, and corrosion by soil and seawater; (3) have a high melting point and high impact resistance; (4) be compatible with the fuel, ablative materials, and specialized coatings; and (5) be fabricable and weldable. The purpose of this task is to develop, in light of these requirements, new cladding alloys specifically for isotopic heat sources for space.

Improved Superalloys (C. T. Liu)

In order to show the effect of the ordered state on the tensile properties of ordered alloy S-4 (43% Ni–32% Co–24% V) and disordered alloy S-3 (45% Ni–46% Co–9% V) at high temperatures, we step-loaded them in a vacuum creep furnace. The results are listed in Table 13.1 together with the data previously obtained at room temperature. An increase from room temperature to 900°C decreases the ultimate tensile strength of

Table 13.1. Tensile Properties of Ordered Alloy S-4 and Disordered Alloy S-3 at High Temperatures

Alloy	Test Temperature (°C)	Ultimate Tensile Strength (psi)	Fracture Ductility (%)
		$\times 10^3$	
S-3	Room	84	40
	750	46	26
	900	28	28
S-4	Room	125	1
	750	102	6.5
	900	96	10

alloy S-3 from 84 to 28 $\times 10^3$ psi and that of alloy S-4, which has the hexagonal close-packed (hcp) type of ordered structure, from 125 to 96 $\times 10^3$ psi. These results indicate that ordered alloy S-4 is much stronger than alloy S-3 at high temperatures and that alloy S-4 is also much less sensitive to increases in temperature.

High-Temperature Alloys (C. T. Liu)

We prepared three ternary Pt-based alloys containing 3 to 4% Mo and 1.8 to 2.5% Ti by electron-beam melting and drop casting into 1 1/2 × 7/8 × 3/16-in. ingots. We found that the Pt–3% Mo–1.8% Ti alloy could be cold forged successfully. The plate will be used as forged for tests of mechanical properties.

An ingot of composition Pt–21 at. % Cr–4 at. % W was prepared in an attempt to improve the temperature capability of the Pt_3Cr alloy by adding W. The alloy, after forging 15% in thickness at room temperature, was sent for machining into specimens for tensile and creep tests. We studied the oxidation behavior of this alloy in air at 1000°C; the results are tabulated in Table 13.2. The initial weight loss is due to the evaporation of platinum oxide at this temperature, and the subsequent weight gain is probably related to the formation of tungsten oxide, which has the brown color,[1] observed on the specimen. The average

Table 13.2. Oxidation Properties at 1000°C in Air of Pt–21 at. % Cr–4 at. % W Alloy

Time (min)	Weight Change (mg/cm^2)	Color of Oxide Layer
	$\times 10^{-3}$	
10	–31	Dark blue
30	–25	Dark blue
70	–24	Dark blue
190	–19	Brown
430	–1	Brown
910	+6	Brown

weight gain between 30 and 910 min was 2.4×10^{-3} mg cm^{-2} hr^{-1}. Therefore, the resistance of this alloy to oxidation is excellent.

Among the noble metals, Ir has a high melting temperature (2450°C) and excellent properties at high temperatures. For instance, the ultimate tensile strength of Ir at 1500°C is 23×10^3 psi (ref. 2). The phase diagram of Ir-Nb (ref. 3) indicates that it may be further strengthened by the formation of short-range and long-range ordered structures among the atoms. The fabricability of an Ir–3.1% Nb alloy prepared by electron-beam drop casting is being evaluated.

Fabrication of Refractory Metals for Fuel Capsules

A. C. Schaffhauser

A simple and inexpensive method for fabricating refractory-metal capsule shapes is desired, especially for the less fabricable Mo alloys. The back extrusion technique offers these advantages and, in addition, (1) does not require expensive sheet as a starting material as does deep drawing, (2) produces a tough, worked structure, and (3) commits only a small amount of material to each operation (unlike the extrusion of tubes). The purpose of this task is to demonstrate the capabilities of this process.

Back Extrusion (R. E. McDonald)

This process involves the extrusion of a solid blank into a closed die and back over an advancing plunger. A cross section of the tooling and its placement in the existing container sleeve of our extrusion press is shown in Fig. 13.1. The advantages of this process are that capsules with large diameters and closed ends can be fabricated from a simple blank, that the geometry can be changed by relatively simple changes in the design of the die and plunger, and that a large amount of deformation is possible below the recrystallization temperature so that a wrought structure with good mechanical properties is produced.

We fabricated a number of capsules of Nb–1% Zr, Mo, and Mo–0.5% Ti that are nominally 2.5 in. in outside diameter, 5 in. long, and 0.25 in. in wall thickness and have hemispherical ends. These were back extruded at extrusion loads of 150 to 300 tons on starting blanks cut from extruded and rolled bar stock heated to 1200°C in a salt bath. Cross-sectional and end views of a Mo capsule are shown in Fig. 13.2.

Initial attempts to back extrude Ta–10% W capsules were unsuccessful, primarily because of contamination of the material by the salt bath. We are now plasma spraying the Ta alloys with a protective coating of Mo and induction heating in an inert atmosphere. This method of protection appeared successful for the back extrusion of T-111 at 1300°C; however, we were not able to obtain a complete back extrusion because of a large heat loss during an excessively long transfer time from the billet heater.

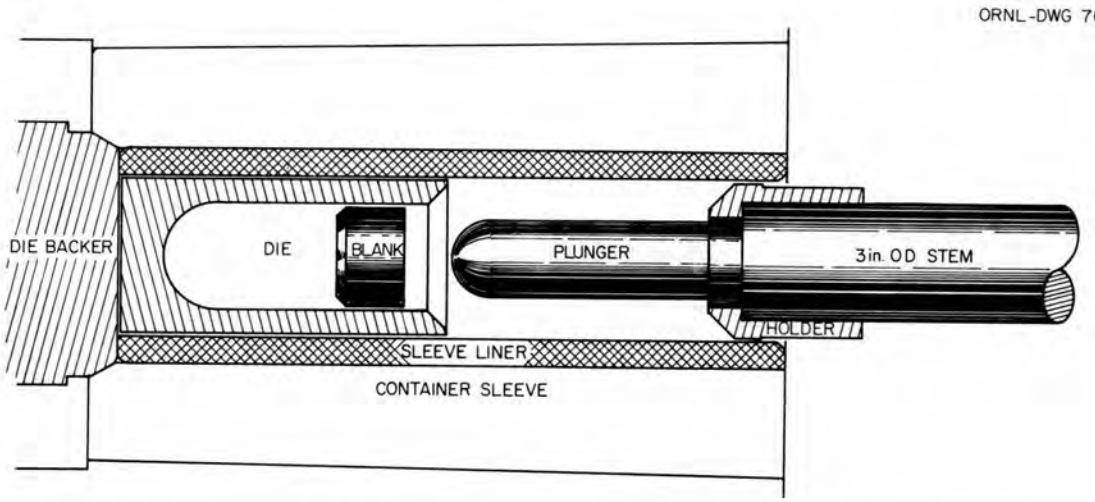

Fig. 13.1. Tooling for Back Extrusion of Refractory Metal Capsules.

Fig. 13.2. Cross Section and End View of Molybdenum Capsule Fabricated by Back Extrusion.

Notes

1. V. D. Barth and G.W.P. Rengstorff, Oxidation of Tungsten, DMIC Report 155 (July 17, 1961).

2. R. W. Douglass et al., High Temperature Properties and Alloying Behavior of the Refractory Platinum-Group Metals, Special Report Np-10939 (Aug. 31, 1961).

3. B. C. Giessen et al., Trans. Met. Soc. AIME 230, 1268 (1964).

14. PHYSICAL AND MECHANICAL METALLURGY OF REFRACTORY ALLOYS

P. Patriarca R. G. Donnelly

The purpose of this program is to provide a broad, base-technology evaluation of high-temperature alloys for use in high-performance nuclear reactors and isotopic heat sources for advanced space, terrestrial, and civilian power applications. Principal emphasis is placed on materials problems that involve Ta-, Nb-, Mo-, and V-based alloys for systems that use alkali metals as thermodynamic working fluids and heat-transfer media.

Physical Metallurgy

H. Inouye

Effects of Interstitials on Mechanical Properties of Refractory Alloys (H. Inouye)

The objective of this task is to determine the effect of low-pressure N_2 on the creep properties of T-111 to simulate its interaction with a nitride fuel. The major components of the creep apparatus were recently received from the vendors. Minor items are in various stages of completion.

Development of Age-Hardening Refractory Alloys (C. T. Liu)

The objective of this task is to develop promising age-hardening refractory alloys for use at elevated temperatures. The previous study[1] of Ta–50% Hf alloys indicated that the uniform precipitation of fine Hf-rich α-phase particles produced by fast quenching and various tempering treatments hardens the alloy significantly. In the current period, the precipitation behavior of a Ta–65% Hf alloy was characterized by isothermal aging as a function of time up to 10^4 min at 850 to 1300°C. As shown in Fig. 14.1, the specimen aged 1 min at 850°C increased sharply in hardness from 367 (as quenched) to 635 DPH, and within a short time (7 min) the hardness reached a maximum value of 710 DPH and thereafter decreased slowly with time. The high hardness in the early stage of aging was due to the precipitation of coherent α-phase particles, and

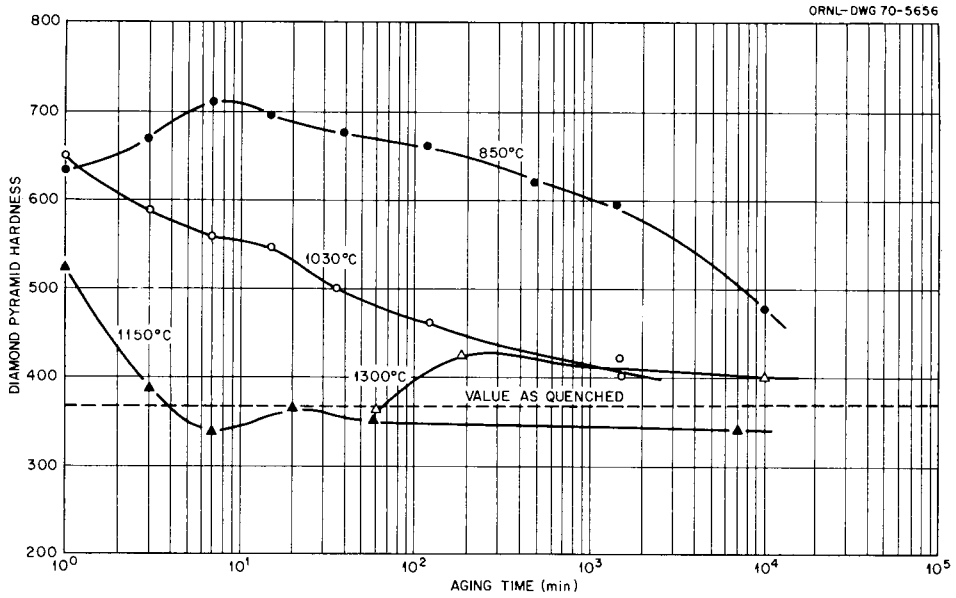

Fig. 14.1. Diamond Pyramid Hardness at Room Temperature Versus Aging Time for Ta–65 wt % Hf Alloy.

x-ray diffraction showed that the {0002} planes of α-phase were crystallographically related to the {110} planes of body-centered cubic (bcc) β-phase matrix. The aging response of this alloy is similar to that of the Ta–50% Hf alloy; however, the peak of hardness on the 850°C curve is little lower for this alloy. Hardness peaks are not observed on the high-temperature (above 1030°C) aging curves, and the steady decrease of hardness after 1 min of aging is related to the precipitation of incoherent particles that continuously coarsen with time. We prepared a Ta-base alloy that contained 64.5% Hf by electron-beam melting and drop casting into a 1 1/2 × 7/8 × 3/16-in. rectangular ingot for tests of mechanical properties. We found that this alloy could be cold forged without difficulty. After proper heat treatments the plate will be machined into tensile specimens.

Since detailed examination of the Nb-Hf and Ta-Hf alloys by x-ray diffraction[1] did not confirm the reported existence of a miscibility gap associated with the bcc β-phases a Ta–40% Zr alloy was prepared for x-ray examination to determine whether the miscibility gap reported in the literature[2] does exist. One difficulty currently associated with this work is that no adequate electrolyte has been found to polish the specimen successfully.

Mechanical Properties of Commercial Refractory Alloys

H. E. McCoy, Jr.

Mechanical Properties of Welds in Refractory Alloys (R. L. Stephenson)

Since most practical devices require joining, we consider the creep properties of welds to be of critical importance in evaluating materials for use at high temperatures. We are studying creep-rupture properties of welds in several refractory-metal alloys.

The effect of heat treatment on the creep-rupture properties of T-111 was reported previously.[3] At low stresses, material annealed at high temperatures (e.g., 1650°C) exhibits a longer rupture time than material annealed at lower temperatures (e.g., 1200°C). At high stresses, the reverse is true. Since heat-affected zones are exposed to a range of temperatures, we would expect them to behave analogously.

The data obtained to date on gas W-arc and electron-beam welds in T-111 are shown in Fig. 14.2. At low stresses (for any given temperature), the rupture times for welds equaled that for the control specimen

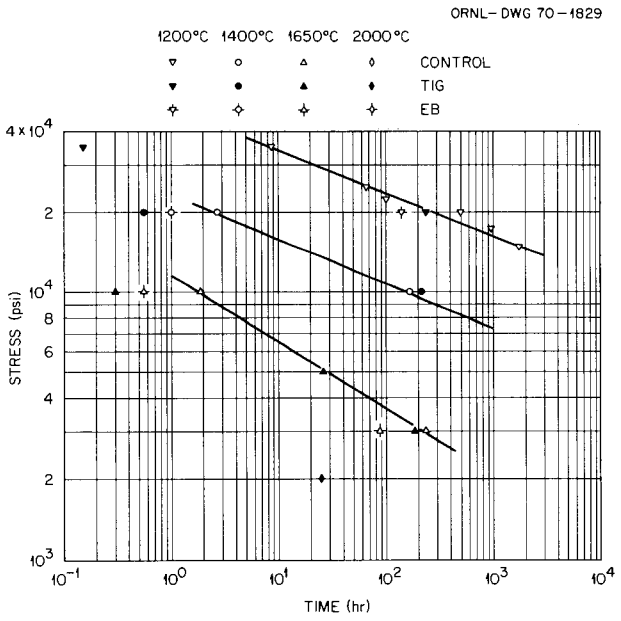

Fig. 14.2. Comparative Stress-Rupture Properties of Welded T-111.

of base metal. (Since the welds were transverse to the stress axis, base metal was included in the gage section, and rupture times significantly greater than those of the control were impossible.) At high stresses, the rupture times of the welds were shorter than those of the control specimens, as the annealing studies led us to expect. Preliminary data on welds in Ta–10% W and T-222 indicated that these alloys behave in the same manner.

Evaluation of Promising Alloys

We are continuing to evaluate the creep-rupture properties of promising refractory-metal alloys. We nearly completed our evaluation of C-129Y (Nb–10% W–10% Hf–0.1% Y). The times to 1, 2, and 5% creep and the time to rupture are shown for C-129Y at 980°C as functions of stress in Fig. 14.3, and the creep-rupture properties at 1095 and 1205°C are shown in Figs. 14.4 and 14.5. The minimum creep rate at each temperature is shown as a function of stress in Fig. 14.6. This particular heat of C-129Y is one of the weaker materials we have tested.

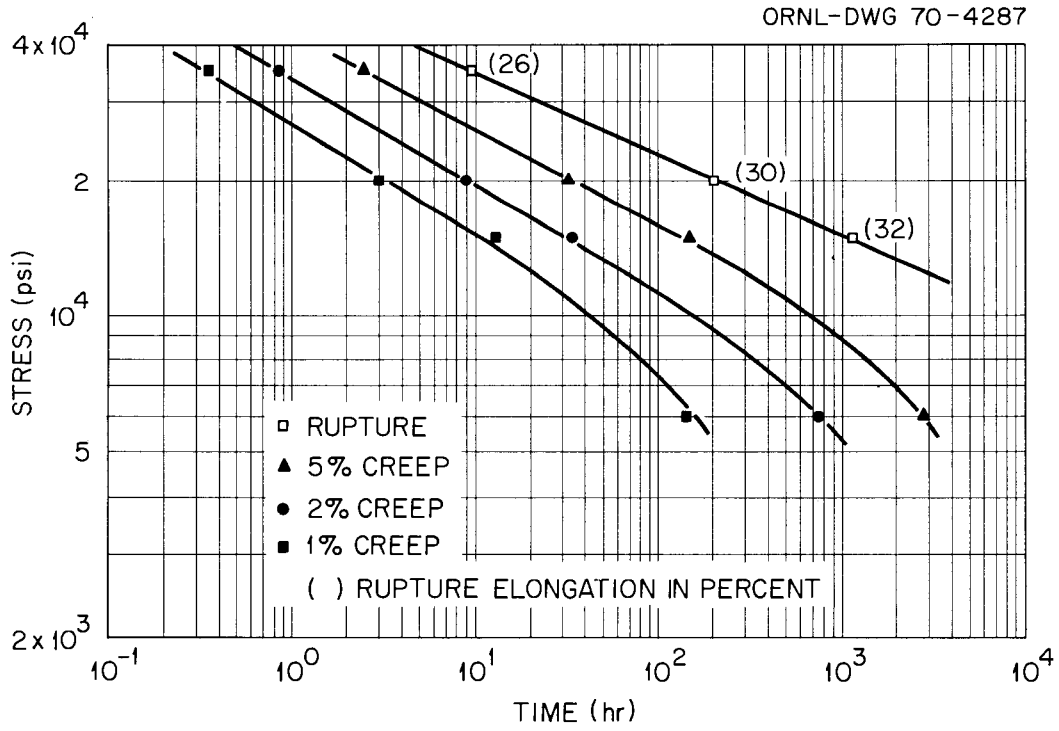

Fig. 14.3. Creep-Rupture Properties of C-129Y at 980°C.

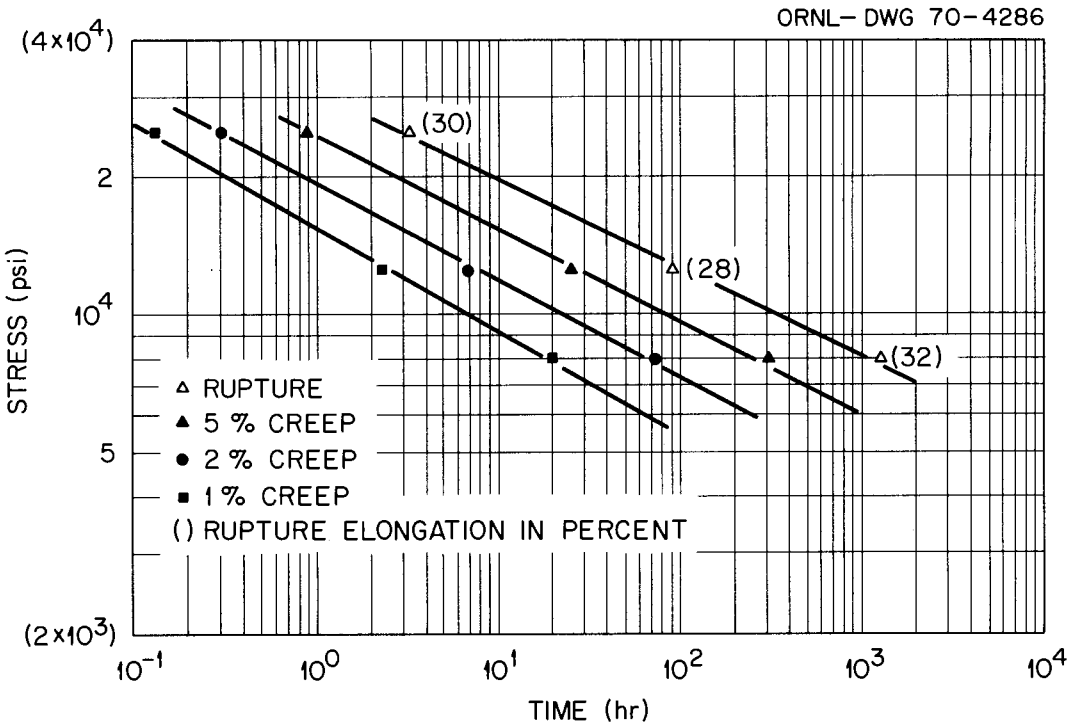

Fig. 14.4. Creep-Rupture Properties of C-129Y at 1095°C.

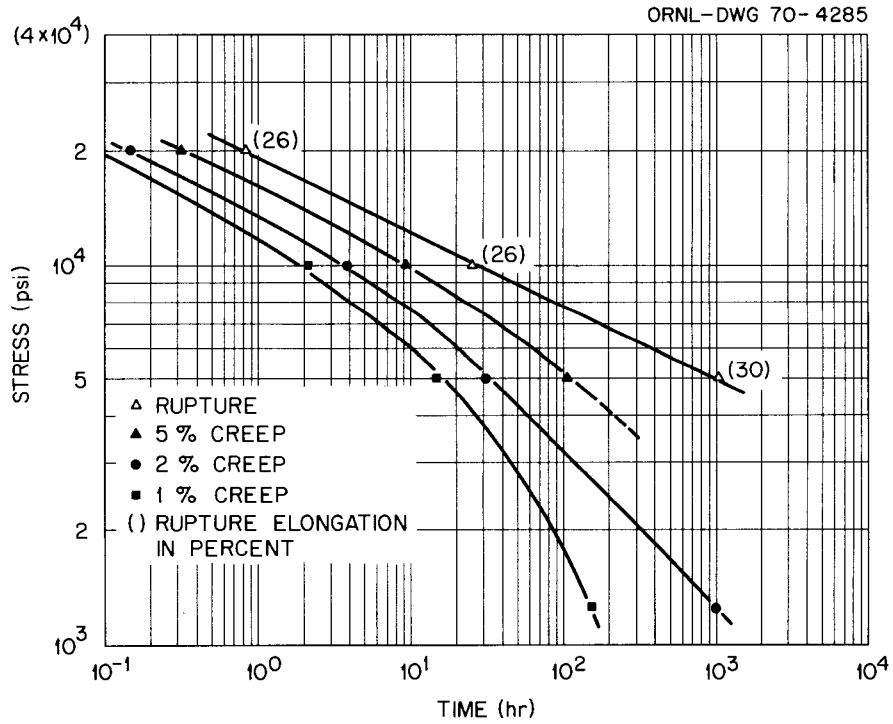

Fig. 14.5. Creep-Rupture Properties of C-129Y at 1205°C.

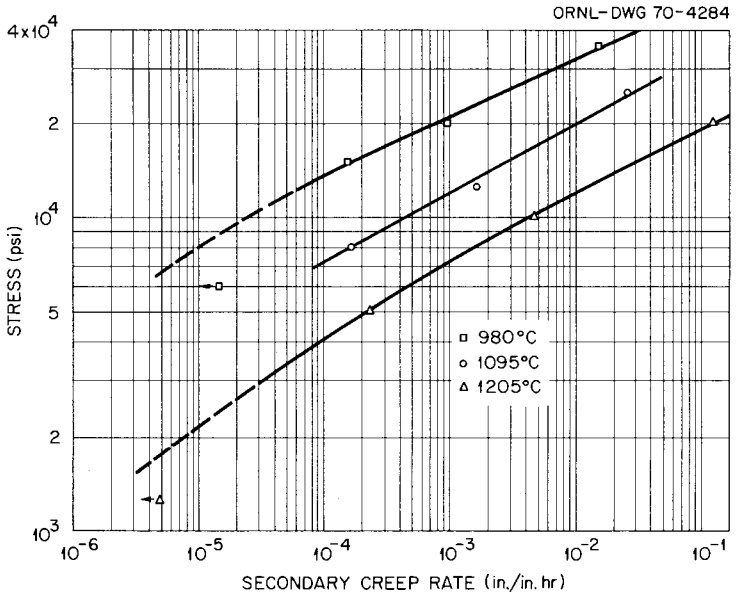

Fig. 14.6. Secondary Creep Rate Versus Stress for C-129Y.

Welding and Brazing

G. M. Slaughter

Studies of Brazing Alloys (Nancy C. Cole, D. A. Canonico)

We concentrated on perfecting our testing methods for determining the remelt temperature of several of our experimental filler metals for brazing. We define the remelt temperature as that temperature at which the braze separates due to an applied measured weight. Initial remelt studies were reported previously.[4] We are revising our techniques so that we can more accurately determine the temperature of the brazed joint when the remelting occurs. Specimens were brazed and are being machined for testing.

Physical Properties

D. L. McElroy

Thermal Conductivity of Tantalum (J. P. Moore, R. K. Williams)

We measured the thermal conductivity, electrical resistivity, and thermopower of a Ta–5% W alloy between 80 and 400°K. These data were

combined with those previously reported[5] for electron-beam-melted Ta and analyzed so that lattice thermal conductivity and electronic Lorenz numbers[6] could be deduced. The result of these calculations conflicts with previous conclusions[5] about the size of the lattice thermal conductivity, presumably because additions of W reduce it in the alloy. We shall investigate this possibility by measuring a Ta–10% W alloy.

Notes

1. C. T. Liu, Fuels and Materials Development Program Quart. Progr. Rept. Dec. 31, 1969, ORNL-4520, pp. 213–215.

2. L. F. Pease and J. H. Brophy, Trans. Met. Soc. AIME 227, 1245 (1963).

3. R. L. Stephenson, Fuels and Materials Development Program Quart. Progr. Rept. June 30, 1969, ORNL-4440, pp. 227–232.

4. D. A. Canonico, Fuels and Materials Development Program Quart. Progr. Rept. Dec. 31, 1969, ORNL-4520, pp. 220–221.

5. R. K. Williams and J. P. Moore, Fuels and Materials Development Program Quart. Progr. Rept. Sept. 30, 1969, ORNL-4480, p. 165.

6. R. K. Williams and W. Fulkerson, "Separation of the Electronic and Lattice Contributions to the Thermal Conductivity of Metals and Alloys," pp. 389–456 in Thermal Conductivity, Proc. 8th Conf., ed. by C. Y. Ho and R. E. Taylor, Plenum Press, New York, 1969.

15. TUNGSTEN METALLURGY

P. Patriarca A. C. Schaffhauser

The objective of this program is to provide the base technology on W alloys for advanced power applications in space. We are developing fabrication processes for W alloys based on modification of conventional extrusion and warm-drawing techniques, direct chemical vapor deposition, and welding. Since the primary criterion for the use of W alloys is based on the creep-rupture properties, we are conducting extensive long-time tests at the temperatures of interest. We are also determining the mechanisms that control the creep behavior and the effect of interactions with the vapor species from an isotope or reactor fuel.

Chemical Vapor Deposition of Tungsten Alloys

J. I. Federer

Chemical Vapor Deposition of High-Purity Tungsten Sheet

We are depositing W sheet stock nominally 0.03 and 0.06 in. thick for welding studies. Five deposits were prepared and more are needed. Since a low F content is needed, the W is being deposited by H_2 reduction of WF_6 on both sides of substrates heated by resistance to 600°C and contained within a water-cooled chamber — conditions that previously[1] yielded W with only 5 to 9 ppm F. Each 2-in.-wide × 17-in.-long deposit provides 16 specimens 3/4 in. wide × 3 1/2 in. long. The specimens are being electropolished to reduce surface roughness and to obtain uniform thickness.

An analytical technique for determining F in W involves reacting the W with water vapor and O_2; the W is oxidized, and F is converted to HF, which is collected for quantitative analysis. We attempted to adapt this analytical technique to the deposition of W with very low F content by using moist H_2 to reduce WF_6. If the F content is significantly lowered without significantly raising the O content, we shall use the technique to deposit additional sheet stock for welding studies.

Chemical Vapor Deposition of Tungsten-Rhenium Sheet and Tubing

The conditions and results of recent experiments on the deposition of W-Re alloys by H_2 reduction of WF_6 and ReF_6 are presented in Table 15.1.

In the first experiment, we deposited a heavy-walled tube and studied the effects of Re content and deposition temperature on the formation of nodules. The tube was deposited on a 3/4-in.-diam × 18-in.-long Mo substrate. The deposition temperature was 700°C, but since the ends of the substrate were cooler, the Re content was higher on the ends, as discussed previously.[2] The surface texture was grainy but contained only a few nodules.

Two sheet deposits were prepared in which the intended Re contents were 1 and 3%. Lower Re contents were actually obtained because a WF_6 flowmeter indicated a flow rate that was about 10% low. These deposits had fewer nodules than deposits that contained about 5% Re. This was the first time that an improved morphology could be associated with a change in deposition conditions (lower ReF_6 content in the gas mixture). We are now hopeful that deposits suitable for determination of mechanical properties can be prepared.

The sheet deposit of W–5% Re included in Table 15.1 was prepared at 600°C. Although some nonuniformity of composition was expected, we used a lower deposition temperature to examine the effect of temperature on the formation of nodules. The deposit ranged from about 12% Re to less than 1% Re over the length and had numerous nodules in the region of highest Re content. There appears to be no benefit in depositing W-Re alloys at temperatures less than 700°C, the approximate minimum temperature required for uniformity of composition.[2]

Deposition of Tungsten with a Dispersion of Fine Particles

We began to study the codeposition of W and compound particulates to provide a material with potentially greater creep strength than unalloyed W. We previously showed that very fine UO_2 particles can be prepared by chemical vapor deposition.[3] We are now attempting to extend this technology to the deposition of W that contains finely dispersed particles of several oxides. Several carbides and nitrides will probably be included in study in the future.

Table 15.1. Conditions and Results of Experiments on Deposition of Tungsten-Rhenium Alloy

Experiment Number	Type Deposit	Deposition Temperature (°C)	Intended Rhenium Content (%)	Actual Rhenium Content at Indicated Distances Along Substrate						Surface Texture
				2 in.	5 in.	8 in.	11 in.	14 in.	17 in.	
222	Tube	700	5	11.7	5.3	4.7	4.4	4.7	10.0	Grainy with a few nodules
223	Sheet	700	3	2.2	1.8	1.7	1.8	2.2		Smooth except for scattered nodules
224	Sheet	700	1	0.2	0.1	0.05	0.2	0.3		Smooth except for scattered nodules
225	Sheet	600	5	12.3	4.7	2.2	1.0	0.5		Very nodular in high-Re region; smooth with scattered nodules over most of remainder

In preliminary experiments we attempted to incorporate 2 to 4 vol % TiO_2 particles in W by reacting a mixture of H_2, WF_6, $TiCl_4$, and H_2O gases. The reactions expected to occur are

$$WF_6 + 3H_2 \rightarrow W + 6HF$$

and

$$TiCl_4 + 2H_2O \rightarrow TiO_2 + 4HCl \ .$$

Chemical analyses of deposits prepared at 800 and 900°C indicated less than 0.1% Ti, but the deposits were about twice as hard as unalloyed chemically vapor deposited W. The possibility of O contamination of the deposits is being investigated. We shall attempt to minimize such contamination by using a substoichiometric amount of water vapor to react with $TiCl_4$.

Temperatures of 800 and 900°C may be too low for deposition of W with a dispersion of TiO_2 particles. If necessary, we shall study the preparation of TiO_2 powder in a separate high-temperature chamber and subsequent transfer of the powder by entrainment into the chamber for deposition of W.

Metallurgical Properties of Tungsten Alloys

H. Inouye

Effect of Low-Pressure Oxygen on the Creep Properties of Tungsten

The creep behavior of W in low-pressure O_2 is being determined at thermionic temperatures to simulate its interaction with the O_2 derived from an oxide fuel. Current results for W in 10^{-5} torr O_2 at 1650 and 2000°C continue to show the deleterious effect of O_2 on the creep strength.

Figure 15.1 compares the creep behavior of W at 1650°C in 7.6×10^{-5} torr O_2 with that obtained in a vacuum of 1.0×10^{-7} torr. Although the steady-state creep rate in O_2, $\dot{\epsilon}_O$, was not well defined, its value was estimated to be 2.5×10^{-5} hr^{-1}. By comparison, the rate in vacuum, $\dot{\epsilon}_V$, was 6.7×10^{-6} hr^{-1}, which gives a ratio of $\dot{\epsilon}_O:\dot{\epsilon}_V$ of 3.7.

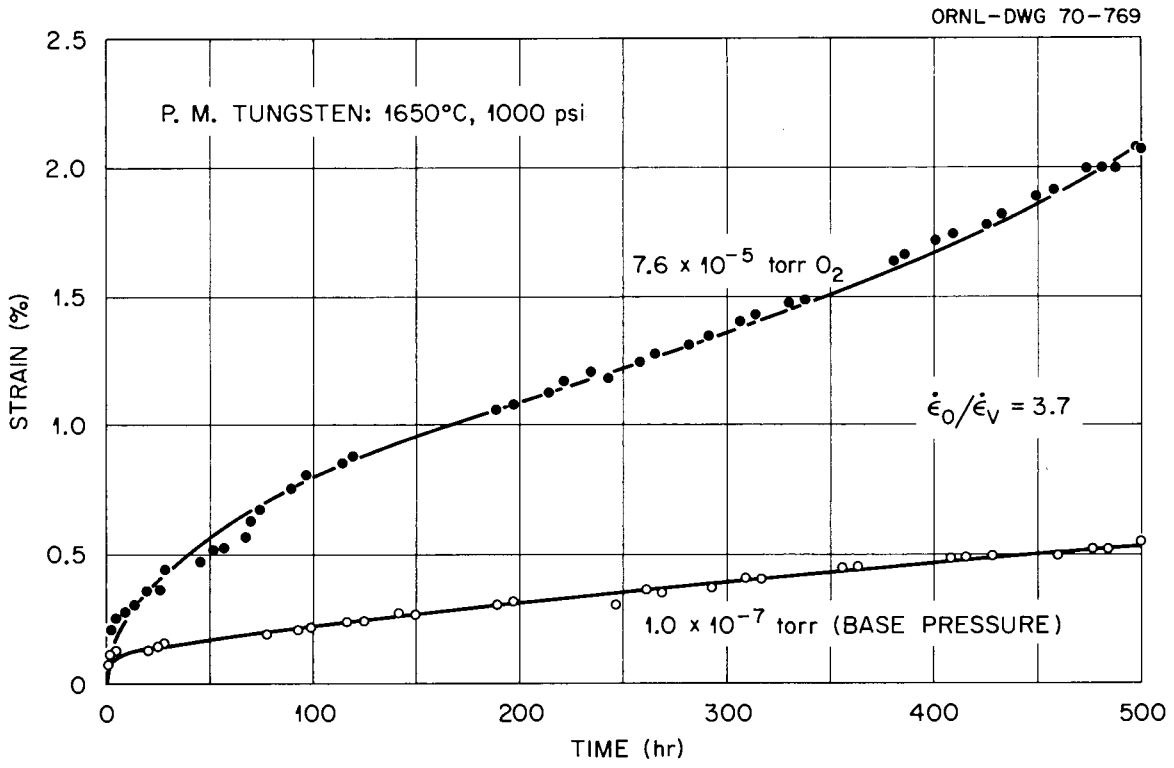

Fig. 15.1. The Effect of Oxygen on the Creep Properties of Tungsten Stressed to 1000 psi at 1650°C.

The time required to produce 0.5% strain in these two environments differed by a factor of about 10. The increase in the creep rate in O_2 can be accounted for by an increase in the creep stress due to sublimation of W as volatile oxides.

Figure 15.2 shows the effect of the O_2 pressure on the creep of W at 2000°C. The results obtained in vacuum at 1.5×10^{-7} torr are shown for comparison. In this case the specimens tested in O_2 do not show a steady-state stage of creep but go immediately into third-stage creep. The test in 8.2×10^{-5} torr O_2 did not last the scheduled 500 hr; the specimen ruptured after 334 hr at a strain of 15.7%.

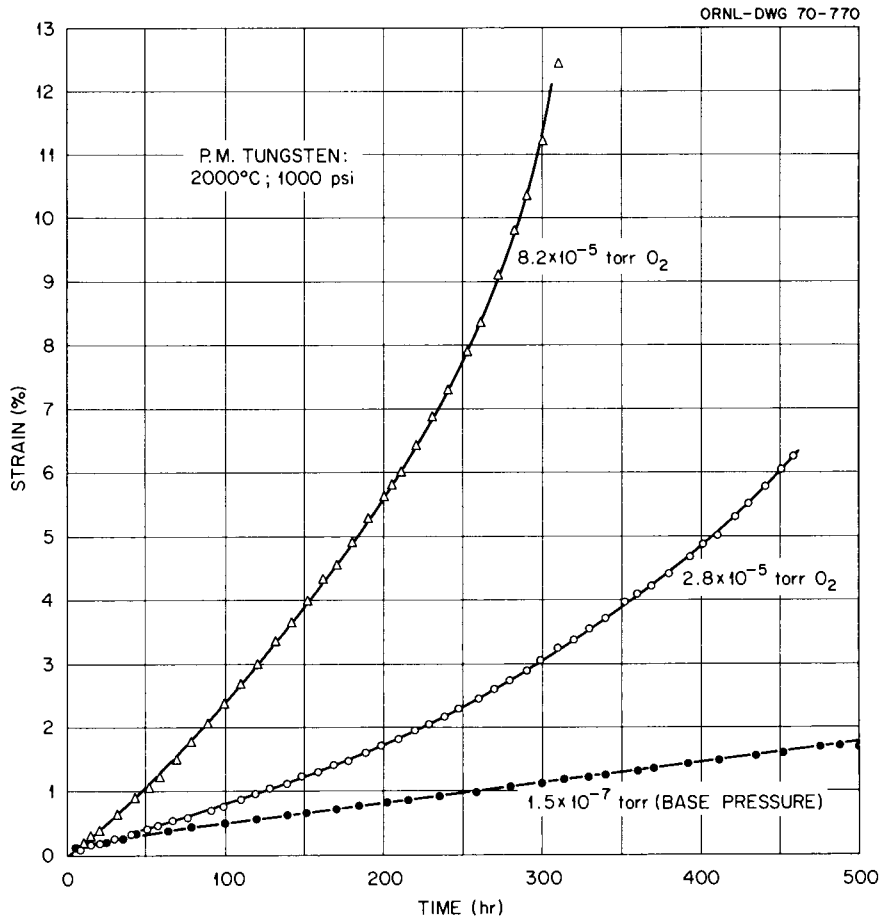

Fig. 15.2. The Effect of Oxygen Pressure on the Creep Properties of Tungsten Stressed to 1000 psi at 2000°C.

Long-Time Creep Properties of Tungsten Alloys

H. E. McCoy, Jr.

Creep-Rupture Properties of Chemically Vapor Deposited Tungsten
(R. L. Stephenson)

The creep properties of chemically vapor deposited W at high temperatures were evaluated several years ago.[4] Recently, the deposition process has been improved to produce higher purity material,[4] and we have undertaken an evaluation of material typical of these more recent deposition techniques. Figure 15.3 gives stress-rupture curves for this material at 1400, 1650, and 2200°C. The strength of this lot of material is very nearly equal to that observed by McCoy and Stiegler.[4] At

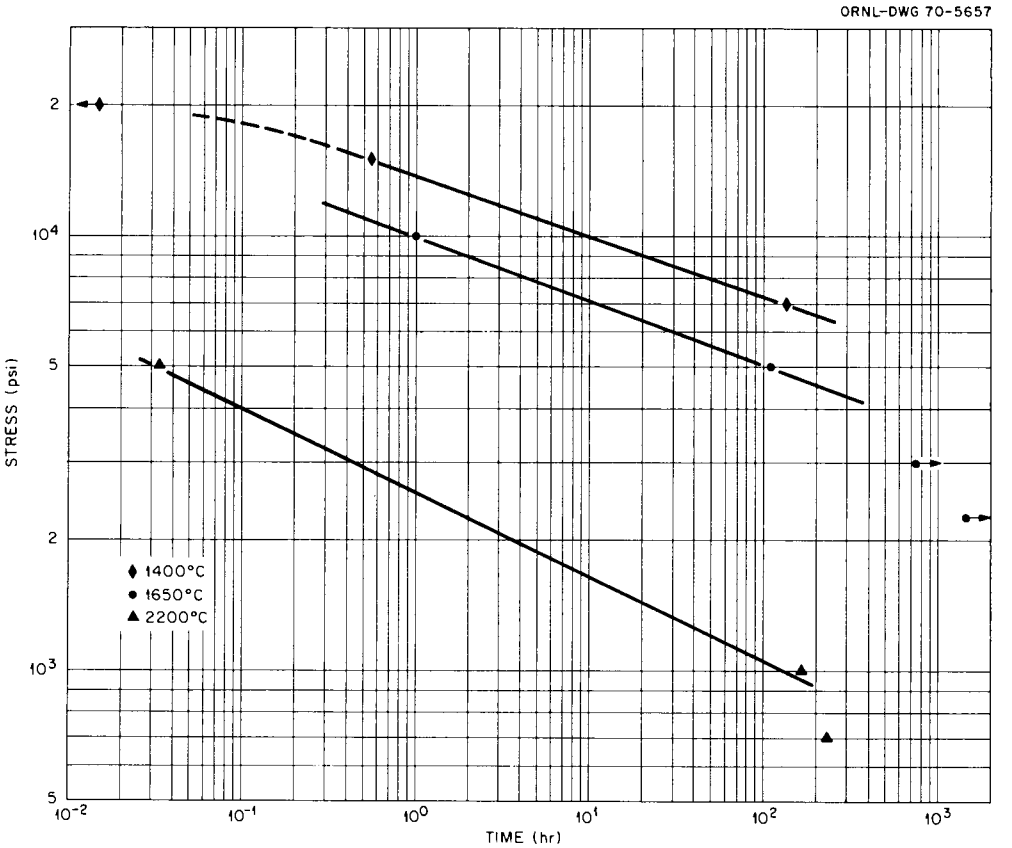

Fig. 15.3. Stress-Rupture Properties of Chemically Vapor Deposited Tungsten.

low temperatures (1400 and 1650°C), fractures occur intergranularly with very little reduction in area, as they did in the material in the previous study. At 2200°C, however, failures were characterized by very high reduction in area, in contrast to the results obtained in the previous study. A more extensive study of the microstructure of this material is under way.

Long-Time Creep Properties of Tungsten-Rhenium Alloys (R. L. Stephenson)

We completed our determination of the creep-rupture properties of W–Re alloys for rupture times to 1000 hr and are now extending our data for low strains to longer times.

In a previous report[5] the available data for time to 1% creep of arc-melted W, W–5% Re, W–26% Re, and W–25% Re–30% Mo were presented in the form of Larson-Miller plots. We now have data to 1000 hr at 1650°C

and are able to compare these data with values predicted from these master curves. Figures 15.4 to 15.7 show the data used to make the prediction (filled symbols), the data determined subsequent to the prediction (open symbols), the prediction for 1650°C (solid lines), and the prediction plus and minus one standard deviation (dotted lines) for each of these materials. For W, the long-time datum point falls within one standard deviation, a very good agreement. For the other three materials, the apparent value at 1000 hr falls outside three standard deviations which, assuming a normal distribution in log time, would correspond to 99% confined limits. These must be considered poor predictions.

Where refractory metals are concerned, contamination always merits consideration. However, since all tests were performed at about the same pressure (about 10^{-6} torr at temperature), one would expect more accurate predictions, regardless of whether contamination produces a cumulative change in strength or an instantaneous change in creep rate [as is the case for W (ref. 6)] in these materials. Another possible cause for such a lack of agreement of predicted and measured values might be inaccurate measurements of strain, although the error would

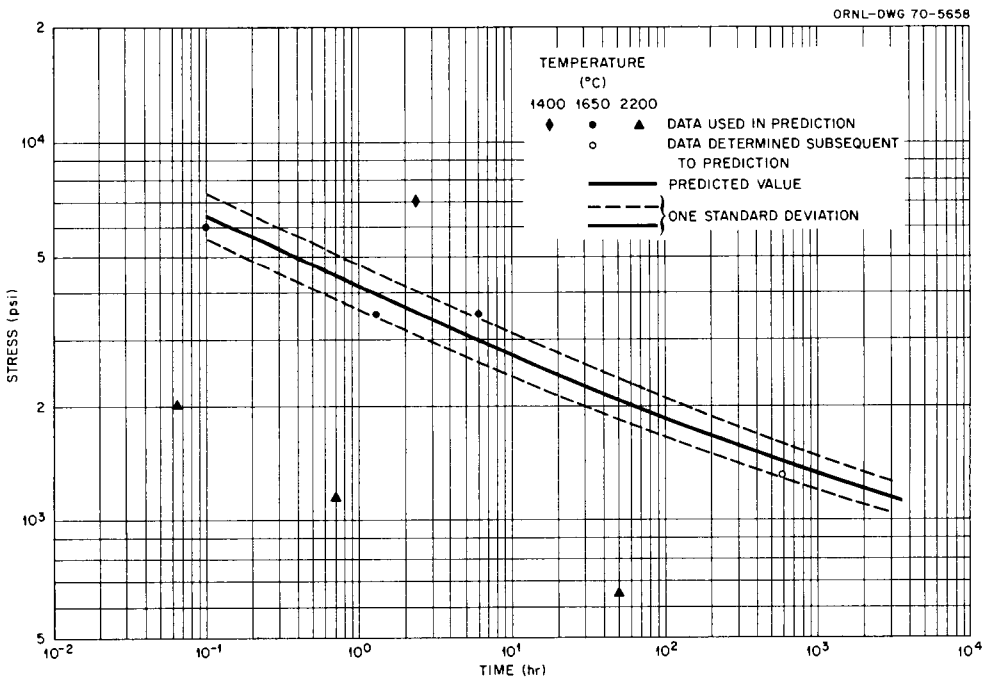

Fig. 15.4. Time to 1% Creep Versus Stress for Unalloyed Tungsten.

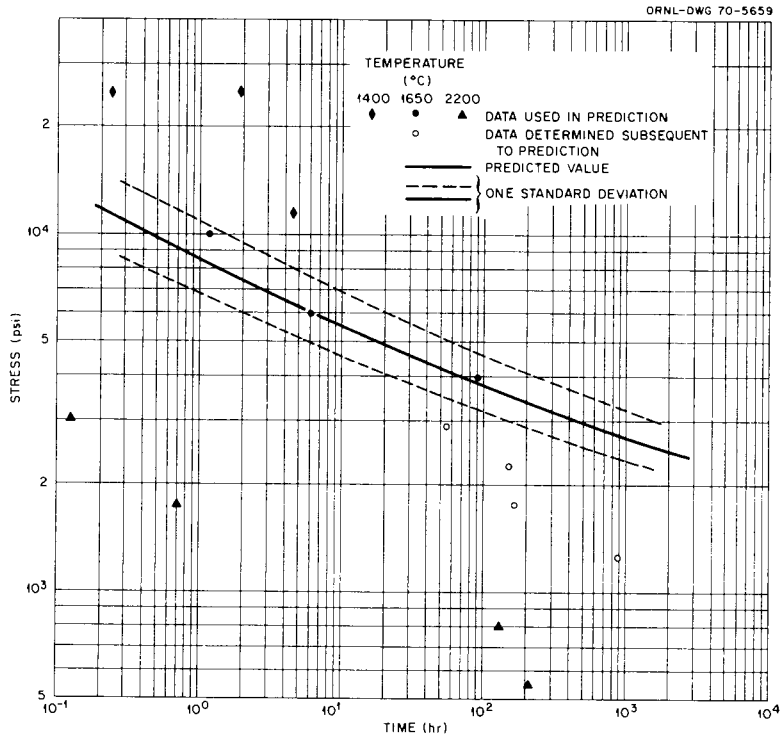

Fig. 15.5. Time to 1% Creep Versus Stress for W–5% Re.

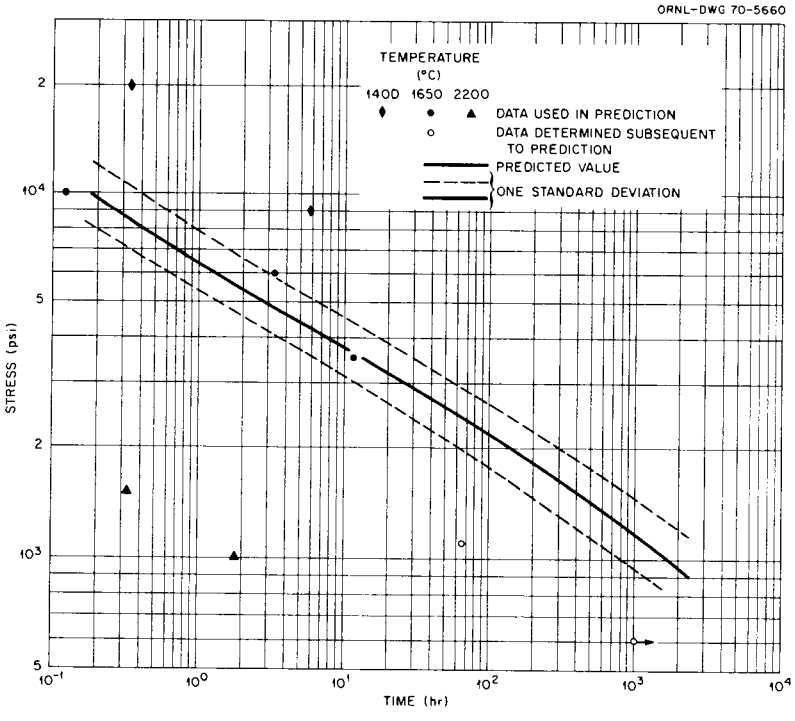

Fig. 15.6. Time to 1% Creep Versus Stress for W–26% Re.

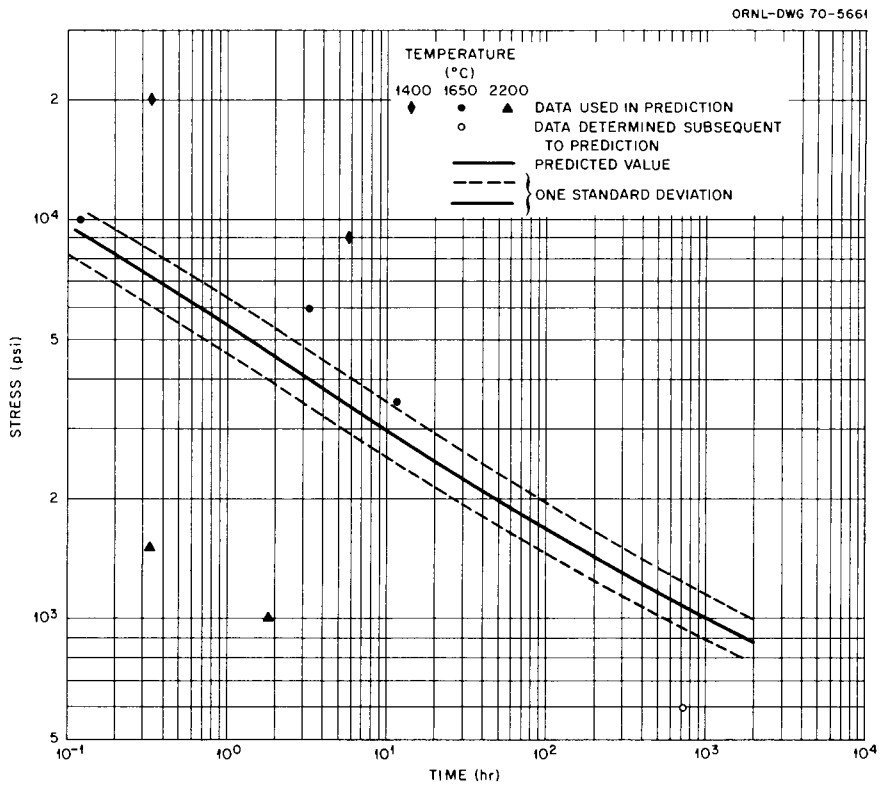

Fig. 15.7. Time to 1% Creep Versus Stress for W–25% Re–30% Mo.

have to be systematic rather than random, or the inaccuracy would produce broad confidence limits rather than confidence limits that did not include the experimental value. Perhaps the most likely possibility is that there were simply too few data to make effective use of a creep parameter.

Evaluation of Methods for Joining Tungsten Alloys

G. M. Slaughter

Gas Tungsten-Arc Welding of Chemically Vapor Deposited Tungsten and Arc-Melted W–25% Re (Nancy C. Cole)

The prime objectives of this program are to develop successful techniques for joining W and its alloys and to determine the properties of these welds. This quarter, we concentrated on gas W-arc welds in both chemically vapor deposited W sheet and arc-melted W–25% Re sheet.

While welding chemically vapor deposited W (nominally 0.050 in. thick), we encountered problems with cracking transverse to the weld (Fig. 15.8). We evaluated several techniques to eliminate the problem, including stress relief at 1000 or 1200°C for 1 to 2 hr before welding, preheating at 150 to 260°C, and stress relief after welding at 1200°C for 2 hr. We also minimized restraint of the workpiece. Thus far, the most reliable procedure for achieving crack-free bead-on-sheet (fusion) welds in chemically vapor deposited W involves the following steps:

1. electropolish in NaOH;
2. stress relieve at 1200°C for 2 hr;
3. preheat to 260°C;
4. W-arc weld at 260 amp, 1/16 in. arc-gap, 10 in./min (for 0.050-in.-thick sheet);
5. loosen restraints and slow cool; and
6. stress relieve at 1200°C for 2 hr.

We continued welding W–25% Re sheet (0.030 in. thick), as reported previously.[7] Using the gas W-arc process, we have now successfully butt welded W–25% Re without preheating. A welding current of 200 amp, an arc length of 1/16 in. and a travel speed of 10 in./min were used. Crater

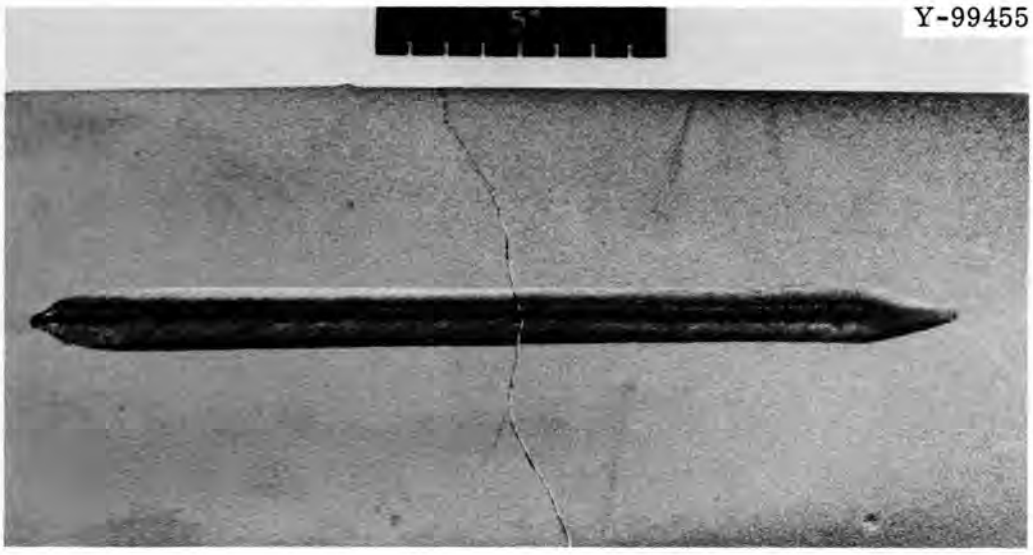

Fig. 15.8. Gas Tungsten-Arc Weld in Chemically Vapor Deposited Tungsten Sheet Showing a Typical Crack Transverse to the Weld.

cracking was eliminated by gradually tapering the current at the beginning and end of the weld. All sound welds will be bend tested to determine their comparative ductile-to-brittle transition temperatures.

Notes

1. J. I. Federer and W. R. Martin, Fuels and Materials Development Program Quart. Progr. Rept. June 30, 1969, ORNL-4440, pp. 148–151.

2. J. I. Federer, Fuels and Materials Development Program Quart. Progr. Rept. Dec. 31, 1968, ORNL-4390, pp. 165–166.

3. J. I. Federer, W. C. Robinson, Jr., and F. H. Patterson, Nucl. Appl. 6, 298–306 (April 1969).

4. H. E. McCoy, Jr. and J. O. Stiegler, Mechanical Behavior of Chemically Vapor Deposited Tungsten at Elevated Temperatures, ORNL-4162 (September 1967).

5. R. L. Stephenson, Fuels and Materials Development Program Quart. Progr. Rept. March 31, 1969, ORNL-4420, pp. 185–187.

6. H. Inouye, "The Effect of Low Pressure Oxygen on the Creep Properties of Tungsten and a Tungsten-Molybdenum Alloy," paper presented at the Vacuum Metallurgy Conference, June 10–19, 1969, Pittsburgh, Penn. To be published in the proceedings.

7. Nancy C. Cole, Fuels and Materials Development Program Quart. Progr. Rept. Dec. 31, 1969, ORNL-4520, pp. 242–244.

16. FAST-NEUTRON IRRADIATION EFFECTS ON ELECTRICAL INSULATORS

G. M. Watson[1] G. W. Keilholtz[1]

The purpose of this program is to establish the effects of fast neutrons on the mechanical, physical, and electrical properties of materials suitable for use as electrical insulators in thermionic converters and to evaluate the mechanisms of neutron damage in these materials up to 1100°C.

General Survey of Fast-Neutron Effects on Electrical Insulators

R. E. Moore[1] D. A. Dyslin[2] H. E. Robertson[1]

An assembly containing four advanced materials[3] as well as polycrystalline alumina was inserted into row 8 of the Experimental Breeder Reactor-II (EBR-II). The advanced materials were (1) synthetic sapphire, (2) single-crystal MgO, (3) transparent Y_2O_3, and (4) silicon oxynitride (Si_2ON_2). The assembly was designed for specimen temperatures of 400 and 800°C.

A low-temperature (below 150°C) assembly containing the first three advanced materials was irradiated in the Engineering Test Reactor (ETR). The purpose of these irradiations is to determine whether any of the advanced materials is more stable than polycrystalline alumina in a fast flux.

Irradiation of High-Density Commercial Al_2O_3 Products Considered for Thermionic Insulators

R. E. Moore[1] D. A. Dyslin[2] H. E. Robertson[1]

Four commercial alumina products of high density are being investigated to establish their behavior in a fast-neutron flux over a broad temperature range. This task is nearly complete. The remaining work includes metallographic and x-ray diffraction examinations of alumina

irradiated in a long-term, high-temperature ETR assembly and in an assembly that was irradiated in row 4 of the EBR-II (ref. 3).

Metal-Clad Al_2O_3 Specimens

R. E. Moore[1] D. A. Dyslin[2] H. E. Robertson[1]

The status of the irradiations of bilayers and trilayers is given in Table 16.1. Irradiation unit 41-42 is now being disassembled in the ORNL hot cells. Unit 0-3 is now undergoing irradiation in row 8 of the EBR-II. It will be removed in the early part of fiscal year 1971.

Table 16.1. Status of Irradiations of Bilayers and Trilayers

Experiment Number	Reactor	Supplier	Design Temperatures (°C)	Fast Fluence [neutrons/cm^2 (> 1 Mev)]	Status
				$\times 10^{21}$	
41-40	ETR	NASA-Lewis Fairchild-Hiller Thermo Electron	600,800 1000,1100	0.6–2.8	Postirradiation examinations nearly complete
41-42	ETR	Thermo Electron Gulf General Atomic	600,800	0.6–2.8	Irradiation completed
0-3	EBR-II	Thermo Electron	700–800		Undergoing irradiation

Notes

1. Reactor Chemistry Division.
2. General Engineering Division.
3. R. E. Moore, D. A. Dyslin, and H. E. Robertson, Fuels and Materials Development Program Quart. Progr. Rept. Dec. 31, 1969, ORNL-4520, p. 245.

17. CORROSION STUDIES OF ADVANCED REFRACTORY METALS

W. O. Harms J. H. DeVan W. R. Huntley[1]

Requirements for auxiliary electricity or ion propulsion for space vehicles necessitate power plants of high efficiency that will operate at high temperatures. For these applications, nuclear power systems have been proposed in which alkali metals are used to transfer heat, drive a turbogenerator, and lubricate rotating components. Accordingly, we are investigating the corrosion properties of candidate alkali metals, primarily Li, K, and Na, under conditions of interest for space applications. Because of the relatively high temperatures (above 1000°C), the investigation is concerned largely with refractory-metal container materials.

Lithium Studies

J. H. DeVan W. R. Huntley[1]

Lithium Forced-Circulation Loop Experiments (C. W. Cunningham,[1] B. Fleischer)

Our program of forced-circulation Li loops is designed to gain information on cladding materials for fuel elements and containment materials for Li-cooled power systems. The first loop in this series (FCLLL-1) is constructed of T-111 and incorporates T-111 test specimens designed to provide information on mechanical properties as well as mass transfer. The loop accumulated 1735 hr of operation at design conditions following its start-up last quarter. Operation was essentially trouble-free until a Li leak occurred after about 1500 hr of operation. Since the rate of leakage increased with time, we decided to stop the test. The leak was located in a vent line leading to the hot leg. We are presently repairing the leak site and parts of the system damaged by the release of Li.

Operating Parameters of FCLLL-1. — The loop was operated with a maximum temperature of 1370°C at the exit from the heater and a minimum

temperature of 1205°C at the radiator exit. The maximum velocity of Li past internal stringers of corrosion specimens was about 15 ft/sec. The pressure in the vacuum chamber decreased from 5×10^{-7} to 3×10^{-8} torr during the period of operation at design conditions.

An energy balance was made between the electrical energy put into the loop (including losses to the bus bars) and the heat energy removed by the chamber cooling circuits. The balance was made with the loop at normal operating conditions and with two specimen furnaces in operation. Results are given in Table 17.1. The power input of 49.6 kw was 2.5%

Table 17.1. Heat Balance for T-111 Lithium Loop (FCLLL-1) with the Loop at Normal Operating Conditions

Location	Power (kw)
Power Input	
Main resistance heater	35.7
Losses[a] to bus bars	8.2
Lithium pump	3.8
1370°C specimen furnace	1.1
1200°C specimen furnace	0.6
Trace heaters for bypass circuit	0.1
Ion pumps	0.1
TOTAL INPUT	49.6
Power Output	
Cooling water for bell	35.5
Cooling water for bowl	5.5
Cooling air for lithium pump	5.9
Cooling air for ion pump	0.6
Cooling water for current feedthroughs	0.9
Losses to ambient air[a]	1.2
TOTAL OUTPUT	49.6

[a]By difference.

greater than the measured heat removal of 48.4 kw. The difference in measurements is believed due to losses from the outside of the bell jar directly to ambient air. The heat balance proved to be useful in finding errors that were originally present in the measurements of electrical input and in diagnosing the behavior of the loop.

Operation of the loop has provided an opportunity to compare the performance of bare-wire and sheathed thermocouples placed on the primary loop circuit. Three configurations of W–25% Re vs W–3% Re thermocouples were used: (1) bare wires (0.005 in. in diameter) that were individually spot welded to the piping, (2) bare wires with a mechanical junction[2] that were held against the pipe by a cover of Ta foil, (3) Ta-sheathed (1/16 in. in outside diameter), BeO-insulated wire assemblies that were held in place with a foil cover. Temperature data obtained during operation confirmed that the spot-welded bare-wire thermocouples provided more accurate measurements because they were an integral part of the pipe wall and suffered less heat loss. At 1370°C, as indicated by the bare-wire thermocouples, the mechanical junctions indicated about 25°C lower and the sheathed thermocouples indicated about 35°C lower. Therefore, we used the temperatures indicated by the spot-welded thermocouples to gage the conditions of loop operation.

A blackbody viewing window was provided on the loop for use with an optical pyrometer to provide a comparison with the thermocouple readings. The pyrometer was calibrated before and after the 1735-hr test to provide a correction factor for the pyrometer readings. In general, the corrected pyrometer readings were about 25°C lower than those of the spot-welded bare-wire thermocouples at 1370°C. The reason for this discrepancy is not yet clear.

Observations of the Lithium Leak. – The first evidence of a Li leak was detected by our residual gas analyzer after 1517 hr of operation at design conditions. A routine scan of the peak currents for residual gas in the vacuum chamber at 1517 hr showed peaks at the mass-to-charge ratios of 6 and 7. These peaks were absent in a scan made 22 hr earlier. We decided to continue operating the loop until the relative size of the leak could be assessed and until we could assure that the leak could be located. Continued monitoring with the residual gas analyzer showed

that the leak was growing larger with time. Finally, the appearance of Li deposits on colder surfaces inside the vacuum chamber indicated that the leak was of a size to preclude further operation. Accordingly, the loop was shut down after having operated 218 hr after the leak occurred.

Readings of partial pressures before and during the leak are shown in Table 17.2. In addition to Li, the analyzer detected K and Na as well as the residual gases normally expected. The source for the K and Na is believed to have been the Li, in which they exist as impurities.

Table 17.2. Concentrations of Residual Gases in Vacuum Chamber Containing Liquid Lithium Loop Test (FCLLL-1)

Gas Species	Pressure, torr[a]					
	Time from Start-Up, hr					
	141	580	1495	1517[b]	1686	1734[c]
	$\times 10^{-8}$	$\times 10^{-8}$	$\times 10^{-8}$	$\times 10^{-8}$	$\times 10^{-8}$	$\times 10^{-8}$
H_2	16.5	4.10	2.13	6.18	2.79	7.53
N_2-CO	6.6	0.82	0.26	0.38	0.29	0.55
Ar	3.1	0.46	0.15	0.31	0.31	0.52
CH_4	1.0	0.18	0.06	0.21	0.12	0.32
CO_2	0.6	0.11	0.01	0.003	0.002	0.003
H_2O	0.6	0.07	0.01	0.005	0.007	0.003
Li^7	0.00	0.00	0.000	0.0035	0.039	0.89
Li^6	0.00	0.00	0.000	0.0003	0.003	0.08
K^{39}	0.08	0.01	0.001	0.0076	0.017	0.38
Na^{23}	0.00	0.00	0.000	0.0019	0.015	0.24
TOTAL[d]	28.5	5.75	2.60	7.10	3.60	10.5

[a]Based on total pressure and ratio of peak currents to sum of peak currents. Ionization probability relative to N_2-CO was taken as 2 for H_2 and 1 for other components.

[b]Lithium leak first detected.

[c]Last scan before shutdown.

[d]Based on hot-filament ionization gage.

The partial pressures of all three alkali metals increased slowly during the first 170 hr of the leak and more rapidly during the final 50 hr. The partial pressure of H_2 was not markedly reduced by the Li on the chamber wall. Only a small amount of H_2 could have been gettered, since the Li was cold (less than 40°C), and the partial pressure of H_2 was low (less than 8×10^{-8} torr).

After we detected the leak, we monitored the windows of the viewing port and the internal chamber surfaces for changes in appearance. Portions of the bowl of the vacuum chamber became darkened and gradually changed to metallic white as a result of the deposition of Li. We also followed the rate at which this film built up by means of an optical pyrometer. A movable quartz shield that could be raised or lowered was positioned between the blackbody and its viewing port to intercept subliming materials whenever pyrometer measurements were not being made. During the period of the leak, we measured blackbody temperature both through the quartz shield and again with the quartz shield raised. The temperature difference between these two measurements uniformly increased at a rate of 35°C/day for the first 160 hr. This rate of change abruptly increased to 140°C/day during the next 25 hr.

A somewhat surprising reduction in transfer of radiant heat to the water-cooled walls of the chamber resulted from the Li coating on the wall. The power required to keep the loop at design temperature levels dropped from 35.6 to 32.8 kw during the leak period. Temperatures of the reflective insulation typically increased from 670 to 765°C. Also the temperature of the loop support structure increased from 365 to 625°C as did the junction temperatures of the thermocouple compensating lead wire mounted on this frame. This resulted in errors in the temperatures indicated by the sheathed thermocouples of about −100°C because of generation of a counter electromotive force.

Visible Effects of Lithium Leak. — The leak site, shown in Fig. 17.1 was readily identified once the vacuum chamber had been opened. It was in the uninsulated tubing of the primary circuit. The line had been filled with static Li during operation, and the temperature at the leak site was calculated to be about 1125°C.

Photo 77631

Fig. 17.1. Site of Lithium Leak in 1/2-in.-OD Vent Line in Primary Circuit as Viewed with a Mirror.

A portion of the Li escaping from the leak reacted with alumina insulators that covered nearby bare-wire thermocouples. Some of these insulators were completely disintegrated; others were coated with reaction products, as can be seen in Fig. 17.2. However, the thermocouples continued to operate satisfactorily in spite of the deterioration of the insulators.

In certain areas, the high-emissivity iron titanate coating flaked off the Cu bus bars as the result of reaction with Li at the operating temperature. Such areas are visible on the specimen furnace in Fig. 17.3 where the iron titanate coating was separated from the Cu conductor. Frozen droplets of Li can be seen both on the bare surfaces of the conductor and on the iron titanate coating. The effect of temperature on

Fig. 17.2. Thermocouple Wires Exposed by Lithium Attack of 0.045-in.-diam Alumina Insulators.

Fig. 17.3. View of Condensed Lithium Droplets on Specimen Furnace and Flaking of Iron Titanate Coating from 1/2-in.-diam Copper Bus Rod.

the reaction of Li with iron titanate is not known; however, coatings were observed to be tightly adhering on one bus that had been at 370°C and loosely attached on another that had been at 590°C.

Portions of the loop piping between electrical bus bars were found to have shifted from the positions in which they had been installed. The major cause of the movement was the overheating of a Cu bus bar that supported the hot leg of the loop. The bus bar had sagged and rotated about its upper anchor point. The overheating and subsequent deflection of the bus bar resulted from the reduction in heat transfer by radiation, which in turn resulted from the deposition of Li on the walls of the chamber. The temperature of the bus bar had increased to at least 590°C during the final 49 hr of operation. The weight of the loop structure above the upper anchor point of the bus bar was sufficient to cause the bus bar to distort and in turn to deflect the hot leg of the loop from its original position.

Disposal of Released Lithium. — As a safety precaution, we admitted a mixture of Ar and dry O_2 into the vacuum chamber to preclude any rapid reaction of finely dispersed Li with air during removal of the bell jar. A mixed stream of Ar at 2 scfh and O_2 at 0.4 scfh was circulated through the chamber at ambient temperature for three days. This stream entered the chamber bowl and was discharged through an oil bubbler at the top of the bell. The Li films, which were still bright after removal of the bell, changed color as moist air entered the tank. The Li deposits inside the bell and bowl were allowed to remain in contact with atmospheric air during a 22-day period of repair activities and did not become moist or fluid as would be the case with alkali metals such as K or Na.

The following cleaning procedure was established for removal of the Li. Accumulations of Li on the walls of the chamber were repeatedly sprinkled or doused with distilled water until bubbling and visible reaction ceased. All accessible areas were flushed or wiped down with a 2% solution of ethanolic acid and then rinsed with distilled water. The acid solution was necessary to remove a residual film that remained after reaction with water. Heavier accumulations were wiped or given an additional flushing with ethanol. Reflective insulation contaminated

with Li was replaced. Most loop piping and support structure within the chamber had no detectable Li film, because its operating temperature had prevented deposition of Li, and, therefore, required no cleanup. The ion pumps also did not require cleaning, since they had been adequately protected from Li by their recessed wells and by the cold chamber wall above the pumps. This applied to the gas analyzer and other electrical and instrumentation feedthroughs as well.

Failure Analysis. – The portion of the vent line tubing that contained the failure was sectioned for visual examination. Lithium residues were removed by immersion in water. The outer surface of the tube exhibited an eroded area about 3/8 in. in diameter, as shown in Fig. 17.4. The inner surface exhibited a crack that apparently was linked with the base of the eroded area. The inside of the tubing also contained many protuberances and crater-like spots, as shown in Fig. 17.5. We also found several cracks in this area that did not penetrate the wall. These suggest that the crack that led to failure emanated from the inner surface of the tubing.

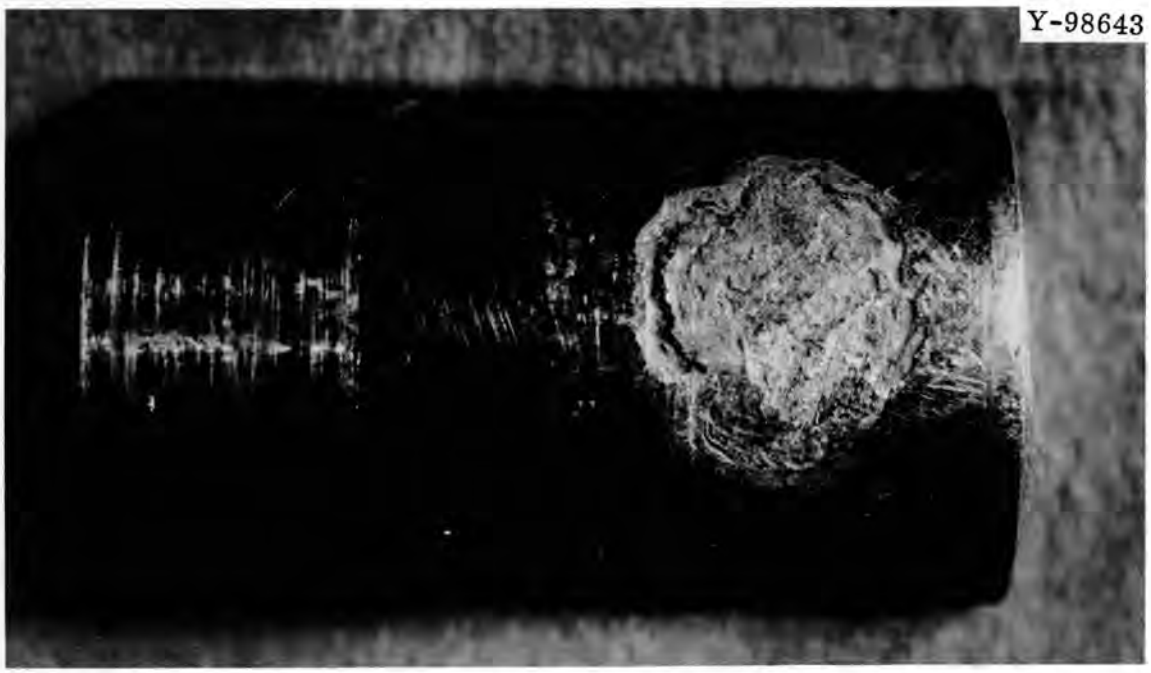

Fig. 17.4. Outer Surface of Failed Vent Line Showing the Corroded Area Surrounding the Failure Site. About 5×.

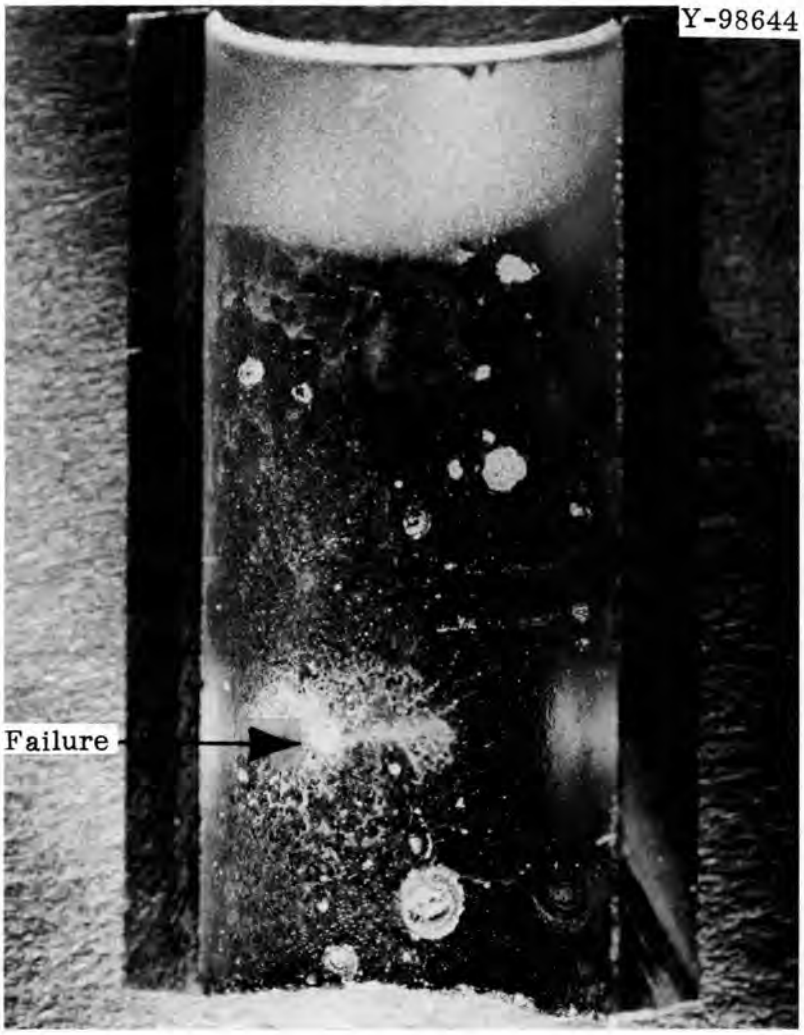

Fig. 17.5. Inside Surface of Failed Vent Line at the Failure Site. About 5×.

Bulk chemical analysis of the wall of the tubing adjacent to the failure showed no significant changes in the quantities of C, O, and N present as compared to that present in the material before the test. The nature of the deposits and cratered reaction spots is being investigated further by electron microprobe analysis and metallographic examination.

Repair of the Loop. — The failure appeared to be associated with foreign material on just one side of the vent tube. This suggested that the contaminants leading to failure were of local origin and that it would be feasible to continue loop operation if we could avoid dependence upon the vent line. Since this line had not been required for

venting during previous operation, we elected to delete the line and cap off the remaining stub.

We cleaned the stub and inserted a T-111 plug into the tube to keep Li, which could not be completely removed from the adjacent tubing, from escaping during subsequent welding. This plug was fusion welded to the tube, and then a cap was put over the stub and welded to the stub base. This final weld was made over an existing T-111 weld bead, which we felt to be of sounder quality than the vent tube itself. To minimize chances of hot cracking, Nb–1% Zr filler metal was used. The completed repair weldment is shown in Fig. 17.6. X-ray and dye penetrant examinations indicated all weldments to be sound.

Both welds were made in a Plexiglas glove box that contained an expandable plastic bladder that provided a means of purging the welding box while maintaining a small positive pressure during both venting and backfilling with inert gas. Welding periods were limited to 10 to 15 sec to minimize contamination from outgassing of the glove-box materials. The box was purged ten times before welding and three times after each welding period. All procedures for field welding were established and practiced by making simulated field welds in the same glove box before making the actual repair.

Repairs of damage caused by the Li are in progress. The bus bar was straightened, and two additional supports were added to preclude sagging in future operation. The Cu brackets for connecting the bus bars and the lugs of the resistance heater were remade with larger surface areas for heat rejection. This modification was needed because the T-111 lugs lost portions of their iron titanate coating and would otherwise operate at too high a temperature. All 16 bare-wire thermocouples were removed. Twelve thermocouples were undamaged and will be reused.

Penetration of Refractory Metals by Alkali Metals (R. L. Klueh)

We previously reported[3] on the penetration of O-doped Nb by Li at 600°C. We concluded that the threshold O concentration for intergranular and transgranular penetration by Li was 400 and 800 ppm, respectively. We have now completed similar tests on the penetration of Nb by K and Na at 600°C; the results are given in Tables 17.3 and 17.4. Again,

Fig. 17.6. Completed Repair Weld of Vent Line Leak Showing 5/8-in.-OD Cap Welded in Place.

Table 17.3. Depth of Penetration of Oxygen-Doped Niobium by Potassium at 600°C[a]

Oxygen Concentration (ppm)	Maximum Depth of Penetration,[b] in.	
	Intergranular	Transgranular
650	0	0
800	0	0
1000	0.0001	0
1500	0.0024	0
1900	0.0026	0
2600	0.0025	0.0002
2900	0.0020	0.0004
4100	0.020	0.0020

[a]Specimens were exposed simultaneously for 20 hr in a container of type 304 stainless steel.

[b]Specimen was 0.04 in. thick; penetration to 0.02 in. represents complete penetration.

Table 17.4. Depth of Penetration of Oxygen-Doped Niobium by Sodium at 600°C[a]

Oxygen Concentration (ppm)	Maximum Depth of Penetration,[b] in.	
	Intergranular	Transgranular
400	0	0
600	0	0
800	< 0.0001	0
1000	0.0001	0
1600	0.0020	0
2000	0.0060	< 0.0001
2600	0.020	0.0001
3400	0.020	0.0015

[a]Specimens were exposed simultaneously for 20 hr in a container of type 304 stainless steel.

[b]Specimen was 0.04 in. thick; penetration to 0.02 in. represents complete penetration.

intergranular and transgranular attack was noted. The threshold concentrations for intergranular and transgranular penetration are about 1000 and 2500 ppm O for K and 800 and 2000 ppm O for Na.

Notes

1. Reactor Division.

2. D. L. Clark, C. W. Cunningham, B. Fleischer, and W. R. Huntley, Fuels and Materials Development Program Quart. Progr. Rept. Sept. 30, 1969, ORNL-4480, pp. 196–201.

3. R. L. Klueh, Fuels and Materials Development Program Quart. Progr. Rept. Sept. 30, 1969, ORNL-4480, pp. 202–204.

PART III

GENERAL REACTOR TECHNOLOGY

FUELS

18. FISSION-GAS RELEASE AND PHYSICAL PROPERTIES OF FUEL MATERIALS DURING IRRADIATION

O. Sisman[1]

The purpose of this work is to measure the variables that control the release of fission gas from highly characterized nuclear fuels and to evaluate these variables in terms of a generalized model for predicting release from operating fuel materials. Thermal diffusivity is measured in-reactor in analogous experiments.

Measurements of Thermal Diffusivity in UO_2 During Irradiation

R. M. Carroll[1] R. B. Perez[1]

Our method of measuring thermal diffusivity during irradiation is to make a stepped change in the fission power generated by the fuel specimen and then measure the dependence of the resulting temperature changes on time. One problem of measuring the thermal diffusivity of UO_2 during irradiation is that there is a large temperature gradient at any realistic power level. This makes it very difficult to measure the temperature at any point except at the center of symmetry of the specimen. By this method we are able to obtain measurements of thermal diffusivity by measuring only the time response of the temperature at the center of symmetry.

In developing this method, we solved many problems involving instrumentation, irradiation technique, computer processing of data, nonfission heating, release of stored energy, and the mathematical formulations of the general theory into computer codes. We completed the computer program for obtaining the values of thermal diffusivity from the general theory.

Behavior of Sol-Gel $(U,Pu)O_2$ During Irradiation

R. M. Carroll[1] R. A. Bradley

A capsule containing 51 microspheres of sol-gel $(U,Pu)O_2$ with 10.8 g/cm^3 density was irradiated in the C-1 facility to a total burnup of 7.13×10^{20} fissions/cm^3 (2.94% heavy metal). The details of the capsule and the characteristics of the specimens were given previously.[2] The primary purpose of this experiment was to compare the irradiation behavior of these specimens with that of specimens prepared from pressed-and-sintered mixed oxide fuel.

The mixed oxide specimens irradiated in the past[3,4] had small interconnected passages that allowed the fission gas to trickle out after irradiation had ceased. As irradiation progressed, these passages would, to some extent, become sintered closed by fission-spike sintering. This lowered the rate at which the fission gas was released as irradiation progressed. The fuel thus contained gas in fragile, closed pockets; and thermal shock, such as rapid heating or cooling, would cause some of these pockets to break and cause cooling and heating bursts. The increased surface area from the opened passages subsequently resulted in a higher steady-state release rate that decreased as the passages once again sintered closed. As burnup progressed, enough gas pressure developed within the fuel to cause breakaway gas release. We were able to measure the relation of temperature and burnup necessary to cause this breakaway gas release.

The rate at which fission gas was released from the sol-gel specimens at the beginning of irradiation was about double that for the previous specimens (after corrections for the different ratios of surface to volume). The sol-gel specimens did not sinter during irradiation to the extent that the other specimens had. There were no cooling bursts when the sol-gel specimens were cooled rapidly, and there was also little of the trickle release of fission gas after cooling that had characterized the previous specimens. These observations all implied that the porosity in the sol-gel specimens was of larger size than that in the pressed-and-sintered mixed oxide specimens.

After a heavy metal burnup of 1.7%, bursts of fission gas were emitted from the sol-gel specimens during irradiation at 880°C. These bursts contained high concentrations of ^{133}Xe, which indicated that trapped pockets of gas were being ruptured. Previous mixed oxide specimens (10.7 g/cm^3 density) had shown such behavior at 880°C after a burnup of 2.7%. The previous specimens had a breakaway gas release that occurred at lower temperatures as burnup progressed because of the greater pressures of fission gas within the fuel. However, the sol-gel specimens apparently relieved their gas pressures at about 880°C after 1.8% burnup, and the relationship of temperature and gas burst did not change with burnup up to 2.9%.

In contrast to the previous experiment, the sol-gel specimens did not show a greater surface area after the pockets of fission gas vented to cause the steady-state bursts. Even though temperatures of 880°C and over caused very high rates of bursts, measurements at lower temperatures showed no change in surface area. Thus, the sol-gel specimens apparently did not swell; instead, the gas pockets either opened microcracks that had closed after the gas was vented or else bubbles migrated to the surface.

These results imply that the sol-gel specimens had a structure that contained large, interconnected porosity and that the structure was not as strong as that of the sintered mixed oxide. Irradiation of the specimens was terminated, and postirradiation examination of the microstructure is under way.

Notes

1. Reactor Chemistry Division.

2. R. M. Carroll, R. A. Bradley, and H. E. Robertson, Fuels and Materials Development Program Quart. Progr. Rept. Dec. 31, 1969, ORNL-4520, pp. 261–264.

3. R. M. Carroll, Fuels and Materials Development Program Quart. Progr. Rept. March 31, 1969, ORNL-4420, pp. 72–74.

4. R. M. Carroll, Fuels and Materials Development Program Quart. Progr. Rept. June 30, 1969, ORNL-4440, pp. 56–58.

19. DEVELOPMENT OF FUEL ELEMENT FABRICATION

G. M. Adamson, Jr.

The purpose of these programs is to devise new combinations of materials or new fabrication techniques to advance the technology for fabricating fuel elements and components for research reactors. We are attempting to improve the performance of advanced research reactors, such as the High Flux Isotope Reactor (HFIR) and Advanced Test Reactor (ATR), by developing fuel elements with lower production cost, longer lives, increased safety or reliability, or all three. The studies include factors affecting both fabrication and irradiation performance. We must also develop sufficient knowledge of the processes used for fabricating Al-base dispersion fuel elements so that we can adequately assist commercial fabricators, purchasers, specification writers, and technical inspectors. Other studies are aimed at improving the reliability and reducing the cost of the required nondestructive inspection techniques.

Irradiation Studies

W. R. Martin

Postirradiation Examination of Miniature Fuel Plates (A. E. Richt, M. M. Martin)

We completed metallographic examination and postirradiation blistering tests on miniature fuel plates from the ORNL 68-1, 69-1, 69-2, and 69-3 irradiation test experiments.[1] As reported previously, all fuel plates from these experiments visually appeared to be in excellent condition, and the amount the fuel core actually swelled agreed well with that predicted by our swelling model.[2]

In general, the microstructure of the fuel plates appeared to be quite normal for the particular type of fuel dispersion and the achieved burnup levels. However, two of the fuel plates exhibited unusual microstructural effects that could indicate incipient failure.

One of these plates (0-56-957) contained 50 wt % high-fired U_3O_8 and had been exposed to an average burnup of 2.24×10^{21} fissions/cm^3. However, this plate was irradiated in a position where a steep flux gradient existed along the length of the plate. Thus, the burnup varied from about 1.9 to 2.54×10^{21} fissions/cm^3 from one end of the plate to the other. This represents the maximum burnup achieved in any of our test specimens. As shown in Fig. 19.1, the microstructure of the end of the plate that achieved low burnup appeared to be quite normal. In spite of extensive reaction between the fuel particles and matrix, no incipient failure was indicated at the end that achieved low burnup. However, at the other end the fuel core contained numerous, large, irregularly shaped voids, which could indicate the onset of breakaway swelling or blistering.

In the second case, small cracks were observed at the corners of fuel particles in plate 0-67-986 (Fig. 19.2). This plate contained 40 wt % high-fired U_3O_8 with 51% fines and had achieved a burnup of 1.8×10^{21} fissions/cm^3. This also could be indicative of the onset of blistering. It should be emphasized, however, that in neither instance could these effects be definitely classified as a failure.

Sections of these fuel plates were heat treated after irradiation to determine the temperature of breakaway swelling or blistering. As shown in Fig. 19.3, results of these tests agree reasonably well with extrapolation of blistering tests on sections from irradiated HFIR fuel elements. However, there does appear to be some subtle differences between the blistering behaviors of these miniature fuel plates. For example, at equivalent levels of burnup, burned U_3O_8 dispersions appear to be somewhat more resistant to blistering than the high-fired U_3O_8 dispersions. The fines content of the dispersions also appears to have some slight effect upon the blistering behavior of the fuel plates. As shown in Fig. 19.4, high-fired U_3O_8 dispersions that contain the most fines appeared to be slightly more resistant to blistering than those that contain less fines. These also appeared to be some tendency for plates that contained more fuel fines to warp during heat treatment after irradiation. This was particularly evident for the burned U_3O_8

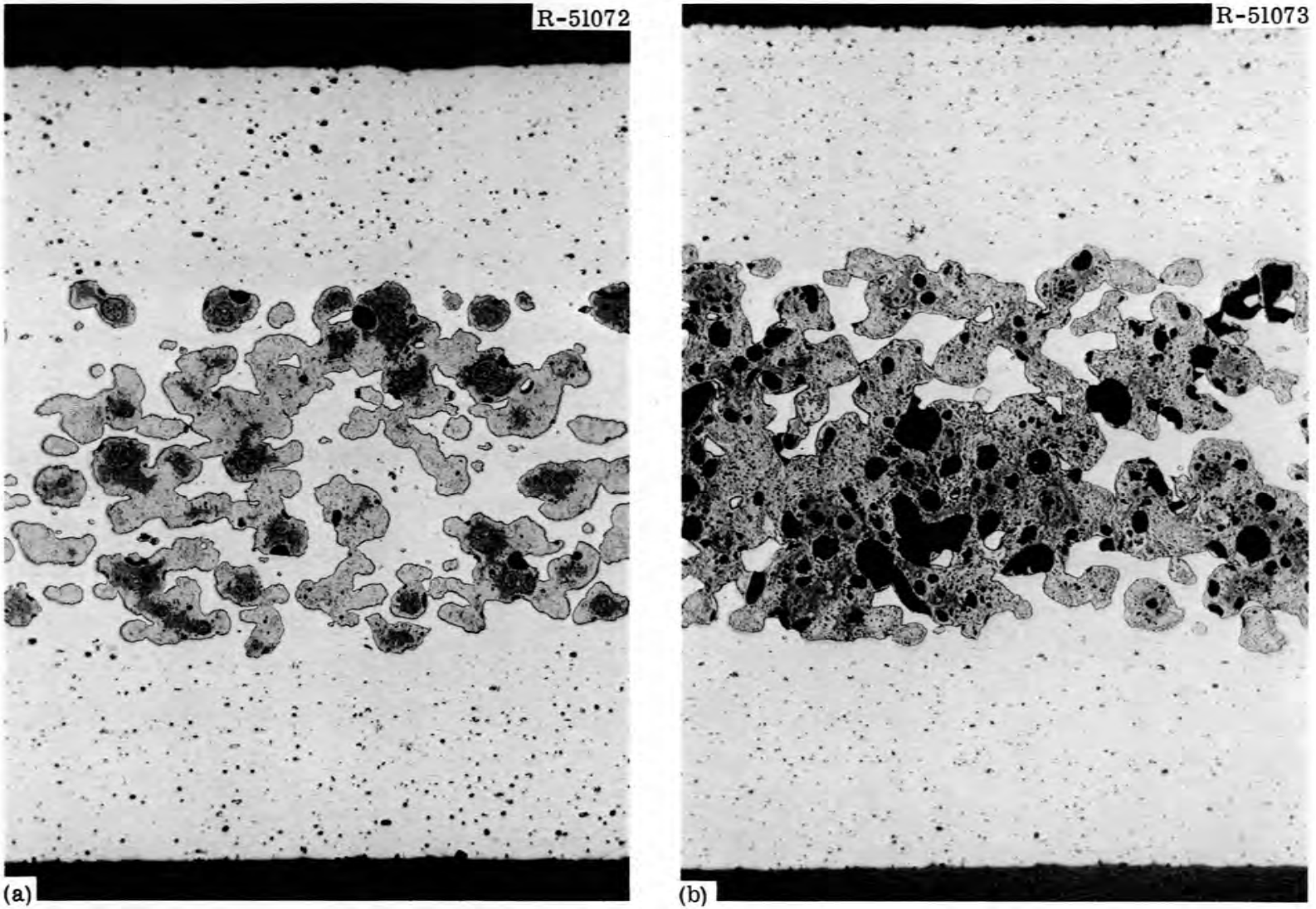

Fig. 19.1. Microstructure of Fuel Plate 0-56-957. (a) End that achieved low burnup, and (b) end that achieved high burnup. As polished. 100×.

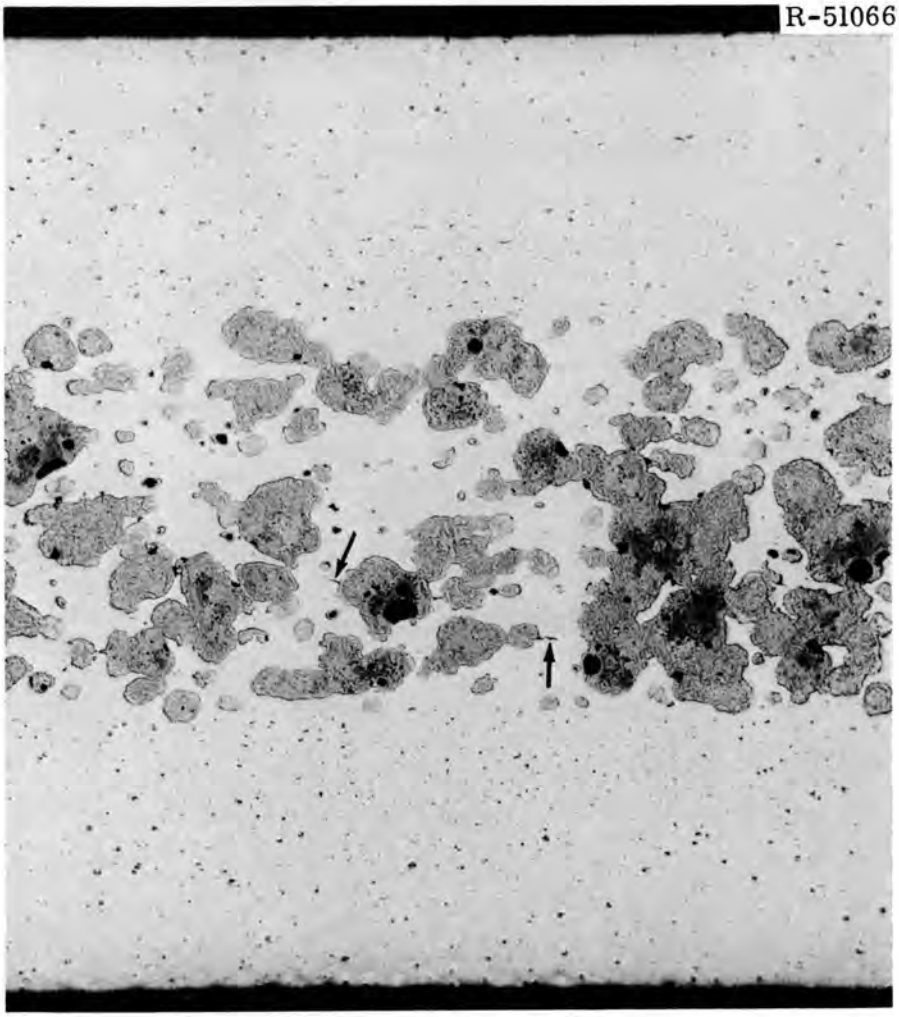

Fig. 19.2. Microstructure of Fuel Plate 0-67-986. Arrows point to small cracks at corners of fuel particles. As polished. 100×.

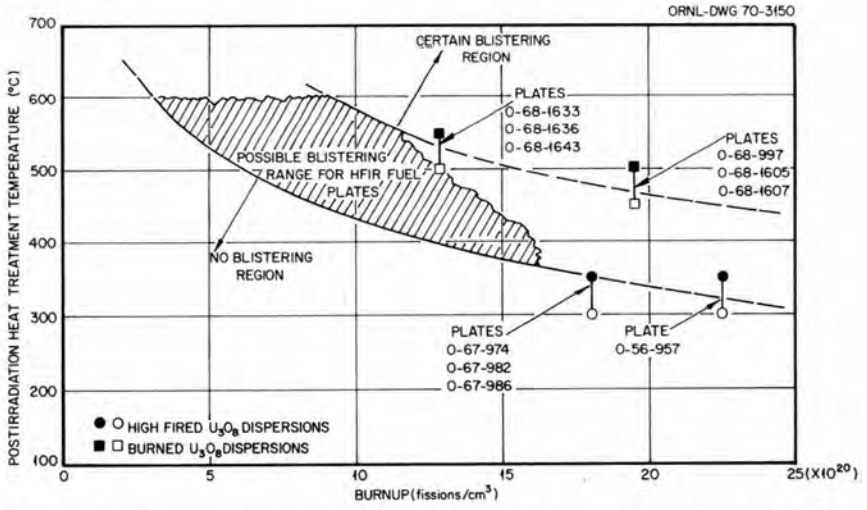

Fig. 19.3. Postirradiation Blistering Temperatures of Aluminum-Based U_3O_8 Dispersion Fuel Plates.

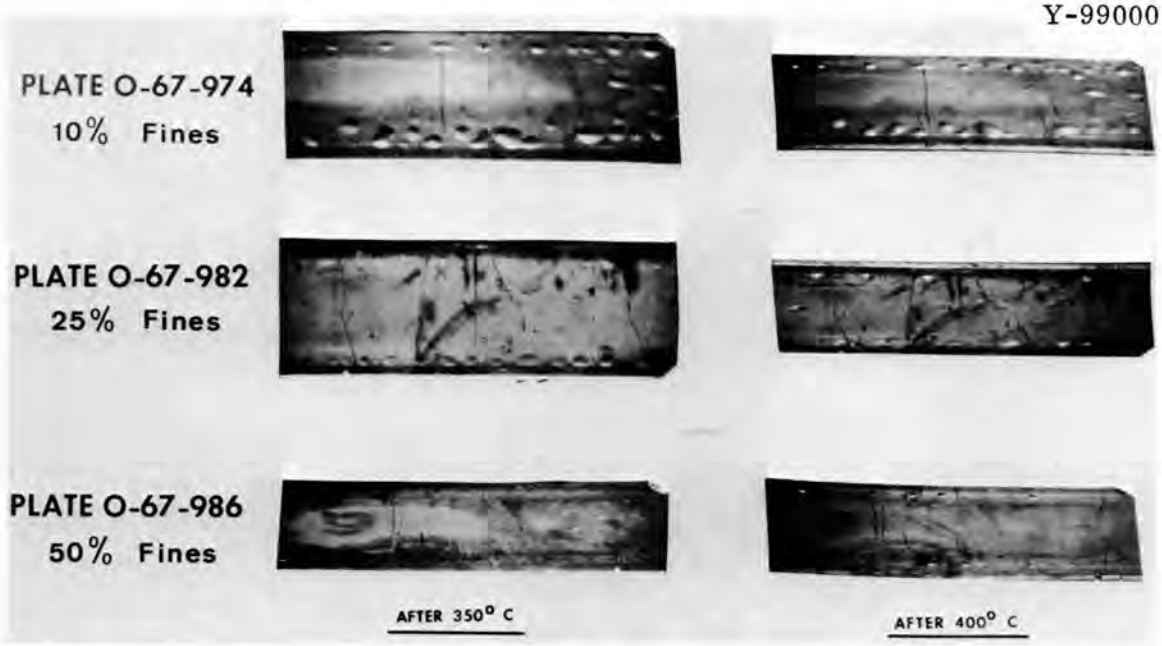

Fig. 19.4. Blistering Patterns Obtained During Heat Treatment of High-Fired U_3O_8 Fuel Plates After Irradiation.

dispersions. An example of this phenomenon is shown in Fig. 19.5; this plate warped severely.

Evaluation and Design of Cermet Fuel Plate for Irradiation Experiments in HFIR (M. M. Martin, W. K. Crowley[3])

Our objective is to determine those factors that influence the performance of Al-clad UAl_x and U_3O_8 dispersions in the ATR and HFIR at a fission density of 1.8 to 2.8 $\times 10^{21}$ fissions/cm^3. An experimental facility that would allow this fission density to be achieved in four reactor cycles is being designed for the reflector region of the HFIR. Each experiment will consist of 18 uninstrumented plates and 3 instrumented plates. Temperatures will be measured by means of thermocouples inside the instrumented plates, and the other plate temperatures will be calculated.

Approval has been obtained from laboratory management to use the facilities for these irradiations.

Table 19.1 summarizes the fuel compositions to be tested in the first experiment. In the first experiment, we should be able to accomplish the following:

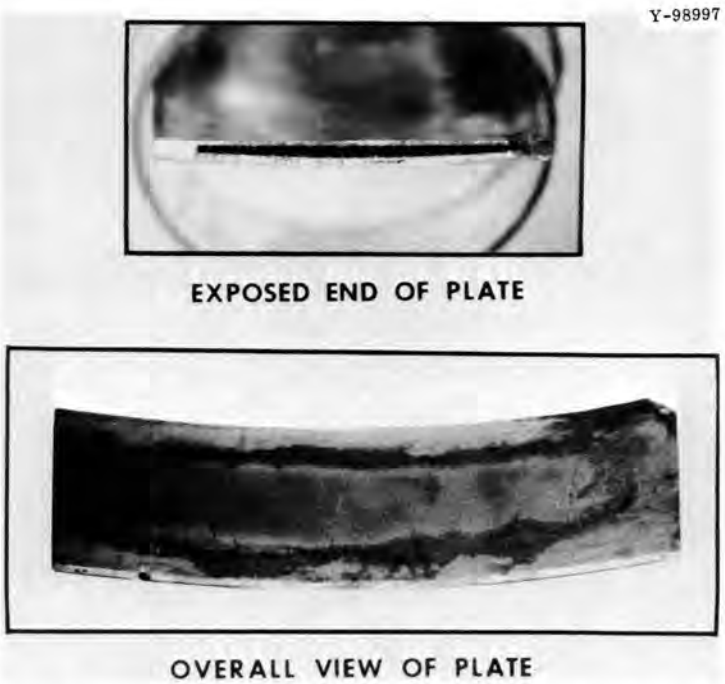

Fig. 19.5. Example of Warping and Core Fracturing of Fuel Plates Containing Burned U_3O_8 During Heat Treatment after Irradiation.

Table 19.1. Fuel Characteristics for Irradiation Test Plates

Plate Number	Type of Fuel	^{235}U Enrichment in Fuel Particle (wt %)	Fuel in Core (wt %)	Concentration ^{235}U (g/cm^3)	Fuel Fines (wt %)
1	Arc-cast UAl_x	93	52	1.30	25
2	Arc-cast UAl_x	93	52	1.30	50
3	Arc-cast UAl_x	93	52	1.30	100
4	Arc-cast UAl_x	93	67	1.61	25
5	Arc-cast UAl_x	93	67	1.61	50
6	Arc-cast UAl_x	93	67	1.61	100
7	Arc-cast UAl_x	a	52	a	25
8	Arc-cast UAl_x	a	52	a	25
9	Arc-cast UAl_x	a	52	a	25
10	Arc-cast UAl_x	a	52	a	50
11	Arc-cast UAl_x	a	52	a	100
12	High-fired U_3O_8	93	40	1.14	10
13	High-fired U_3O_8	93	49	1.42	10
14	Burned U_3O_8	93	42	1.14	10
15	Burned U_3O_8	93	50	1.42	10
16	High-fired U_3O_8	a	40	a	10
17	High-fired U_3O_8	a	40	a	50
18	Burned U_3O_8	a	42	a	10

[a]Fuel depleted in ^{235}U.

1. establish the magnitude of swelling for ATR plates that contain the normal loading of 1.3 g $^{235}U/cm^3$ or a higher loading of 1.61 g $^{235}U/cm^3$, which corresponds to a 25% fuel-clumping concentration;
2. establish the magnitude of swelling for both high-fired and burned oxide plates that contain the normal HFIR loading of 1.14 g $^{235}U/cm^3$ or a higher loading of 1.42 g $^{235}U/cm^3$, which corresponds to a 25% fuel-clumping concentration;
3. investigate the effect of fuel fines on the performance of plates that contain UAl_x at fuel loadings of 1.3 and 1.61 g $^{235}U/cm^3$;
4. evaluate the stability of fabrication voids produced by cold working of depleted UAl_x plates;
5. compare the relative stability of fabrication voids produced by hot and cold working of depleted UAl_x plates; and
6. investigate the reaction of depleted UAl_x and U_3O_8 with Al as a function of fuel fines.

Recent measurements revealed that our experimental position in HFIR, VXF-17, had an axial flux of only 3.6×10^{14} neutrons cm^{-2} sec^{-1} averaged over a length of ±4 in. about the reactor midplane. Since this flux is lower than we had anticipated, our experimental fuel plates will be exposed for five reactor cycles instead of the four cycles originally planned.[4] We shall submit the experimental design to the Reactor Experimental Review Committee for approval before we fabricate the experimental assembly.

Development of a HFIR Core with Increased Fuel Loading

W. R. Martin

Commercial Fabrication of Plates with Increased Fuel Loading (R. W. Knight, M. M. Martin, J. H. Erwin)

Four lots of 18 fuel plates each were fabricated[5] at Metals and Controls, Inc. All plates were manufactured in accordance with standard HFIR processes except for the U_3O_8 loading. The two lots of plates for the inner annulus (I-744 and I-746) were loaded with high-fired and burned U_3O_8, respectively, to 134.95% of the present standard loading; likewise,

the two lots for the outer annulus (0-1537 and 0-1556) were loaded with high-fired and burned U_3O_8 to 125.01% of the present standard loading.

These plates were produced with little difficulty, but two changes would be required for manufacturing such plates on a production basis: (1) either some Al powder would have to be removed from the core or the pressure used to press the compacts would have to be increased to assure that the compact is of the proper thickness, and (2) a slight change in the rolling schedule might be required to assure that the fuel core is of the proper length. Dimensional inspection results for these plates are given in Table 19.2. Boron content of the inner plates are given in Table 19.3. Ultrasonic inspection was completed on all lots but 0-1556, which will require new ultrasonic standards, a recalibration of the equipment, and a change in the transducer and collimator. The plates were not x-ray scanned for homogeneity; however, five plates from each lot were scanned at slow speeds to determine x-ray bias to aid in establishing new x-ray standards (see Table 19.3).

In the four lots rolled, four plates were rejected because of blisters and one because of fuel in a no-fuel zone. Since ultrasonic scanning and homogeneity scanning have not been completed, a final rejection rate cannot be established; for the work completed, however, the rejection rate is no greater than that for standard fuel plates.

Fabrication Development

W. R. Martin

Effect of Dispersoid Concentration on Void Content of Composite Plates (M. M. Martin)

Voids introduced into composites during fabrication can enhance irradiation performance of dispersion fuel plates. Our deformation studies on U_3O_8-Al and UAl_x-Al dispersions of about 41 vol % of fuel compound showed that cold rolling increased the void content of the clad fuel cores.[6] To provide more information in support of our findings and to examine the maximum fuel concentration that can be incorporated into test plates, we are investigating the effect of cold rolling for

Table 19.2. Results of Dimensional Inspection of Fuel Plates with Increased Loading

Lot Number	Final Thickness of Cold-Rolled Plate,[a] in.			Reference Plate Edge to Adjacent Fuel Edge,[b] in.			Opposite Plate Edge to Opposite Fuel Edge,[c] in.			Top End of Plate to Top End of Fuel,[d] in.		Bottom End of Plate to Bottom End of Fuel,[d] in.		Thickness of Cladding,[e] in.		
	Maximum	Minimum	Average	Maximum	Minimum	Average	Maximum	Minimum	Average	Maximum	Minimum	Maximum	Minimum	Top Average	Bottom Average	Minimum
I-744	0.051	0.0505	0.0508	0.219	0.199	0.206	0.379	0.359	0.369	2.179	1.959	2.194	1.984	0.0116	0.0114	0.0096
I-746	0.0512	0.0508	0.0508	0.214	0.189	0.200	0.379	0.354	0.367	2.039	1.829	2.169	1.849	0.0114	0.0112	0.0094
0-1537	0.0510	0.0506	0.0509	0.209	0.189	0.199	0.259[f]	0.229	0.241	2.089	1.869	2.099	1.889	0.0116	0.0115	0.0090
0-1556	0.0514	0.0509	0.0512	0.204	0.184	0.193	0.249	0.219	0.229	2.019	1.799	2.089	1.789	0.0112	0.0112	0.0090

[a] Specification tolerance: all lots, 0.051 to 0.049 in.

[b] Specification tolerance: lots I-744 and I-746, 0.233 to 0.170 in.; lots 0-1537 and 0-1556, 0.218 to 0.169 in.

[c] Specification tolerance: lots I-744 and I-746, 0.389 to 0.326 in.; lots 0-1537 and 0.1556, 0.257 to 0.209 in.

[d] Specification tolerance: all lots, 2.250 to 1.750 in.

[e] Specification minimum: all lots, 0.008 in.

[f] Accepted on remeasure.

Table 19.3. Results of Analytical Inspection of Fuel Plates with Increased Loading

Lot Number	Boron Content, g									X-Ray Attenuation Bias	
	Sample B1-5[a]			Sample B6-10[b]			Sample B11-15[c]			Loading of U_3O_8 Relative to Present Standard (%)	Bias (%)
	Maximum	Minimum	Average	Maximum	Minimum	Average	Maximum	Minimum	Average		
	$\times 10^{-6}$	$\times 10^{-6}$	$\times 10^{-6}$	$\times 10^{-6}$	$\times 10^{-6}$	$\times 10^{-6}$	$\times 10^{-6}$	$\times 10^{-6}$	$\times 10^{-6}$		
I-744	503	460	482	169	151	162	300	269	284	134.95	-3.9
I-746	503	470	480	179	159	167	305	269	291	134.95	+5.25
0-1537										125.01	+2.16
0-1556										125.01	+8.17

[a]Specification tolerance: 656 to 316 $\times 10^{-6}$ g.

[b]Specification tolerance: 212 to 102 $\times 10^{-6}$ g.

[c]Specification tolerance: 384 to 185 $\times 10^{-6}$ g.

dispersoid content over the entire concentration range of 0 to 100 wt %. The miniature fuel plates used for the investigations are dispersions of high-fired U_3O_8-Al and α-phase Al_2O_3-Al clad with type 6061 Al alloy by conventional techniques of hot roll bonding. The fabrication procedure and void contents before cold rolling were reported.[7]

After hot rolling and annealing, the plates were reduced 31% in thickness at room temperature in four rolling passes at each of 10 mill settings. We annealed the cold-rolled plates for 3 hr at 490°C and then slowly cooled them to produce the "0" temper condition in the type 6061 Al cladding.

The void content of the dispersions was determined at five stages during fabrication: after cold rolling to 8, 16, 25, and 31% reductions in thickness and after final annealing. In general, we found that cold rolling increased the void content of both oxide-Al cores, but the amount of the change depended on the type and concentration of the oxide. Figures 19.6 and 19.7 show these effects. We have presented only the

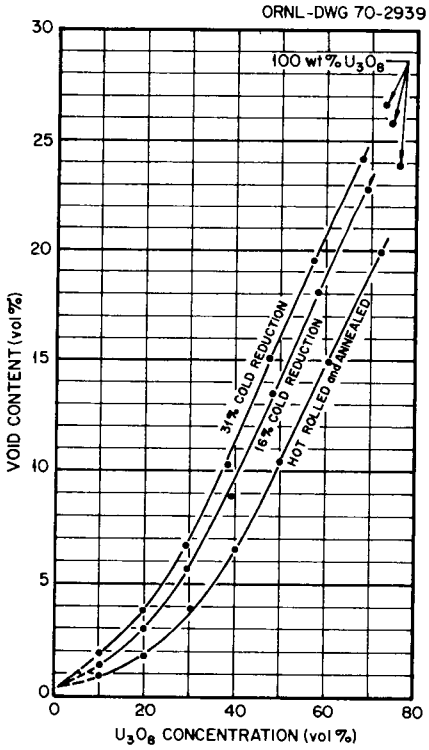

Fig. 19.6. Effect of U_3O_8 Concentration on the Void Content of High-Fired U_3O_8-Al Dispersions.

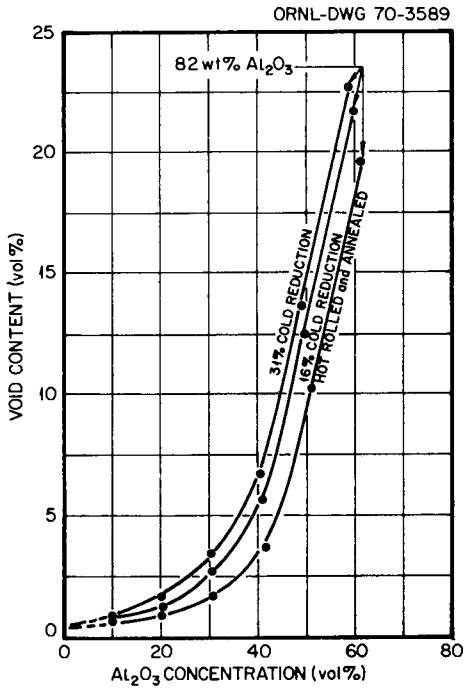

Fig. 19.7. Effect of Al_2O_3 Concentration on the Void Content of Alpha-Phase Al_2O_3-Al Dispersions.

data for plates hot rolled and annealed, cold rolled 16%, and cold rolled 31%, since the oxide content depended linearly on the amount of cold rolling. For oxide contents of 0 to 40 vol %, the U_3O_8-Al dispersions contain more voids than the Al_2O_3-Al dispersions. For oxide contents between 40 and 50 vol %, depending upon the void content, the continuous phase of both dispersions changes from Al metal to oxide. For oxide contents above 50 vol %, the rate at which voids are produced with increasing oxide content is constant, but is greater for the Al_2O_3 than for the U_3O_8 cermets. On the basis of these observations, we conclude that the voids produced during cold rolling are physically associated with the oxide phase; as such, they should enhance the irradiation performance of dispersion fuel plates.

The final annealing treatment produced little, if any, changes in the void content of the U_3O_8 and Al_2O_3 dispersions. The curves in Figs. 19.6 and 19.7 labeled "31% cold reduction" adequately represent the final annealed condition.

Hot rolling will remove a significant portion of the void volume introduced into the core during cold rolling. For example, we found

that the void content of the "31% cold reduction" dispersions shown in Fig. 19.6 was reduced to the level of the "16% cold reduction" curves by one hot-rolling pass of 15% reduction in thickness at 490°C. This void content should be constant for additional hot-rolling passes.[6]

Deformation Characteristics of U_3O_8-Al and UAl_x-Al Dispersion Fuel Plates with Increased Loading (M. M. Martin)

We continued our investigation of dogboning in U_3O_8-Al and UAl_x-Al dispersions that contain about 41 vol % of the fuel compound. The fabrication and core density of the 44 miniature fuel compacts being used in this study were reported for each stage of their processing into clad fuel plates.[6] The fuel compacts initially varied between 82 and 94% of theoretical density, depending on the compacting pressure and the degassing temperature. The completed clad cores were 90 ± 1% of theoretical density regardless of their compacting and degassing conditions.

After each of the nine hot-rolling passes and the second, fourth, and sixth cold-rolling mill settings used in fabrication, the billets are analyzed for dogboning by continuous scanning x-ray attenuation techniques.[8] We completed the scanning and the recording and condensation of the data for all plates, hot-rolling passes, and cold-rolling mill settings. We formed the following tentative conclusions:

1. As expected, there was more dogboning in the UAl_x-Al dispersions than in the U_3O_8-Al dispersions.

2. Degassing temperatures of 400 to 500°C do not affect the dogboning of UAl_x-Al dispersions pressed at 30 psi during compaction; a similar indifference to temperature was noted for U_3O_8 compacts from 400 to 600°C.

3. Dogboning is independent of pressing pressure at 20, 30, and 50 tsi.

4. Reproducibility of dogboning in identical compacts was poor.

Development of Nondestructive Inspection Techniques

R. W. McClung

Radiation Scattering[9] (B. E. Foster, S. D. Snyder)

We continued studies of the use of scattered and fluorescent radiation for measuring the thickness of Al cladding on fuel plates. We investigated the angle, intensity, and energy of the radiation scattered from three base materials, Al, Pb, and U.

With the incident angle of the radiation beam held constant, scattered radiation reached a maximum intensity at 140° and decreased nearly linearly to a minimum intensity at 105°. Similar results were obtained when the detector angle was held constant and the incident angle of the radiation beam was varied. The maximum intensity was at an incident angle of 90°.

We are now adding Al shims of different thicknesses to the base materials for calibration and evaluation of sensitivity to a given change in thickness of Al.

Study of Particle Variations by X-Ray Attenuation (B. E. Foster, S. D. Snyder)

We continued systematic investigation of the effect of particle size on the calibration curve for x-ray attenuation for both high-fired and burned U_3O_8 powders in fuel plates.[10] Total U content for each of the 26 sets of plates (two duplicate plates per set) was determined from the x-ray attenuation scans and the original HFIR calibration. These contents were compared with the actual U loadings. This comparison showed that the U content of the high-fired oxide determined by x-ray attenuation deviated from the actual U loading by as much as −8%, for the coarse powders (−170 + 200 mesh), to +3% for the fine powders (−325 + dust). It appears that the powders used in the plates from which the original calibration was developed had a mesh size of about −270 + dust. We tried to correlate an average particle diameter, calculated from Coulter Counter measurements of samples from each mesh-size batch, with the deviation of the HFIR calibration from actual U

content. Figure 19.8 is a plot of data for burned oxide fuel. Point scatter indicated the possibility of a mix-up in sample identification, and samples from two powder batches (PB-20 and PB-22) were resubmitted for Coulter Counter measurements. The results from these latter measurements showed only that there is either poor reproducibility in sampling or in the Coulter Counter measurements. We obtained average particle diameters of 40.1 and 20.2 μm for the two determinations for the PB-20 powder batch and 44.9 and 16.1 μm for the PB-22 powder batch. Consequently, we have not found a parameter completely representative of the starting powder that can specifically and quantitatively be correlated with x-ray attenuation. However, this work has shown a general relationship between the deviation of the HFIR calibration from the actual loading and the broad ranges of powder mesh sizes. These data will be normalized by weighing the data for distribution of particle sizes with the particle area or volume, and we expect an even better correlation between particle or mesh size and variations in fuel loading.

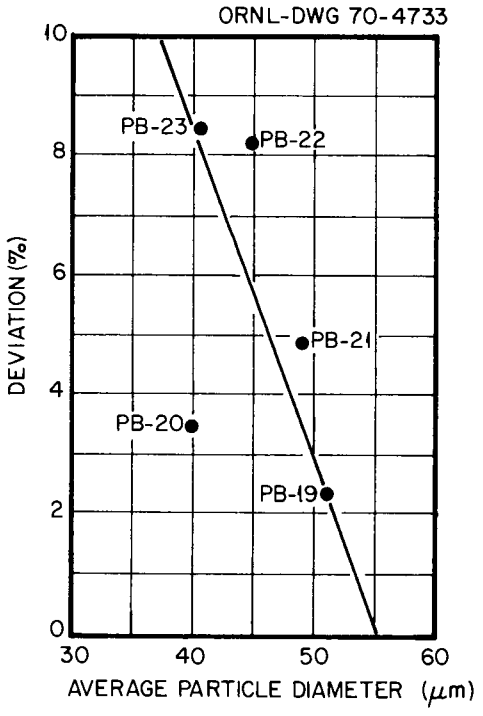

Fig. 19.8. Percent Deviation of the Uranium Content Determined from the Original High Flux Isotope Reactor Attenuation Calibration from the Uranium Content Determined from the Core Area and Loading Versus the Initial Average Particle Diameter of the Fuel.

Standards for Burned U_3O_8 and Increased Loadings of High-Fired U_3O_8
(B. E. Foster, S. D. Snyder)

We have completed the x-ray attenuation scanning at both 50 kilovolts constant potential (kvcp) and 2.5 ma and 60 kvcp and 2.5 ma of 14 HFIR plates fabricated by Metals and Controls, Inc. Six of these plates contain high-fired U_3O_8, and eight contain burned U_3O_8. The high-fired U_3O_8 plates are one inner and one outer annulus plate with standard loading and two inner and two outer annulus plates with an increased loading (inner = 134.95% of standard; outer = 125.01% of standard). The burned U_3O_8 plates are identical in loading characteristics to the high-fired plates, but there are two each of the inner and outer annulus plates with standard loading. This work is preliminary to the machining of samples from the plates for determinations of U content by chemical analysis. These results will be used to establish the calibration curves for determinations of U content by chemical analysis. These results will be used to establish the calibration curves for U content versus x-ray attenuation. In turn, these calibration curves will be used in conjunction with the relationship of Al thickness to x-ray attenuation to design the contoured Al standards necessary for inspection of the homogeneity of the fuel of plates that contain burned oxide.

Notes

1. M. M. Martin, Fuels and Materials Development Program Quart. Progr. Rept. Sept. 30, 1969, ORNL-4480, pp. 214–216.
2. A. E. Richt and M. M. Martin, Fuels and Materials Development Program Quart. Progr. Rept. Dec. 31, 1969, ORNL-4520, pp. 266–272.
3. General Engineering Division.
4. M. M. Martin and W. K. Crowley, Fuels and Materials Development Program Quart. Progr. Rept. Sept. 30, 1969, ORNL-4480, pp. 213–214.
5. R. W. Knight, Fuels and Materials Development Program Quart. Progr. Rept. Sept. 30, 1969, ORNL-4480, pp. 224–228.
6. M. M. Martin, Fuels and Materials Development Program Quart. Progr. Rept. Dec. 31, 1969, ORNL-4520, pp. 277–282.

7. M. M. Martin, Fuels and Materials Development Program Quart. Progr. Rept. Dec. 31, 1969, ORNL-4520, pp. 277–282.

8. B. E. Foster, S. D. Snyder, and R. W. McClung, Continuous Scanning X-Ray Attenuation Technique for Determining Fuel Inhomogeneities in Dispersion Core Fuel Plates, ORNL-3737 (January 1965).

9. This work is jointly supported by the Nondestructive Testing Program and is also discussed in Chapter 23 of this report.

10. B. E. Foster, S. D. Snyder, and M. M. Martin, Fuels and Materials Development Program Quart. Progr. Rept. Sept. 30, 1969, ORNL-4480, pp. 239–241.

20. TECHNICAL ASSISTANCE IN PROCUREMENT OF FUEL ELEMENTS

G. M. Adamson, Jr. W. R. Martin

The purpose of this program is to provide technical assistance and inspection surveillance to the U.S. Atomic Energy Commission (AEC) Division of Reactor Development and Technology (RDT) in its effort to procure fuel and neutron-absorber components from commercial sources for research reactors owned by the AEC. Through this program, immediate technical help can be made available to analyze and solve problems as they arise in manufacturing plants of commercial vendors.

Technical Assistance in Solving Pressing Manufacturing and Inspection Problems

W. R. Martin

Determination of Void Volume in ATR Plates of Types 8 and 19

(R. W. Knight, M. M. Martin, J. H. Erwin)

Two Advanced Test Reactor (ATR) fuel plates (ATR 976-1-19 and 975-2-8) manufactured at ORNL were measured for core void volume. Pertinent data concerning the plate fabrication and other data on void volume may be found elsewhere.[1,2] We wrote a standard operating procedure for measuring void volume. Our method of calculating void volume is expressed by the formula

$$V = 1 - \left[\frac{Z}{t\left(\frac{x-y}{s} - \frac{x-z}{r}\right)}\right] 100$$

where

V = void volume fraction of fuel core, percent

Z = weight of core in air, grams

x = weight of plate in air, grams

y = weight of plate in water, percent

s = density of water, grams per cubic centimeter

r = density of cladding, grams per cubic centimeter

t = theoretical density of core, grams per cubic centimeter, based on the toluene density of its components.

The values obtained for the two ATR plates are shown in Table 20.1. The percentage of voids for the type 19 fuel plate shown in Table 20.1 is significantly different from the 0% voids reported by a commercial vendor.

Table 20.1. Void Volume for Types 8 and 19 ATR Fuel Plates

	ATR Plate Number	
	976-1-19	975-2-8
Void volume fraction of fuel core, %	8.2	6.9
Weight of core in air, g	186.823	135.848
Weight of plate in air, g	853.870	387.729
Weight of plate in water, g	556.291	257.779
Density of water (20.3°C), g/cm^3	0.99814	0.99814
Density of cladding, g/cm^3	2.7092	2.7092
Theoretical density of core, g/cm^3	3.9186	3.9186

Notes

1. M. M. Martin, J. H. Erwin, B. E. Foster, and S. D. Snyder, Fuels and Materials Development Program Quart. Progr. Rept. Dec. 31, 1968, ORNL-4390, pp. 234–238.

2. M. M. Martin, Fuels and Materials Development Program Quart. Progr. Rept. Dec. 31, 1969, ORNL-4520, pp. 277–282.

CLADDING AND OTHER STRUCTURAL MATERIALS

21. BEHAVIOR OF REFRACTORY MATERIALS UNDER IRRADIATION

G. M. Watson[1] G. W. Keilholtz[1]

The purpose of this program is to evaluate the effects of high fast-neutron fluences at temperatures up to 1100°C on the properties of refractory nuclear materials for both space and civilian power reactors. The present program has two major objectives: (1) to determine the effects of He gas produced by fast neutrons in depleted UN fuels, and (2) to investigate the effects of fast neutrons on B_4C as part of a program for developing this material as a neutron absorber for control of reactivity in fast-flux reactors.

Irradiation Damage to Nonfissionable Refractory Materials

R. E. Moore[1] D. A. Dyslin[2] H. E. Robertson[1]

Some work is still in progress on this task to define mechanisms of neutron damage to carbides. A long-term, low-temperature (below 150°C) assembly containing carbides of Ti, Zr, Ta, Nb, and W was irradiated in the Engineering Test Reactor (ETR). The results will be correlated with results from an identical assembly that had been irradiated for a very short period of time.[3] These data and data from annealing of irradiated carbide specimens out-of-reactor will be used to define damage mechanisms. The damage model that we presented previously[3] has now been extended to a more comprehensive form. A detailed report describing the model will be issued soon.

Effects of Irradiation on LMFBR Fuels

R. E. Moore[1] D. A. Dyslin[2] H. E. Robertson[1]

We are evaluating the effects of the generation of He gas through the $^{14}N(n,\alpha)^{11}B$ reaction within nitride fuels.[4] Depleted fuels are

used in the irradiations to eliminate the production of fission gases.

An uninstrumented assembly in which the temperature of the specimens was about 150°C was irradiated in the J-12 core position of the ETR. It contained specimens of UN, $U^{15}N$, and UN-UC (50-50 mole %). A high-temperature (1000°C) assembly containing the same types of specimens is still undergoing irradiation and will be removed from the ETR in June 1970 after it has received about the same neutron fluence as the low-temperature assembly.

Fast-Neutron Effects on Materials for Neutron Absorption in Fast Reactors

R. E. Moore[1] D. A. Dyslin[2] H. E. Robertson[1]

This task is aimed at the development of B_4C as a neutron absorber for control of reactivity in fast reactors.[5] Planning and engineering design work have been done on a comprehensive experiment for row 7 of the Experimental Breeder Reactor-II (EBR-II). The work in this task will continue after July 1, 1970, as part of another program that involves all phases of the development of B_4C as a neutron absorber.

Notes

1. Reactor Chemistry Division.
2. General Engineering Division.
3. R. E. Moore, D. A. Dyslin, and H. E. Robertson, Fuels and Materials Development Program Quart. Progr. Rept. Sept. 30, 1969, ORNL-4480, pp. 245–254.
4. R. E. Moore, D. A. Dyslin, and H. E. Robertson, Fuels and Materials Development Program Quart. Progr. Rept. Dec. 31, 1969, ORNL-4520, p. 296.
5. R. E. Moore, D. A. Dyslin, and H. E. Robertson, Fuels and Materials Development Program Quart. Progr. Rept. Dec. 31, 1969, ORNL-4520, p. 297.

22. JOINING RESEARCH ON NUCLEAR MATERIALS

J. R. Weir, Jr. G. M. Slaughter

The purpose of this program is to gather the fundamental and applied data needed to understand the weldability of materials that are either being considered or are currently used for nuclear applications. Fundamental studies are concerned with the effects of minor constituents on the behavior of weldments. We are especially interested in the austenitic stainless steels and the alloys that are rich in Ni, such as Incoloy 800 and Inconel 600. In addition, a modest program concerned with the influence of weld defects will provide reference results in this much-talked-about but little-investigated field.

As a result of this broad-based program, we plan to suggest modifications in both alloy composition and procedures needed to improve the quality of weldments used in the various activities of the Commission.

The Effect of Minor Variations in Chemical Composition on Weldability

Our continuing investigation of the effect of minor variations in those elements usually present in structural material has included Inconel 600, Incoloy 800, and stainless steel.

Weldability of Incoloy 800 (D. A. Canonico, W. J. Werner)

Welding Studies. — The welding conditions used for Incoloy 800 welds with experimental heats of filler metal were reported previously.[1] The results of tensile tests at room temperature are compared in Table 22.1 with those for welds made with an electroslag-remelted heat of commercial Incoloy 800 and Inconel 82T, a commercial filler metal recommended for joining Incoloy 800.

The Inconel 82T filler metal appeared to possess superior tensile properties at room temperature. This weld failed in the base metal, while all other welds failed in the weld metal. The weld made with electroslag-remelted Incoloy 800 had the best ductility (36% vs about 25%) and highest ultimate tensile strength (77,000 psi vs about 72,000 psi).

Table 22.1. Results of Tensile Tests at Room Temperature on Welds Made in Incoloy 800 with Experimental Filler Metals

Weld Identification	Addition to Nominal Composition[a] of Filler Metal, wt %				Tensile Strength, psi		Elongation in 3 in. (%)	Location of Failure
	Al	Ti	S	P	Yield	Ultimate		
143	0.38	0.15			27,100	70,200	23.7	Weld metal
144	0.38	0.60			35,200	73,500	25.5	Weld metal
145	0.15	0.38			21,900	72,100	24.8	Weld metal
146	0.60	0.38			24,300 31,500	68,800 72,600	23.9 24.3	Weld metal Weld metal
175	0.15	0.15			21,400	72,300	23.7	Weld metal
176	0.38	0.38			25,700	71,500	26.5	Weld metal
177	0.60	0.60			20,000	71,600	28.5	Weld metal
187	0.38	0.38		0.010	30,200	73,300	25.4	Weld metal
189	0.38	0.38		0.02	38,200	70,600	23.9	Weld metal
191	0.38	0.38	0.015	0.015	25,600	66,000	17.4	Weld metal
Electroslag-remelted[b] Incoloy 800					23,800	77,200	35.9	Weld metal
Inconel 82T[c]					31,400	79,500	44.5	Base metal

[a]Nominal composition of Incoloy 800: Fe–31.5% Ni–21.5% Cr.

[b]Nominal composition of electroslag-remelted Incoloy 800: Fe–32.5% Ni–21% Cr.

[c]Nominal composition of Inconel 82T: Ni–20% Cr–3% Mn–1% Fe–2.5% Nb.

Alloys 187 and 189, which contained P, had the highest yield strengths and greatest loss of ductility. Indeed, if reduction in area is used as the criterion for ductility, alloy 189 is superior to both Inconel 82T and the electroslag-remelted Incoloy 800.

The presence of nominally 0.05% S (alloy 191) reduced ductility and strength. A macroscopic study of the fracture surface indicates that microfissures may be present in the weld metal. Metallographic studies now under way should provide quantitative data.

Identical specimens are being tested at 650°C. Similar data will be obtained for these specimens.

Hot-Ductility Studies. — A study of hot ductility by means of the Duffers Gleeble[2] is under way on experimental heats of Incoloy 800. The results of this study were reported[3] for heats containing Al; Ti; Al and Ti; Al, Ti, and S; Al, Ti, and P; and Al, Ti, P, and S. We are now extending these studies to include other experimental compositions that contain Al, Ti, S, P, S and P, and C alone. Table 22.2 contains the nominal compositions of the alloys being studied. The starting stock and melting and fabrication practice were reported.[3] The results to date are shown in Figs. 22.1 and 22.2. The presence of nominally 0.38% Ti and 0.38% Al [Fig. 22.1(a) and (b), respectively] resulted in

Table 22.2. Nominal Chemical Composition of Experimental Incoloy 800 Alloys

Alloy Designation	Composition, wt %				
	Al	Ti	S	P	C
208		0.38			
209	0.38				
235			0.015		
236				0.015	
237			0.015	0.015	
238					0.01
239					0.04
240					0.08

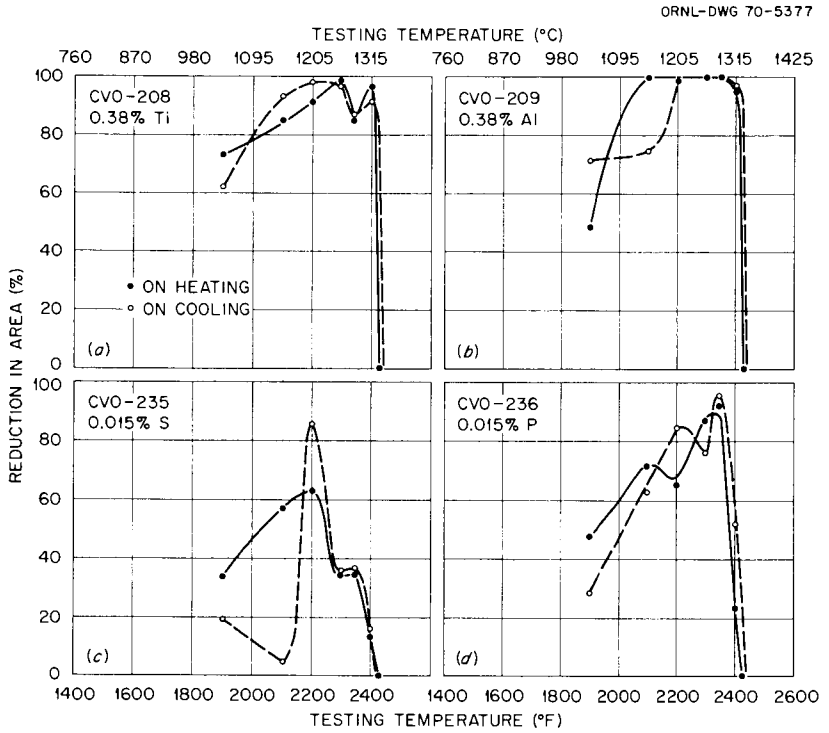

Fig. 22.1. The Effect of the Addition of Various Individual Elements on the Hot Ductility of Experimental Incoloy 800 Alloys. (a) Titanium, (b) aluminum, (c) sulfur, and (d) phosphorus.

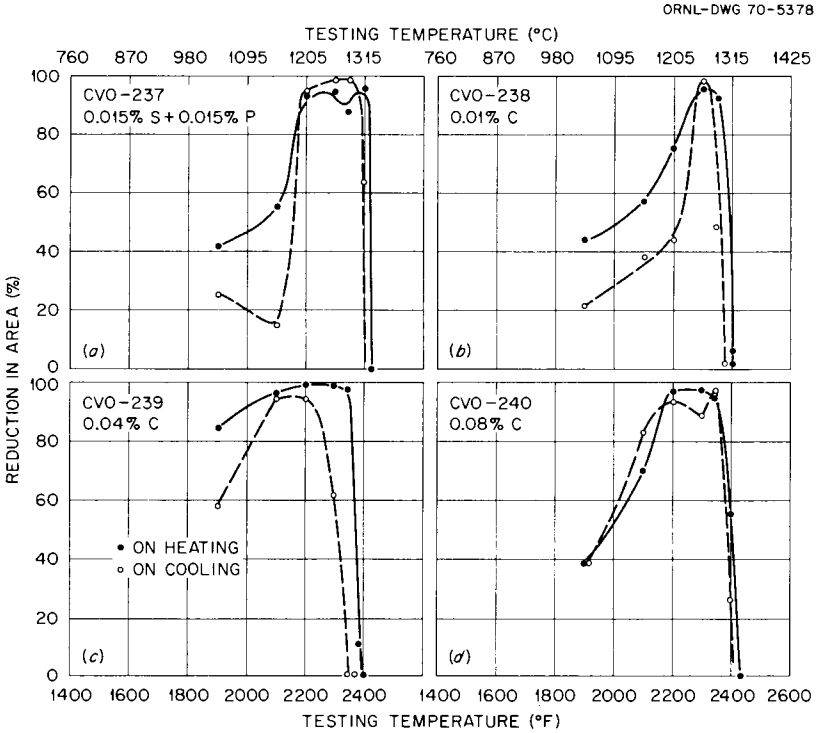

Fig. 22.2. The Effect of Additions of Sulfur, Phosphorus, and Carbon on the Hot Ductility of Experimental Incoloy 800 Alloys. (a) 0.015% S and 0.015% P, (b) 0.01% C, (c) 0.04% C, and (d) 0.08% C.

a slightly higher zero ductility temperature (1330°C or 2425°F) than what was previously reported for alloys that contain both Ti and Al (1316°C or 2400°F). The ability of the alloy to recover ductility after a thermal excursion through the zero ductility temperature was not impaired. Adding only S to a nominal Incoloy 800 composition appreciably reduced on-heating ductility. The on-cooling ductility was drastically lowered at 1150°C (2100°F). This detrimental effect of S is shown in Fig. 22.1(c). Phosphorus also had an effect on the on-heating ductility, but it was minor. Figure 22.1(d) illustrates this effect. Combining both S and P improved both the on-heating and on-cooling ductilities; however, the low ductility at 1150°C (2100°F) that is evident in Fig. 22.1(c) persisted. Figure 22.2(a) shows the results for the hot ductility of the alloy that contained both S and P. Additions of 0.01 and 0.04% C reduced the zero ductility temperature to 1316°C (2400°F) and also affected the on-cooling ductility. Increasing the C seemed to alleviate this effect. Figure 22.2(b), (c), and (d), respectively, illustrates the hot ductility results for the Incoloy 800 alloys that contain 0.01, 0.04, and 0.08% C.

We investigated the effect of heating the 0.01 and 0.04% C alloys to a peak temperature of 1330°C (2425°F) and then tested them on-cooling at 1260°C (2300°F). The low-C alloy suffered some from this exposure to elevated temperature. Its reduction in area at 1260°C (2300°F) was 54% after an excursion to 1330°C (2425°F) vs 99% after an excursion through 1316°C (2400°F). The ductility of the 0.04% C alloy on-cooling at 1260°C (2300°F) was improved after a thermal excursion through the higher peak temperature of 1330°C (2425°F). Metallographic examinations now being conducted will help explain these results.

Effect of Certain Minor Elements on the Ductility of Inconel 600 at Intermediate Temperature (W. J. Werner, D. A. Canonico)

Our studies of the joining of Inconel 600 concentrated on the effects of minor elements on weldability. We used both the Duffers Gleeble and the TIGAMAJIG[4] tests. The TIGAMAJIG test evaluates the propensity of hot weld metal to crack under strain; the Gleeble test evaluates the

heat-affected zone of an alloy in terms of loss of ductility or strength at high temperatures. Intermediate-temperature ductility can also affect the properties of weldments in Ni-rich alloys. It is an established fact that materials rich in Ni lose ductility between 760 and 870°C. This loss of ductility can also contribute to the cracking propensity of a weldment rich in Ni. We subsequently showed that at intermediate temperatures the properties of our special Incoloy 800 alloys were significantly affected by certain minor elements.[5]

Our continuing studies in this area are now concentrated on Inconel 600; we are studying the ductility of this class of alloys at intermediate temperatures. We are now determining the tensile properties of several of the special Inconel 600 alloys at various test temperatures. The tests are being run at a strain rate of 0.002 min^{-1} on an Instron Universal Testing Machine.

Weldability of Stainless Steels (A. J. Moorhead, D. A. Canonico)

Our study of low-Ni alloys centered about the effect of chemical composition on the quantity, morphology, and composition of the phases present in the wrought alloy and subsequently in the weld metal. Previously, we described[6] the composition of the experimental alloys under study. These alloys were designed to provide single-phase (austenite) and two-phase (austenite and ferrite) microstructures. During this quarter, we conducted microstructural studies on the homogenized (1150°C for 1 hr in H_2) experimental alloys. The alloys, except for one (5409), are all ternary Fe-Ni-Cr compositions; alloy 5409 also contains Mn. We concentrated our efforts on four alloys, 5409, 5410, 5419, and 5420, whose compositions and predicted ferrite contents, based on a Schaeffler diagram, are given in Table 22.3.

All the alloys studied except the alloy 5409, which contained Mn, contained ferrite levels that approximated the predicted value. The microstructure of alloy 5409 should have been 100% austenitic, but it did contain a measurable amount of a second and, perhaps, third phase.

Table 22.3. Composition of Experimental Alloys of Austenitic Stainless Steel

Alloy Number	Nominal Chemical Composition, wt %				Predicted Ferrite Content (%)
	Ni	Cr	Mn	Fe	
5409	12	19	5	36	0
5410	10	19	5	34	10
5419	14	24	5	43	10
5420	16	24	5	45	6

Figure 22.3 contains photomicrographs of alloy 5409: Fig. 22.3(a) is unetched; Fig. 22.3(b) is etched to reveal the ferrite. The area that was photomicrographed in the unetched condition was identified to assure that the etched photomicrographs were taken from exactly the same location. This technique was employed throughout the microstructural study.

Two alloys with quite different chemical compositions (alloys 5410 and 5419) were designed to provide identical levels of ferrite (10%). The Ni and Cr equivalents were varied to obtain these similar microstructures. In Fig. 22.4(a) and (b), respectively, photomicrographs of the etched alloys 5410 and 5419 are shown. The size and distribution of the ferrite (the darker phase) is striking. We are now measuring the percentage of ferrite in each alloy.

The fourth alloy studied, alloy 5420, was designed to provide about 6% ferrite. In Fig. 22.5(a) and (b), respectively, photomicrographs of the unetched and etched alloy are shown. There is a decided difference between the amounts and distributions of the ferrite in alloys 5419 and 5420, yet the compositions of these alloys differ by only 2% Ni content.

We began analysis of these alloys by means of electron-beam microprobe. Table 22.4 contains the results of this investigation. As expected, the Ni and Cr partition to the austenite and ferrite, respectively. An interesting relationship evolved between the Ni and Cr in the matrix. The ratio of Cr:Ni is 1.5, even though the ratio of the

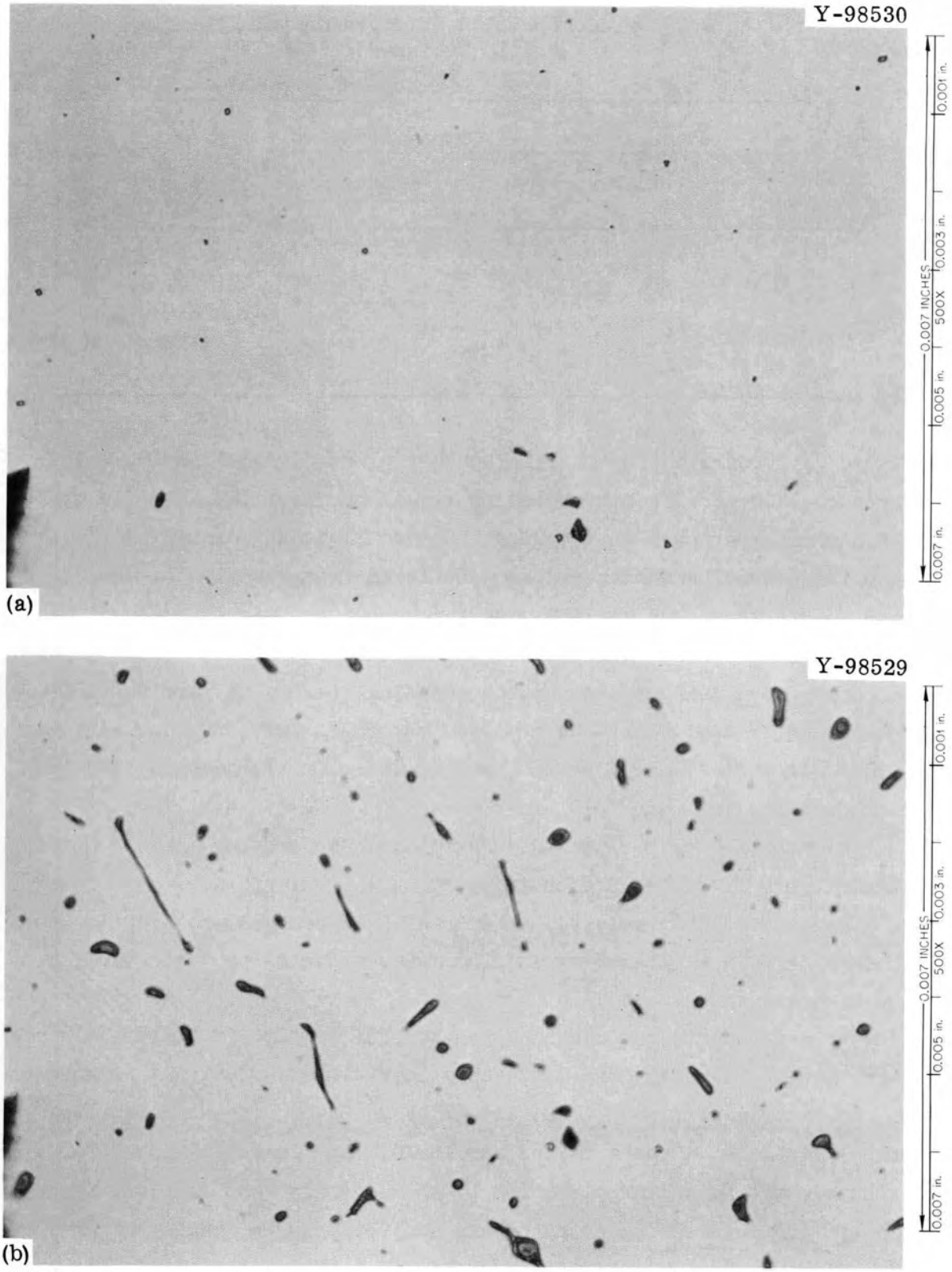

Fig. 22.3. Photomicrographs of Identical Location in Alloy 5409 After Homogenization at 1150°C for 1 hr in Hydrogen. (a) As polished, (b) etched with Murakami's Etch.

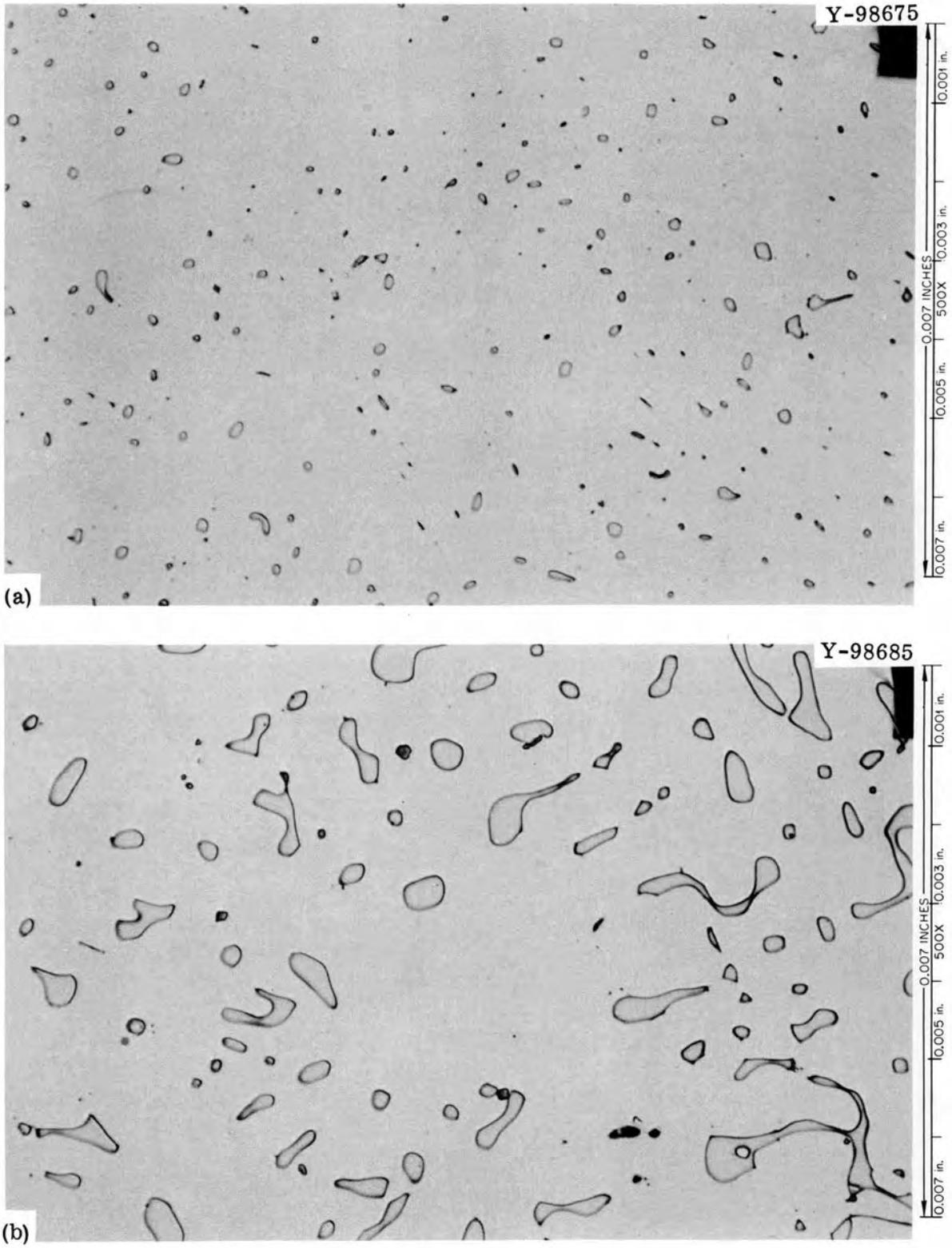

Fig. 22.4. Photomicrographs of (a) Alloy 5410 (Nickel Equivalent, 10; Chromium Equivalent, 19) and (b) Alloy 5419 (Nickel Equivalent, 14; Chromium Equivalent, 24). Both alloys were designed to provide microstructures that would contain 10% ferrite.

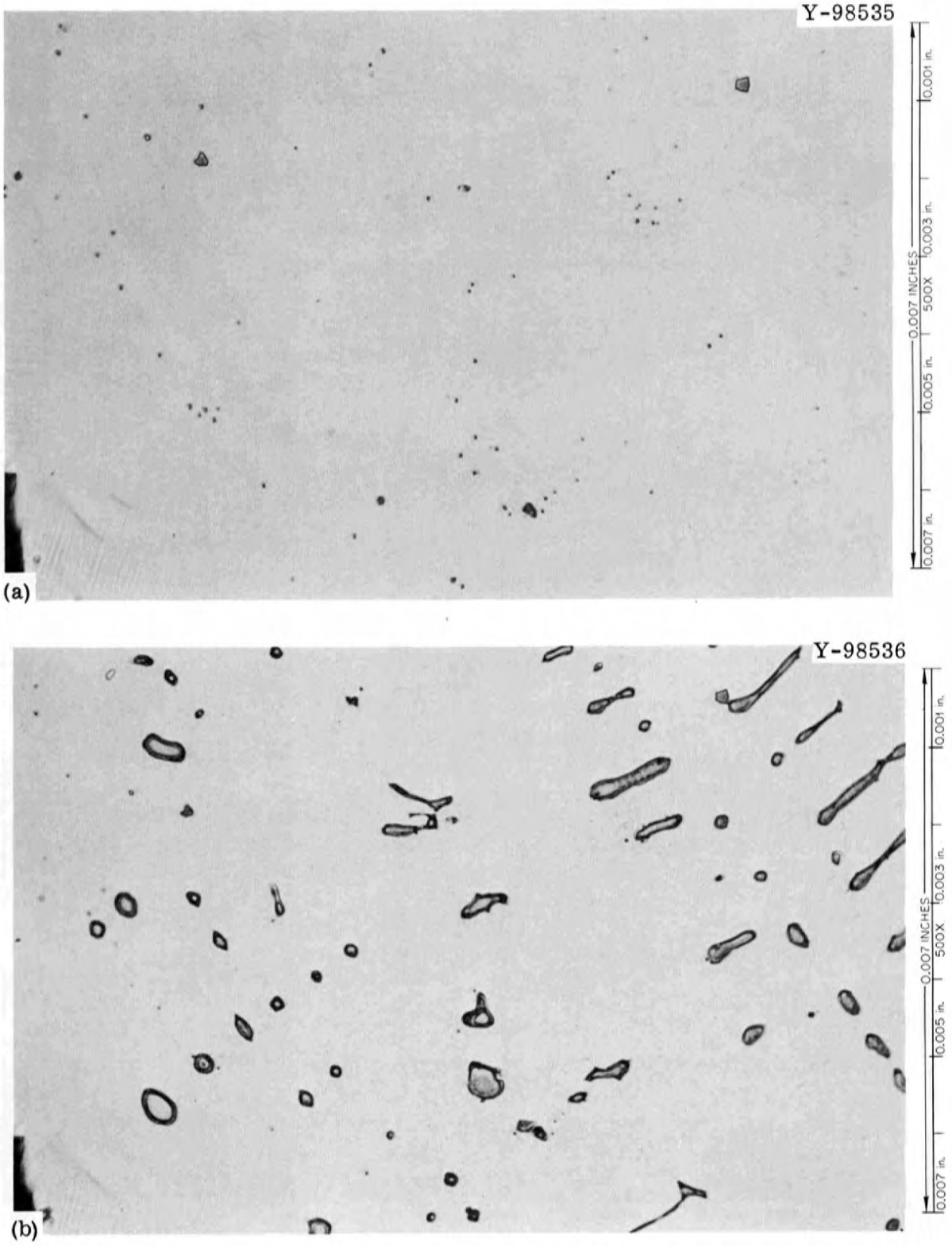

Fig. 22.5. Photomicrographs of Alloy 5420. (a) As polished, (b) etched with Murakami's Etch.

Table 22.4. Results of Analysis of Alloys 5409, 5410, 5419, and 5420 by Electron-Beam Microprobe

Alloy Number	Constituent Analyzed	Chemical Composition, wt %			
		Ni	Cr	Fe	Mn
5409	Desired composition	12	19	64	5.0
	Matrix	13	19.5	64.5	4.3
	Ferrite	5.3	29.1	62.6	3.8
	Precipitate	9.6	19.5	62.8	5.5
5410	Desired composition	10	19	71	
	Matrix	13.1	19.6	73.3	
	Ferrite	5.8	24.0	73.3	
5419	Desired composition	14	24	62	
	Matrix	15.0	22.4	64.1	
	Ferrite	8.9	28.4	61.5	
5420	Desired composition	16	24	60	
	Matrix	16.7	24.7	58.9	
	Ferrite	7.3	35.2	55.3	

nominal composition ranges from almost 2 (alloy 5410) to 1.5 (alloy 5420). The ratios are as follows:

Alloy Number	Ratio
5409	1.50
5410	1.50
5419	1.49
5420	1.48

Subsequent studies will determine whether this observation is real or only a happenstance for these alloys.

The results of the analysis of ferrite content varied over a wide range and did not correlate with the nominal composition of the bulk material. This may be due to the sampling procedure, since the islands of ferrite are small and since analysis is complicated by the composition and presence of the matrix.

Notes

1. D. A. Canonico and W. J. Werner, Fuels and Materials Development Program Quart. Progr. Rept. Dec. 31, 1969, ORNL-4520, pp. 298–300.

2. E. F. Nippes et al., Welding J. (N.Y.) 34(4), 183-s–196-s (April 1955).

3. D. A. Canonico, W. F. Savage, W. J. Werner, and G. M. Goodwin, "Effect of Minor Additions on Weldability of Incoloy 800," pp. 68–92 in Effects of Minor Elements on the Weldability of High-Nickel Alloys (Proceedings of a Symposium), The Welding Research Council, New York, July 1969.

4. G. M. Goodwin, The Effect of Minor Elements on the Hot Cracking of Inconel 600, Ph.D. Dissertation, Rensselaer Polytechnic Institute (June 1968).

5. W. J. Werner, An Investigation of the Effect of Certain Minor Elements on the Elevated Temperature Ductility of Incoloy 800, ORNL-4504 (March 1970). M.S. Thesis, the University of Tennessee (December 1968).

6. D. A. Canonico, A. J. Moorhead, and W. J. Werner, Fuels and Materials Development Program Quart. Progr. Rept. Dec. 31, 1969, ORNL-4520, pp. 300–303.

23. NONDESTRUCTIVE TESTING

W. O. Harms R. W. McClung

Our task is to develop new and improved methods of nondestructively testing reactor materials and components. We are studying various physical phenomena, developing instruments and other equipment, devising techniques, and designing and fabricating reference standards. Among the methods being studied for both normal and remote inspection are electromagnetics (with major emphasis on eddy currents), ultrasonics, penetrating radiation, and holography.

Electromagnetic Inspection Methods (Eddy Currents)

Solutions for Electromagnetic Induction Problems (C. V. Dodd, W. A. Simpson)

We developed the equations and, using a time-sharing computer, calculated the response that would be received for the case of a coil above a flat plate of varying thickness with a defect on the side farthest from the coil. Figure 23.1 shows how the impedance change of a standard defect varies as a function of variables of both coil and conductor. There is an optimum value for a given plate thickness. However, neither the mean radius of the coil nor the orientation of the defect is fixed. The size of the coil can be increased or decreased at will to produce a relative change in the mean radius of the coil, in the thickness of the plate, and in the volume of the defect. For maximum change in impedance due to the defect, the optimum value is that which makes the mean radius of the coil about 1.6 times the thickness of the plate. A coil with a mean radius of 1.2 to 2.4 times the thickness of the plate will give a change in impedance within 10% of the maximum. To ensure a favorable orientation of random defects, successive scans on the plate should be within at least one mean radius of the coil of each other.

We wrote a new computer program to aid in the design of coil systems for use with the phase-sensitive eddy-current instrument. This

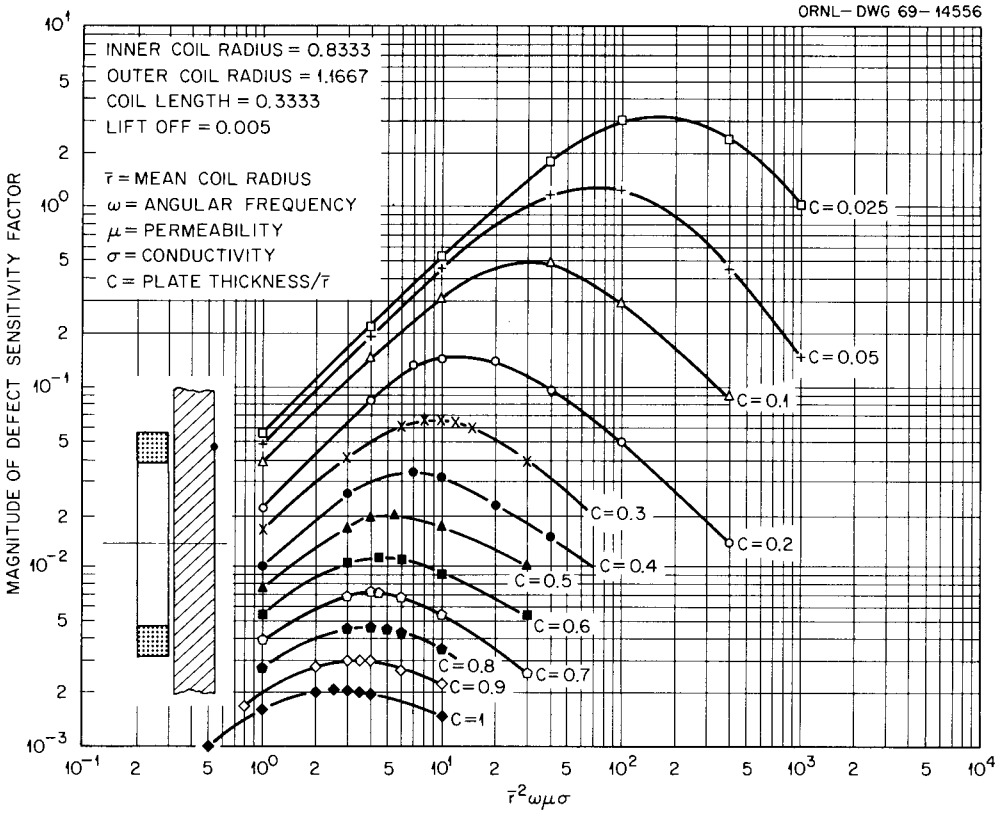

Fig. 23.1. Curves Showing Sensitivity to Defects on the Far Side of a Plate as Plate Thickness and Other Test Conditions Vary.

program calculates the amplitude and phase of the voltages in the instrument. We can study the changes in amplitude and phase caused by variations in temperature and other effects for the various coil systems.

Improvements to the Phase-Sensitive Instrument (C. V. Dodd, W. A. Simpson)

We further improved the accuracy, stability, and sensitivity of the phase-sensitive eddy-current instrument. We modified it for use of a digital voltmeter with a readout of ±12.000 v full scale. At maximum sensitivity, the instrument has a resolution of ±0.0025° and a short-term stability of 0.01°. We constructed a passive phase shifter, which varies from +90 to −90° in 10° steps, to calibrate the instrument. By calibrating the instrument, we can make more accurate, absolute measurements. If these compare favorably to theoretical calculations, then we may be able to eliminate the necessity of standards in later measurements.

Ultrasonic Inspection Methods

Optical Visualization of Ultrasound (H. L. Whaley, Jr., K. V. Cook)

The method of blocking out and eliminating the undeviated zero'th order light is very important since it limits, to a great extent, the ultimate sensitivity of the schlieren system. We investigated a new method for accomplishing this: we used two polarizing filters with their planes of polarization perpendicular and an adjustable width of overlap. The technique did not improve response.

Ultrasonic Frequency Analysis (H. L. Whaley, Jr., K. V. Cook)

We are studying the spectral variations in a broad-banded ultrasonic pulse as a function of the nature of the acoustical discontinuity from which it has been reflected. Such a study should lead to improvements in the characterization by ultrasonic inspection of hidden flaws in materials.

We observed spectral variations as a function of the size, shape, and orientation of the reflector. We developed an analytical model that assumes that interference of the waves received from the extremes of the reflecting surface is responsible for the spectral redistribution after reflection.

Equation (23.1) is the analytical expression derived for the diameter of a reflector in water, d, in terms of its angle, θ, the ultrasonic velocity in water, v, the average frequency interval between consecutive interference peaks, Δf, the distance, D, and a quantity, a, that is proportional to the radius of the transducer:

$$d = \frac{v}{(2 \sin\theta + a/D)\, \Delta f} \quad , \tag{23.1}$$

Table 23.1 presents spectral data and calculated flaw diameters [from Eq. (23.1)] for three sizes of brass reflectors. The average reflector diameter determined from spectral analysis was within about

Table 23.1. Spectral Data and Calculated Diameters for Three Sizes of Brass Reflectors

Incident Angle (deg)	Average Interval Between Consecutive Interference Peaks (MHz)	Diameter of Rod, in.		
		Measured	Calculated	Average Calculated
4.6	1.00	0.281 (9/32)	0.288	0.279
7.7	0.63		0.298	
11.3	0.54		0.250	
5.6	1.20	0.188 (3/16)	0.215	0.192
6.4	1.13		0.194	
8.5	0.92		0.188	
10.8	0.75		0.186	
18.3	0.50		0.175	
6.5	1.38	0.125 (1/8)	0.157	0.139
8.0	1.25		0.147	
9.9	1.06		0.143	
12.5	0.92		0.134	
16.2	0.75		0.130	
25.5	0.50		0.122	

5% of the actual value. Figure 23.2 is a photograph of the experimental apparatus. The reflectors were the flattened ends of brass rods located on the horizontal axis of the ultrasonic transducer (lower right). The center of the reflecting end of the rod is coincident with the axis of the turntable, so that the angle of the reflector may be changed without displacing it from the axis of the transducer.

The technique was also shown to be applicable to the problem of characterizing reflecting discontinuities in metal. Figure 23.3 shows one type of Al sample in position, a solid cylinder in which a flat-bottomed hole had been drilled (from a flattened side) perpendicular to the axis with a depth that placed the flat bottom of the hole on the axis of the cylinder. This type of sample eliminated a number of variables by allowing changes in the angle of the flaw while maintaining normal incidence of the ultrasonic beam to the surface of the sample and keeping the flaw on the axis of the transducer. Table 23.2 compares the calculated results (from spectral data) for the diameter of the reflector

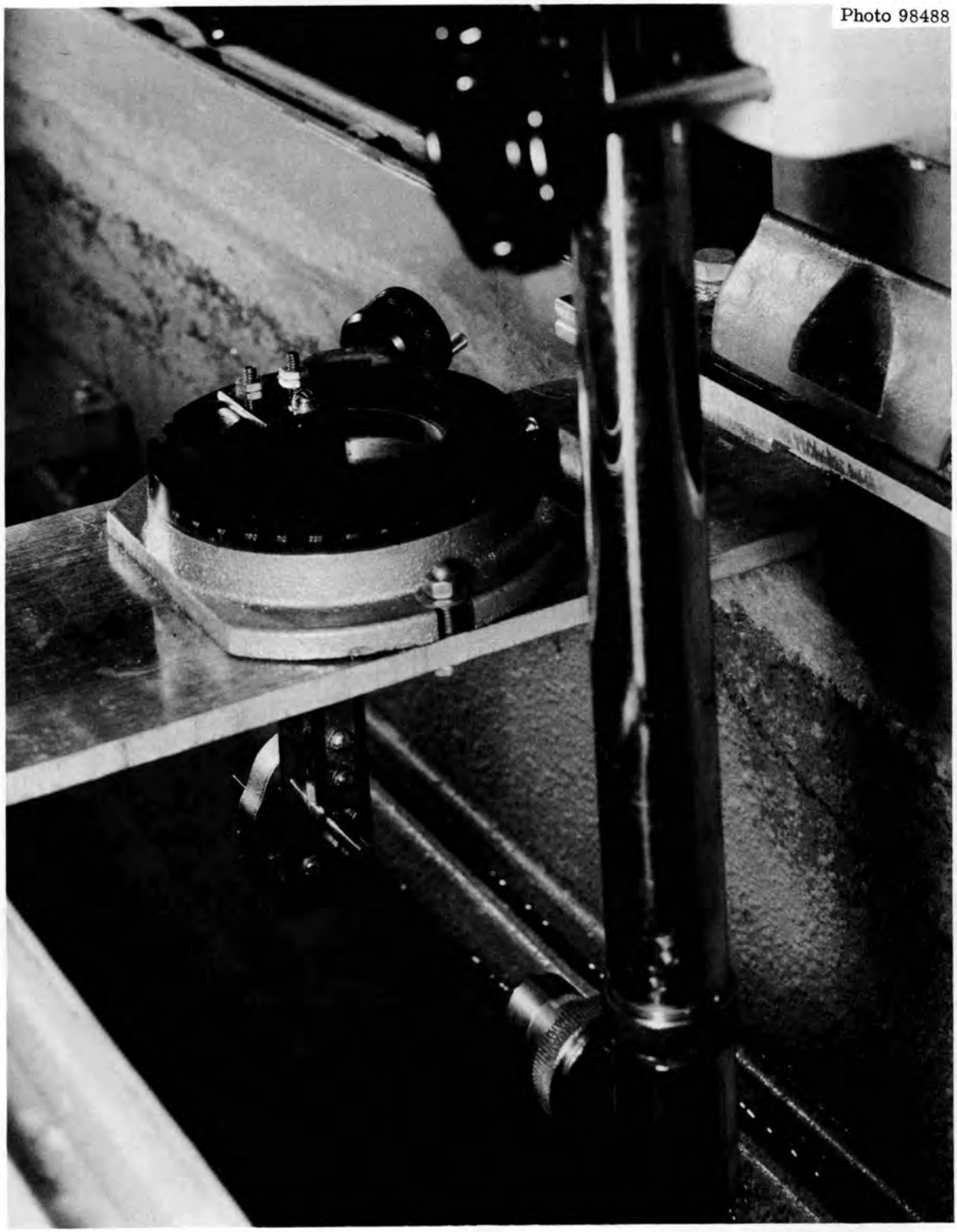

Fig. 23.2. Photograph of Apparatus Used for Measuring Reflection for Brass Rods.

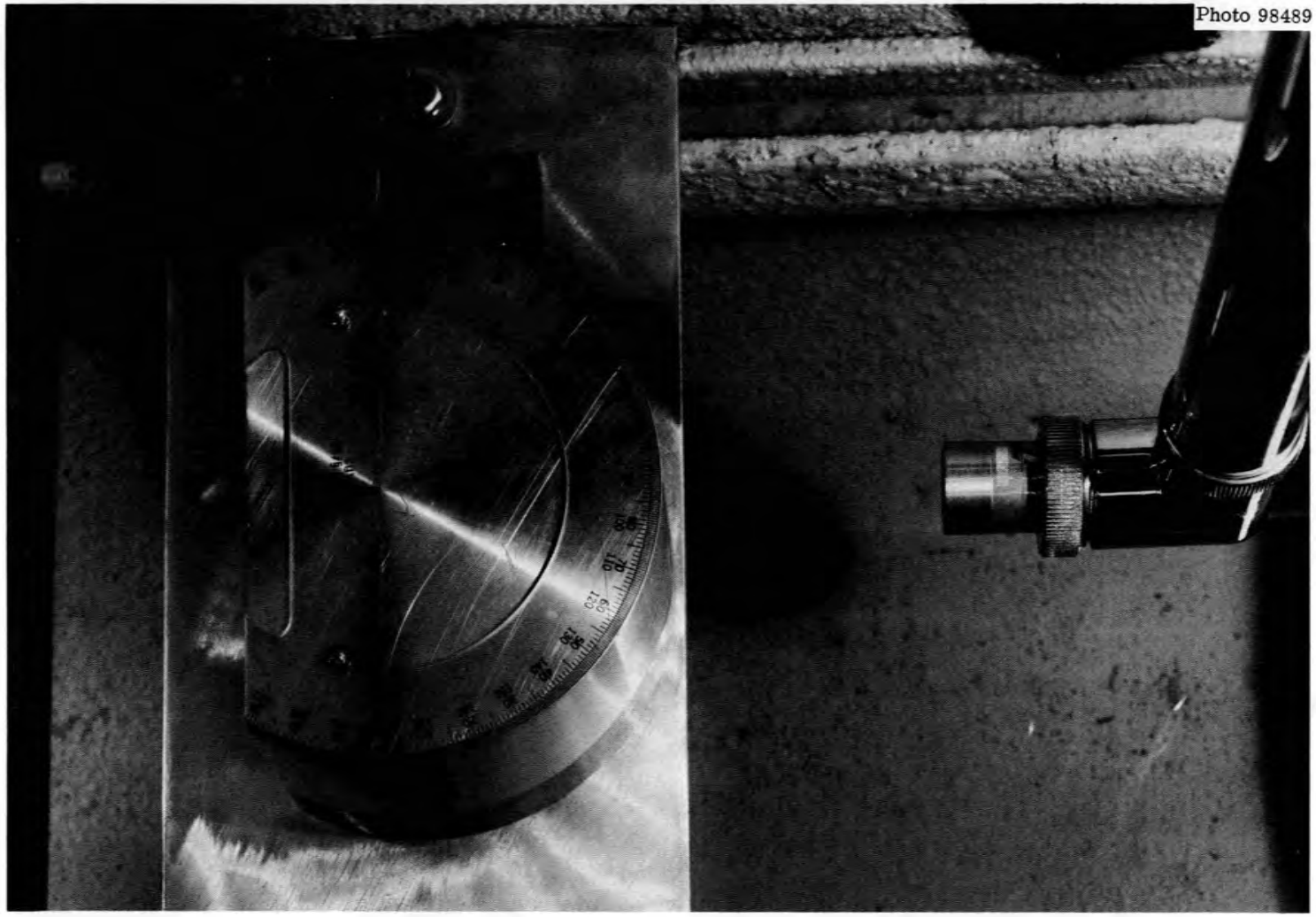

Fig. 23.3. Photograph of an Aluminum Sample Used in the Reflection Experiments.

Table 23.2. Data and Calculated Results for Cylindrical Aluminum Specimens

Incident Angle (deg)	Average Interval Between Consecutive Interference Peaks (MHz)	Diameter of Hole, in.	
		Measured	Calculated
10	1.23	0.500	0.509
15	0.87	0.500	0.502
20	0.68	0.500	0.500
25	0.57	0.500	0.489
30	0.48	0.500	0.495
35	0.44	0.500	0.476
40	0.37	0.500	0.507
15	1.50	0.250	0.291
20	1.21	0.250	0.281
25	1.01	0.250	0.276
30	0.90	0.250	0.264
35	0.80	0.250	0.262
40	0.71	0.250	0.264
45	0.70	0.250	0.243
30	1.52	0.125	0.156
35	1.31	0.125	0.160

with the actual size of the hole for three such specimens. The only change required in Eq. (23.1) was to substitute the velocity of ultrasound in Al for that in water. Angular positions below which multiple peaks were not obtained are not listed. In the case of the 0.125-in.-diam hole, the reflected signal was extremely weak and noisy due to the combination of a small reflector and a large angle from perpendicular.

A second type of Al sample used was more realistic in terms of use for characterizing flaws in an actual inspection. It was a flat, rectangular block ($3 \times 3 \times 6$ in.) in which flat-bottomed holes were drilled with axes at different angles to the flat top of the block. In this case, normal incidence of the ultrasonic beam to the surface of the sample was not always desired. Therefore, in some cases, the refracted angle of the incident beam was added to the angle at which the hole was drilled to give an effective angle larger than the drilled angle. Table 23.3 compares the actual diameters of the holes to the diameters calculated from the spectral data at various angles for this specimen. The agreement is

Table 23.3. Data and Calculated Results for Flat Aluminum Specimen

Angle to Which Hole Was Drilled (deg)	Angle of Incidence to Surface (deg)	Angle for Calculations (deg)	Average Interval Between Consecutive Interference Peaks (MHz)	Diameter of Hole, in.	
				Measured	Calculated
10	0	10.0	1.25	0.500	0.520
10	~ 1	14.3	1.11	0.500	0.425
10	~ 2	18.6	0.75	0.500	0.495
10	~ 5	32.0	0.55	0.500	0.417
20	0	20.0	1.35	0.250	0.258
20	~ 1	24.3	0.99	0.250	0.294
20	~ 2	28.6	0.81	0.250	0.308

very good at the normal angle of incidence (0°), which can be determined precisely. At incident angles other than 0°, the uncertainty in incident angle contributed to a relatively large error in the effective angle used in the calculations. An improved manipulator will be constructed so that incident angles other than 0° can be determined with precision.

Fabrication of Reference Discontinuities (K. V. Cook, H. L. Whaley, Jr.)

We are continuing work on the problems encountered in inspecting tubing by ultrasonic methods. A major problem is the fabrication of reference notches that can be used as realistic standards for calibration. Since electrodischarge machining appears to be a reliable method for making notches on both inner and outer surfaces, we are continuing our studies of notch fabrication. As we encounter new alloys, we are generating appropriate reference curves for both longitudinal and transverse notches.

We are also generating reference curves for making small, circular discontinuities from 0.004 to 0.045 in. in diameter. These curves are being generated for Ta and W electrodes for electrodischarge machining discontinuities in alloys or metals in which they are required for calibration of ultrasonic or eddy-current test equipment. Initial results

indicate that the pits are about 0.003 to 0.005 in. larger in diameter than the cutting electrode (depending on the electrode material and etching voltage).

Penetrating Radiation and Holographic Inspection Methods

Radiation Scattering[1] (B. E. Foster, S. D. Snyder)

We continued our studies on the use of scattered and fluorescent radiation for measuring the thickness of coatings or claddings on reactor components. We investigated the scatter angle, intensity, and energy of the radiation scattered from three base (or target) materials (Al, Pb, and U) with a constant scatter angle and a varying angle of incidence and also with a constant angle of incidence and a varying scatter angle. We found that, for the ^{147}Pm source with a constant angle of incidence, there was no detectable change in the scattered energies as the detector was moved to different angles (scatter angles), however the intensity showed a near linear decrease from a scatter angle of 140° to one of 105°. When the angle of the detector was held constant and the angle of incidence was varied, the count rate again showed a near linear decrease from an incident angle of 90° to one of 30°. Similar results were obtained from all three target materials, and, in addition, some low-energy peaks were seen for Al that were not observed for U and Pb. Figure 23.4 shows the scatter spectrum (curve A) from the bare U target with the most intense peak at about 15 kev and that (curve B) for the U target covered with 0.021 in. of Al. The intensity of the 15-kev peak is greatly reduced, but that of the 37-kev peak (coherent scattering of the 38-kev source energy by the Al) is significantly increased. The apparent shift in energy of the 15-kev peak between curves A and B is due to the nonlinearity of the analyzer at these low energies and represents less than 2 kev. We are now adding different thicknesses of Al shims to the target materials for calibrating and evaluating sensitivity to a given change in thickness.

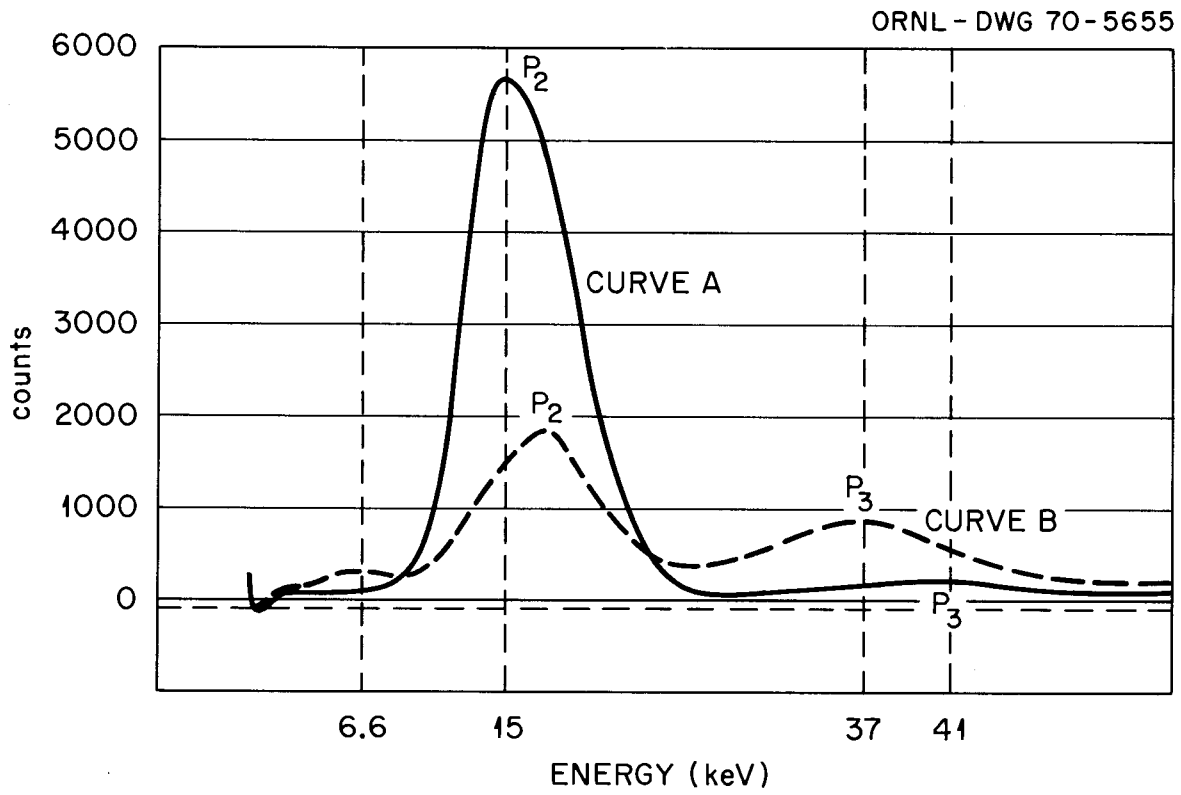

Fig. 23.4. Scatter Spectra from Bare Targets of Uranium and Uranium Covered with Thin Aluminum.

Notes

1. This work is jointly supported by the Fuel Element Fabrication Development Program and is also discussed in Chapter 19 of this report.

24. IMPROVEMENT OF HASTELLOY N AND RELATED COMPOSITIONS

J. R. Weir, Jr. H. E. McCoy, Jr.

This program is aimed at defining and understanding the metallurgical variables that affect the engineering performance of Ni-based structural alloys in reactor environments. Such alloys have been shown to have reduced stress-rupture properties and greatly reduced fracture strain after exposure to thermal-neutron fluences. Our work has concentrated on Hastelloy N. We have found that small additions of Ti, Zr, Hf, and Nb effectively reduce the deterioration of properties caused by irradiation. The end products sought by this program are a better understanding of the factors important in controlling irradiation damage in Ni-based alloys and development of a modified Hastelloy N with improved resistance to irradiation damage.

Mechanical Properties of Hastelloy N and Related Compositions

Effect of Alloying on Creep Behavior of Alloys of the Modified Hastelloy N Type (C. E. Sessions)

We continued our studies of alloying effects on irradiation damage and aging of modified Hastelloy N. Our primary aim has been to optimize the alloy composition with respect to Ti, Nb, Hf, Si, and C so that the metallurgical properties of the alloy will be acceptable for reactor application at 700°C. We have used irradiation temperatures of 650 and 760°C to study the effects of temperature on carbide stability and irradiation damage in these modified alloys. During this quarter, we evaluated several new alloy compositions after irradiation at 760°C and after aging at 650 and 760°C.

Table 24.1 lists some alloy compositions and the mechanical properties of these alloys after irradiation. We listed only alloys that had shown postirradiation creep ductilities of 4% or greater.

We previously discussed the superior creep-rupture behavior of alloy 184, an alloy containing 1.2% Ti plus 1.2% Hf. Several recent results (Table 24.1) indicate that alloys containing as little as

Table 24.1. Creep Properties at 650°C of Modified Hastelloy N Alloys After Irradiation at 760°C to a Thermal Fluence of 5×10^{20} neutrons/cm^2

Alloy	Additions,[a] %				Stress (psi)	Rupture Life (hr)	Fracture Strain (%)	Minimum Creep Rate (%/hr)
	Ti	Nb	Hf	Si[b]				
					$\times 10^3$			
291	2.0				40	388	4.7	0.008
					47	168.6	6.8	0.027
					63	0.2	1.1	
292	2.4				55	71.6	1.4	0.0055
					40	1009	0.9	0.0006
300	0.8	1.3	0.7		47	141	6.1	0.038
302			0.5		40	226	9.4	0.032
184	1.2		1.2		63	2.3	15.4	1.82
					47	23.5	13.7	0.15
					35	2292	22.7	0.005
232			1.2		40	405	13.3	0.02
299			0.5		46	56.4	5.4	0.075
307		0.9	0.8		55	20	6.4	
309	0.5		0.4		55	9.7	4.2	0.339
310	0.1	0.6	0.5		63	6.2	4.7	
					55	133	16.7	0.094
					40	Test in progress		0.003
311	0.4	0.8	0.3		55	43.9	6.8	0.135
312	0.2	0.6	0.4		55	36.3	8.1	0.21
314	0.8	1.3	0.6	0.35	55	77.1	7.2	0.08

[a]The base composition of these alloys is Ni–12% Mo–7% Cr–4% Fe–0.05% C.

[b]All alloys contained a residual concentration of < 0.01% Si as an impurity; Si was intentionally added only to alloy 314.

0.3 to 0.5% Hf plus Ti or Nb can produce postirradiation rupture lives and ductilities comparable to those of alloy 184. The results in Table 24.1 represent screening tests for a given heat treatment and irradiation condition. Since considerably more is known about the mechanical

properties of alloy 184, we compare the properties of new alloys to those of alloy 184, which to date is the optimum alloy composition for resistance to irradiation damage at 760°C.

Consider first the properties of alloy 184, both unirradiated and after irradiation, as shown in Fig. 24.1. The stress to produce rupture in 1000 hr at 650°C for the unirradiated alloy is 45,000 psi; the expected fracture strain at this stress would be about 55%. After irradiation at 760°C, the stress to produce rupture in 1000 hr was reduced to 37,000 psi; the expected ductility would be approximately 20% at this stress level. At higher stress levels the ductility of alloy 184 after irradiation would be lower, and values of 14 and 15% elongation were measured at 47,000 and 63,000 psi, respectively. Thus, even after irradiation at 760°C, alloy 184 exhibits 15 to 20% rupture ductility at 650°C. The

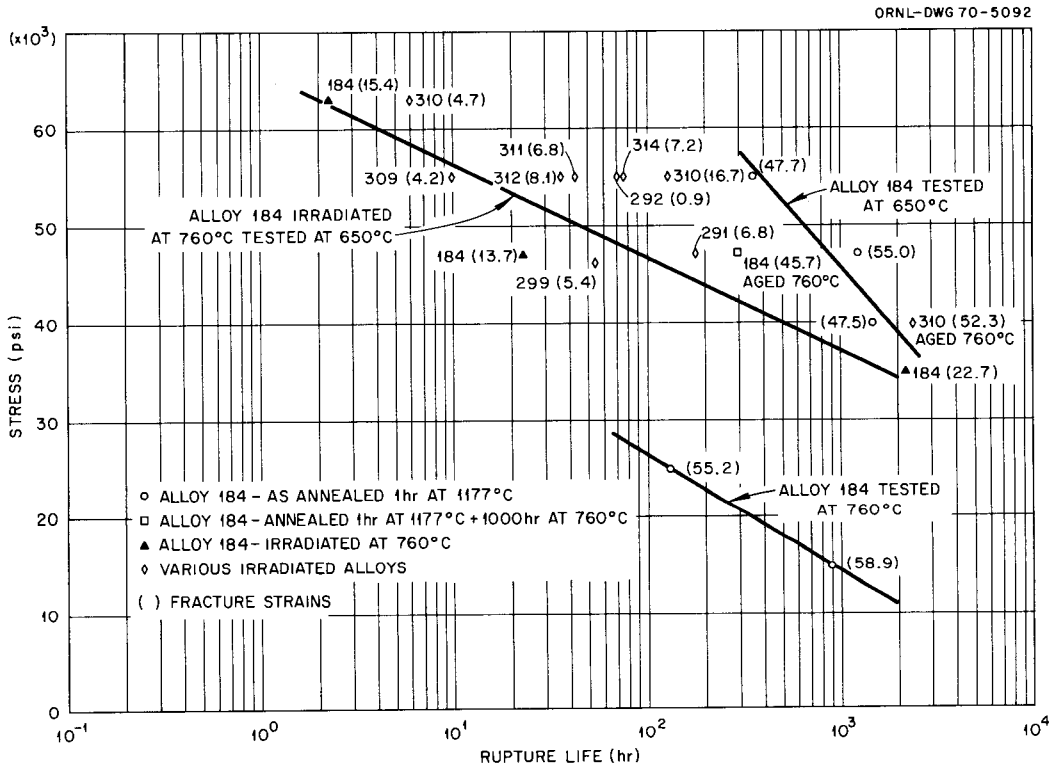

Fig. 24.1. Effect of Alloy Composition on the Creep-Rupture Properties of Several Modified Hastelloy N Alloys. Samples were annealed 1 hr at 1177°C before testing or irradiation to a thermal fluence of 3×10^{20} neutrons/cm^2. The first number by each point designates the alloy and the second number (in parentheses) designates the fracture strain.

properties of unirradiated alloy 184 tested at 760°C are also quite good. Comparative postirradiation creep-rupture results of alloys 229 (0.5% Hf), 309 (0.5% Ti, 0.4% Hf), 310 (0.1% Ti, 0.6% Nb, 0.5% Hf), 311 (0.4% Ti, 0.8% Nb, 0.3% Hf), 312 (0.2% Ti, 0.6% Nb, 0.4% Hf) and 314 (0.8% Ti, 1.3% Nb, 0.6% Hf, 0.3% Si) are also shown in Fig. 24.1. The properties of alloys 299 and 309 fall close to the line drawn for irradiated alloy 184. The fracture strains, shown in parentheses, are lower than those found for alloy 184 but are still quite acceptable. The rupture lives of alloys 312, 311, 314, and 310 are greater than that of alloy 184, but only alloy 310 has a postirradiation ductility that is greater than 10% and, thus, comparable to that of alloy 184. Since the compositions of alloys 310, 311, and 312 are similar, the difference in ductility after irradiation must be due either to a few tenths of one percent HF or to statistical scatter of the test results.

Figure 24.2 gives the minimum creep rates determined at different stress levels for the irradiated and some unirradiated specimens. Curves

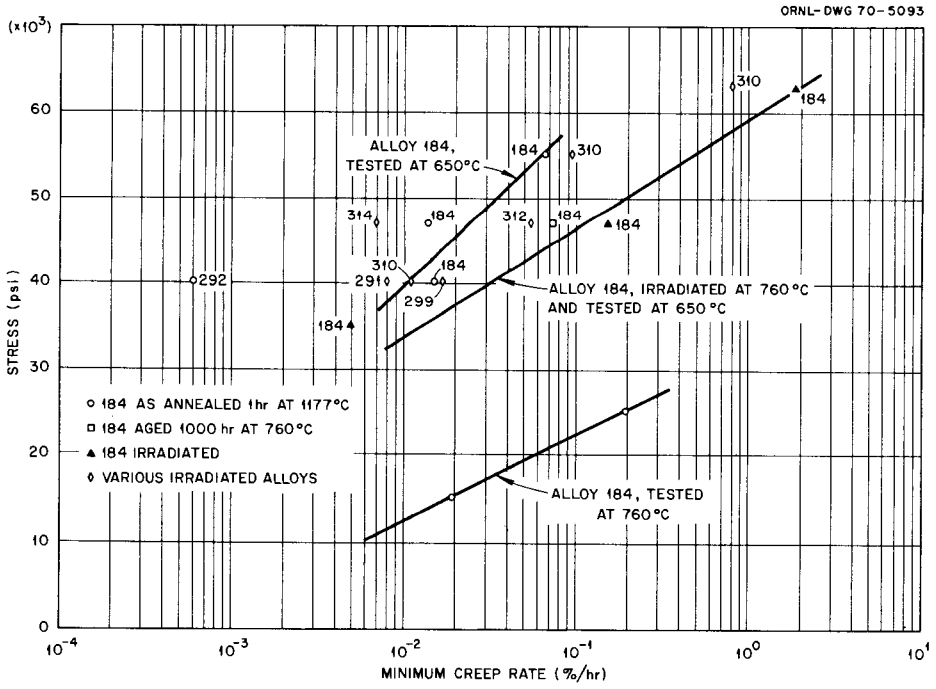

Fig. 24.2. Effect of Alloy Composition on the Minimum Creep Rate of Several Modified Hastelloy N Alloys. Samples were annealed 1 hr at 1177°C before testing or irradiation to a thermal fluence of 3×10^{20} neutrons/cm^2 at 760°C.

again are drawn through the few data points for alloy 184, both unirradiated and tested at 650 or 760°C and irradiated at 760°C and tested at 650°C. A large effect of test temperature (650 vs 760°C) on the creep rate is evident. The curve drawn for samples irradiated at 760°C indicates little or no effect of irradiation on the creep rate at low stress levels but possibly an increase of an order of magnitude in creep rate at high stress levels. The creep rates for alloys 299, 310, 312, and 314 irradiated at 760°C are about the same as those for the irradiated and control samples for alloy 184. The creep rate of alloy 314 is lower than the creep rates of the other alloys.

A point plotted in Fig. 24.2 for alloy 292 shows that after irradiation at 760°C the creep of this alloy modified with 2.4% Ti is only about one-tenth as fast as that of any other modified alloy shown. We tentatively concluded that precipitation of the intermetallic compound Ni_3Ti is responsible for this reduced creep rate and low fracture strain (Table 24.1) but as yet have not positively identified the intermetallic. If intermetallics are found, these higher Ti concentrations would not be desirable for our application. Alloy 291 contains 2.0% Ti, creeps at a rate comparable to those of the other alloys, and has 6.8% fracture strain. Thus the threshold for intermetallic precipitation at 760°C lies between 2.0 and 2.4% Ti.

The influence of aging at 650 and 760°C on the tensile behavior of several of these modified alloys was discussed previously.[1] Some additional creep tests were completed at 650°C after aging at 760°C; the results are given in Table 24.2. Aging 1000 hr at 760°C causes a large decrease in rupture life and an increase in creep rate for alloy 184 at 47,000 psi, but the ductility is not changed significantly. Alloys 299 and 310 show equivalent creep rates at 40,000 psi, but the ductility and rupture life of alloy 299 are lower. Alloy 314 resisted creep well after aging at 760°C, but the ductility (24.8%) was lower than that found for most other alloys listed in Table 24.2.

A comparison of the effect of aging at 760°C and irradiation at 760°C on the stress-rupture life at 650°C is shown in Fig. 24.3 for five alloys. For most alloys, too few points are available to determine a line, but lines are shown for the postirradiated tests at 650°C on

Table 24.2. Creep Properties at 650°C of New Compositions of Modified Hastelloy N After Certain Aging Treatments

Alloy	Aging Treatment[a]		Stress (psi)	Rupture Life (hr)	Fracture Strain (%)	Minimum Creep Rate (%/hr)
	Time (hr)	Temperature (°C)				
			$\times 10^3$			
184	Solution Anneal		55	356	47.7	0.067
	Solution Anneal		45	1234	55.0	0.014
	Solution Anneal		40	1484	47.5	0.015
	1000	760	47	288	45.7	0.083
299	1000	760	40	1200	35.8	0.016
310	1000	650	55	97.3	36.6	0.15
	1000	760	55	96.7	24.8	0.22
	1000	760	40	2388	52.3	0.011
312	1000	760	47	484	57.9	0.055
314	1000	760	47	1721	24.8	0.007

[a]All aging treatments were preceded by a solution anneal for 1 hr at 1177°C.

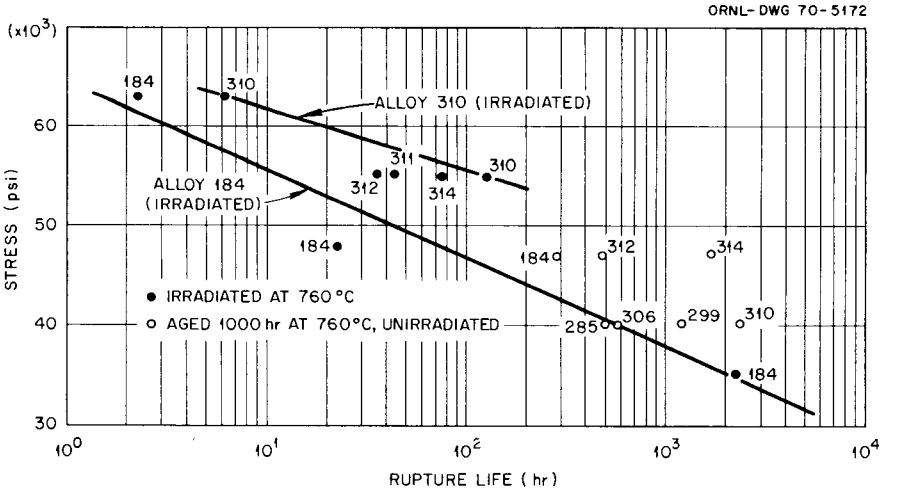

Fig. 24.3. Comparison of Aged and Irradiated Creep-Rupture Life at 650°C for Various Compositions of Hastelloy N.

alloys 184 and 310. Although alloy 310 had a longer rupture life, the ductility at 63,000 psi after irradiation was higher for alloy 184 than for alloy 310 (Fig. 24.1). However, both of these alloys had excellent properties after irradiation.

From the limited data available, the creep rates observed after irradiation at 760°C or after aging at 760°C seem comparable. The creep curves for solution annealed and irradiated samples of alloy 184 are compared in Fig. 24.4. At 47,000 psi, irradiation reduced the elongation from 53 to 14%, decreased the rupture life from 1250 to 23 hr, and caused an increase in creep rate from 0.067 to 0.15%/hr. The changes in ductility and rupture life are undoubtedly significant. The effects of irradiation are greater at high stress levels than at low stress levels.

Electron Microscopy of Modified Hastelloy N Alloys (R. E. Gehlbach)

Electron microscopy studies of Hastelloy N have concentrated primarily on characterizing the effects of alloying additions on the microstructure of several modifications of the alloy after exposure at 650 and 760°C. The resistance to radiation damage is altered markedly by the addition of small amounts of Ti, Nb, and Hf. Silicon is also important in determining the type of precipitate formed. The concentration

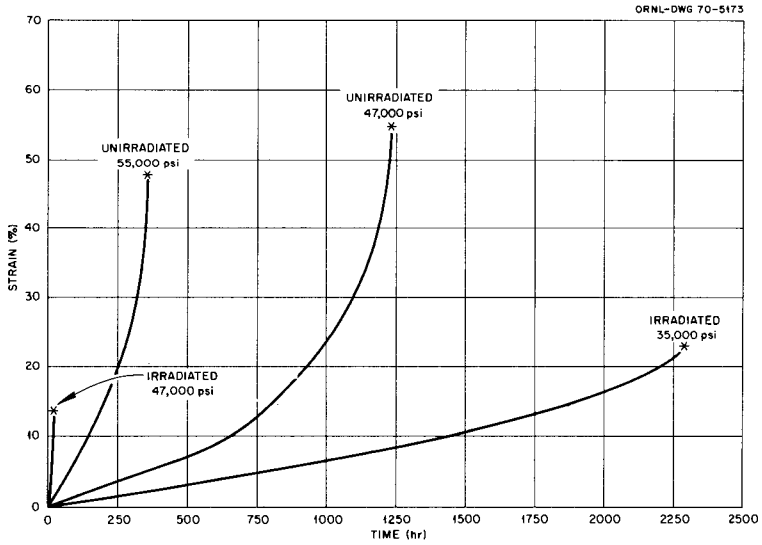

Fig. 24.4. Creep Curves at 650°C for Irradiated and Unirradiated Alloy 184 at Various Stresses. All samples annealed 1 hr at 1177°C before testing or irradiation. Irradiated samples were irradiated at 760°C to a thermal-neutron fluence of 3×10^{20} neutrons/cm^2.

of Si is controlled largely by the melting practice; it is high (0.5%) for alloys prepared by electroslag remelting[2] or air melting and low (< 0.1%) for vacuum-melted alloys.

A number of 2-lb laboratory melts were prepared to evaluate the influence of Ti, Nb, Hf, and Si on precipitation and resistance to irradiation damage. Several of these alloys were aged at 650 and 760°C. Precipitates were extracted electrolytically and identified by x-ray diffraction. The alloys with their compositions and the precipitates detected are listed in Table 24.3.

Table 24.3. Alloy Compositions and Precipitate Types[a] Observed in Several Heats of Modified Hastelloy N

Alloy	Composition,[b] %				Aging Temperature[c]					
					650°C			760°C		
	Ti	Nb	Hf	Si	MC	M_2C	M_6C	MC	M_2C	M_6C
292	2.4							X		
285		0.5				X[d]			X	
306		0.55		0.27	X[e]		X			X
286	0.23	0.5			X[f]	X		X[f]	X	
287	0.12	0.6		0.14	X	X	X	X[f]	X	X
310	0.15	0.57	0.54					X		
313			0.7					X	X	
314	0.8	1.3	0.65	0.35				X		X

[a] In the precipitate designations, the metal content of the carbide is denoted by M.

[b] All alloys have a nominal composition of 12% Mo, 7% Cr, 4% Fe, 0.2% Mn, 0.06% C, bal Ni.

[c] Aged 1000 hr at the indicated temperature except alloys 292, 310, 313, and 314, which were aged 200 hr at 760°C.

[d] Plus unidentified phase.

[e] Very fine unidentified precipitate observed by electron microscopy.

[f] Stacking fault morphology observed by electron microscopy.

The effects of Ti additions on precipitation were discussed previously.[3,4] Precipitation of carbides of the MC type (where M represents the metal content) often occurs in a stacking fault morphology at Ti concentrations up to the 1.2% level. Examination of an alloy (alloy 292) that contained 2.4% Ti and had been aged 200 hr at 760°C revealed the absence of this morphology, although much of the MC type of carbide (a_o = 4.29 A) was present as films and very fine particles in the jagged grain boundaries and as particles in the matrix. Gamma prime (Ni_3Ti) was not detected in this material.

The effects of small amounts of (1) Nb, (2) Nb and Ti, and (3) Nb, Ti, and Si on the microstructure after aging at 760°C are shown in Fig. 24.5. The addition of 0.5% Nb alone (alloy 285) resulted in a relatively coarse precipitate of the M_2C type [Fig. 24.5(a)], which is typical of the base alloy. No precipitate was observed on stacking faults in these alloys. A combination of 0.5% Nb and 0.23% Ti (alloy 286) resulted in a somewhat finer precipitate at the grain boundaries [Fig. 24.5(b)] than that observed in the alloy without Ti (alloy 285). The combination of 0.14% Si, 0.12% Ti, and 0.6% Nb (alloy 287) resulted in the formation of large blocky carbides of the M_6C type in both the grain boundaries and the matrix, as shown in Fig. 24.5(c). These Si-rich carbides are very stable and are not dissolved during annealing as described elsewhere.[5] After the Si is consumed in the M_6C type of carbide, which contains about 3.3% Si, further precipitation of carbides at grain boundaries is similar to that in the Si-free alloy (alloy 286), although smaller amounts are present. Relatively small carbides were also precipitated in the matrix in alloy 287. There was some precipitation in the stacking fault morphology in alloys 286 and 287, which contained Ti, but not in alloys 285 or 306, which do not contain any Ti. There is some question as to the structure of the planar precipitate in the Nb-doped alloys. Aging at 650°C resulted in a much finer M_2C type of carbide than that produced at the higher temperature (760°C). In addition to a large quantity of the M_6C type of carbide, a small amount of a very fine MC type of carbide was dispersed throughout the matrix in alloy 306 after aging at 650°C; however only the M_6C type of carbide was present after aging at 760°C.

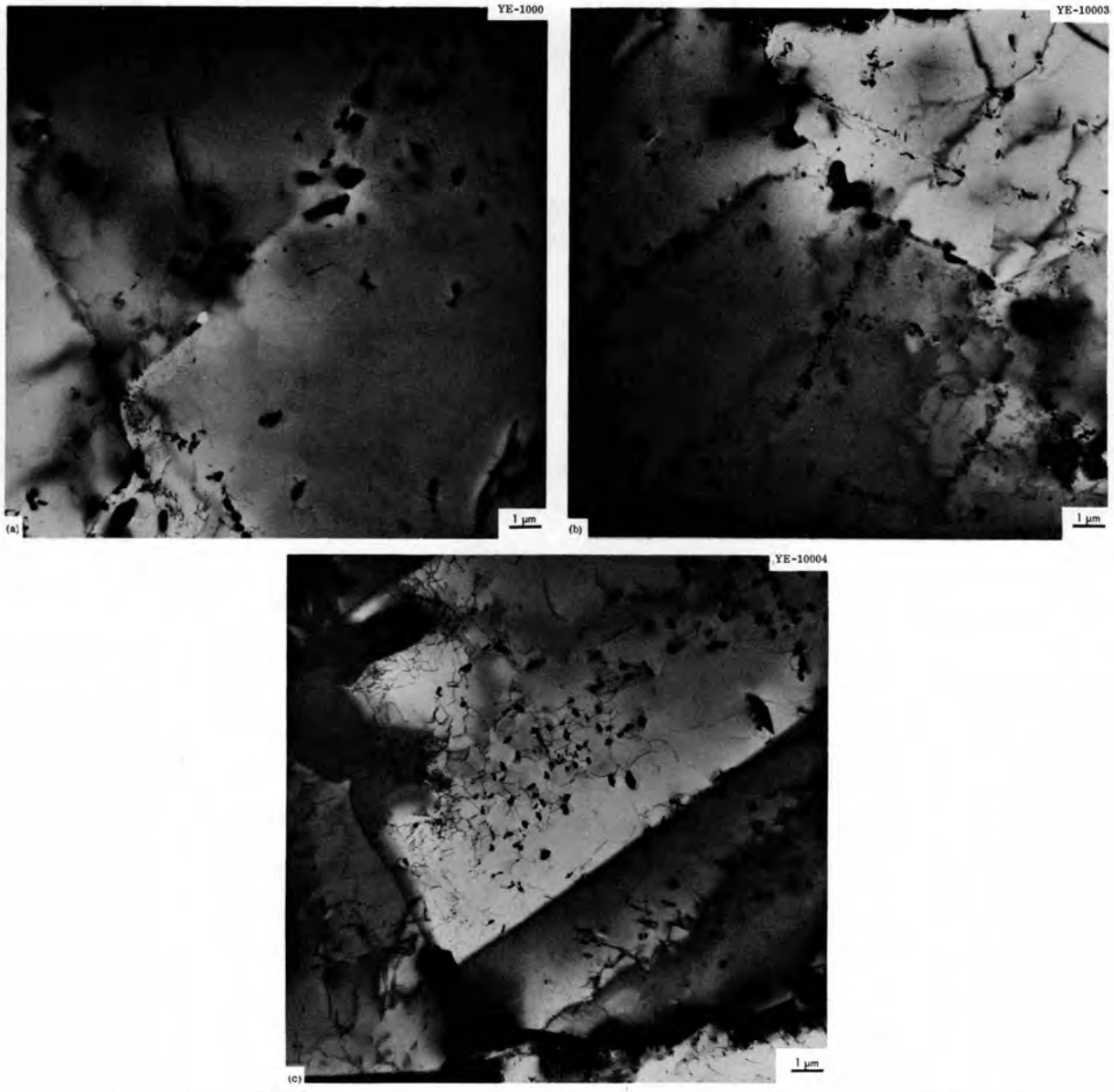

Fig. 24.5. Microstructures of Hastelloy N Modified with (a) 0.5% Nb, (b) 0.5% Nb and 0.23% Ti, and (c) 0.6% Nb, 0.12% Ti, and 0.14% Si after Aging 1000 hr at 760°C. 10,000×.

The MC type of carbide formed in Hf-modified alloys has a morphology different from that in the Ti-modified alloys. The structure shown in Fig. 24.6(a) is typical of an alloy that contains 0.7% Hf (alloy 313) aged 200 hr at 760°C. As shown in Fig. 24.6(b), 0.15% Ti and 0.57% Nb in combination with Hf (alloy 310) did not significantly affect the morphology of the carbides formed at 760°C. A comparison of Fig. 24.6(b) with Fig. 24.5(b) shows the effect of Hf at comparable levels of Ti and Nb. A similar microstructure was previously shown[6] for an alloy containing 1% Hf and 1% Ti (alloy 184). The presence of 0.35% Si in an alloy containing 0.8% Ti, 1.3% Nb, and 0.65% Hf (alloy 314) resulted in large, stable precipitates of the M_6C type of carbide in the matrix and grain boundaries with subsequent precipitation of fine MC type of carbide [Fig. 24.6(c)], as in the alloys without Si. Due to the high level of Si in alloy 314, much of the C was tied up in the M_6C type of precipitate with little available for precipitation of the MC type of carbide during aging. No stacking-fault morphology was found in the Hf-modified alloys.

We examined the phases present in four new commercial alloys (Table 24.4). Two are electroslag-remelted heats containing 0.7% Ti and 2.3% Nb (heat 69-344) and 1.07% Ti and 0.97% Hf (heat 69-345). Both contained high concentrations of Si and had large amounts of the M_6C type of carbide after annealing. Small quantities of the MC type of carbide were also present in both alloys.

Precipitates in the two vacuum-melted heats were examined after exposure at 650°C. One contained 0.53% Ti and 2.1% Nb (heat 69-648) and the other 0.8% Ti and 0.75% Hf (heat 69-641). Both had only trace levels of Si, and no M_6C type of precipitate was found. Two carbides of the MC type were present in heat 69-648, and three in heat 69-641.

We identified the precipitates formed in Hastelloy N as a function of the Mo concentration. These alloys have no Si additions. Only the M_2C type of carbide precipitated at 650°C for Mo levels of 10 to 16%. At 19% Mo, the only precipitate formed was an M_6C type of carbide with a large lattice parameter (a_o = 11.23 A), probably Ni_2Mo_4C.

Our observations on the effects of alloy modifications on the microstructure of the heats are consistent with our previous observations:[6]

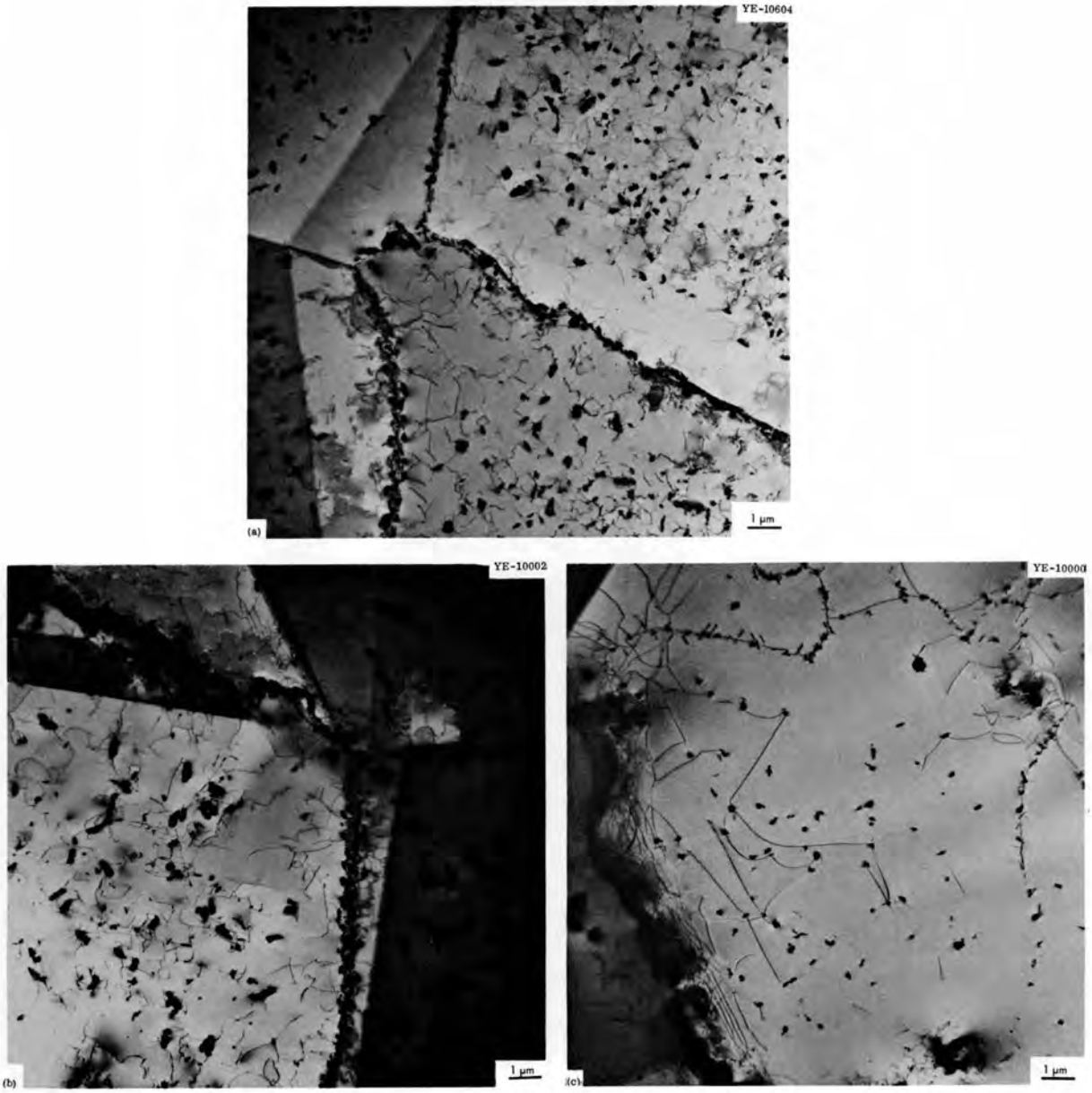

Fig. 24.6. Microstructures of Hafnium-Modified Hastelloy N after Aging 200 hr at 760°C. (a) 0.7% Hf, (b) 0.54% Hf, 0.57% Nb, and 0.15% Ti, and (c) 0.65% Hf, 1.3% Nb, 0.8% Ti, and 0.35% Si. 10,000×.

Table 24.4. Precipitates in Commercial Modified Hastelloy N

Alloy	Additions to Composition,[a] %				Types of Carbide Phases[b] Present
	Ti	Nb	Hf	Si	
69-344[c]	0.7	2.3		0.51	M_6C (S) + MC (W)
69-345[c]	1.07		0.97	0.50	M_6C (S) + MC (W)
69-648[d]	0.53	2.1	0.10	0.04	MC
69-641[d]	0.8	0.02	0.75	< 0.01	MC

[a]All alloys have a nominal composition of 12% Mo, 7% Cr, 0.2% Mn, 0.06% C, bal Ni.

[b](S) = Strong, (W) = Weak.

[c]Annealed 1 hr at 1177°C. Alloys contain 4% Fe.

[d]Annealed 1 hr at 1177°C plus 1000 hr at 650°C.

the formation of particular types of precipitates is dependent on the alloying additions. The M_2C type of carbide is stable in the base alloy, and additions of Ti, Nb, and Hf in sufficient quantities produce the MC type of carbide. The M_2C type of carbide is coarser at 760°C than at 650°C; it is the higher temperature which is of primary interest to us, however, since the operating temperature of a molten salt breeder reactor will be about 700°C. The postirradiation mechanical properties of materials that form the coarse M_2C type of carbide deteriorate markedly at the irradiation temperature.

The beneficial effect of the MC type of carbide on the postirradiation mechanical properties appears to depend on the morphology of the precipitate or at least on the alloying addition used. Titanium alone in sufficient quantities improves the postirradiation creep-rupture life, but may reduce the fracture ductility too much at high creep stresses. The most obvious microstructural modification in the Ti-modified alloys that form the MC type of carbide is the formation of massive stacking-fault precipitates.

The Nb-modified heats discussed do not contain sufficient quantities of Nb to stabilize the MC type of precipitate. Based on microstructural

observations we would not expect these alloys to have good properties after irradiation. Higher concentrations of Nb would be expected to produce good properties if the MC type of carbide were formed in a desirable morphology. We shall study several alloys with larger additions of Nb.

Additions of Hf appear to control the type of microstructure even with large quantities of Ti and Nb in the alloy. These alloys are characterized by small discrete particles in the matrix and grain boundaries, and the mechanical properties after irradiation are outstanding.

Small quantities of Si cause the formation of a Si-rich, stable, M_6C type of carbide that is very coarse. This is undesirable in that it results in a grain-boundary structure approaching that of standard Hastelloy N rather than permitting the generation of a controlled microstructure by judicious alloying and heat treatment. Thus, the electroslag-remelting process is virtually eliminated from further consideration as a production method for an improved Hastelloy N. However, small amounts of Si may possibly be tolerated, particularly when Hf is used as the modifying addition.

Notes

1. C. E. Sessions, Fuels and Materials Development Program Quart. Progr. Rept. Dec. 31, 1969, ORNL-4520, pp. 315–320.

2. C. E. Sessions and R. E. Gehlbach, Fuels and Materials Development Program Quart. Progr. Rept. Sept. 30, 1969, ORNL-4480, pp. 279–291.

3. R. E. Gehlbach, Fuels and Materials Development Program Quart. Progr. Rept. March 31, 1969, ORNL-4420, pp. 162–167.

4. C. E. Sessions and R. E. Gehlbach, Fuels and Materials Development Program Quart. Progr. Rept. June 30, 1969, ORNL-4440, pp. 141–142.

5. R. E. Gehlbach, MSR Program Semiann. Progr. Rept. Feb. 29, 1968, ORNL-4254, pp. 206–213.

6. R. E. Gehlbach and C. E. Sessions, Fuels and Materials Development Program Quart. Progr. Rept. Sept. 30, 1969, ORNL-4480, pp. 291–295.

25. ADVANCED MATERIALS FOR STEAM GENERATORS

P. Patriarca G. M. Slaughter

The purpose of this program is to determine the corrosion resistance of welds in several high-temperature alloys being considered for use in steam generators for advanced high-temperature gas-cooled reactors. We need to know how well these weldments will resist both general and preferential corrosion in steam at 595 to 760°C.

The program includes four areas of investigation: (1) general corrosion (formation of a uniform scale) at 595 and 650°C, including an evaluation of the general weldability of various combinations of base and filler metals; (2) general corrosion at 705 to 760°C; (3) preferential corrosion (e.g., oxidation at the fusion line, pitting, and stress cracking); and (4) mechanical properties.

General Corrosion at 595 and 650°C and Weldability

Measurements of Weight Gains (J. P. Hammond)

The amounts of corrosion to be expected for the weldments between similar metals after 20 years of exposure to steam at 595 and 650°C, as extrapolated from data for weight gains after 8000 hr, are presented in Table 25.1. These calculated amounts of corrosion are given in terms of metal consumed and depth penetrated to provide a better grasp of the significance of the curves previously presented[1] for corrosion after 1 year. The values in Table 25.1 were determined by means of the following equation and certain simplifying assumptions:[2]

$$\Delta W = \Delta W_o + K_\ell T \quad ,$$

where

ΔW = total weight gained (0), mg/dm^2;

ΔW_o = extrapolated intercept of linear portion of curve (T = 0), mg/dm^2;

K_ℓ = rate constant of linear part of curve, mg/dm^2; and

T = exposure time.

Table 25.1. Corrosion and Metal Penetration Calculated[a] from Weight Gains of Weldments Between Similar Metals

Weldment			Intercepts and Slopes of Weight-Gain Curves[b] With Standard Errors		Calculated Metal Consumed in 20 Years	Calculated Penetration in 20 Years	
Code	Base Metal	Filler Metal	ΔW_o[c] (mg/dm^2)	K_ℓ (mg/dm^2-1000 hr)	(mg/cm^2)	(μm)	(in.)
			Exposed at 595°C				$\times 10^{-4}$
A9	Inconel 625	Inconel 625	10.6 ± 0.53	0.50 ± 0.05	3.09	3.7	14
A5	Hastelloy X	Hastelloy X	11.4 ± 0.67	0.47 ± 0.08	2.78	3.4	13
A18	IN 102	IN 102	19.1 ± 0.32	1.77 ± 0.29	10.8	12.7	50
A2	Incoloy 800	Inconel 82	11.4 ± 0.71	0.91 ± 0.12	4.72	5.8	23
A3	Inconel 600	Inconel 82	−3.98 ± 2.19	7.18 ± 0.37	40.1	48.1	1.89
A4	Type 304 stainless steel	Type 308 stainless steel	34.2 ± 0.65	0.63 ± 0.11	3.57	4.5	18
			Exposed at 650°C				
A9	Inconel 625	Inconel 625	12.2 ± 0.72	1.24 ± 0.12	7.31	8.7	34
A5	Hastelloy X	Hastelloy X	13.3 ± 1.07	1.55 ± 0.18	8.14	9.9	39
A18	IN 102	IN 102	18.1 ± 1.19	0.75 ± 0.20	4.90	5.7	23
A2	Incoloy 800	Inconel 82	24.9 ± 2.71	3.27 ± 0.17	16.6	20.5	81
A3	Inconel 600	Inconel 82	−1.19 ± 8.13	10.9 ± 0.45	60.9	73.0	2.87
A4	Type 304 stainless steel	Type 308 stainless steel	26.8 ± 1.47	1.86 ± 0.25	8.77	10.9	43

[a] Amounts of corrosion do not allow for oxide flaking during test and are based on the following calculated concentrations of metal in the scales of the respective weldments: A9, 76.1%; A5, 74.1%; A18, 76.7%; A2, 73.5%; A3, 76.2%; and A4, 71.3%.

[b] ΔW (mg/dm^2) = ΔW_o (mg/dm^2) + K_ℓ (mg/dm^2-1000 hr) T (1000 hr), where ΔW is weight gain, ΔW_o is intercept, K_ℓ is slope, and T is time.

[c] The standard error of the intercept is for an individual specimen.

Note in Table 25.1 the very low corrosion rates for the Inconel 625 (A9) and Hastelloy X (A5) weldments as contrasted to the comparatively high rates for Inconel 600 welded with Inconel 82 (A3). The calculated amount of metal penetration in 20 years was acceptably low (0.0005 in. or less) at both 595 and 650°C for Inconel 625, Hastelloy X, and IN 102 welded with themselves and was less than 0.002 and 0.003 in. for Inconel 600 welded with Inconel 82 at these respective temperatures. Type 304 stainless steel welded with type 308 stainless steel (A4) showed high initial amounts of corrosion but surprisingly low linear rates, which are suspect since we showed type 304 stainless steel susceptible to spallation.[2] The linear rates of corrosion on all weldments between similar metals were greater at 650°C than at 595°C except for the IN 102 weldment (A18), for which the reverse was true. Measurements of scale thicknesses showed that this reversal was consistent with metallographic observations, since the IN 102 alloys had thicker scales after exposure at 595°C than after exposure at 650°C (Table 25.2). Note finally that the level and rate of corrosion of the weldment of Incoloy 800 with Inconel 82 (A2), although favorably low, were considerably higher at 650°C than at 595°C.

Measurements of Scale Thickness

Table 25.2 lists the thicknesses of scales formed on the individual base metals and weld deposits of weldments at 595 and 650°C for times to 8000 hr.

The scales were considered to have two components: first, a continuous oxide layer of generally uniform thickness and, second, oxide protrusions that extended from the surface layer into the substrate. These protrusions generally consisted of intergranular penetrations, a transgranular Widmanstätten type of formation, or a sporadic pit type of formation (bulky).[1] Eberle[3] indicated that the surface scales that form on many ferritic, austenitic, and high-Ni alloys generally consist of two distinct layers. This was found to be true for some of the present materials, but, in many instances, delineation of separate scales was not successful, and, consequently, the surface scale was considered as an integral unit.

Table 25.2. Thickness of Scale on Alloys When Used as Base Metals and as Filler Metals as Functions of Time and Temperature of Exposure to Steam

Alloy	Exposure Time (hr)	Scale Thickness,[a] μm							
		As Base Metal				As Filler Metal			
		595°C		650°C		595°C		650°C	
		Surface Scale Only	Surface Scale Plus Protrusions Into Parent Metal	Surface Scale Only	Surface Scale Plus Protrusions Into Parent Metal	Surface Scale Only	Surface Scale Plus Protrusions Into Parent Metal	Surface Scale Only	Surface Scale Plus Protrusions Into Parent Metal
2.25% Cr–1% Mo low-alloy steel	2000	166	173	1462	1474				
	4000	232	243						
	8000	312	323						
Inconel 625	4000	0.2	1.4[b]	1.0	1.9[c]	0.8	1.4[d]	0.9	1.7[c]
	8000	0.7	1.5[b]	1.3	2.3[c]	0.9	1.4[d]	1.1	2.7[c]
Hastelloy X	4000	0.7	1.3[d]	1.0	2.0[e]	0.6	1.4[d]	0.6	1.6[e]
	8000	0.8	1.6[d]	0.9	2.1[e]	0.6	1.4[d]	0.6	1.4[e]
IN 102	4000	0.5	3.2[b]	0.4	f	0.6	1.4[d]	0.4	0.9[d]
	8000	0.4	4.9[b]	0.8	2.2[d]	0.6	1.6[d]	0.7	1.7[d]
Incoloy 800	4000	0.6	1.5[g]	2.1	4.1[h]				
	8000	0.7	1.7[g]	2.5	4.4[h]				
Inconel 600	4000	1.2[i]	9.7[j]	2.3[i]	11.6[j]				
	8000	1.8[i]	13.2[j]	2.0[i]	14.4[j]				
Inconel 82	4000					0.8	1.9[d]	0.9	2.6[d]
	8000					0.5	2.2[d]	1.1	2.7[d]
Hastelloy W	4000					0.3	2.5[k]	0.6	6.5[l]
	8000					0.6	4.1[k]	0.3	2.7[k]
Type 304 stainless steel	4000	0.4	f	0.7	f				
	8000	0.6	1.3[d]	0.8	f				
Type 308 stainless steel	4000					0.6	f	0.7	f
	8000					0.9	f	0.9	f

[a] At least nine readings averaged to the nearest tenth of a micrometer.

[b] Moderate number of protrusions, bulky, generally integral with surface layer.

[c] Many protrusions, bulky, generally integral with surface layer.

[d] Few protrusions, bulky, generally integral with surface layer.

[e] Few protrusions, bulky, some integral with surface layer and some disconnected.

[f] Very few protrusions – not measured.

[g] Moderate number of protrusions, both transgranular and intergranular, continuous with surface layer.

[h] Many protrusions, both transgranular and intergranular, continuous with surface layer.

[i] Highly irregular in thickness.

[j] Very many protrusions, deep, intergranular, continuous with surface layer.

[k] Few protrusions, both Widmanstätten platelets and bulky oxides, integral with surface (many very faint Widmanstätten platelets protruded deeper into the parent metal but were not measured).

[l] Very many protrusions, transgranular Widmanstätten platelets, continuous with surface layer.

We measured the depths of the integrated surface layer and of the total scale, which consisted of both the integrated surface layer and the protrusions. We usually made these two measurements, one right after the other, taking care to make the latter measurement where the protrusion extended deepest for a particular area. The thicknesses of these scales are given in Table 25.2 for the various alloys, when used as base metal and as filler metal, as functions of temperature and time of exposure to steam.

Because the surface layer often was not very uniform in thickness, nine or more measurements were averaged to establish each value given. We measured Inconel 82 eighteen times and Incoloy 800 twenty-seven times, since they appear in several weldments. Small mushrooming growths, apparently fed from superficial inclusions, appeared in many of the scales, but we considered these atypical and did not average them with the other measurements.

Note in Table 25.2 that the total depth of the scales on Inconel 625, Hastelloy X, and IN 102 at 595 and 650°C, when they were used either as base metal or filler metal, never exceeded 3 μm except in the case of the IN 102 alloy used as base metal at 595°C. Usually, the scales were thinner on these alloys when they were used as filler metal rather than as base metal. The scales formed on Incoloy 800 used as base metal (about 4.5 μm thick after exposure at 650°C) and on Inconel 82 used as filler metal (less than 3 μm thick after exposure at 650°C) were comparable in thickness to those of the foregoing alloys, while the scale on Hastelloy W used as filler metal usually penetrated further and increased significantly with the amount of cold working in the substrate. The scale penetrated into the Inconel 600 alloy still more because it tended to protrude into the substrate intergranularly. As expected, the scales formed on the 2.25% Cr–1% Mo low-alloy steel were extremely thick, indicating questionable usefulness even at 595°C. All scales were held intact during testing except for ones associated with the stainless steel weldment and possibly the scale of the Inconel 600 used as base metal. The scales on Inconel 625, Hastelloy X, IN 102, and Inconel 82 were very tenacious.

We are continuing studies of the general corrosion of specimens synthesized to simulate the root pass in composition and structure for the more important alloy combinations. Additional corrosion specimens are being introduced into the 595 and 650°C steam autoclaves, so that we now have under investigation specimens with surface finishes as welded, electropolished, sand blasted, belt ground (100 mesh), and belt ground and annealed.

Preferential Corrosion

Development of High-Pressure Corrosion Loop (J. P. Hammond)

The construction of the high-pressure corrosion loop equipped for injecting Cl and O contaminants to investigate stress-corrosion cracking of weldments is nearing completion. Shakedown tests of the loop will begin in May, and corrosion tests of weldment specimens, first using superheated steam devoid of moisture, should begin in July 1970.

Notes

1. J. P. Hammond, Fuels and Materials Development Program Quart. Progr. Rept. Dec. 31, 1969, ORNL-4520, pp. 327–331.

2. J. P. Hammond, "Corrosion of Advanced Steam Generator Alloy Weldments in 1100 and 1200F (595 and 650C) Steam," paper presented at National Association of Corrosion Engineers 26th National Conference, March 2–6, 1970, Philadelphia. To be published in the proceedings.

3. F. Eberle and J. H. Kitterman, "Scale Formations on Superheater Alloys Exposed to High Temperature Steam," pp. 67–113 in Behavior of Superheater Alloys in High Temperature, High Pressure Steam, American Society of Mechanical Engineers, New York, 1968.

Previous reports in this series:

ORNL-4330	Period Ending June 30, 1968
ORNL-4350	Period Ending September 30, 1968
ORNL-4390	Period Ending December 31, 1968
ORNL-4420	Period Ending March 31, 1969
ORNL-4440	Period Ending June 30, 1969
ORNL-4480	Period Ending September 30, 1969
ORNL-4520	Period Ending December 31, 1969

ORNL-4560
UC-25 — Metals, Ceramics, and Materials

INTERNAL DISTRIBUTION

1–3. Central Research Library
4. ORNL — Y-12 Technical Library
Document Reference Section
5–34. Laboratory Records Department
35. Laboratory Records, ORNL RC
36. ORNL Patent Office
37. R. E. Adams
38. G. M. Adamson, Jr.
39. S. E. Beall
40. R. J. Beaver
41. M. Bender
42. R. G. Berggren
43. D. S. Billington
44. N. C. Binkley
45. E. E. Bloom
46. A. L. Boch
47. E. S. Bomar
48. C. D. Bopp
49. B. S. Borie
50. R. A. Bradley
51. R. J. Breeding
52. R. B. Briggs
53. R. E. Brooksbank
54. D. A. Canonico
55. R. W. Carpenter
56. R. M. Carroll
57. J. V. Cathcart
58. D. L. Clark
59. G. W. Clark
60. Nancy C. Cole
61. K. V. Cook
62. W. H. Cook
63. G. L. Copeland
64. W. B. Cottrell
65. C. M. Cox
66. F. L. Culler
67. C. W. Cunningham
68. J. E. Cunningham
69. V. A. DeCarlo
70. W. E. Deeds
71. J. DeLuca
72. J. H. DeVan
73. J. R. DiStefano
74. C. V. Dodd
75. R. G. Donnelly
76. D. A. Dyslin
77. T. Eck
78. J. H. Erwin
79. K. Farrell
80. J. I. Federer
81. D. E. Ferguson
82. R. B. Fitts
83. B. Fleischer
84. B. E. Foster
85. A. P. Fraas
86. J. H Frye, Jr.
87. W. Fulkerson
88. L. C. Fuller
89. R. E. Gehlbach
90. T. G. Godfrey, Jr.
91. G. M. Goodwin
92. J. M. Googan (Y-12)
93. R. J. Gray
94. W. R. Grimes
95. A. G. Grindell
96. H. D. Guberman
97. L. L. Hall
98. W. O. Harms
99. R. F. Hibbs
100–104. M. R. Hill
105. D. O. Hobson
106. H. W. Hoffman
107. F. J. Homan
108. R. W. Horton
109. W. R. Huntley
110. H. Inouye
111. D. H. Jansen
112. J. D. Jenkins
113. W. H. Jordan
114–146. P. R. Kasten
147. G. W. Keilholtz
148. R. T. King
149. R. L. Klueh
150. R. W. Knight
151. W. J. Lackey
152. C. E. Lamb
153. J. A. Lane
154. J. M. Leitnaker
155. B. C. Leslie
156. C. S. Lever

157. T. B. Lindemer
158. C. T. Liu
159. H. R. Livesey
160. B.T.M. Loh
161. E. L. Long, Jr.
162. A. L. Lotts
163. C. D. Lundin
164. J. W. Luquire
165. R. N. Lyon
166. R. E. MacPherson
167. M. M. Martin
168. W. R. Martin
169. R. S. Mateer
170. R. W. McClung
171. H. E. McCoy, Jr.
172. H. C. McCurdy
173. R. E. McDonald
174. W. T. McDuffee
175. D. L. McElroy
176. C. J. McHargue
177. A. J. Miller
178. E. C. Miller
179. J. P. Moore
180. R. E. Moore
181. A. J. Moorhead
182. C. S. Morgan
183. J. G. Morgan
184. F. H. Neill
185. T. A. Nolan (K-25)
186. K. Notz
187. A. R. Olsen
188. M. F. Osborne
189. P. Patriarca
190. W. H. Pechin
191. R. B. Perez
192. A. M. Perry
193. S. Peterson
194. L. E. Poteat
195. R. A. Potter
196. M. K. Preston
197. W. W. Proaps
198. R. E. Reed
199. G. A. Reimann
200. A. E. Richt
201. P. L. Rittenhouse
202. H. E. Robertson
203. M. W. Rosenthal
204. D. J. Rucker
205. C. F. Sanders
206. G. Samuels
207. A. W. Savolainen
208. J. E. Savolainen
209. A. C. Schaffhauser
210. J. L. Scott
211. J. D. Sease
212. C. E. Sessions
213. W. A. Simpson
214. O. Sisman
215. G. M. Slaughter
216. S. D. Snyder
217. I. Spiewak
218. J. E. Spruiell
219. W. J. Stelzman
220. R. L. Stephenson
221. J. O. Stiegler
222. D. A. Sundberg
223. R. W. Swindeman
224. V. J. Tennery
225. K. R. Thoms
226. D. B. Trauger
227. T. N. Washburn
228. G. M. Watson
229. S. C. Weaver
230. M. S. Weschler
231. A. M. Weinberg
232. J. R. Weir, Jr.
233. W. J. Werner
234. H. L. Whaley, Jr.
235. G. D. Whitman
236. F. W. Wiffen
237. J. M. Williams
238. L. C. Williams
239. R. K. Williams
240. R. O. Williams
241. J. C. Wilson
242. R. G. Wymer
243. F. W. Young, Jr.
244. C. S. Yust
245. C. M. Adams, Jr. (Consultant)
246. Leo Brewer (Consultant)
247. L. S. Darken (Consultant)
248. Walter Kohn (Consultant)

EXTERNAL DISTRIBUTION

AIR FORCE MATERIALS LABORATORY, Wright-Patterson Air Force Base

249. C. H. Armbruster
250. H. M. Burte
251. G. Glenn
252. Technical Director

AIR FORCE WEAPONS LABORATORY, Kirtland Air Force Base

253. D. Brooks

AMES LABORATORY

254. O. N. Carlson
255. W. L. Larsen
256. M. Smutz
257. F. H. Spedding

ARGONNE NATIONAL LABORATORY

258. L. Baker
259. J. H. Kittel
260. M. V. Nevitt
261. P. G. Shewmon
262. R. C. Vogel

LMFBR PROGRAM OFFICE, Argonne National Laboratory

263. A. Amorosi
264. L. Burris
265. L. Kelman
266. J. M. McKee

AEC-RDT SITE REPRESENTATIVES

267. M. E. Jackson, Argonne National Laboratory
268. D. J. Wille, Atomic Power Development Associates
269. R. L. Morgan, Atomics International
270. J. V. Levy, General Electric, Sunnyvale
271. R. H. Ball, Gulf General Atomic
272. J. E. Hebert, Idaho
273. D. A. Moss, Idaho
274. K. A. Trickett, Idaho
275. D. F. Cope, Oak Ridge National Laboratory
276. C. L. Matthews, Oak Ridge National Laboratory
277. P. G. Holsted, Battelle-Northwest
278. J. Sako, Battelle-Northwest
279. Theodore Iltis, Westinghouse Advanced Reactor Division
280. Atomic Energy Commission Library, Washington

DIVISION OF NAVAL REACTORS, AEC, Washington

281. R. H. Steele

DIVISION OF REACTOR DEVELOPMENT AND TECHNOLOGY, AEC, Washington

282. J. C. Crawford, Jr.
283. G. W. Cunningham
284. A. Giambusso
285. H. G. Hembree
286. K. E. Horton
287. J. R. Hunter
288. E. E. Kintner
289. W. H. Layman
290. W. H. McVey
291. J. J. Morabito
292. R. E. Pahler
293. A. J. Pressesky
294. M. A. Rosen
295. J. M. Simmons
296. E. E. Sinclair
297. B. Singer
298. A. Taboada
299. A. N. Tardiff
300. A. Van Echo
301. C. E. Weber
302. M. J. Whitman

DIVISION OF RESEARCH, AEC, Washington

303. P. W. McDaniel
304. D. K. Stevens

DIVISION OF SPACE NUCLEAR SYSTEMS, AEC, Washington

305. R. E. Anderson
306. D. Beard
307. J. F. Griffo
308. C. E. Johnson
309. A. P. Litman
310. J. A. Powers
311. F. C. Schwenk

OAK RIDGE OPERATIONS OFFICE

312. Laboratory and University Division
313. Patent Office

ATOMIC POWER DEVELOPMENT ASSOCIATES

314. E. C. Kovacic
315. A. A. Shoudy

ATOMICS INTERNATIONAL

316. T. A. Moss
317. H. Pearlman
318. J. G. Asquith

BABCOCK AND WILCOX COMPANY, Lynchburg, Virginia 24505

319. C. Baroch
320. S. P. Grant
321. C. Johnson
322. L. Weissert

BATTELLE MEMORIAL INSTITUTE, Columbus, Ohio

323. W. Berry
324. D. Keller
325. S. J. Paprocki
326. Defense Materials Information Center

BATTELLE-NORTHWEST, Richland, Washington

327. A. L. Bement
328. J. J. Cadwell
329. T. T. Claudson
330. D. L. Condotta
331. E. Evans
332. J. E. Hanson
333. B. R. Hayward
334. B. M. Johnson
335. W. E. Roake
336. D. W. Shannon
337. J. C. Tobin
338. R. G. Wheeler
339. Technical Information File

FAST FLUX TEST FACILITY, Battelle-Northwest

340. E. R. Astley

BROOKHAVEN NATIONAL LABORATORY

341. D. H. Gurinsky
342. C. Klamut

BUREAU OF MINES

343. Haruo Kato, Albany Metallurgy Research Center, P.O. Box 70, Albany, Oregon 97321
344. T. Sullivan, Bureau of Mines, Boulder City, Nevada 89005

COMBUSTION ENGINEERING

345. W. P. Chernock
346. S. S. Christopher

GENERAL ELECTRIC, Cincinnati

347. D. H. Ahmann
348. H. C. Brassfield
349. V. P. Calkins
350. E. Hoffman
351. J. McGurty

GENERAL ELECTRIC, Nuclear Systems Programs, Cincinnati

352. E. E. Hoffman

GENERAL ELECTRIC, San Jose

353. R. Duncan
354. H. Klepfer

GENERAL ELECTRIC, Pleasanton

355. H. W. Alter

GENERAL ELECTRIC, Sunnyvale

356. K. P. Cohen
357. F. Comprelli
358. R. Skavdahl
359. C. Spalaris
360. E. L. Zebroski

GULF GENERAL ATOMIC

361. D. B. Coburn
362. A. J. Goodjohn
363. J. P. Howe
364. S. Jaye
365. J. F. Watson

IDAHO NUCLEAR CORPORATION

366. W. C. Francis
367. William Yuill

ILLINOIS INSTITUTE OF TECHNOLOGY RESEARCH INSTITUTE

368. D. J. McPherson

JET PROPULSION LABORATORY (NASA)

369. J. Davis

KNOLLS ATOMIC POWER LABORATORY

370. R. F. Wojciescak
371. Document Library

LOS ALAMOS SCIENTIFIC LABORATORY

372. R. D. Baker
373. D. B. Hall
374. J. A. Leary
375. R. Perkins
376. R. E. Peterson
377. Reports Library

MOUND LABORATORY

378. R. G. Grove

NASA HEADQUARTERS

379. J. J. Lynch

NASA, LEWIS RESEARCH CENTER

380. M. Ault
381. J.W.R. Creagh
382. J. J. Lombardo
383. T. P. Moffitt
384. F. E. Rom
385. L. Rosenblum
386. N. D. Sanders
387. N. Saunders
388. C. M. Scheuermann
389. H. Schwartz

NAVAL RESEARCH LABORATORY

390. J. R. Hawthorne
391. C. Serpan
392. L. E. Steele

NORTH CAROLINA UNIVERSITY, Raleigh, North Carolina 27607

393. J. Beeler
394. R. E. Dahl

NUCLEAR MATERIALS AND EQUIPMENT CORPORATION

395. C. Caldwell
396. K. Puechl

OHIO STATE UNIVERSITY, Columbus, Ohio 43212

397. M. G. Fontana
398. R. W. Staehle

RENSSELAER POLYTECHNIC INSTITUTE

399. W. Dickinson
400. W. F. Savage
401. C. B. Willingham, Jr.

SANDIA CORPORATION

402. J. Read Holland
403. J. Jacobs
404. D. R. Johnson

SAVANNAH RIVER LABORATORY

405. P. H. Permar
406. S. P. Rideout

TRW SYSTEMS (NASA), Redondo Beach, California 90278

407. H. Lurie

UNION CARBIDE CORPORATION, New York

408. J. A. Swartout

UNION CARBIDE CORPORATION, Materials Systems Division, Indianapolis

409. C. F. Leitten, Jr.

UNITED NUCLEAR CORPORATION

410. A. Strasser

UNIVERSITY OF CALIFORNIA, Lawrence Radiation Laboratory, Livermore

411. W. R. Holman
412. J. S. Kane
413. L. W. Roberts
414. A. J. Rothman
415. B. Rubin

U.S. NAVAL AIR SYSTEM COMMAND (AIR-52031B)

416. T. Kearns
417. I. Machlin

USAEC Scientific Representative, American Embassy, Box 40 FPO, N.Y. 09510

418. W.L.R. Rice

WESTINGHOUSE, Advanced Reactor Division, Waltz Mill Site

419. E. C. Bishop
420. A. Boltax
421. J.C.R. Kelly
422. P. J. Levine
423. P. Murray
424. W. E. Ray
425. G. A. Whitlow

WESTINGHOUSE, Astronuclear Laboratory

426. R. T. Begley
427. D. C. Goldberg

WESTINGHOUSE, Atomic Power Division

428. T. Stern

WESTINGHOUSE, Bettis

429. R. H. Fillnow
430. P. N. Gustafson
431. Westinghouse Bettis Laboratory Library

432–636. Given distribution as shown in TID-4500 under Metals, Ceramics, and Materials category (25 copies – CFSTI)